



Interaction between Flow Induced Pulsations and Multiphase Flows in Gas Liquid Systems

Francesco Sanna

► To cite this version:

Francesco Sanna. Interaction between Flow Induced Pulsations and Multiphase Flows in Gas Liquid Systems. Mechanics [physics.med-ph]. Le Mans Université, 2016. English. NNT : 2016LEMA1008 . tel-01346616

HAL Id: tel-01346616

<https://theses.hal.science/tel-01346616>

Submitted on 19 Jul 2016

HAL is a multi-disciplinary open access archive for the deposit and dissemination of scientific research documents, whether they are published or not. The documents may come from teaching and research institutions in France or abroad, or from public or private research centers.

L'archive ouverte pluridisciplinaire **HAL**, est destinée au dépôt et à la diffusion de documents scientifiques de niveau recherche, publiés ou non, émanant des établissements d'enseignement et de recherche français ou étrangers, des laboratoires publics ou privés.

Thèse de Doctorat

FlowAirS



Francesco SANNA

*Mémoire présenté en vue de l'obtention du
grade de Docteur de l'Université du Maine
sous le sceau de l'Université Bretagne Loire*

École doctorale : Science pour l'Ingénieur, Géosciences, Architecture

Discipline : 60-Mécanique

Spécialité : Acoustique

Unité de recherche : LAUM (UMR 6613) et TNO

Soutenue le 15 avril 2016

Thèse N° : 81049

INTERACTION BETWEEN FLOW INDUCED PULSATIONS AND MULTIPHASE FLOWS IN GAS LIQUID SYSTEMS

JURY

Rapporteurs :	Avraham HIRSCHBERG , Professeur, Technische Universiteit Eindhoven Christophe SCHRAM , Professeur, the von Karman Institute for Fluid Dynamics
Examineurs :	Yves GERVAIS , Professeur, Université de Poitiers
Invité(s) :	Stefan P.C. BELFROID , Chercheur, TNO, (Pays-Bas)
Directeur de Thèse :	Yves AURÉGAN , Directeur de Recherches, LAUM, CNRS
Co-encadrant de Thèse :	Joachim GOLLIARD , Docteur, TNO, (Pays-Bas)

*What does not kill you
makes you stronger*

Ad maiora semper...

Résumé

Le couplage entre un écoulement instable et des résonances acoustiques dans des systèmes de conduites peut conduire à des phénomènes d'oscillations auto-induites. Ce type de phénomènes trouve principalement place dans des conduites latérales fermées, par exemple dans des systèmes de transport ou de compression de gaz. L'objectif de ce travail est d'étudier les oscillations auto-induites dans le cas où le fluide transporté ne se limite pas à un gaz, mais est un mélange de gaz et de liquide. Les pulsations sont mesurées dans des conduites latérales fermées, pour deux types de configurations (en tandem et en croix), avec écoulement d'un mélange variable d'air et d'eau. La position de l'injection d'eau est variable afin d'obtenir plusieurs régimes d'écoulement diphasique. Les résultats indiquent que la présence d'eau a un effet important sur les niveaux de pulsations dans les conduites. Cet effet a pu être attribué à deux mécanismes dus à la présence d'eau : les instabilités de couches de mélange sont modifiées et l'amortissement des ondes acoustiques est amplifié.

Le deuxième mécanisme a été quantifié à l'aide de mesures sur un montage expérimental dédié conçu pour avoir un écoulement stratifié. On a observé que, dans tous les cas, la présence d'eau augmente l'amortissement. Cette augmentation a pu être attribuée à la réduction de la section effective de la conduite (due au remplissage partiel par l'eau) et à l'augmentation de la friction turbulente à l'interface entre les phases liquide et gazeuse.

Mots clés :

Oscillations auto-induites ; Turbulence ; Conduites latérales fermées ; Cavités résonnantes profondes ; Ecoulement diphasique stratifié ; Amortissement acoustique ; Acoustique.

Abstract

Coupling between flow instabilities and acoustic resonances in ducts with closed side branches leads to Flow Induced Pulsations (FIPs). This is a typical phenomenon in engineering applications (gas transport systems, compressor installations, and chemical plants). The objective of this work is to extend the knowledge about FIPs when the transported medium is not uniquely gas but a combination of gas and (a small quantity of) liquid. For two configurations of double side branches (in *tandem* and in *quasi-cross*), the amplitude of pressure pulsations in the side branches was measured for different liquid injection rates. This was repeated with the liquid injection point located at different places to allow different flow regimes at the pipe connections. The results show a strong effect of the water content on the pulsations. On basis of these results and additional measurements, the following hypotheses for the effect of liquid were made: (1) interaction of the liquid with the flow instability and (2) increase of the acoustical damping in the ducts in presence of liquid.

The effect of liquid on damping was measured with a dedicated test setup designed to have a stratified flow. It was found that the liquid always increases the acoustical damping, mainly due to the reduction of the effective cross section by the liquid, and because of the increased turbulent friction at the interface between gas and liquid.

Keywords :

Flow Induced Pulsations; Turbulence; Side branch; Deep cavities; Multiphase stratified flow ; Acoustical damping; Acoustics.

Aknowledgements

This Ph.D. thesis is the final product of the work conducted between October 2012 and October 2015 within the Marie Curie European Project FlowAirS (Silent Air Flows in transport, building and power generation) FP7-PEOPLE-2011-ITN-289352.

The last three years have been really short but not enough to have a big impact on my future, not only for the knowledge and competences acquired, but also and especially for the people I have met and I would like to thank here.

TNO is the place where I spent most of my time during the last three years. I am not afraid to say that I feel at home here. It has been a long story. I am particularly grateful to Joachim Golliard and Stefan Belfroid. I really appreciated the dedication and the attention you gave me to support my work. Thanks also to Garrelt Alberts for your attention in addressing new challenges which are always “part of the game”.

My staying here at TNO was not only made of work, experiments, or plots. TNO is also the place where I have met friends and not only colleagues: the discussions, dinners, and drinks that I had with Jesper van der Putte and Pejman Shoeibi Omrani are really hard to forget. I am really thankful because a “how are you” or “wil je een kopje koffie” helped me more than the rest. Thanks also to Daniele Violato for his nice and explicative drawings on the whiteboard, to my official officemate Aris for listening to my Italian complaints, to Tom, and to Can for the nice chit-chats. Thanks also for the useful technical support of Olav Vijlbrief, Andries van Wijhe and Jan Kuijt.

I am also really grateful to all the people involved in FlowAirS. First, Yves Aurégan. Thanks for building up the consortium and for supporting me as my supervisor. It was a great pleasure to be part of such a nice group of scientists, with whom I had the possibility to challenge new topics and to explore new cultures and new places. The weird meeting in Paris Montparnasse with Deepesh, dancing salsa in Le Mans with Karim and Konstantine, the disco in Leuven with Antonio, the crazy night in Munich with Karim, Joowha, Antonio and Konstantine, the dinner in the desert of Cairo are just some of our experiences ... They are really too many to recall!

Un grazie infinito va a tutti gli amici italiani di Delft. E’ grazie a loro se le serate piovose non sono diventate monotonia ma un utile strumento per vedersi... Grazie soprattutto al fedele Angelo, alla caciara Beatrice, all’intramontabile Cecilia, al latitante Giulio, all’attentissima Lavinia, e al mio chitarrista Marco. Grazie anche a Calzolari, Fagiani, Fiscaletti, Greta, Katerina, Mariani, Sivia e a tutti coloro che sono arrivati e partiti!

Non ci dimentichiamo delle storiche amicizie. Prima di tutto Pisa, vituperio delle genti e la mia città di formazione. Per gli ultimi tre anni sono estremamente riconoscente a due persone in particolare. Ad Andrea Viti, come sempre, grazie per le chiamate, le lamentele e per essere, volente o nolente, coinvolto in tutti i miei stornelli serali contro #youknowwho2. Grazie all. Avv. Viviana Trapani per le mail giornaliere, per le bevute e per esserci supportati per il raggiungimento dei famosi titoli, e chist invatt...Un grazie poi a tutti gli altri: Francesco, Alessandro, Laura, Antonio, Nicoletta, Maria e Serena.

E come da tradizione il cerchio si chiude sempre nella mia terra, la mia amata Sardegna. Ormai si parla di amicizie quasi trentennali. Come sempre, grazie a Paola per la sua presenza e per le conversazioni infinite, a Fabrizio, Federica, Roberta e Rossana.

Last but not least, un grazie enorme alla mia famiglia: ai miei genitori e ai miei fratelli, ognuno dei quali in maniera diversa contribuisce giornalmente al mio successo. Grazie anche a mia nonna e zia Nanna, a tutti gli zii e tutti i cugini. E un grazie anche a chi purtroppo non c'è più e che mi guarda e guida da lassù.

That's the very end of a very difficult chapter to write... from now on, it will be a memory, a good memory.

The End

Delft, February 19th, 2016

Contents

Aknowledgements	v
Contents.....	vii
List of figures	xi
List of tables	xvii
1. Introduction	19
Résumé	19
1.1. The FlowAirS Project.....	20
1.2. Thesis outline.....	20
2. On the effect of liquid on flow-induced pulsations in a pipe with two closed side branches: two case studies	23
Résumé	23
Nomenclature.....	24
2.1. Introduction	24
2.1.1 Flow-Induced Pulsations in closed side branches	25
2.1.2 Multiphase flow background	26
2.1.3 Flow-Induced Pulsations in pipes transporting gas-liquid mixture.....	27
2.2. Setup and experimental technique	28
2.2.1 Supply system.....	29
2.2.2 Test setup	29
2.2.3 Data acquisition and analysis.....	33
2.3. Experimental Results	33
2.3.1 Tandem Configuration.....	33
2.3.2 Quasi-Cross Configuration	43
2.4. Discussion.....	49
2.4.1. Amplitudes.....	49
2.4.2. Frequency	51
2.4.3. Strouhal number.....	52
2.5. Conclusions	53
References	54
3. On the effect of water film on flow-induced pulsations in closed side branches in tandem configuration	59
Résumé	59
Nomenclature.....	60
3.1 Introduction	60
3.2 Design of the experimental setup and experimental method	61
3.2.1. Setup	61

3.2.2. Experimental technique and post-processing.....	62
3.3. Flow visualizations recordings	64
3.4 Experimental results	65
3.4.1. Results – Far Injector.....	66
3.4.2. Results– Close Injector – Top Injection.....	68
3.4.3. Results – Close Injector – Bottom Injection	70
3.5. Discussion.....	71
3.6. Conclusions	73
References	74
4. Acoustical damping in a smooth horizontal pipe with stratified/stratified wavy air-water mixture flows.....	77
Résumé	77
Nomenclature.....	78
4.1. Introduction	78
4.1.1. Different contributions to the acoustical damping	80
4.1.2. Multiphase flow in a duct	82
4.2. A new model to describe the interaction between turbulent multiphase flows and acoustics at low frequencies and low Mach numbers	86
4.3. Setup and experimental procedure.....	87
4.3.1. Test facility	88
4.3.2. Test Setup	88
4.3.3. Test Matrix	91
4.3.4. Experimental technique and post-processing.....	93
4.3.5. Presentation of the results	96
4.4. Experimental Results	97
4.4.1. Dry pipe – No mean flow (Campaign #1).....	97
4.4.2. Only gas mean flow (Campaign #2)	98
4.4.3. Quiescent water without gas mean flow (Campaign #3)	101
4.4.4. Mean gas flow and liquid (Campaign #4).....	103
4.5. Conclusions	110
References	111
5. Conclusions and Perspectives	115
Résumé	115
References	118
A. Evaluation and calibration of capacitance probes for hold-up estimation: a comparison between different methods for a stratified (wavy) air-water mixture.....	119
Abstract.....	119
A.1. Capacitance probes	119
A.1.1. Literature review.....	119
A.1.2. Description of a capacitance probe	120
A.1.3. Calibration of the probe without flow	120

A.1.4. Use of the calibrated capacitance probe with flow	123
A.2. Validation of the use of the capacitance probes for an experimental campaign	124
A.2.1. Hold-up estimated by means of two capacitance probes	125
A.2.2. Hold Up estimated by means of flow visualizations	125
A.2.3. Hold Up estimated by means of OLGA simulations.....	128
A.2.4. Comparison and discussion.....	129
References	131
B. Calibration of the microphones	135
B.1. Empirical calibration of the relative distance between microphones	137
B.2. Empirical calibration of the sensitivity of the microphones, including the effect of non-perfect reflection coefficients and acoustical damping	138
B.2.1. Correction on the reflection coefficient	138
B.2.2. Implementation of acoustical damping	139
B.2.3. Empirical calibration of the sensitivity of the microphones.....	140
B.3. Relative calibration between the transducers located upstream and downstream the test object	141
B.4. Script (Only for the upstream source)	142
C. Acoustic damping in corrugated pipes: An experimental study	143
Nomenclature.....	143
C.1. Introduction.....	143
C.2. Experimental setup and experimental method	144
C.3. Results.....	145
C.3.1. Results – Smooth pipe.....	145
C.3.2. Results – Corrugated pipe: configuration A and Configuration B	147
References	150
Curriculum Vitae.....	153

List of figures

Figure 2.1. Pressure distribution in the tandem configuration (a) and in the cross configuration (b).	25
Figure 2.2. Flow Pattern map for a horizontal smooth pipe with inner diameter $D_{mp} = 0.0525$ m (Shoham, 2006). Experiments were conducted in the range of U_{SG} and U_{SL} highlighted by the red dashed rectangle.	27
Figure 2.3. Distribution of water in stratified wavy dispersed flow (a) and annular dispersed flow (b).	28
Figure 2.4. Experimental setup.	29
Figure 2.5. Step 1 of tuning: non-dimensional pulsation [-] measured at the closed end of the upstream T-junction as function of the superficial gas velocity U_{SG} [m/s] for different lengths of the downstream side branch.	31
Figure 2.6. Step 2 of tuning: non dimensional pulsation [-] measured at the closed end of the upstream T-junction as function of the superficial gas velocity [m/s] for different lengths of the upstream side branch.	31
Figure 2.7. Scheme of the BETE-PJ nozzle (a) and BETE-P (b) (BETE).	32
Figure 2.8. Tandem configuration, far injector. Dry gas: dimensional pressure pulsations [Pa] as function of the superficial gas velocity U_{SG} [m/s].	34
Figure 2.9. Tandem configuration, far injector. Dry gas: non-dimensional pulsations [-] as function of the Strouhal number [-] based on the superficial gas velocity U_{SG} [m/s].	34
Figure 2.10. Tandem configuration, far injector. Wet gas: non-dimensional pulsations [-] as function of the liquid volumetric flow rate [m^3/s] (a) and of the percentage ratio of the liquid volumetric flow rate to the gas volumetric flow rate [%] (b).	35
Figure 2.11. Tandem configuration, far injector. Wet gas: non dimensional pulsation pressure [-] as function of the superficial gas velocity U_{SG} [m/s] in the Q_L range $0-1.3e^{-5} m^3/s$	36
Figure 2.12. Tandem configuration, far injector. Wet gas: pulsation frequency [Hz] as function of the superficial gas velocity U_{SG} [m/s] in the Q_L range $0-1.3e^{-5} m^3/s$. The dots mark the frequency at which the peak of maximum of pressure amplitude occurs.	36
Figure 2.13. Tandem configuration, far injector. Wet gas: non-dimensional pulsation pressure [-] as function of the Strouhal number [-] based on the superficial gas velocity [m/s] in the Q_L range $0-1.3e^{-5} m^3/s$ (0-800 ml/min).	36
Figure 2.14. Tandem configuration, far injector. Wet gas: non-dimensional pulsation pressure [-] as function of the superficial gas velocity U_{SG} [m/s] in the Q_L range $2.8e^{-5}-1.0e^{-4} m^3/s$. The data for dry gas and for $Q_L = 1.3e^{-6} m^3/s$ (800 ml/min) are also provided for reference.	37
Figure 2.15. Tandem configuration, far injector. Wet gas: pulsation frequency [Hz] as function of the superficial gas velocity U_{SG} [m/s] in the Q_L range $2.8e^{-5}-1.0e^{-4} m^3/s$ (1700-6000 ml/min). The data for dry gas and for $1.3e^{-5} m^3/s$ (800 ml/min) are also provided for reference. The dots mark the frequency at which the peak of maximum of pressure amplitude occurs.	37
Figure 2.16. Tandem configuration, far injector. Wet gas: non-dimensional pulsation pressure as function of the Strouhal number in the Q_L range $2.8e^{-5}-1.0e^{-4} m^3/s$ (1700-6000 ml/min). a) Superficial gas velocity used as reference; b) actual gas velocity used as reference.	38
Figure 2.17. Tandem configuration, far injector. Wet gas: non-dimensional pulsation pressure [-] as function of the Strouhal number [-] based on the actual gas velocity U [m/s] and effective side branch width D_{eff} [m] of Table 2.4. The data for dry gas is also provided for reference.	39
Figure 2.18. Tandem configuration, far injector. Wet gas: non dimensional pulsation pressure [-] as function of the superficial gas velocity U_{SG} [m/s] in the Q_L range $1.3e^{-5}-2.8e^{-5} m^3/s$ (800-1700 ml/min). The data for dry gas is also provided for reference.	39
Figure 2.19. Tandem configuration, far injector. Wet gas: pulsation frequency [Hz] as function of the superficial gas velocity U_{SG} [m/s] in the Q_L range $1.3e^{-5}-2.8e^{-5} m^3/s$ (800-1700 ml/min). The data for dry gas is also provided for reference.	40

Figure 2.20. Tandem configuration, far injector. Wet gas: non-dimensional pulsations [-] based on the superficial gas velocity U_{SG} [m/s] as function of the Strouhal number [-] in the Q_L $1.3e^{-5}$ - $2.8e^{-5}$ m^3/s (800-1700 ml/min). The data for dry gas is also provided for reference.	40
Figure 2.21. Tandem Configuration. Dry gas: comparison between the non-dimensional pressure pulsations [-] measured at the upstream side branch as function of the superficial gas velocity U_{SG} [m/s] for the case of far and close injector.....	41
Figure 2.22. Tandem configuration, close injector. Wet gas: non-dimensional pulsations [-] as function of the superficial gas velocity U_{SG} [m/s] in the Q_L range $0-1.0e^{-4}$ m^3/s	41
Figure 2.23. Tandem configuration, close injector. Wet gas: non dimensional pulsation pressure [-] as function of the Strouhal number Sr [-] based on superficial gas velocity U_{SG} [m/s] in the Q_L range $0-1.3e^{-5}$ m^3/s	42
Figure 2.24. Tandem configuration, close injector. Wet gas: pulsation frequency [Hz] as function of the superficial gas velocity U_{SG} [m/s] in the Q_L range $0-1.3e^{-5}$ m^3/s	42
Figure 2.25. Tandem configuration, close injector. $Q_L = 1.0e^{-5}$ m^3/s , at the entrance of the downstream side branch. The mixture flows from left to right.	43
Figure 2.26. Quasi-cross configuration, far injector. Dry gas: peak pressure pulsations [Pa] as function of the superficial gas velocity U_{SG} [m/s]......	44
Figure 2.27. Quasi-cross configuration, far injector. Wet gas: mon dimensional pulsation pressure [-] as function of the superficial gas velocity [m/s]. (Black lines: $0-3.0e^{-5}$ m^3/s ; blue lines: $3.0e^{-5}-1.0e^{-4}$ m^3/s).	44
Figure 2.28. Quasi-cross configuration, far injector. Wet gas: pulsation frequency [Hz] corresponding to the maximum pulsation pressure as function of the liquid volumetric flow rate Q_L [m^3/s] (a) and the percentage volume fraction [%] (b).	45
Figure 2.29. Quasi-cross configuration, far injector. Wet gas: non-dimensional pressure pulsation [-] as function of the Strouhal number [-] based on the superficial gas velocity U_{SG} (a) and on the actual gas velocity U (b)....	46
Figure 2.30. Quasi-cross configuration, far and close injector. Dry gas: comparison between the non-dimensional pressure pulsations [-] measured at the upstream side branch as function of the superficial gas velocity U_{SG} [m/s]......	47
Figure 2.31. Quasi-cross configuration, close injector. Wet gas: non-dimensional pulsation pressure [-] as function of the superficial velocity U_{SG} [m/s]......	47
Figure 2.32. Quasi-cross configuration, close injector. Wet gas: non-dimensional pressure pulsation [-] as function of the Strouhal number [-] based on the superficial gas velocity U_{SG} [m/s]......	48
Figure 2.33. Quasi-cross configuration, close injector. Wet gas: pulsation frequency [Hz] corresponding to the maximum pulsation pressure as function of the liquid volumetric flow rate Q_L [m^3/s]......	48
Figure 2.34. Non-dimensional pulsation [-] as function of the volumetric liquid flow rate Q_L [m^3/s].	50
Figure 2.35. Pulsation frequency [Hz] as function of the liquid volumetric flow rate Q_L [m^3/s].	52
Figure 2.36. Strouhal number [-] based on the superficial gas velocity U_{SG} [m/s] as function of the liquid volumetric flow rate Q_L [m^3/s].	53
Figure 3.1. Double side branch - Tandem configuration. Generation of the vortex shedding and mechanism loop (a), and pressure distribution (b)......	60
Figure 3.2. Geometrical details of the configuration tested.	61
Figure 3.3. Flow pattern map for horizontal smooth pipes with inner diameter $D_{mp} = 0.025$ m (Shoham, 2006).63	
Figure 3.4. Inside view sketch of the upstream T-junction: a) Far liquid injection, b) Close top liquid injection, c) Close bottom liquid injection.	63
Figure 3.5. Location of cameras.	64
Figure 3.6. Tandem configuration, far injector. Flow visualizations at the upstream T-junction for different liquid volumetric flow rate Q_L and no-slip liquid volume fractions λ : a) $Q_L = 1.1 \times 10^{-6}$ m^3/s , $\lambda = 1.46 \times 10^{-4}$; b) $Q_L = 1.9 \times 10^{-6}$ m^3/s , $\lambda = 2.53 \times 10^{-4}$; c) $Q_L = 4.2 \times 10^{-6}$ m^3/s , $\lambda = 5.59 \times 10^{-4}$; d) $Q_L = 6.9 \times 10^{-6}$ m^3/s , $\lambda = 9.19 \times 10^{-4}$; e) $Q_L = 1.1 \times 10^{-5}$ m^3/s , $\lambda = 1.46 \times 10^{-3}$. The superficial gas velocity is the one corresponding to the peak. The air/water mixture flows from right to left.	65
Figure 3.7. Tandem configuration, close-top injector. Flow visualizations at the upstream T-junction for different liquid volumetric flow rate Q_L and no-slip liquid volume fractions λ : a) $Q_L = 1.7 \times 10^{-7}$ m^3/s , $\lambda = 2.46 \times 10^{-5}$; b) $Q_L = 1.1 \times 10^{-6}$ m^3/s , $\lambda = 1.59 \times 10^{-4}$; c) $Q_L = 2.5 \times 10^{-6}$ m^3/s , $\lambda = 3.62 \times 10^{-4}$; d) $Q_L = 2.7 \times 10^{-6}$ m^3/s , $\lambda = 3.91 \times 10^{-4}$; e) $Q_L = 3.0 \times 10^{-6}$ m^3/s , $\lambda = 4.34 \times 10^{-4}$. The superficial gas velocity is the one corresponding to the maximum amplitude ($U_{SG} \approx 14$ m/s). The air/water mixture flows from right to left. Left photos for Camera 1, right photos of Camera 2.	65

Figure 3.8. Tandem configuration, far injector. Dry gas: pressure pulsation amplitude [Pa] as function of the superficial gas velocity U_{SG} [m/s].	66
Figure 3.9. Tandem configuration, far injector. Wet gas: pressure pulsations [Pa] as function of the superficial gas velocity U_{SG} [m/s].	67
Figure 3.10. Tandem configuration, far injector. Wet gas: pulsation frequency [Hz] as function of the superficial gas velocity U_{SG} [m/s].	67
Figure 3.11. Tandem configuration, far injector. Wet gas: non-dimensional pulsations [-] as function of the Strouhal number [-] based on the superficial gas velocity U_{SG} [m/s].	68
Figure 3.12. Tandem configuration, close-top injection. Dry gas: pressure pulsations [Pa] as function of the superficial gas velocity U_{SG} [m/s].	69
Figure 3.13. Tandem configuration, close-top injector. Wet gas: pressure pulsations [Pa] as function of the liquid volumetric flow rate Q_L [m ³ /s], for $U_{SG} = 14.3$ and 14.7 m/s.	69
Figure 3.14. Tandem configuration, close-bottom injection. Dry gas: pressure pulsations [Pa] as function of the superficial gas velocity U_{SG} [m/s].	70
Figure 3.15. Tandem configuration, close-bottom injection, wet gas: Pressure pulsations [Pa] as function of liquid volumetric flow rate Q_L [m ³ /s], for $U_{SG} = 14.7, 15.3$ and 15.9 m/s.	71
Figure 3.16. Comparison of the pressure measurements results.	71
Figure 3.17. Extrapolated experimental data and quadratic fitting of damping measurements [1/m] at 320 Hz as function of the percentage ratio (Golliard et al., 2013).	72
Figure 3.18. Comparison between the experimental results and the 1D acoustical model as function of the percentage volume fraction [%].	73
Figure 4.1. Flow pattern map for 25.0 mm horizontal smooth pipe (Shoham, 2006). Experiments were conducted in the range of U_{SG} and U_{SL} highlighted by the red dashed rectangle.	82
Figure 4.2. 1D multiphase flow simulations with the software OLGA: estimation of the liquid hold up β_L in a 25.0 mm inner diameter pipe at different superficial liquid and gas velocities.	83
Figure 4.3. Scheme of a stratified gas-liquid flow in a fully horizontal pipe.	85
Figure 4.4. Experimental facility and setup.	87
Figure 4.5. Upstream 45 m hose used as anechoic boundary condition. A similar one is used downstream.	88
Figure 4.6. Acoustical preliminary test results: reflection coefficient [-] of a 45 m hose as function of frequency [Hz].	88
Figure 4.7. Hold-up interpolation curves as function of the voltage difference $V - V_0$ [V].	89
Figure 4.8. Hold-up [-] as function of the superficial liquid velocity (U_{SL}) for constant superficial gas velocity (U_{SG}): (a) $U_{SG} \sim 2.5$ m/s, (b) $U_{SG} \sim 5.5$ m/s, (c) $U_{SG} \sim 10.5$ m/s.	90
Figure 4.9. Frequency range [Hz] for each 2 microphones' combination.	91
Figure 4.10. Scheme of the four experimental campaigns: no mean flow (a), only gas mean flow (b), different liquid void fractions (c), and gas and liquid mixture flow (d).	92
Figure 4.11. Definitions and notation for diffraction matrix of the tested object.	95
Figure 4.12. No gas mean flow, no liquid: transmission coefficient T [-] as function of frequency [Hz].	97
Figure 4.13. No gas mean flow, no liquid: damping coefficient α [1/m] as function of frequency [Hz].	98
Figure 4.14. No gas mean flow, no liquid: damping coefficient ratio α/α_0 [-] as function of frequency [Hz].	98
Figure 4.15. Only gas mean flow: damping coefficient α [1/m] (a), the ratio of the measured damping to the Kirchhoff damping α_0 (b), as function of frequency [Hz] in the direction of the flow (-) and against flow (-) at different gas velocities U_{SG} : 0 m/s (magenta), ~ 2.5 m/s (green), ~ 10.5 m/s (red).	98
Figure 4.16. Comparison between the different models used to take into account the convection effects (Davies, and Dokumaci) and their approximation for different Mach numbers at 320 Hz.	99
Figure 4.17. Comparison between the different models used to take into account the convection effects (Davies, and Dokumaci) and their approximation for different frequencies at Mach $M = 0.03$.	99
Figure 4.18. Only gas mean flow: damping coefficient ratio corrected by the convection term of Davies (1988) - $1 \pm M$ - (a), and by the convection term of Golliard (2015) as approximation of Dokumaci (1995) - $1 \pm 2M$ - (b) as function of frequency [Hz] in the direction of the flow (-) and against flow (-) at different gas velocities U_{SG} : 0 m/s (magenta), ~ 2.5 m/s (green), ~ 10.0 m/s (red).	100
Figure 4.19. Only gas mean flow: estimate of the ratio of the acoustic boundary layer δ_{ac} to the sub-viscous boundary layer δ_1 as function of frequency [Hz].	100

Figure 4.20. No gas mean flow, only liquid ($U_{SL} = 0$ m/s): Acoustical damping coefficient [1/m] as function of frequency [Hz] measured at different liquid hold-up β_L [-]. The grey surface indicates a range of frequency where data it not considered reliable.	101
Figure 4.21. No gas mean flow, only liquid ($U_{SL} = 0$ m/s): ratio of the acoustical damping coefficient α to the Kirchhoff damping α_0 and as function of frequency [Hz] by using the full and the corrected hydraulic diameter in the direction of (a1 and a2) and against (b1 and b2) flow. The legend is the same as in Figure 4.20. The grey surface indicates a range of frequency where data is not considered reliable.....	102
Figure 4.22. Flow visualizations at different gas and liquid velocities.....	103
Figure 4.23. Gas and liquid mean flow: ratio of the acoustic boundary layer to the viscous sublayer. The latter has calculated with the friction coefficient estimated (a) with the shear stress at the wall by using the actual gas velocity and the hydraulic diameter and (b) with the interfacial shear stress calculated with Tzotzi and Andritsos model (2013).	104
Figure 4.24. Gas and liquid mean flow: acoustical damping coefficient [1/m] measured as function of frequency [Hz] in the direction of (a) and against flow (b) at a superficial gas velocity $U_{SG} \sim 2.5$ m/s. As a reference, the damping measured without any flow (magenta) and with a flow of dry air (green) is provided.	105
Figure 4.25. Acoustical damping coefficient measured at 320 Hz for an (almost) constant superficial gas velocity ($U_{SG} \sim 2.5$ m/s) as function of the superficial liquid velocity U_{SL} [m/s].	106
Figure 4.26. Mean gas flow and liquid: $U_{SG} \sim 2.5$ m/s. Damping coefficient ratio [-] as function of frequency [Hz] without corrections in direction (a1, solid lines) and against flow (b1, dashed lines). Damping coefficient ratio [-] as function of frequency [Hz] including the effects of convection and the hydraulic diameter (a2-b2). Additionally, the uncertainty margin is provided (a2-b2) by using the hold-up values $\beta_L \pm$ the standard deviation σ (see Section 4.3.2). The legend is the same as in Figure 4.24.	107
Figure 4.27. Gas and liquid mean flow: $U_{SG} \sim 5.5$ m/s: acoustical damping coefficient [1/m] measured as function of frequency [Hz] in the direction of (a) and against flow (b) at a superficial gas velocity $U_{SG} \sim 5.5$ m/s. As a reference, the damping measured without (magenta) and with (green) flow is provided.....	107
Figure 4.28. Mean gas flow and liquid: $U_{SG} \sim 5.5$ m/s. Damping coefficient ratio [-] as function of frequency [Hz] without corrections in direction (a1, solid lines) and against flow (b1, dashed lines). Damping coefficient ratio [-] as function of frequency [Hz] including the effects of convection and the hydraulic diameter (a2-b2). Additionally, the uncertainty margin is provided (a2-b2) by using the hold-up values $\beta_L \pm$ the standard deviation σ (see Section 4.3.2). The legend is the same as in Figure 4.27.	108
Figure 4.29. Gas and liquid mean flow: $U_{SG} \sim 10.5$ m/s: acoustical damping measured in the direction of (a) and against flow (b) at a superficial gas velocity $U_{SG} \sim 10.5$ m/s. As a reference, the damping measured without (magenta) and with (green) flow is provided.....	109
Figure 4.30. Mean gas flow and liquid: $U_{SG} \sim 10.5$ m/s. Damping coefficient ratio [-] as function of frequency [Hz] without corrections in direction (a1, solid lines) and against flow (b1, dashed lines). Damping coefficient ratio [-] as function of frequency [Hz] including the effects of convection and the hydraulic diameter (a2-b2). Additionally, the uncertainty margin is provided (a2-b2) by using the hold-up values $\beta_L \pm$ the standard deviation σ (see Section 4.3.2). The legend is the same as in Figure 4.29.	109
Figure 4.31. Mean gas flow and liquid: $U_{SG} \sim 10.5$ m/s. Comparison between the measured acoustical damping (solid lines) and the estimated with Sanna's hybrid model (dashed lines), in the direction of (a) and against (b) flow. The legend is the same as in Figure 4.29.....	110
Figure A.1. Capacitance probes scheme (left) and real probe (right).	120
Figure A.2. "Twin-T" measurement circuit. The input is a high frequent AC signal, the connection to the sensor is replacing one of the two capacitors. The output is in the center of the diamond formed by the diodes and the capacitor in the schematic. The output signal is an AC signal which is biased depending on the capacitance of C_1 and C_2 , which needs to be low-pass filter to obtain a DC output signal.	120
Figure A.3. Geometrical details of the capacitance probe.	121
Figure A.4. Measured voltage [V] as function of the weight [g], for the upstream and downstream capacitance probes.	122
Figure A.5. Hold-up measurements [-] as function of the absolute measured voltage [V].....	122
Figure A.6. Hold-up interpolation curves as function of the voltage difference $V-V_0$ [V].....	123
Figure A.7. Flow pattern map for a horizontal smooth horizontal pipe with an inner diameter equal to 0.025 m (Shoham, 2006). Experiments were conducted in the range of U_{SG} and U_{SL} highlighted by the red dashed rectangle.	124

Figure A.8. Hold-up [%] estimated at $U_{SG} \sim 2.5$ m/s (a), $U_{SG} \sim 5.5$ m/s (b), $U_{SG} \sim 10.5$ m/s (c) by means of the capacitance probes: average value (-) and standard deviation $\pm\sigma$ (--).	125
Figure A.9. Graph paper used to calibrate the optical distortion.	126
Figure A.10. Order the horizontal line with respect to the axis of the pipe.	127
Figure A.11. Fitting curve expressing the location of the points.	127
Figure A.12. Frames of the videos recorded during the measurements.	128
Figure A.13. Hold-up estimated by means of the visualizations. at three and constant gas velocities U_{SG} : ~ 2.5 m/s (blue diamonds), ~ 5.5 m/s (red squares), ~ 10.5 m/s (green triangles).	128
Figure A.14. Hold-up estimated by means of OLGA simulations at three and constant gas velocities U_{SG} : ~ 2.5 m/s (blue diamonds), ~ 5.5 m/s (red squares), ~ 10.5 m/s (green triangles).	129
Figure A.15. Final comparison for the hold-up estimate with different techniques for the three different superficial gas velocities U_{SG} : ~ 2.5 m/s (a), ~ 5.5 m/s (b), and ~ 10.5 m/s (c).	131
Figure B.1. Scheme of the experimental test for the calibration of the 8 microphones.	135
Figure B.2. Measured and computed transfer functions between upstream microphone 1 and the other upstream microphones, and between downstream microphone 6 and the other microphones.	136
Figure B.3. Measured and computed transfer functions after the optimization on microphone positions.	137
Figure B.4. Measured and computed transfer functions after the optimization on microphone positions and considering the reflection of the blind flange.	138
Figure B.5. Measured and computed transfer functions after the optimization on microphone positions, considering the reflection of the blind flange and the acoustic damping in the complex wave number.	139
Figure B.6. Measured and computed transfer functions after the optimisation on microphone positions, considering the reflection of the blind flange, the acoustic damping in the complex wave number, and the correction in amplitude.	140
Figure B.7. Damping coefficient for a horizontal smooth pipe in both directions, with (-) and against (--) flow. No relative calibration between the two groups of transducers is considered.	141
Figure B.8. Percentage ratio between the acoustical damping measured in the direction of the flow (α^+) to the damping measured against flow (α^-).	141
Figure C.1. Configurations tested: a) smooth pipe; b) Corrugated pipe - Conf. A (see Table C.2); c) Corrugated pipe - Conf. B (see Table C.2). The flow is going from the left to the right.	144
Figure C.2. Geometrical parameters of a corrugated pipe [Nakiboğlu et al., 2010].	145
Figure C.3 Smooth pipe: transmission coefficient T [-] of the scattering matrix (a) and measured damping [1/m] as function of frequency [Hz] in direction (-) and against (--) flow.	146
Figure C.4. Smooth pipe (30 mm), 400 Hz: approximation of Davies (1988) and Dokumaci (1995) for the convection effects.	146
Figure C.5. Smooth pipe: damping coefficient ratio [-] as function of frequency [Hz] without any correction.	146
Figure C.6. Smooth pipe: damping coefficient ratio α/α_0 [-] as function of the frequency [Hz] corrected by the convection term proposed by Dokumaci (1995).	147
Figure C.7. Smooth pipe: (a) the boundary layers ratio δ_{ac}/δ_i and (b) comparison between the experimental results and the turbulence model of Howe (1995) as function of frequency [Hz].	147
Figure C.8. Acoustical damping [1/m] without gas mean flow as function of frequency [Hz] in the positive (-) and in the negative (--) direction for the three different configurations: smooth pipe (cyan), corrugated pipe - Conf. A (black), corrugated pipe - Conf. B (green).	148
Figure C.9. Corrugated pipe - configuration A (a1-a2) and configuration B (b1-b2): damping measured without and with gas mean flow in the direction of (solid lines) and against (dashed lines) flow.	149
Figure C.10. Corrugated pipe, configuration A: comparison between the first (positive) and the second (negative) peak of the damping coefficients between the experiments of Sanna (diamonds) and Golliard et al. (2013a) (squares).	149
Figure C.11. Corrugated pipe, configuration A (a) and configuration B (b). Measured non-dimensional time-averaged source power for a single pitch of the 30 mm pipe as function of the (shifted) Strouhal number.	150

List of tables

Table 2.1. Experimental matrix for tuning the system. All the lengths are in m.	30
Table 2.2. Physical and equivalent acoustical lengths of the experiments setup (Figure 2.4).	32
Table 2.3. Nozzle and water flow rates tested (BETE).....	32
Table 2.4. Variation of diameter D_{eff} necessary to have constant Strouhal number equal to 0.42 (Sr for $Q_L = 0$ ml/min), calculated by using the actual velocity U.....	38
Table 3.1. Physical and equivalent acoustical lengths of the experiments setup (Figure 3.2).	62
Table 4.2. Minimum and maximum frequency obtained by combining 2 microphones.	91
Table 4.3. Campaign #2: test matrix for the tests with only gas mean flow ($U_{SL} = 0$ m/s; $\beta_L = 0$ %).	92
Table 4.4. Campaign #3: test matrix for the tests with water poured in the pipe ($U_{SG} = 0$ m/s; $U_{SL} = 0$ m/s; hold-up $\beta_L > 0$ %).	92
Table 4.5. Campaign #4: test matrix at different water velocity U_{SL} [m/s], gas velocity U_{SG} [m/s] and hold-up β_L [%].	92
Table 4.6. Calibration of the piezometric transducers: final correction of the relative distances and amplitude..	94
Table A.1. Geometrical details of the capacitance probes.	121
Table A.2. Coefficients values of the fitting polynomial for the hold-up as function of the difference $V-V_0$	123
Table A.3. Input parameters for OLGA simulations.	129
Table A.4. Hold-up estimates with different techniques.	130
Table B.1. Distance between the transducers and the reference transducer.	136
Table B.2. Corrected relative distances between the transducers.	137
Table B.3. Correction factors on amplitude for the transfer functions, considering the corrected relative distance, the reflection coefficient of the blind flange, and the damping in the complex wave number.	140
Table C.1. Relative distance [m] between microphones.....	144
Table C.2. Geometrical details of the three test objects (see Figure C.2).....	145
Table C.3. Test Matrix: Mach number M [-] for each configuration.....	145

Chapter 1

Introduction

Résumé

Le couplage entre un écoulement instable et les résonnances acoustiques dans un système de conduits peut conduire à des phénomènes d'oscillations auto-induites. Ce type de phénomènes existe principalement en présence de conduites latérales fermées, par exemple dans des systèmes de transport ou de compression de gaz.

TNO, dans le projet européen Marie Curie FlowAirS, a comme objectif principal de comprendre comment la présence d'écoulement diphasique peut influencer le mécanisme à la base des oscillations auto-induites. Pour cette recherche deux configurations acoustiques bien connues (conduites latérales en croix ou en tandem) sont étudiées. Dans le chapitre 2, les variations d'amplitudes dans les tubes latéraux sont mesurées avec différentes quantités de liquide.

Ces variations d'amplitude sont discutées dans les Chapitres 3 et 4 en fonction de deux hypothèses. La première hypothèse est que l'interaction entre la couche mélange et le liquide entraîne une forte diminution des pulsations. Toutefois, la variation de l'amortissement peut aussi jouer un rôle important dans la décroissance des pulsations. Dans le chapitre 4, cette seconde hypothèse (amortissement augmenté par la présence d'eau) a été vérifiée par la mesure de l'atténuation dans un conduit horizontal avec un mélange d'air/eau stratifié.

The coupling between flow-instabilities and acoustic resonances in ducts with closed side branches can lead to strong pulsations, the so-called Flow Induced Pulsations (FIPs). This phenomenon is often experienced and has a relevant effect especially on engineering applications (transport systems, compressor installations, electric power stations and chemical plants). In gas transport systems, this can lead to intense noise, alteration of relief valves, mechanical stresses, and possible acoustic fatigue failure. As a consequence, the production and transport of gas and, most importantly, safety of the system can be highly compromised. Thus, during the preliminary design of the piping layout, the occurrence of Flow Induced Pulsations has to be considered in order to prevent their occurrence.

The goal of this work is to extend the current knowledge about FIPs when the transported medium is not uniquely gas but a combination of gas and liquid. This work has been performed within the European Commission project FlowAirS.

1.1. The FlowAirS Project

The FlowAirS project (FP7-PEOPLE-2011-ITN-289352) is a multidisciplinary and multi-sectoral collaborative training research network funded by the 7th Framework Program. The project focuses in general on the generation, propagation and reduction of sound in flow ducts for transport, buildings and power generation. In particular, FlowAirS aims at building a strong knowledge and expertise to mitigate the practical problems associated to noisy air flows. This translates into multidisciplinary researches on a multiplicity of disciplines such as fluid dynamics, acoustics, and structural dynamics.

A research work programme has been defined, consisting of eight cross-linked work packages. The FlowAirS network is composed of the following beneficiaries: 5 universities (Laboratoire d'Acoustique de l'Université du Maine (UMR CNRS 6613), Kungliga Tekniska Högskolan KTH, Technische Universiteit Eindhoven, Katholieke Universiteit Leuven, Technischen Universität München, Ain Shams University), 2 research centers (Netherlands Organization for Applied Scientific Research TNO, von Karman Institute for fluid dynamics VKI), and 3 companies (LMS International, AUDI, Müller-BBM). In addition, 5 more partners from the private sector are associated to the consortium (AIRBUS Operations SAS, Bombardier Transportation, Scania, Sontech Noise Control, Centre Technique des Industries Aéronautiques et Thermiques).

TNO is the beneficiary n. 2 and it is mainly linked to the second work package “Flow Induced Pulsations” and to the sixth work package “Source and System identification”. Our contribution to FlowAirS project concerns the coupling between multiphase flows and acoustics in ducts. More in detail, with this Ph.D. thesis, TNO aimed at understanding more on the interaction between liquid and Flow Induced Pulsations generated by hydro dynamic instabilities when gas flows in pipes with T-junctions.

1.2. Thesis outline

The Ph.D. thesis consists of three main chapters and three appendices.

In Chapter 2 the phenomenon of Flow-Induced Pulsations (FIPs) is considered, as well as its consequences experienced in diverse applications. In this chapter the goal is to familiarize with the phenomenon and introduce the effects of liquid on FIPs. Two configurations are considered as reference to investigate the effect of liquid, namely the *tandem* and the *quasi-cross* configuration. The experiments have been conducted by measuring the acoustical perturbations at the closed end of each closed side branch for the first acoustic mode. Depending on the amount of liquid injected in the main pipe, different flow pattern with consequently different FIPs trends

have been observed. From the analysis of the results, two main hypotheses have been proposed as reasons of the different behaviors of the FIPs. In particular, the interaction between liquid and the shear layer instability, and the increase of acoustic damping due to the presence of water.

Chapter 3 is dedicated to the interaction between liquid and the vortex shedding. In a configuration slightly different from the tandem resonator used in Chapter 2, three cases are considered. By means of an injector, a liquid film has been injected on the wall at the upstream edge of the upstream side branch. These results have been compared with the results obtained by experiments with the water injector located at the bottom of the main pipe, first far from the upstream T-junction and second close to it. Two main features have been noticed: first, when the liquid is interfering with the shear layer, a 60 % of decrease of pulsations amplitude is observed, second, the overall behavior is the same for the three cases. This similarity is attributed to the only element in common: the water between the two side branches. Again, this indicates that the decrease of pulsation is related to the increase of acoustical damping due to the presence of water in the horizontal side of the resonator, between the two side branches.

Chapter 4 aims at quantifying this parameter: the acoustic damping is measured in presence of a mixture of air and water. By means of the two-microphone method, the acoustical damping is measured for a 2 m smooth horizontal pipe with a gas mean flow at a constant velocity in the pipe together with water at different liquid velocities. The results have been compared with the damping in dry case, with and without mean flow, and with a test set with different amounts of water, but without mean flow. An increase of the acoustical damping in the flow direction and against the flow was observed in presence of liquid. It was found that the increase could, for a large part, be related to the changes of the hydraulic diameter due to the presence of water. The effect of convection without and with liquid is similar, provided the actual gas velocity is used. As the gas velocity increases, it is also necessary to consider the effect of turbulence on damping. For a stratified wavy flow, it is important to take into account not only the turbulence at the wall but also the turbulence generated at the interface.

Three more appendices complete the comprehension of this work. They aim at providing the description of some tools, either experimental or analytical, needed to conduct the investigations. In Appendix A, an overview of the possible methods used for hold-up measurements is provided, with particular focus on the capacitance probes method, used for this work. The calibration of the piezometric transducers used for the work on damping with liquid (Chapter 4) is described in Appendix B. An extra work on damping in a configuration of corrugated pipe has been presented in Appendix C.

All the work in this Ph.D. thesis was fully conducted by F. Sanna. All the experiments have been performed at TNO, except for the experiments presented in Appendix C which were conducted in Le Mans with Y. Aurégan. F. Sanna has been the first author of the all work presented in these chapters.



Chapter 2

On the effect of liquid on flow-induced pulsations in a pipe with two closed side branches: two case studies

Résumé

L'objectif de ce chapitre¹ est de mesurer les effets d'un mélange de gaz et de liquide sur les oscillations auto-induites. Sur deux configurations acoustiques bien connues (en tandem et en croix), les pulsations sont mesurées dans des conduites latérales fermées avec l'écoulement d'un mélange variable d'air et d'eau. La position de l'injection d'eau est variable afin d'obtenir plusieurs régimes d'écoulement diphasique.

Sur la base de la comparaison des résultats obtenus sur les deux configurations, il est montré que la présence d'eau a un effet important sur les niveaux de pulsations dans les conduites. Cet effet a été attribué à deux mécanismes dus à la présence d'eau: les instabilités de couches de mélange sont modifiées et l'amortissement des ondes acoustiques est augmenté.

¹ This work is the combination of two experimental investigations presented in two international conferences: 1) Sanna, F., and Golliard J., 2014, "Effect of water-droplets on Flow-Induced Pulsations in pipe with two closed-side branches: an experimental study," *20th AIAA/CEAS Aeroacoustics Conference*, Atlanta, Georgia, United States; 2) Sanna, F., and Golliard J., 2014, "Flow-Induced Pulsations in closed side branches with wet gas," *ASME Pressure Vessels & Piping Conference*, Anaheim, California, United States.

Nomenclature

A	Upstream length [m]	FIP	Flow Induced Pulsation
A_{mp}	Cross-sectional area of the main pipe [m^2]	FIV	Flow Induced Vibrations
$A_{mp,L}$	Cross-sectional area of the main pipe occupied by liquid [m^2]	K	Nozzle factor [-]
B	Middle length [m]	P_{nozzle}	Inlet pressure of the nozzle [Pa]
C	Downstream length [m]	p'	pressure pulsation amplitude [Pa]
c_0	Speed of sound [m/s]	Q_L	Volumetric liquid flow rate [m^3/s]
D	Injector location [m]	Q_G	Volumetric gas flow rate [m^3/s]
D_{eff}	Effective diameter of the side branch [m]	Sr	Strouhal number [-]
D_{inj}	Diameter of the injector [m]	U	Actual Gas velocity [m/s]
D_{mp}	Inner diameter of the main pipe [m]	U_{SG}	Superficial Gas Velocity [m/s]
D_{sb}	Inner diameter of the side branch [m]	U_{SL}	Superficial Liquid Velocity [m/s]
D1	Length of the upstream side branch [m]	$x_{III,end}$	Acoustic end correction [m]
D2	Length of the downstream side branch [m]	β_L	Liquid void fraction [-]
f	Frequency [Hz]	δ	Ratio of the main pipe diameter to the side branch diameter [-]
FCV	Flow Control Valve	ρ	Density of the gas [kg/m^3]
FFT	Fast Fourier Transform		

2.1. Introduction

Acoustic resonances in ducts with closed side branches can result in an excitation of strong pulsations, the so-called Flow Induced Pulsations (FIPs). This phenomenon has a relevant effect especially on engineering applications. It is indeed often encountered in transport systems, compressor installations, electric power stations and chemical plants. In gas transport systems they can for instance significantly impact on the operation. Intense noise with discrete frequencies, alteration of relief valves, mechanical stresses (severe structural vibrations), and possible fatigue failure are some of the consequences led by the occurrence of these resonances. Overall, both the safety of system and the production and transport of gas can be highly compromised. Therefore, they need to be considered during the design of piping layouts and eventually implement counter-measures (Ziada and Bühlmann, 1992; Ziada, 1993). This is why configurations characterized by multiple side branches along a main pipe have been extensively examined during the last decades. However, researchers have been investigating this problem only with dry gas. In this paper, the effect of air and water mixtures on FIPs is considered at different water injection rates in two different acoustical resonators.

From 1940 to 1960 Oklahoma Gas and Electric Company experienced disrupting and unusual noise, vibrations and the consequent failure of safety valves (Tonon et al., 2011a). This led to deeper investigations of the occurring phenomenon. Chen and Stürchler (1977) as well as Gillessen and Roller (1989) reported resonances in multiple side branches, while Coffman (1980), Bernstein (1989), and Webb (1995) reported valve wear and failure in safety valves due to flow-induced sonic vibrations. Few years later, Baldwin solved resonance problems in safety relief valves by proposing a procedure based on the use of Strouhal number, Mach number and stub dimensions aimed at eliminating or preventing problems in piping systems (Baldwin and Simmons, 1986). Firstly, in 1973 Gorter reported in the Dutch gas transport system (Ommen, The Netherlands) strong pulsations on a long side branch of 0.5" (0.0127 m) used as connection to a manometer needed for static pressure measurements along a 12" (0.3048 m) main pipe (Gorter et al., 1989). Lately, Bruggeman (1987) analyzed the advent of low frequency resonances in one of the compressor stations of N.V. Nederlandse Gasunie, characterized by multiple closed side branches. Continuum Dynamics, Inc. reported high frequencies with Flow-Induced Vibrations (FIVs) in the geometry of the Columbia standpipes and safety valve inlets, with

operating conditions of 60-70% of allowable power (Continuum Dynamics, Inc., 2002). Also in the Dutch gas transport system, FIPs were reported several times as aeroacoustic oscillations related to the instability of grazing flow in a gas transport pipe with closed side branches (Gorter et al., 1989; Peters and Bokhorst, 2000; Peters and Riezebos, 2001). Recently, high cycle fatigue cracks occurred in the steam dryer in the boiling water reactor of Quad cities Unit 2 (Deboo et al., 2007). Acoustic modes in the standpipes of safety valves enhanced pressure amplitudes in such a way that the resonance propagated to the main steam lines, into the reactor dome, damaging the steam dryer (NRC, 2002).

2.1.1 Flow-Induced Pulsations in closed side branches

Acoustic resonances typically occur when one or more closed side branches are located along a main pipe.

For such particular configurations, when a flow is grazing in the main pipe, small perturbations in the shear layer which spans the mouth of the cavity can be amplified. Due to the convection of the unsteady shear layer vorticity in the sound field, sound power is produced and flow tones are generated. For resonant conditions, in which the inherent unstable shear layer is at the frequency of the acoustic field, the hydrodynamic field is strongly coupled with the acoustic one and the resonant sound field is enhanced. In turn, standing pressure waves extract energy from the mean flow, exciting the initial velocity fluctuations in the shear layer into large scale vortex-like structures. This feedback loop between the unstable flow and the resonant sound can be extremely strong, severely affecting the whole system (Rockweel and Naudascher, 1978; Rockwell, 1983; Blake, 1986; Blake and Powell, 1986; Bruggeman, 1987; Stoneman et al., 1988; Graf, 1989; Powell, 1990; Peters, 1993; Ziada, 1994-2010; Howe, 1984, 1997, 1998a-b).

Amplitudes of such pressure pulsations, categorized as FIP, are determined by the non linear gain of the feedback loop and the losses due to friction, heat conduction and radiation damping. They can be so high that they induce vibrations and, over time, fatigue failures (see, for example, Chen & Florjancic, 1975; Chen and Stürchler, 1977; Coffman and Bernstein 1980; Chen and Ziada, 1982; Baldwin and Simmons, 1986; Bernstein and Bloomfield, 1989).

The excited modes are typically those consisting of an odd number of quarter wavelengths along the length of the branch. That is because the particle velocity of the resonant modes is maximum at the location of the shear layer (Ziada and Shine, 1999). Therefore, the pressure amplitude varies depending on the configuration of the side branches along the main pipe (Tonon 2009, 2010). Two typical tested configurations are

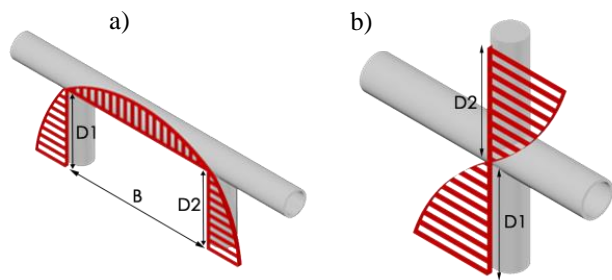


Figure 2.1. Pressure distribution in the tandem configuration (a) and in the cross configuration (b).

the tandem configuration and the cross configuration, whose pressure distribution is shown in Figure 2.1. Such configurations are sometimes accidentally chosen in industrial applications (Peters and Riezebos, 2001), but also present an academic interest. These resonators are used here as academic prototypes, the acoustic pressure distribution being well known. The tandem configuration (Figure 2.1a) is a resonator characterized by the relative distance between the two side branches which is equal to the double of the length of each closed side branch, while for the cross configuration (Figure 2.1b), the two closed side branches are aligned. That means

that the first resonance acoustic mode is characterized by a wavelength and a half wavelength respectively for the tandem and the cross configuration. The standing pressure wave has maxima at the closed ends of each T-junction and nodes (pressure equal to zero) at the intersection between the Tees and the main pipe. Moreover, the high quality factor implies small acoustic leakages in the duct. This makes the two configurations the most dangerous ones in terms of pressure amplitudes. Graf and Ziada (1992) in fact reported for coaxial branches that the acoustic power in the branches radiated into the main pipe is only and equal to 2%. The cross configuration is indeed the most severe configuration. Although the two resonators exhibit similar acoustic and hydrodynamic characteristics, pulsations in the tandem configuration are lower. This difference is due to visco-thermal losses in the pipe segment B and the differences in the aeroacoustic sources at the T-junctions (Tonon, 2011b). Several authors have been investigating the effect of different geometrical and flow properties on FIPs, firmly distinguishing the analysis for shallow ($D1/D_{sb} < 1$) and deep ($D1/D_{sb} > 1$) cavities.

Properties of pressure oscillations of discrete frequencies of a flow across the mouth of a rectangular and cylindrical cavity have been extensively studied (East, 1966; Demetz and Farabee, 1977; Elder, 1978; Elder et al., 1982; Parthasarathy et al., 1985; Rockwell and Naudascher, 1978; Rockwell, 1979-1983). The mechanism loop has been numerically investigated by predicting the transfer of acoustic power to the sound field by using Howe's (Howe, 1975) integral (Hourrigan et al., 1986). Hourrigan et al. (1990) made experimental and numerical investigations of the resonant sound generated by flow in a duct with two sets of baffles. Finite element method is used to calculate the resonant sound field and the discrete-vortex model to predict the separated flow (Hourrigan et al., 1990). Junkowski investigated the effect of the ratio of the side branch to the main pipe diameters (D_{sb}/D_{mp}) on pulsation amplitudes and on the Strouhal number, developing also a simple equivalent model based on a hypothetical oscillatory piston and two transfer matrices (Jungowski et al., 1989).

Further numerical and experimental investigations on resonant oscillations in a main duct with side branches have been conducted by Bruggeman and Kriesels (Bruggeman et al., 1989-1991; Kriesel et al., 1995). The influence of different parameters such as the distance between the side branches, the static pressure, upstream turbulence level, and the angle between the branches has been also experimentally investigated (Ziada and Bühlmann, 1992). Ziada made investigations to predict the acoustic resonances at which the critical flow velocities are excited in a piping system with closed side branches and classified the coupling for various side branch configurations (Ziada and Bühlmann 1992; Ziada and Shine, 1999). During the last years, further numerical and experimental studies on double side branches have been conducted (Peters and Bokhorst, 2000; Peters and Riezebos, 2001; Tonon et al., 2009, 2010, 2011a-b; Graf and Ziada, 2010; Nakiboğlu et al., 2010; Ziada and Lafon, 2013).

2.1.2 Multiphase flow background

For the purpose of this paper, the authors intend here to provide an insight about multiphase flows to relate the effects of multiphase flows onto acoustics.

A multiphase flow is characterized by two or more immiscible phases of matter (gas, liquid or solid). For this experimental campaign an air/water mixture is used.

As soon as water and air are mixed up together in a pipe, a different distribution of the two phases along the cross sectional area A_{mp} is reported, depending on the combination of the superficial liquid and gas velocities, the surface tension, on the properties (geometry and roughness) of the pipe, and on the slope. The ratio of the pipe cross-sectional area occupied by the liquid phase $A_{mp,L}$ to the whole cross sectional area is called the liquid volume fraction or liquid hold-up β_L . As the injection rate varies, the hold-up changes and its effect can play a determinant role so that the effective gas velocity is different. For that reason, two velocities are usually used: the superficial and the actual velocities. The superficial velocity U_S is defined as the velocity that a phase (gas or liquid) would obtain when flowing alone in a pipe. As reported in Eq. (1.1), the actual velocity U of one phase takes into account the ratio of cross section area occupied by this phase to the total cross-section area of the pipe (the phase hold-up):

$$\beta_L = \frac{A_{mp,L}}{A_{mp}} \quad ; \quad U_G = \frac{U_{SG}}{1 - \beta_L} \quad (1.1)$$

where the subscript G and L stand for the gas and liquid phases.

Furthermore, to easily predict the multiphase flow behavior, flow pattern or flow regimes maps are normally used. For a different combination of superficial liquid and gas velocities, different flow patterns will occur: dispersed bubbly flow, slug flow, churn or froth flow, stratified (wavy) and annular dispersed flow. For instance, Figure 2.2 shows the different patterns for a smooth horizontal pipe with an inner diameter 5.25×10^{-2} m. A flow is considered stratified wavy if the wave amplitude increases as the gas velocity increases, whereby liquid drops may be entrained in the gas stream and annular dispersed when the liquid travels as an annular film on the wall of the tube and partly as small droplets distributed in the gas flowing in the center (Oliemans, 2008).

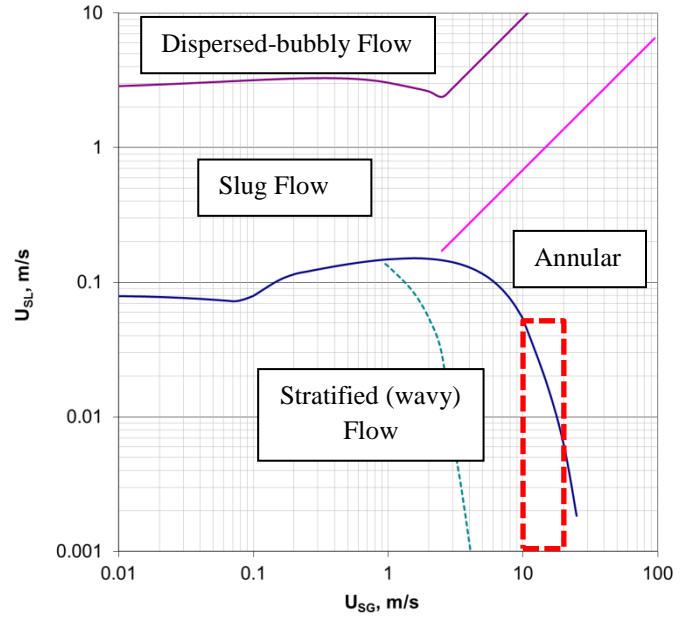


Figure 2.2. Flow Pattern map for a horizontal smooth pipe with inner diameter $D_{mp} = 0.0525$ m (Shoham, 2006). Experiments were conducted in the range of U_{SG} and U_{SL} highlighted by the red dashed rectangle.

2.1.3 Flow-Induced Pulsations in pipes transporting gas-liquid mixture

To the author's knowledge, there are only a few studies on the effect of water/air mixture on acoustics in piping systems (Belfroid et al., 2013, 2014; Shoeibi Omrani et al., 2012; Uchiyama and Morita, 2013-2015). The presence of liquid was showed to reduce or eliminate Flow-Induced Pulsations in closed side branch resonators (Shoeibi Omrani et al., 2012; Sanna et al., 2015), and in corrugated pipes (Belfroid et al., 2013, 2014). The experimental investigations presented in this work therefore aim at understanding the effects of multiphase flows on acoustics in configurations of pipes in presence of T-junctions.

The resonators chosen for these experimental investigations are characterized by two closed side branches, in tandem configuration and in quasi-cross configuration. The latter is similar to the cross configuration, but the two side branches of equal length are separated by a distance much smaller than the length of the side branches.

In spite of this difference, the aeroacoustic behavior of the quasi-cross configuration is very similar (Tonon et al., 2011b) to the one of the cross configuration since the spacing is small compared to the acoustic wavelength of the first acoustic mode (Ziada and Bühlmann, 1992). The operating conditions for these experimental investigations are different from the ones in previous experiments, covering a broader range of cases (Shoeibi Omrani et al., 2012). Compared to the experiment of Shoeibi Omrani (2012) the multiphase flow patterns are different due to the different range of gas velocities. In the experiment of Shoeibi Omrani (2012) the superficial gas velocity corresponding to the first mode pulsation peak was at 47 m/s and the flow was mainly fully annular. In the case discussed here, a maximum liquid flow rate of 6 l/min is injected and the superficial gas velocity range is between 12-21 m/s for both configurations. The operating range of superficial gas and liquid velocities highlighted by the red dashed line (Figure 2.2) is such that the flow is stratified wavy (Figure 2.3a) at low injection rates and at high injection rates the flow tends to become annular-dispersed (Figure 2.3b).

Pressure amplitudes are measured at the closed end of each side branch. Two positions of the spray nozzle used for water injection are considered. Depending on the location of the injector, i.e. the distance between the injection point and the upstream side branch, the type of flow at the T-junction is different. Indeed, if the distance is large, the droplets will deposit on the walls of the tubing and the flow has time to develop to its natural flow pattern at the given conditions (as estimated in the flow map of Figure 2.2). If the injector is very close to the T-junction, small droplets sprayed by the nozzle are still in the bulk of the flow, and the droplets which have deposited on the walls are still distributed on the full circumference of the pipe.

In Section 2.2, the details of the setup, as well as the experimental technique are provided. In section 2.3 the results for each configuration are explained, followed by a resuming discussion aimed at highlighting the relation between acoustics and multiphase flows' aspects.

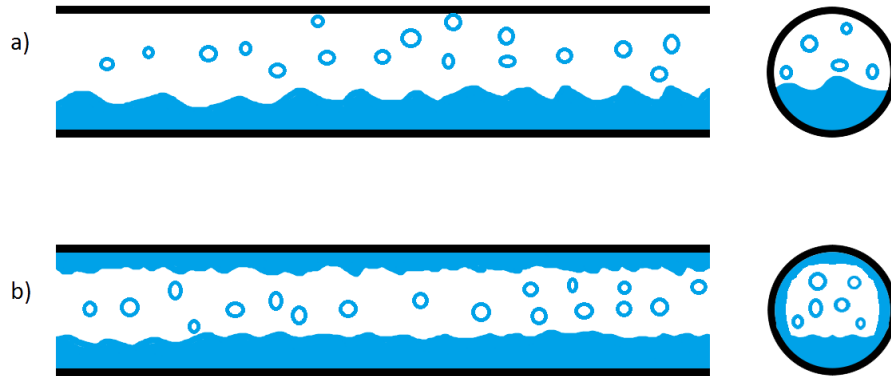


Figure 2.3. Distribution of water in stratified wavy dispersed flow (a) and annular dispersed flow (b).

2.2. Setup and experimental technique

The effect of liquid on FIPs is tested on two configurations characterized by two T-junctions located along a main circular pipe. The two configurations used for this study are the tandem configuration and the quasi-cross configuration. Three sets of experiments are conducted for each configuration. While the first set was performed with only dry gas, the other two consisted of injecting liquid with the liquid injector far upstream (at a distance D of about 25 times the main pipe diameter D_{mp}) or with the injector close to the upstream side branch. Each experiment consists of measuring pressure pulsations at the closed end of the two side branches when a mixture of water and gas passes along the main pipe of the configurations tested. More specifically, different and constant water injection rates (up to $10^{-4} \text{ m}^3/\text{s}$) are injected via an injector nozzle. The (superficial) gas velocity

U_{SG} was varied between 11 m/s and 20 m/s for a pipe cross section area $A_{mp} = 2.16 \times 10^{-3} \text{ m}^2$, corresponding to an air mass flow in the range $3.6 \times 10^{-2} \text{ kg/s}$ and $5.2 \times 10^{-2} \text{ kg/s}$. In order to reach high injection rates, different BETE-PJ and BETE-P nozzles are used (BETE, 2013). Furthermore, in order to understand the relation between the flow pattern and pressures amplitudes, i.e. the Flow-Induced Pulsations trend, a camera is used to record videos.

2.2.1 Supply system

The experimental equipment located in the TNO laboratories (Delft) consists of an open circuit system. One of three measuring lines equipped with flow meter, pressure and temperature transducers drives air from a pressure vessel (7 barg) towards two flow control valves. They regulate the flow mass rate of air, i.e. the superficial velocity of the grazing flow in a range between 12 and 20 m/s. Air is at atmospheric pressure. Upstream of the configuration shown in Figure 2.4, the supply system is provided by an expansion chamber, i.e. a silencer, which aims at reducing the noise generated by the flow control valve.

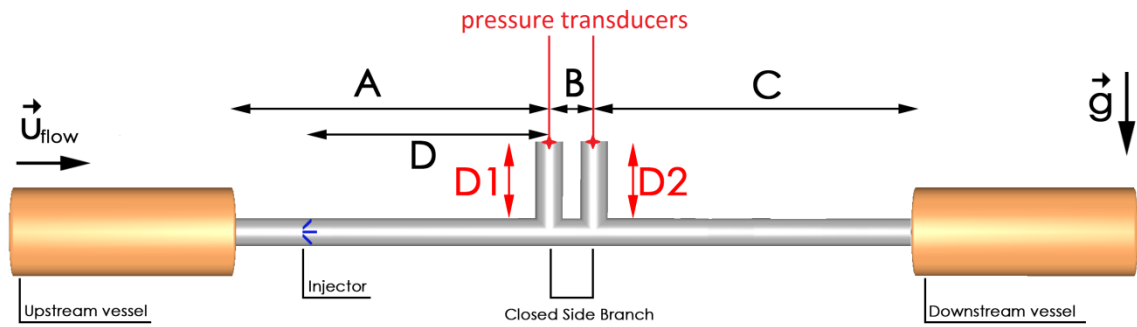


Figure 2.4. Experimental setup.

2.2.2 Test setup

Two identical cylindrical vessels set the boundary conditions of the experimental setup, working as expansion chambers. Figure 2.4 and Table 2.2 provide their location and the distance from the two side branches. The length and the inner diameter of each expansion chamber are respectively 0.495 m and 0.18 m, while the ratio of the radius of the pipe to the radius of the expansion chamber is 0.272. Their reflection coefficients were measured and are equal to around 0.7 around 160 Hz. The downstream vessel is also used as an air/water separator to drive the water from the system to the sink.

The main pipe of the test setup has an inner diameter D_{mp} of $5.25 \times 10^{-2} \text{ m}$, whereas the side branches have an inner diameter D_{sb} of $4.4 \times 10^{-2} \text{ m}$ and the edges of the T-junctions are sharp. Note that the two branches are both mounted upwards to avoid the accumulation of water due to gravity. For the quasi-cross configuration, the angle between the axes of the two side branches is equal to 90° , which prevents turbulence possibly generated by the upstream T-junction to disturb the shear layer at the downstream T-junction.

Since the length B for the tandem configuration was chosen equal to 1.0 m, the acoustical lengths of each side branches D1 and D2 are equal to 0.5 m.

The upstream and downstream lengths A and C were chosen based on two considerations: minimal influence of other acoustic resonances on the whistling resonance in the velocity bandwidth of interest and sufficient multiphase flow development length.

An acoustic model was built to study the influence of other resonances on the main resonances. This model is based on lumped elements (Bodén and Åbom, 1986; Dowling and Ffowcs Williams, 1983; Munjal, 1987; Pierce, 1981; Polifke, 2007). No flow is considered in this model. The system (Figure 2.4) has been divided into

basic elements: straight pipe, T-junction, area expansion, closed end. In straight pipes, variables are related by the plane wave conditions. At the T-junctions, as well as for area expansions, continuity of the acoustic volume flow and the continuity of the acoustic pressure are imposed. At each T-junction, a unitary source Δp is also added to represent the sound source term. The multiphase development length is always a concern. Based on formed droplets diameter, equilibrium is expected in several tenths of diameters. In general, annular flow requires even larger development lengths (Lopez de Bertodano et al., 1997). The length available ($25D_{mp}$) is on the short side. However, as only a limited re-entrainment is expected (Ishii, 2003) the length is deemed sufficient.

Furthermore, in the experimental setup, the length of the side branches was made adjustable. This is to find the optimum length, maximizing the pulsation level. Provided that the upstream A and downstream lengths C were decided, the length of each T-junction was adjusted for the dry gas (injector far upstream) configuration and remained unchanged.

Both side branch lengths were independently tuned. Two piston mechanisms were used to slightly vary each length. The tuning procedure has been split into two different steps. The first group of investigations aimed both at verifying that the slight difference in length of the side branches would not drastically affect the peak pulsation and at finding which the best length difference ought to be to the largest peak pulsations amplitude while the superficial gas velocity varies. The second group of investigations was conducted to find the best configuration.

Table 2.1. Experimental matrix for tuning the system. All the lengths are in m.

Tuning – Step 1	
Length upstream T-junction	Length downstream T-junction
0.500	0.500
0.500	0.502
0.500	0.498
0.500	0.504
Tuning – Step 2	
0.486	0.490
0.491	0.495
0.496	0.500

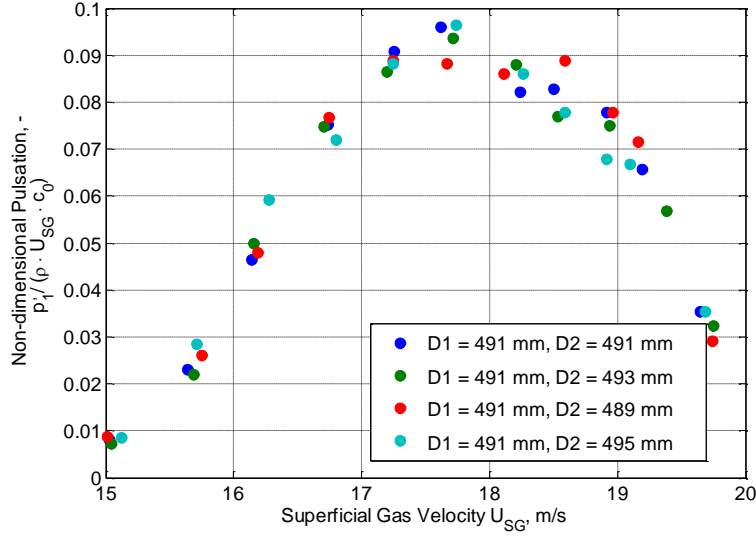


Figure 2.5. Step 1 of tuning: non-dimensional pulsation [-] measured at the closed end of the upstream T-junction as function of the superficial gas velocity U_{SG} [m/s] for different lengths of the downstream side branch.

The combination with 4 mm of difference between the upstream and the downstream side branch length is considered the best (Figure 2.5). In the second step for the tuning, both lengths of the side branches are changed by ± 5 mm, keeping their relative difference constant (4 mm). Figure 2.6 shows that the best configuration found is 0.491 m and 0.495 m respectively for the upstream and the downstream side branch.

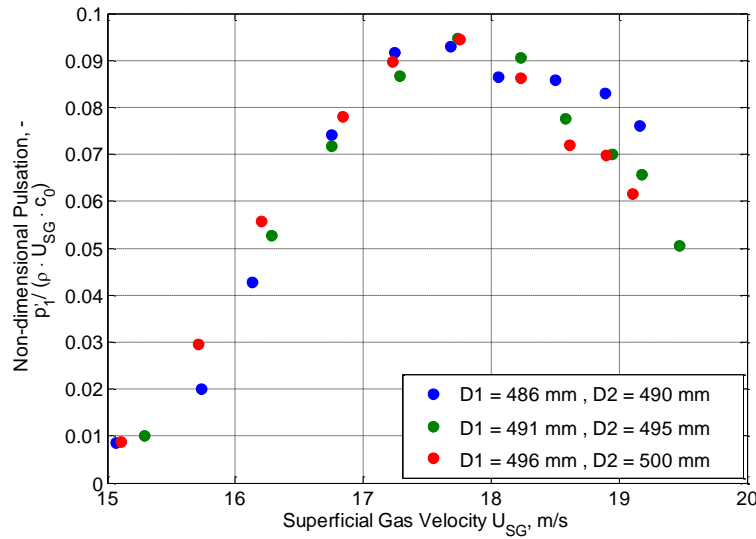


Figure 2.6. Step 2 of tuning: non dimensional pulsation [-] measured at the closed end of the upstream T-junction as function of the superficial gas velocity [m/s] for different lengths of the upstream side branch.

This is in line with the model proposed by Nederveen et al. This model introduces two parts for calculating the end correction $x_{III,end}$ with zero mean flow (Nederveen et al., 1998).

$$\begin{aligned}
 x_{III,end} &= t_i + t_m \\
 t_i &= (0.82 - 1.4\delta^2 + 0.75\delta^{2.7}) \frac{D_{sb}}{2} \\
 t_m &= \frac{D_{sb}\delta}{16} (1 + 0.207\delta^3)
 \end{aligned} \tag{2.2}$$

The two parts are the inner end correction t_i and the other t_m compensates for the volume resulting from the joining of the ducts. $\delta = D_{sb}/D_{mp}$ is the diameter ratio between the side branch D_{sb} and the main pipe D_{mp} .

Table 2.2. Physical and equivalent acoustical lengths of the experiments setup (Figure 2.4).

Physical length [m]	A	B	C	D	D1	D2
Tandem configuration* – Far Injector	1.48	1.00	1.48	1.25	0.491	0.495
Tandem configuration* – Close Injector	1.48	1.00	1.48	0.1	0.491	0.495
Quasi-Cross configuration[§] – Far Injector	1.48	0.07	1.48	1.25	0.491	0.495
Quasi-Cross configuration[§] – Close Injector	1.48	0.07	1.48	0.1	0.491	0.495
Length correction [m]	0.018	0	0.018	--	0.009	0.009
Acoustical length [m]	1.50	1.00* 0.07 [§]	1.50	--	0.500	0.504

All the dimensions of the setup are reported in Table 2.2. The length D can slightly change because of the geometrical properties of the different nozzles used.

Water droplets are injected at the injector in the main pipe. From an external tank, it is driven to the injector through a pump Nilfisk C125.3.

Different nozzles of the Series BETE-P and BETE-PJ (BETE) are installed to regulate the required flow rates of water in the system (Table 2.3). That amount is regulated by a manual operated needle valve. A pressure sensor is mounted in the injector, measuring the inlet pressure of the nozzle. The volumetric flow rate of water injected Q_L is given by:

$$Q_L = K\sqrt{p_{nozzle}} \quad (2.3)$$

Where p_{nozzle} is the driving pressure across the nozzle measured in [bar] and the volume flow rate is measured in [m³/s].

Table 2.3. Nozzle and water flow rates tested (BETE).

Nozzle model	BETE PJ15	BETE PJ28	BETE PJ40	BETE P80	BETE P120
K factor $\left[\frac{1}{\min \sqrt{\text{bar}}}\right]$	0.0843	0.296	0.638	2.46	5.54
Q_L [10 ⁻⁶ m ³ /s]	1.6* 2.5 [§]	6.7* [§] 10.0* [§] 13.0* [§]	17.0* [§] 23.0* [§] 28.0* [§] 30.0* [§]	37.0* [§] 42.0* [§] 43.0* [§] 70.0* [§]	100.0* [§]
* Only for the tandem configuration § Only for the quasi-cross configuration					

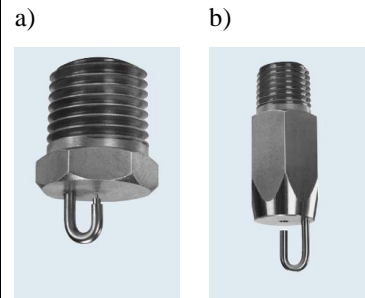


Figure 2.7. Scheme of the BETE-PJ nozzle (a) and BETE-P (b) (BETE).

As reported in Table 2.3 and Figure 2.7, the nozzles differ with respect to injection capacity and spray pattern. Nevertheless, all nozzles spread water with a 90° angle cone with droplet size smaller than 50 μm for BETE-PJ and in the range 25-400 μm for BETE-P. Furthermore, it is important to remark that the area of the injector is partially obstructed by the presence of the nozzle. This might generate turbulence, as well as reflections. For the tests with far injector, this effect is negligible, as the injector is positioned far upstream (at

25 D_{mp}) from the upstream side branch, i.e. from one of the two sources of whistling. However, it can have an effect on tests performed with close injector.

2.2.3 Data acquisition and analysis

Dynamic pressure measurements are conducted with two flush-mounted piezometric sensors (PCB Piezotronics Pressure Division) type 116A located at the closed end of the two side branches. The static pressure and temperature are measured with two Rosemount pressure sensors and two temperature probes Tempcontrol-PT100 are located at the upstream vessel and at the downstream vessel. A pressure sensor mounted in the injector measures the inlet pressure of the nozzle p_{nozzle} . It is used to estimate the flow injection rates Q_L .

Pressure signals are recorded by a DEWETRON 801 (48 channels) acquisition system at acquisition frequency of 20,000 Hz for a total time of 30 seconds.

The software DEWESoft 6.6.7 (DEWESoft) is used to store the signals and the FFT (Fast Fourier Transform) is used to compute the spectrum of pressure measurements. Data were processed in the MATLAB environment and the peak amplitude is considered.

With a dewe-cam-fw-70 camera, videos were recorded to describe the flow pattern.

2.3. Experimental Results

For each configuration (tandem or quasi-cross), the analysis of the results is divided into two sections: first, the results obtained with the injector located far upstream ($\sim 25 D_{mp}$) the upstream side branch are discussed, second, the ones associated to the injector located close ($\sim 2 D_{mp}$) to the upstream side branch. For each section, the results obtained with dry gas and with wet gas are reported in two different subsections. It is important to highlight that, for each configuration, with and without liquid, the analysis of the amplitude, the frequency, and the Strouhal number is reported. The discussion and summary of the results is provided in Section 2.4.

2.3.1 Tandem Configuration

From the spectrum of each measurement, the frequency and the pressure amplitude of the peak are reported.

For the analysis of the results, the average of the quantities on 30-seconds time is used.

Tandem Configuration – Injector at 25 D_{mp} upstream

Dry gas

The maximum peak of pulsations for the first acoustic mode is around 18 m/s. Pulsations at the closed end of each side branch have nearly equal amplitudes p' ; for the case with only dry gas a 4% difference is measured at the peak.

Firstly, the results for dry gas are presented in Figure 2.8. The pulsation amplitude has a maximum at the frequency of $f = 170.9$ Hz, which is close to the analytical frequency corresponding to the first acoustic mode $f_1 = 171.25$ Hz. The latter is calculated by using a speed of sound $c_0 = 342.5$ m/s as estimated from the measurements of air temperature $T = 18.5^\circ\text{C}$ at the downstream vessel.

Figure 2.9 shows the trend of the non-dimensional pulsations with respect to the Strouhal number. The peak corresponds to a Strouhal number of 0.42.

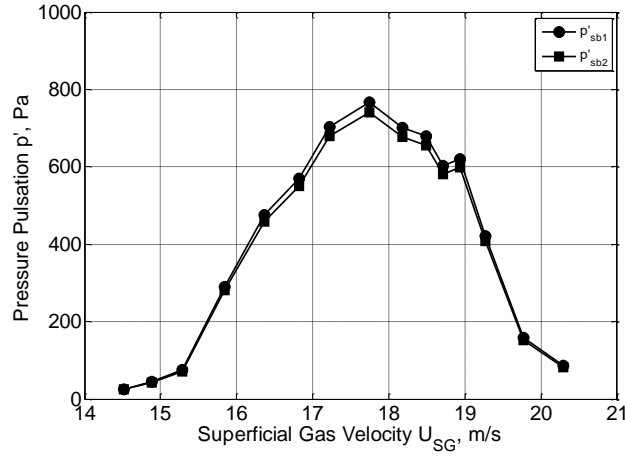


Figure 2.8. Tandem configuration, far injector. Dry gas: dimensional pressure pulsations [Pa] as function of the superficial gas velocity U_{SG} [m/s].

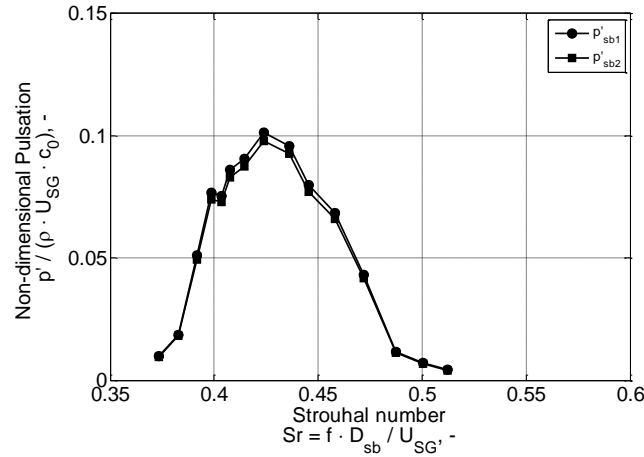


Figure 2.9. Tandem configuration, far injector. Dry gas: non-dimensional pulsations [-] as function of the Strouhal number [-] based on the superficial gas velocity U_{SG} [m/s].

Wet gas

Liquid was injected at constant flow rates with different nozzles at the injector located far from the upstream side branch (See Table 2.2, Tandem configuration - Far Injector).

For each experiment, the maximum pulsation level is shown in Figure 2.10 as a function of the liquid volumetric flow rate Q_L (upper plot) and of the percentage ratio of the liquid to the gas volumetric flow rate Q_L/Q_G (lower plot).

Three ranges of liquid flow rates Q_L can be distinguished. In the first range, the amplitude decreases with increasing liquid rate. The intermediate range $1.3\text{--}2.8 \cdot 10^{-5} \text{ m}^3/\text{s}$ (800-1700 ml/min) shows an increase in pressure pulsations. The pulsations decrease again when the injection rates are greater than $2.8 \cdot 10^{-5} \text{ m}^3/\text{s}$. The results are presented independently for the three different ranges. The pressure is made dimensionless with the average gas density (ρ), average gas velocity (superficial U_{SG} or actual U) and the (gas only) speed of sound (c_0). Density and speed of sound are calculated through air temperature measurements in the downstream vessel (see Figure 2.4).

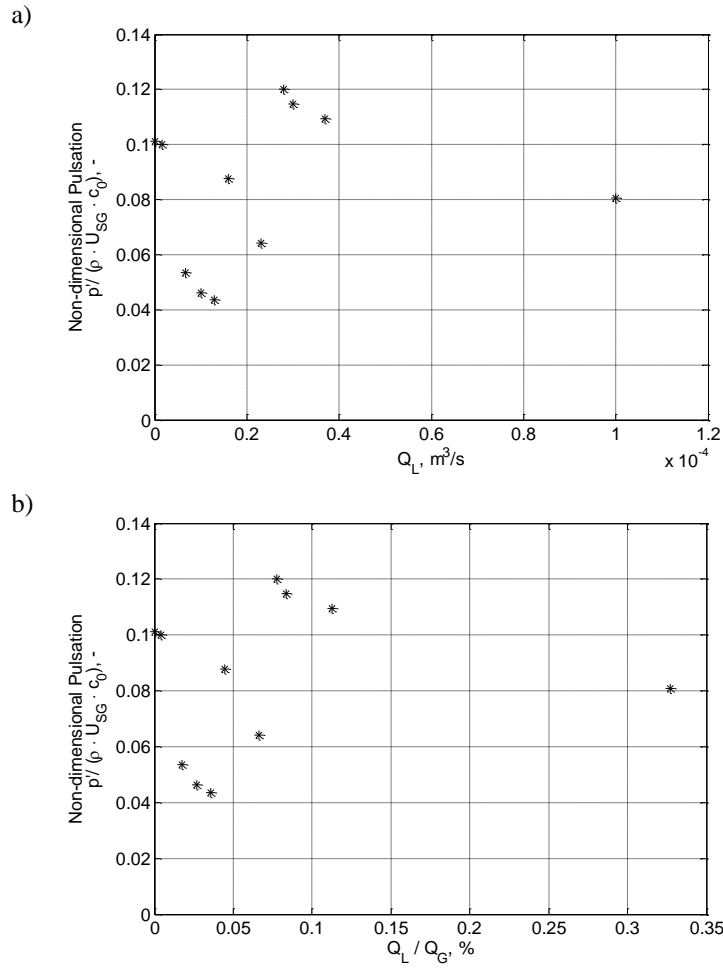


Figure 2.10. Tandem configuration, far injector. Wet gas: non-dimensional pulsations [-] as function of the liquid volumetric flow rate [m^3/s] (a) and of the percentage ratio of the liquid volumetric flow rate to the gas volumetric flow rate [%] (b).

For the first range ($0-1.3 \times 10^{-5} \text{ m}^3/\text{s}$), the results are plotted in Figure 2.11, Figure 2.12, and Figure 2.13. These figures show respectively the non-dimensional pulsations amplitudes and the frequency trend as function of the gas velocity, and the Strouhal number. A decrease of the pulsations is observed when the liquid injection rate increases. This trend was previously observed by Shoeibi Omrani et al. (2012). Figure 2.12 also shows a maximum decrease of 2% in frequency when Q_L increases. In this range the flow pattern is stratified.

Figure 2.13 shows that the range of the Strouhal number for the maximum pulsation peaks is 0.43-0.45. As soon as the flow rate Q_L increases, the Strouhal number increases for a max 3.5%.

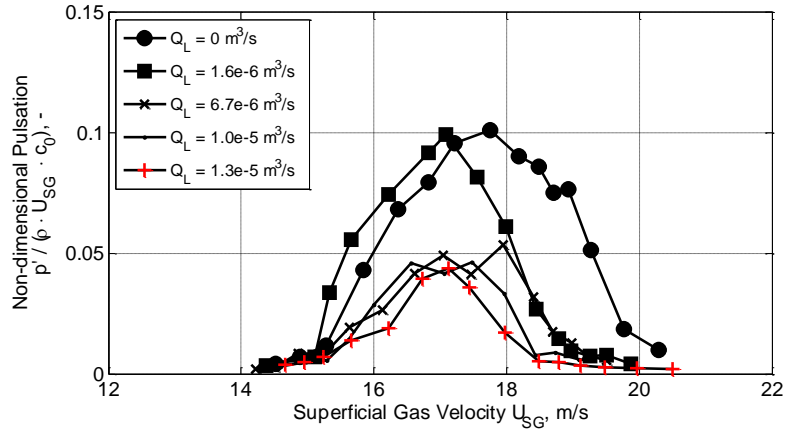


Figure 2.11. Tandem configuration, far injector. Wet gas: non dimensional pulsation pressure [-] as function of the superficial gas velocity U_{SG} [m/s] in the Q_L range $0-1.3 \times 10^{-5} \text{ m}^3/\text{s}$.

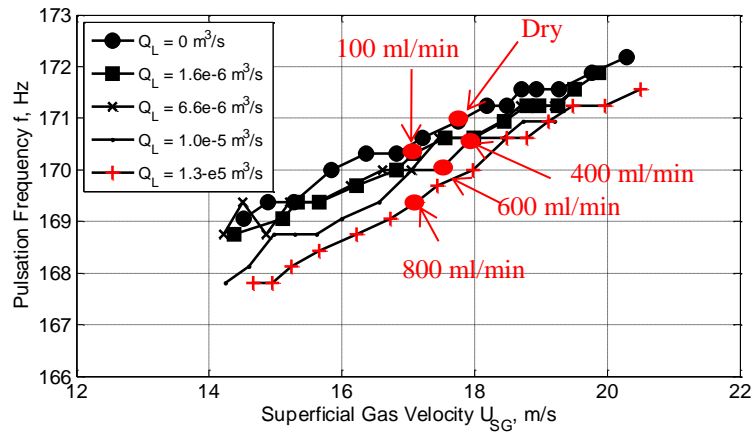


Figure 2.12. Tandem configuration, far injector. Wet gas: pulsation frequency [Hz] as function of the superficial gas velocity U_{SG} [m/s] in the Q_L range $0-1.3 \times 10^{-5} \text{ m}^3/\text{s}$. The dots mark the frequency at which the peak of maximum of pressure amplitude occurs.

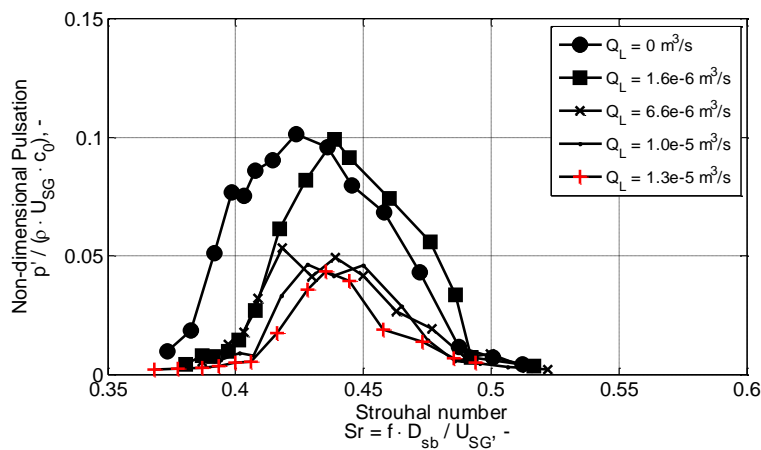


Figure 2.13. Tandem configuration, far injector. Wet gas: non-dimensional pulsation pressure [-] as function of the Strouhal number [-] based on the superficial gas velocity [m/s] in the Q_L range $0-1.3 \times 10^{-5} \text{ m}^3/\text{s}$ (0-800 ml/min).

The results for the high injection rates 2.8×10^{-5} - $1.0 \times 10^{-4} \text{ m}^3/\text{s}$ (1700-6000 ml/min) are given in Figure 2.14, Figure 2.15 and Figure 2.16 which, respectively, show the characteristic non-dimensional pulsations, frequency and

Strouhal number. Within the third range the pulsation amplitudes decrease as the amount of liquid increases. In this range, the flow regime varies according to the amount of liquid and to the velocity. The flow at $2.8 \times 10^{-5} \text{ m}^3/\text{s}$ is characterized by a stream of water at the bottom of the main pipe and droplets entrained, fast convected as the gas velocity increases. From visualizations, at $Q_L = 3.7 \times 10^{-5} \text{ m}^3/\text{s}$, the flow starts being stratified and it becomes at around 15 m/s almost annular. It also corresponds to the flow pattern map for air water reported in Figure 2.2.

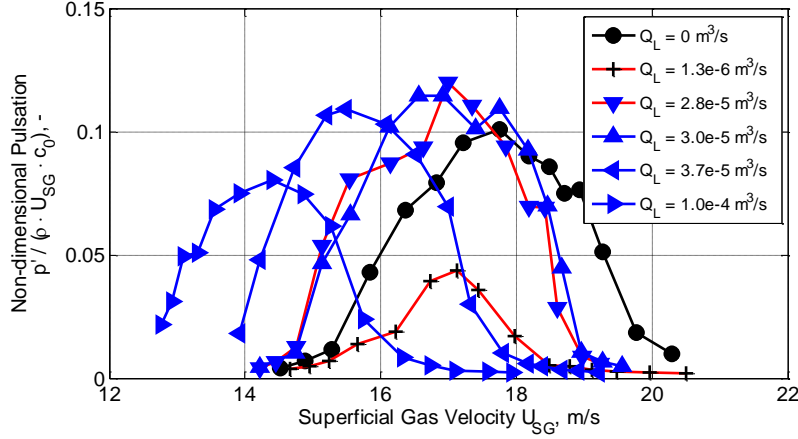


Figure 2.14. Tandem configuration, far injector. Wet gas: non-dimensional pulsation pressure [-] as function of the superficial gas velocity U_{SG} [m/s] in the Q_L range 2.8×10^{-5} - $1.0 \times 10^{-4} \text{ m}^3/\text{s}$. The data for dry gas and for $Q_L = 1.3 \times 10^{-6} \text{ m}^3/\text{s}$ (800 ml/min) are also provided for reference.

It is interesting that again in this range of liquid injection the frequency corresponding to the peak decreases (Figure 2.15) when the liquid rate increases. The frequency corresponding to the peaks are shown together with the frequency trend.

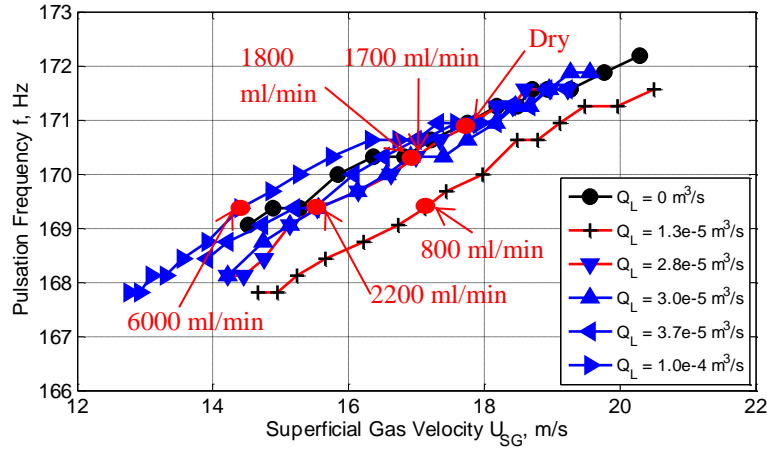


Figure 2.15. Tandem configuration, far injector. Wet gas: pulsation frequency [Hz] as function of the superficial gas velocity U_{SG} [m/s] in the Q_L range 2.8×10^{-5} - $1.0 \times 10^{-4} \text{ m}^3/\text{s}$ (1700-6000 ml/min). The data for dry gas and for $1.3 \times 10^{-5} \text{ m}^3/\text{s}$ (800 ml/min) are also provided for reference. The dots mark the frequency at which the peak of maximum of pressure amplitude occurs.

On the other hand, the Strouhal number increases with the liquid rate. As seen in Figure 2.16, the shift to higher Strouhal numbers is not (only) due to the hold up. The lower plot of Figure 2.16 shows the non-dimensional pulsation with respect to the Strouhal number, calculated by using the actual velocity, i.e. considering the effect of the hold-up. The latter is based on calculations assuming a fully developed flow, using one-dimensional multiphase flow simulation solver OLGA (OLGA).

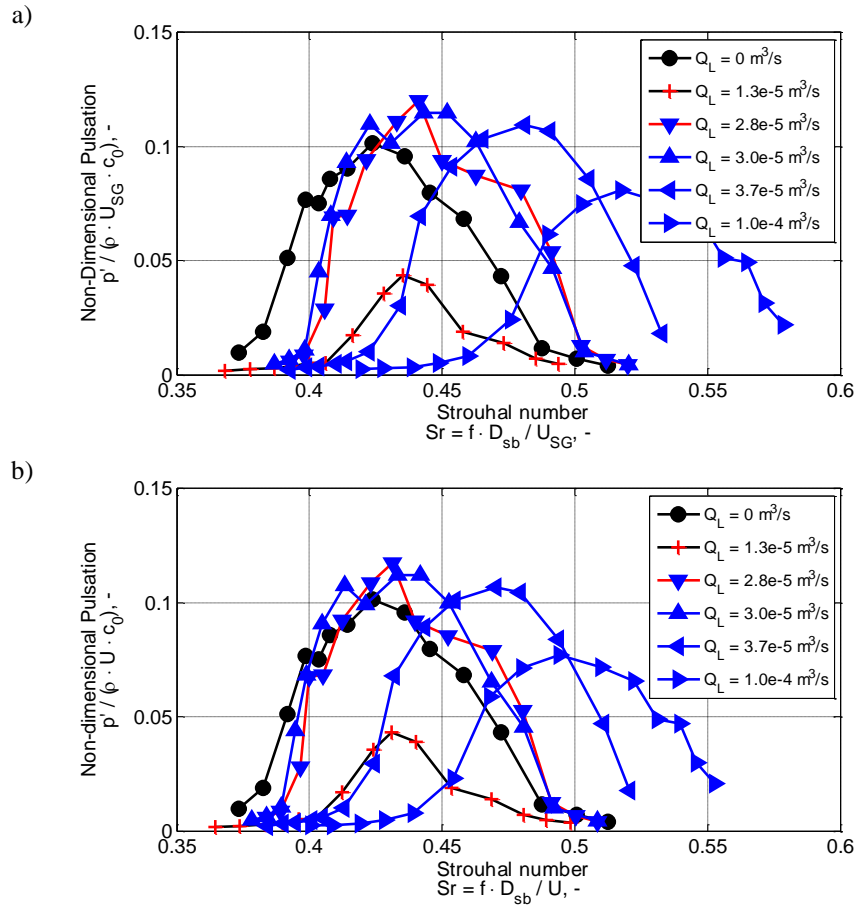


Figure 2.16. Tandem configuration, far injector. Wet gas: non-dimensional pulsation pressure as function of the Strouhal number in the Q_L range 2.8×10^{-5} - $1.0 \times 10^{-4} \text{ m}^3/\text{s}$ (1700-6000 ml/min). a) Superficial gas velocity used as reference; b) actual gas velocity used as reference.

A possible explanation for this shift of Strouhal number is that some water deposits at the edges of the T-junction inside the side branch. Accumulation of water at the edge would actually reduce the effective diameter of the side branch. In Table 2.4, the effective diameter of the side branch D_{eff} , which is the diameter that would give a constant Strouhal number (equal to the Strouhal number for dry gas at peak $Sr = 0.42$) is evaluated. Within the error margin of this approach to evaluate the effective diameter (in absence of visualization inside the T-junction), one can consider the following: the effective diameter does not change for 2.8×10^{-5} and $3.0 \times 10^{-5} \text{ m}^3/\text{s}$, but reduces for $3.7 \times 10^{-5} \text{ m}^3/\text{s}$ and $1.0 \times 10^{-4} \text{ m}^3/\text{s}$. According to the visual observation the flow was annular for liquid injection rates above $3.7 \times 10^{-5} \text{ m}^3/\text{s}$. The non-dimensional pulsations are plotted against the Strouhal number based on this effective length in Figure 2.17.

Table 2.4. Variation of diameter D_{eff} necessary to have constant Strouhal number equal to 0.42 (Sr for $Q_L = 0 \text{ ml/min}$), calculated by using the actual velocity U .

Q_L [$10^{-6} \text{ m}^3/\text{s}$]	U [m/s]	f [Hz]	D_{eff} [m]	Q_L/Q_G [%]
28.0	17.37	170.3	0.043	0.078
30.0	17.39	170.3	0.043	0.084
36.0	15.84	169.40	0.039	0.112
100.0	15.08	169.37	0.037	0.327

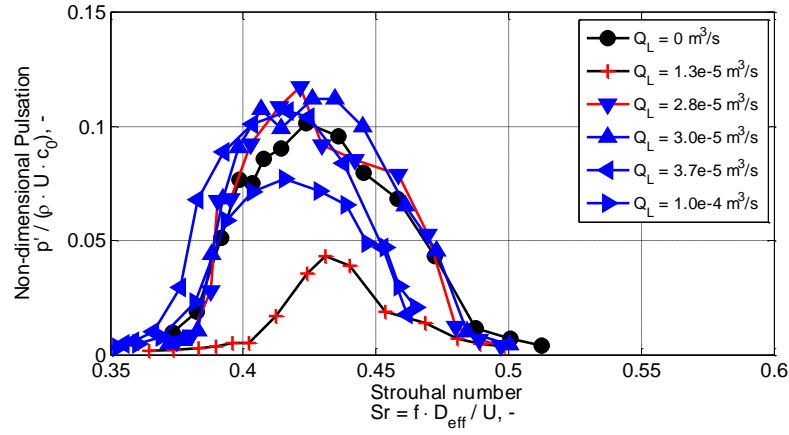


Figure 2.17. Tandem configuration, far injector. Wet gas: non-dimensional pulsation pressure [-] as function of the Strouhal number [-] based on the actual gas velocity U [m/s] and effective side branch width D_{eff} [m] of Table 2.4. The data for dry gas is also provided for reference.

The last range to analyze is the transition between the two regions discussed above: between $Q_L = 1.3e^{-5}$ m³/s and $Q_L = 2.8e^{-5}$ m³/s. Figure 2.18 shows that as the amount of liquid increases, pulsations increase, reaching amplitudes higher than the ones measured for dry gas. The exact reason of this increase is not known. In this region, only a single type of nozzle is used (BETE-PJ40). Therefore, it is unlikely that a different droplet distribution is the cause.

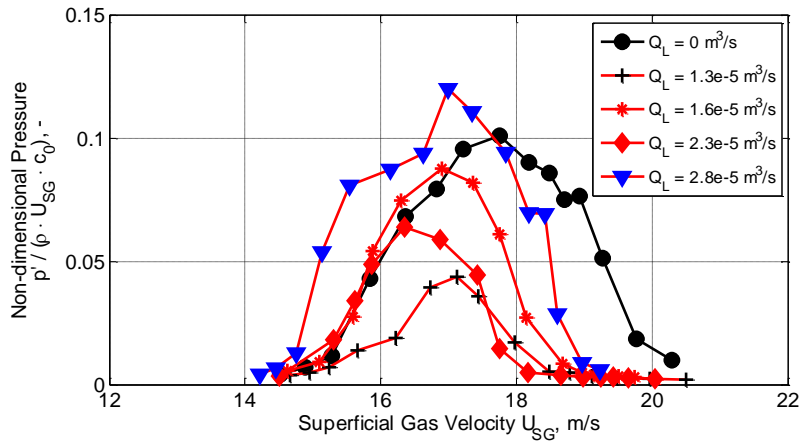


Figure 2.18. Tandem configuration, far injector. Wet gas: non dimensional pulsation pressure [-] as function of the superficial gas velocity U_{SG} [m/s] in the Q_L range $1.3e^{-5}$ - $2.8e^{-5}$ m³/s (800-1700 ml/min). The data for dry gas is also provided for reference.

Figure 2.19 shows the trend of frequency within this range and the frequencies corresponding to the maximum pulsations. It is higher than the frequency of the tests in the first range (see Figure 2.12). Moreover, Figure 2.19 shows that frequencies at different amounts of liquid collapse in one line at superficial gas velocities greater than 17 m/s, which means that the Strouhal number of the pulsations is constant.

Figure 2.20 shows that the Strouhal number at the peak of the non-dimensional pulsation is also larger than the Strouhal in the first range. Moreover, the Strouhal corresponding to the peaks is at most the 4.6% higher than the Strouhal of the dry gas case, except for $Q_L = 2.3e^{-5}$ m³/s.

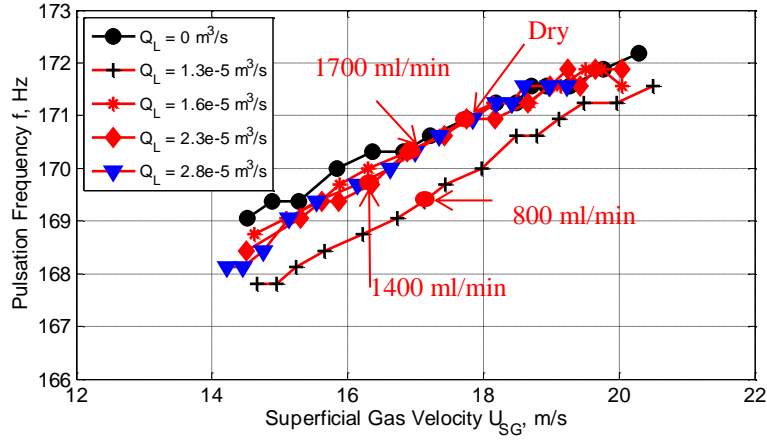


Figure 2.19. Tandem configuration, far injector. Wet gas: pulsation frequency [Hz] as function of the superficial gas velocity U_{SG} [m/s] in the Q_L range $1.3e^{-5}$ - $2.8e^{-5}$ m^3/s (800-1700 ml/min). The data for dry gas is also provided for reference.

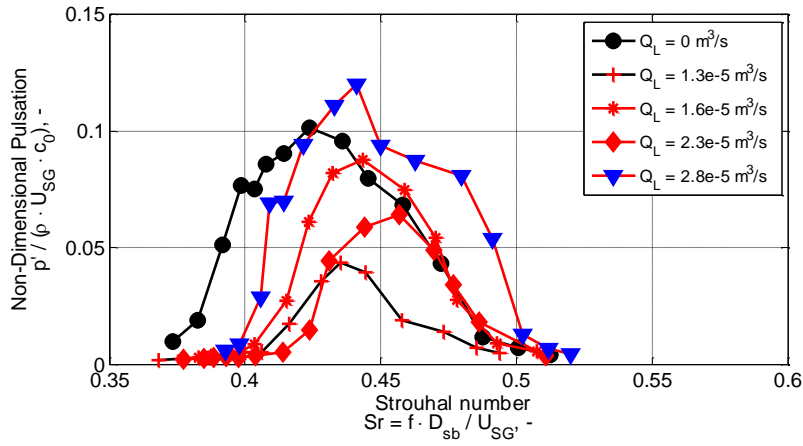


Figure 2.20. Tandem configuration, far injector. Wet gas: non-dimensional pulsations [-] based on the superficial gas velocity U_{SG} [m/s] as function of the Strouhal number [-] in the Q_L $1.3e^{-5}$ - $2.8e^{-5}$ m^3/s (800-1700 ml/min). The data for dry gas is also provided for reference.

Tandem Configuration – Injector at $2 D_{mp}$ upstream

Dry gas

The non-dimensional pulsations measured at the upstream side branch for the tandem configuration with the injector close to the upstream T-junction are shown in Figure 2.21. The pressure is plotted as function of gas velocity for the dry gas experiments with the injector close by and far upstream. In case of the close injector, the measured amplitudes are 32% lower. This difference can be related to the presence of the nozzle which is a small bluff body in the pipe. This locally accelerates the flow and also increases the turbulence level at a short distance from the source in the upstream T-junction. Furthermore, the injector has a smaller diameter than the main pipe ($D_{inj} = 0.049$ m, $D_{mp} = 0.0525$ m) and it represents for the flow a small step, generating additional turbulence.

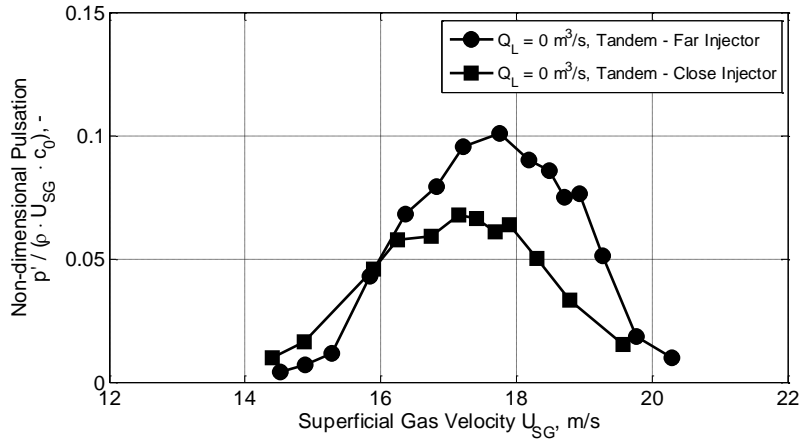


Figure 2.21. Tandem Configuration. Dry gas: comparison between the non-dimensional pressure pulsations [-] measured at the upstream side branch as function of the superficial gas velocity U_{SG} [m/s] for the case of far and close injector.

Wet gas

One set of experiments is performed at low injection rates ($0-1.3 \times 10^{-5} \text{ m}^3/\text{s}$), and at high injection rates ($2.8 \times 10^{-5}-1.0 \times 10^{-4} \text{ m}^3/\text{s}$). The results with respect to the dimensionless amplitude are plotted in Figure 2.22. With the injector close to the side branch, a clear trend is observed with a sharp decrease in the amplitude with increasing injection rate.

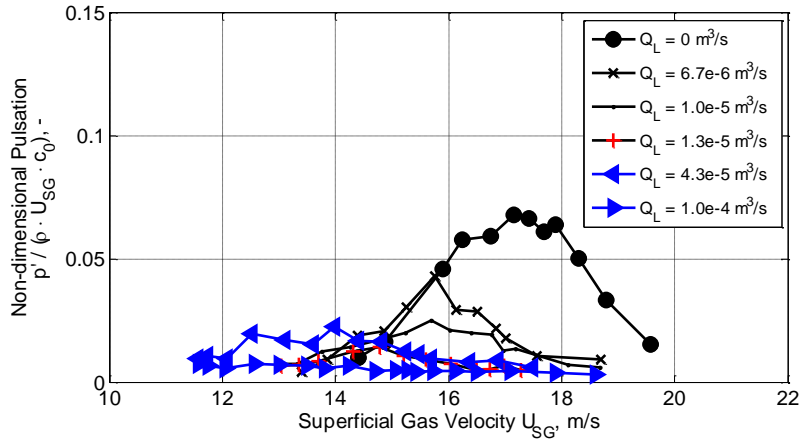


Figure 2.22. Tandem configuration, close injector. Wet gas: non-dimensional pulsations [-] as function of the superficial gas velocity U_{SG} [m/s] in the Q_L range $0-1.0 \times 10^{-4} \text{ m}^3/\text{s}$.

Contrary to the case with the far injector, pulsations are almost totally eliminated for low injection rates. Furthermore, the Strouhal number increases with increasing injection rates (Figure 2.23).

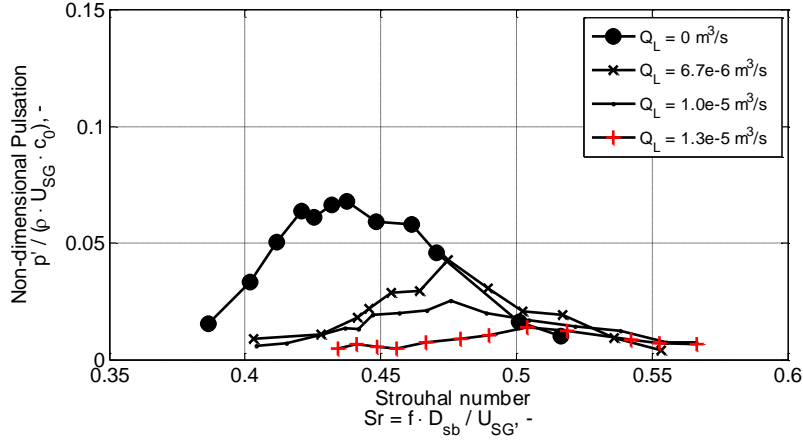


Figure 2.23. Tandem configuration, close injector. Wet gas: non dimensional pulsation pressure [-] as function of the Strouhal number Sr [-] based on superficial gas velocity U_{SG} [m/s] in the Q_L range 0 - $1.3 \times 10^{-5} \text{ m}^3/\text{s}$.

Depending on the nozzle used, the distance between the spray nozzle and the upstream edge of the T-junction is between 50 mm and 77 mm, which corresponds to ~ 1 to $\sim 1.5 D_{mp}$. The spray cone of the nozzle is 90 deg. The distance to the side branch is set such that the flow at the upstream edge is nearly dispersed flow. The distance to the side branch is thus sufficiently short to have a large part of the sprayed droplets in the bulk of the flow and not yet deposited at the pipe wall. On the other hand, the droplets which have deposited at the wall did not have time to drop to the lowest part of the tube yet. The liquid distribution at the first T-junction is thus largely annular for this case, while it was stratified with the injector far upstream. Although the amount of liquid Q_L is low in the first range (0 - $1.3 \times 10^{-5} \text{ m}^3/\text{s}$), the presence of a thick layer of water would change the geometry of the main pipe, as well as the one of the T-junction.

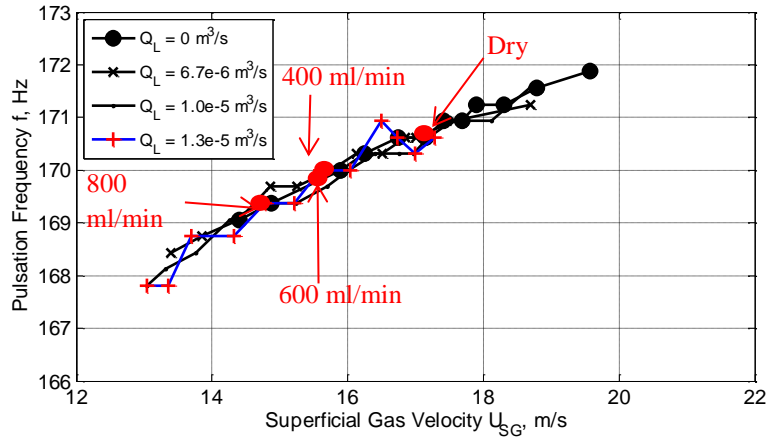


Figure 2.24. Tandem configuration, close injector. Wet gas: pulsation frequency [Hz] as function of the superficial gas velocity U_{SG} [m/s] in the Q_L range 0 - $1.3 \times 10^{-5} \text{ m}^3/\text{s}$.

Furthermore, as for the case with far injector, frequencies corresponding to the maximum peak pulsation decrease while the amount of liquid increases (Figure 2.24).

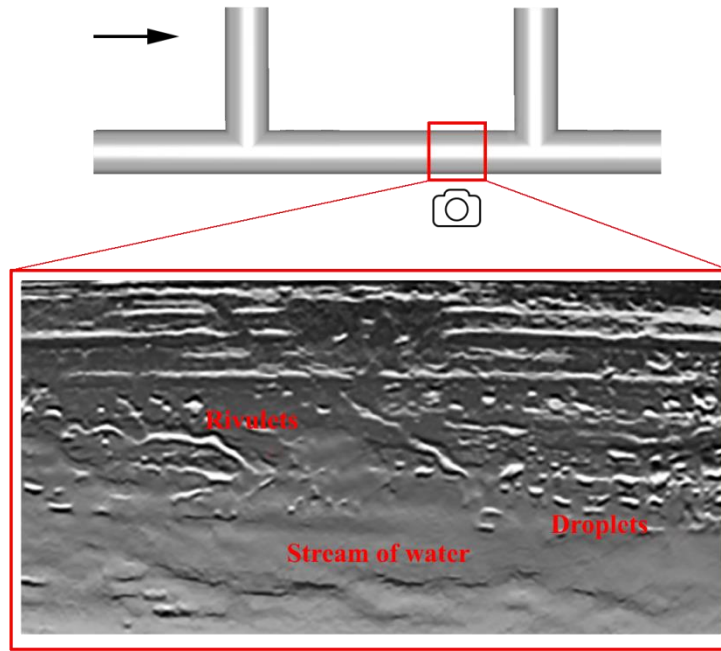


Figure 2.25. Tandem configuration, close injector. $Q_L = 1.0 \times 10^{-5} \text{ m}^3/\text{s}$, at the entrance of the downstream side branch. The mixture flows from left to right.

At higher amounts of liquid, it is not possible to define a typical trend and sometimes the two side branches do not have the peak at the same frequency. This can be related to the extremely different type of flow at the two T-junction: at the upstream T-junction the flow is annular dispersed, while at the downstream T-junction the flow pattern depends on the gas velocity. Figure 2.25 indeed shows that at $Q_L = 1.0 \times 10^{-4} \text{ m}^3/\text{s}$ the flow at downstream T-junction is not annular, while for the far injector and at the same amount of liquid it was already annular at low velocity.

2.3.2 Quasi-Cross Configuration

The other configuration chosen is the *quasi-cross configuration*. Also for this configuration, each measurement consists of injecting a constant amount of water while increasing the gas velocity, first a far distance from the upstream T-junction and later at a close one.

Quasi Cross Configuration – Injector at $25 D_{mp}$ upstream

Dry gas

In Figure 2.26, the results for dry gas are presented. In the range of velocities between 12 m/s and 21 m/s, the pulsations corresponding to the first acoustic mode are analyzed. In this range, the maximum peak occurs around 16.5 m/s. The peak of the dimensional pulsation amplitudes observed for this *quasi-cross* configuration for dry gas is more than the 50% higher than the peak for the *tandem configuration* (Section 2.3.1). Because of a shorter overall length of the resonators (half an acoustic wavelength instead of a full acoustic wavelength), the lower acoustical damping (viscous-thermal losses) is the responsible of such a high increase. This was also confirmed by using the aforementioned 1D acoustic lumped model.

The measured frequency corresponding to the peak of the pressure pulsations is equal to 163 Hz, which is close to the theoretical frequency of 160 Hz. The latter is calculated by using the speed of sound $c_0 = 342.5 \text{ m/s}$ estimated from gas temperature $T = 18.5 \text{ }^\circ\text{C}$ measured at the downstream vessel (Figure 2.4).

The peak of pulsations corresponds to a Strouhal number of 0.43 (Figure 2.29).

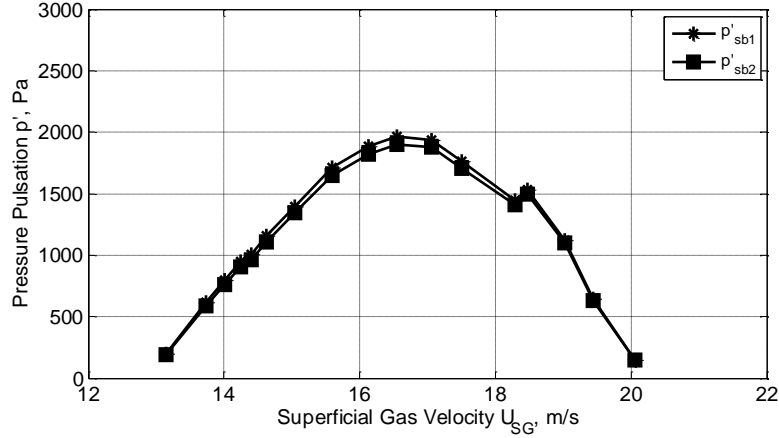


Figure 2.26. Quasi-cross configuration, far injector. Dry gas: peak pressure pulsations [Pa] as function of the superficial gas velocity U_{SG} [m/s].

Wet gas

Table 2.3 shows that different amounts of liquid (up to $1.0 \times 10^{-4} \text{ m}^3/\text{s}$) were injected with different nozzles at the center of the main pipe through an injector located far from the upstream side branch.

The effect of the liquid on the non-dimensional pulsations is presented in Figure 2.27. The pressure pulsations are made dimensionless by using the gas density, the speed of sound calculated through the temperature measured at the downstream vessel (see Figure 2.4) and the upstream velocity.

Two different behaviors can be distinguished, respectively at low (up to $3.0 \times 10^{-5} \text{ m}^3/\text{s}$) and high injection rates (3.0×10^{-5} – $1.0 \times 10^{-4} \text{ m}^3/\text{s}$).

In the range of injection rates 0 – $3.0 \times 10^{-5} \text{ m}^3/\text{s}$ (black lines in Figure 2.27), neither a significant decrease of pulsations can be seen, nor a shift in the peak velocity. In this configuration of two side branches along a main pipe, the injection rate seems not to have significant effect on pulsation amplitudes. Indeed, the non-dimensional pressure amplitude corresponding to the peak at $3.0 \times 10^{-5} \text{ m}^3/\text{s}$ is the 87% of the non-dimensional pressure amplitude corresponding for dry gas. Note that the flow pattern here is stratified and stratified wavy.

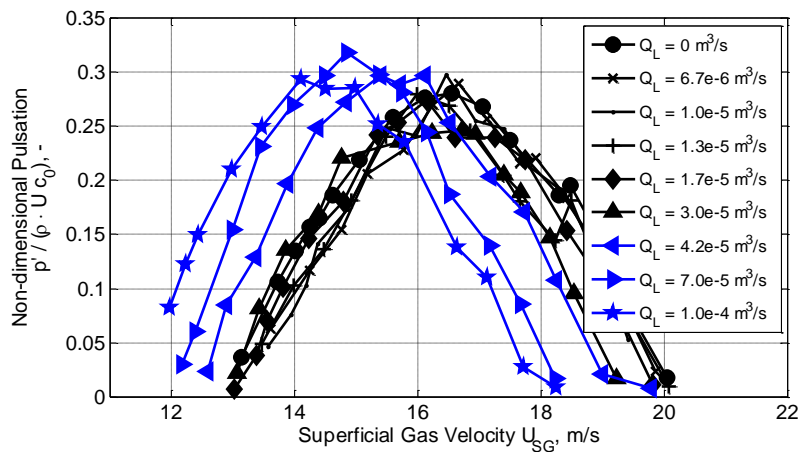


Figure 2.27. Quasi-cross configuration, far injector. Wet gas: non dimensional pulsation pressure [-] as function of the superficial gas velocity [m/s]. (Black lines: 0 – $3.0 \times 10^{-5} \text{ m}^3/\text{s}$; blue lines: 3.0×10^{-5} – $1.0 \times 10^{-4} \text{ m}^3/\text{s}$).

At high injection rates (3.0×10^{-5} – 1.0×10^{-4} m³/s), the blue lines in Figure 2.27 show that no clear trend can be distinguished. A 15% decrease between the velocity corresponding to the non-dimensional pulsation peak for dry gas and 1.0×10^{-4} m³/s is reported. The shift of the peak to lower velocities was also reported in experiments on the *tandem* configuration and it was equal to 18%. Nevertheless, the shift for the *quasi-cross* configuration here analyzed is less significant than the one observed in the *tandem* configuration. Furthermore, for high injection rates ($Q_L > 3.0 \times 10^{-5}$ m³/s), the pulsation amplitudes corresponding to the peak are higher than the peak pulsation measured for dry gas ($Q_L = 0$ m³/s). Pulsations initially increase and then decrease with an increase in the Q_L .

Concerning the frequency at the peak of the pulsations, it decreases while the flow rate increases. Only at 1.0×10^{-4} m³/s (6000 ml/min) an increase of 0.5 Hz is observed (Figure 2.28).

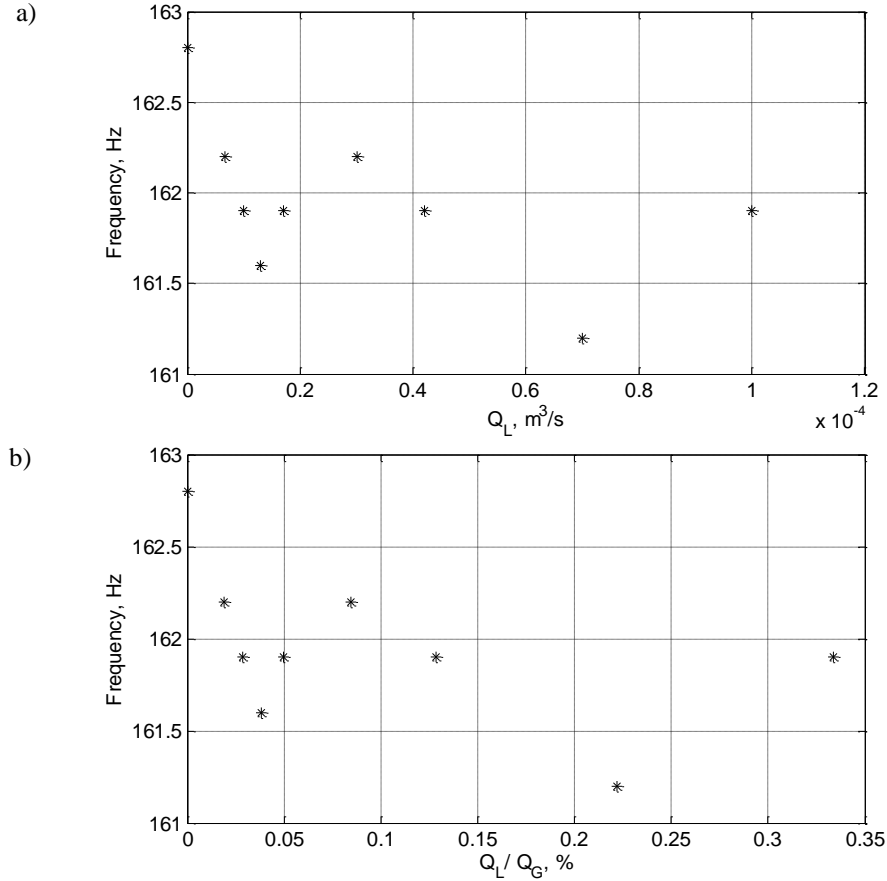


Figure 2.28. Quasi-cross configuration, far injector. Wet gas: pulsation frequency [Hz] corresponding to the maximum pulsation pressure as function of the liquid volumetric flow rate Q_L [m³/s] (a) and the percentage volume fraction [%] (b).

Finally, at high injection rates, the Strouhal number increases. As said before even for the tandem, at high injection rates the effect of hold-up can play a determinant role, because of the reduction of the effective area occupied by one phase. For that reason, Figure 2.29 shows the trend of Strouhal number both with superficial velocity (a) and with actual velocity (b). The latter is estimated with the one-dimensional multiphase flow simulation solver OLGA (OLGA), assuming a fully developed flow with a gas velocity equal to 17 m/s. As seen by comparison of the two plots of Figure 2.29, the Strouhal number based on the actual velocity offers a better scaling.

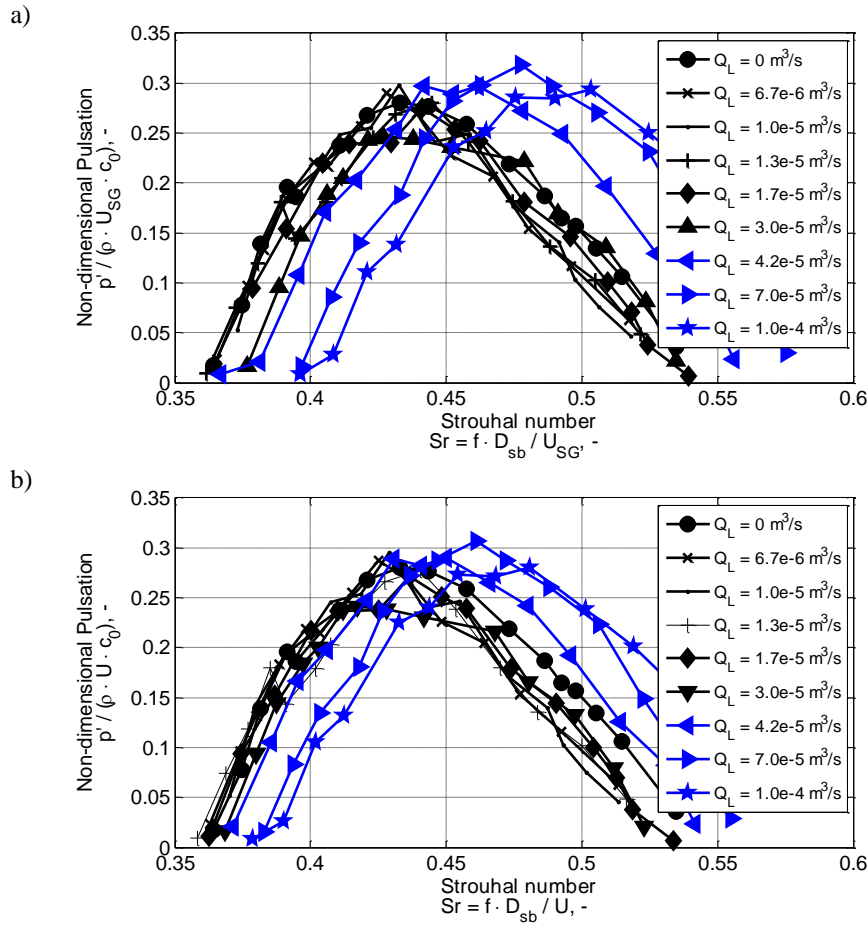


Figure 2.29. Quasi-cross configuration, far injector. Wet gas: non-dimensional pressure pulsation [-] as function of the Strouhal number [-] based on the superficial gas velocity U_{SG} (a) and on the actual gas velocity U (b).

Quasi Cross Configuration – Injector at $2 D_{mp}$ upstream

The tests reported in preceding sections were repeated also locating the injector close to the upstream side branch. In this case, the injector is at ~ 10 cm upstream of the upstream side branch.

Dry gas

Figure 2.30 shows the non-dimensional pulsations measured at the upstream side branch corresponding to dry gas with respect to the superficial gas velocity for the configuration with far and close injector.

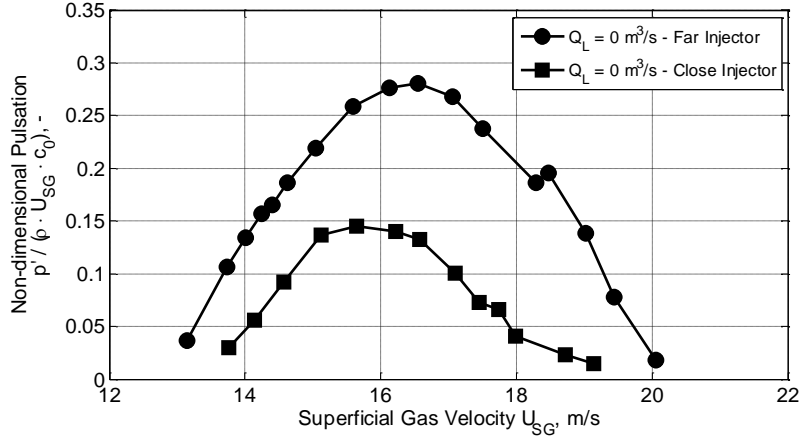


Figure 2.30. Quasi-cross configuration, far and close injector. Dry gas: comparison between the non-dimensional pressure pulsations [-] measured at the upstream side branch as function of the superficial gas velocity U_{SG} [m/s].

A 50% decrease in pulsation amplitude and a shift to lower velocities is observed. This decrease was also observed in the experimental investigation with the *tandem* configuration when the injector was located at $2D_{mp}$ upstream (Section 2.3.1). The nozzle is a large obstacle in the flow (aerodynamic blockage equal to 22.5%), which modifies the velocity profile of the flow at the T-junctions. This might cause the decrease in the pulsation amplitude. When the injector is instead located far from the upstream side branch ($25 D_{mp}$), the effect of this disturbance can be neglected.

The frequency corresponding to the peak is 162.8 Hz.

Wet gas

The results concerning the non-dimensional pulsations are shown in Figure 2.31.

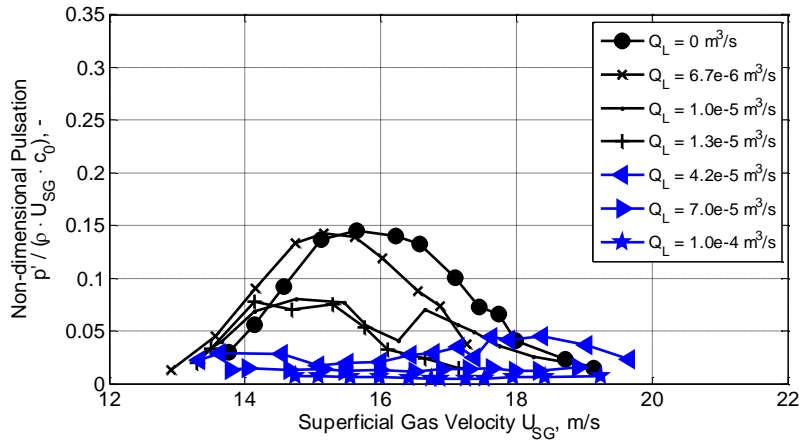


Figure 2.31. Quasi-cross configuration, close injector. Wet gas: non-dimensional pulsation pressure [-] as function of the superficial velocity U_{SG} [m/s].

Pulsations are completely eliminated at high injection rates. For amounts of liquid Q_L larger than $6.7e-6 \text{ m}^3/\text{s}$, a decrease of pulsations higher than 60% is observed. With the injector close to the upstream side branch, a film of water is expected to be present at the wall. The thickness of the film at the top of the main pipe increases as the amount of liquid increases. The presence of the film can be the responsible of such a large decrease of

pulsations. Furthermore, the shift of the peak to lower velocities reported for dry gas is also present with liquid. Note that, since the flow is not developed, it was not possible to evaluate the liquid hold-up (and thus the actual air velocity) for this configuration.

The non-dimensional pulsations are plotted with respect to the Strouhal number in Figure 2.32. The Strouhal number increases while the amount of water injected increases. Also, in the quasi-cross configuration, the Strouhal corresponding to the peak of the pulsations is in the range between 0.45 and 0.5. At high injection rates it is not possible to define any clear trend.

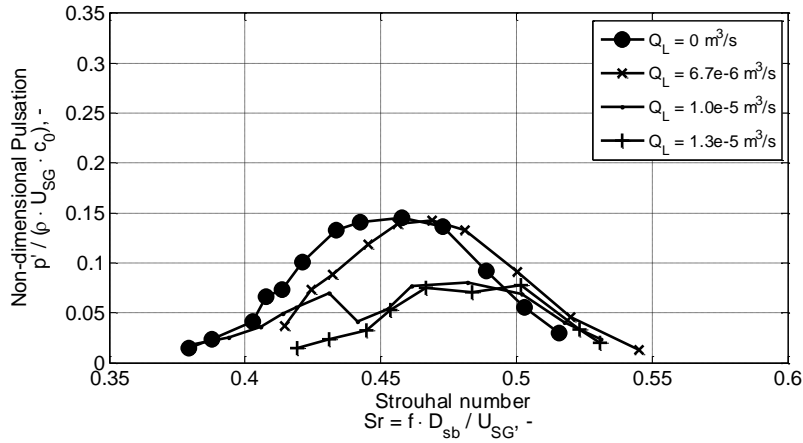


Figure 2.32. Quasi-cross configuration, close injector. Wet gas: non-dimensional pressure pulsation [-] as function of the Strouhal number [-] based on the superficial gas velocity U_{SG} [m/s].

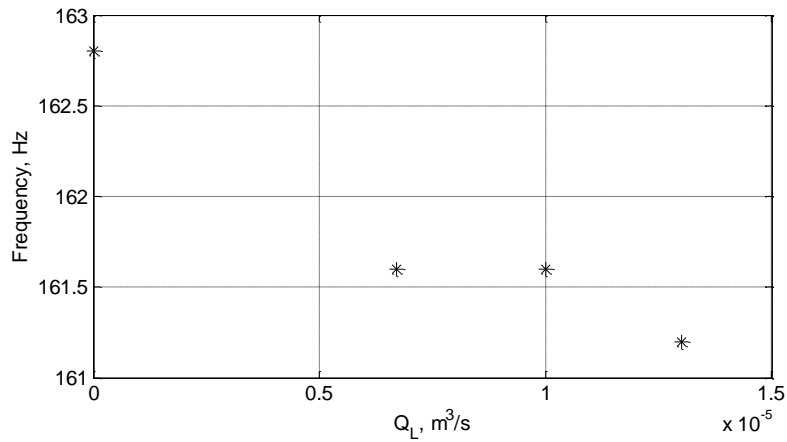


Figure 2.33. Quasi-cross configuration, close injector. Wet gas: pulsation frequency [Hz] corresponding to the maximum pulsation pressure as function of the liquid volumetric flow rate Q_L [m³/s].

As well as for the configuration with far injector (Figure 2.28), in the range 0-1.3e⁻⁵ m³/s the frequency does decrease. Moreover, for close injector, frequencies are lower than frequencies measured with the injector located far from the side branch (Figure 2.28). Not all the frequencies are reported, since not a real peak of the non-dimensional pulsation is observed at high injection rates (Figure 2.33).

2.4. Discussion

In the previous sections, the analysis has been made for each configuration independently. The results will be here analyzed by range of liquid injection rates for each location of the injector. The analysis is made independently for the amplitudes, frequencies, and Strouhal numbers. The relation between the flow pattern and the pulsations trend is emphasized.

2.4.1. Amplitudes

In Figure 2.34, the maximum amplitude of pulsations is plotted versus the water injection rate for the different configurations reported in this paper. The two red curves present the results with the injector at $25 D_{mp}$ from the upstream side branch. Comparison between these two curves show that, at $Q_L = 0 \text{ m}^3/\text{s}$, the non-dimensional pulsations are higher for the *Quasi-cross* configuration (red squares) than for the tandem configuration (red circles). One of the reasons of the difference in pulsation amplitudes is that the visco-thermal losses act on a longer distance between the two side branches in the *Tandem Configuration* (Tonon et al., 2011b). The same is observed for the case with injector located at $2 D_{mp}$ (black curves in Figure 2.34). Note that for the same configuration, at $Q_L = 0 \text{ m}^3/\text{s}$, the pulsations are always lower when the injector is close to the upstream side branch ($2 D_{mp}$) because of the turbulence generated by the nozzle, as explained in Sections 2.3.1 and 2.3.2.

Low and middle Injection Rates ($Q_L < 0.3e^{-4} \text{ m}^3/\text{s}$)

At low injection rates (lower than $0.13e^{-4} \text{ m}^3/\text{s}$), the flow pattern is stratified or stratified wavy. In this range of liquid flow rates, water accumulates at the bottom of the main pipe, both for the tandem configuration and the quasi-cross configuration. The same nozzles are used and the droplets-size distribution is therefore expected to be similar. However, two different behaviors can be distinguished when the injector is located at $25 D_{mp}$ (red curves, Figure 2.34). In particular, at low injection rates (up to $0.13e^{-4} \text{ m}^3/\text{s}$), the 50 % decrease observed for the *Tandem configuration* (red circles) is not observed for the *Quasi-Cross* configuration (red squares). There are two important things to consider. First, the two configurations have been chosen because the acoustic standing wave is trapped within the resonator, as explained in Section 2.1.1. It means that minimal external losses are expected. Second, it is known from literature that water can contribute in different manners to the increase of the acoustical damping (Howe, 1998a; Golliard et al., 2013). On the basis of these two aspects, a possible explanation of the decrease observed for the tandem and not for the quasi cross configuration for Q_L up to $0.13e^{-4} \text{ m}^3/\text{s}$ (red circles and squares) is that the water in the middle section of the *Tandem Configuration* adds acoustical damping, reducing the pulsations. Moreover, since the flow pattern is stratified or stratified wavy, the stream of water at the bottom of the main pipe does not interfere with the shear layer, i.e. hydrodynamic instability. Damping is therefore considered the most consistent reason to explain the different behavior at low injection rates.

In the middle liquid flow range ($0.13\text{-}0.28 e^{-4} \text{ m}^3/\text{s}$), when the injector is located far from the upstream side branch, the pulsations increase with increasing liquid injection even above the pulsations observed with dry gas (see red lines, Figure 2.34). This happens for the two configurations. It is not clear what causes this increase of pulsations. It is remarkable that the pulsations are larger than the pulsations with dry gas, have always been considered as the most conservative condition. Further investigations are therefore needed.

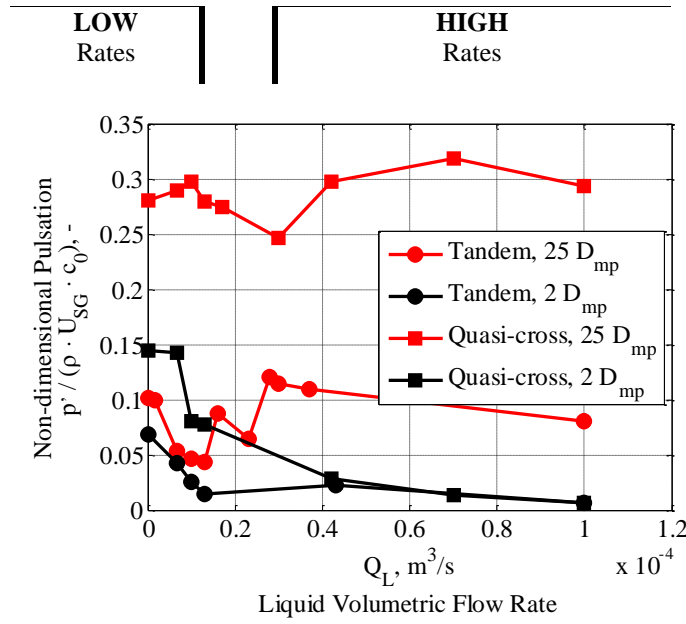


Figure 2.34. Non-dimensional pulsation [-] as function of the volumetric liquid flow rate Q_L [m³/s].

For the case with close injector (black curves in Figure 2.34), pulsations amplitudes also decrease for low and medium injection rates for the Tandem configuration (black circles) and for the Quasi-Cross Configuration (black squares). However, the decrease of pulsations does not occur at very low injection rates for the quasi cross configuration (black squares, Figure 2.34). Two mechanisms are probably playing a role. Note that the increase of pulsation reported for the injector at $25 D_{mp}$ at medium injection rates does not occur for the injector at $2 D_{mp}$.

As said for low injection rates for the far injector, the added acoustical damping can play a role for the tandem configuration. However, if the added damping were the sole mechanism, no decrease in amplitude was expected for the *quasi-cross*. In this case, it is possible that the film of liquid at the wall modifies the behavior of the shear-layer in the side branch opening. Indeed, for the case with close injector, a thicker water film is expected at the wall: water is spread with a 90 degrees angle and it is likely that, due to the high gas velocities, it does not have enough space to develop and to eventually accumulate at the bottom of the main pipe, upstream the T-junction. A large part of the water is injected against the pipe walls. Therefore, the flow is annular-dispersed. Furthermore, it was observed that the liquid film becomes thicker when more water is injected. This hypothesis was also confirmed in tests on a tandem configuration reported in Sanna et al. (2015). In these tests, a high-speed camera was used to record the flow pattern at the junction from a transparent closed end of the upstream side branch. A sudden decrease of pulsations (by 60%) is observed when water is interfering with the shear layer. At very low injection rates, the film is too thin to disturb the shear layer. The fact that pulsations decrease anyhow for the tandem configuration (where damping in the middle section can be increased by the water injection) but not for the quasi-cross configuration indicates the acoustical damping is dominating the decrease of pulsations at very low injection rates.

For higher injection rates, when the liquid film is thicker, the decrease in amplitude is similar for the two configurations and the interaction between liquid and the shear layer is the most likely reason.

High Injection Rates ($Q_L > 0.3e^{-4} \text{ m}^3/\text{s}$)

At high injection rates, $Q_L > 1800 \text{ ml/min}$ ($0.3e^{-4} \text{ m}^3/\text{s}$), flow visualizations show that the flow pattern is fully annular for the tandem configuration and it tends to be annular for the quasi-cross configuration, when the injector is located far from the upstream side branch. On the other side, when the injector is located close to the upstream side branch, the flow is expected to be annular. The distribution of water and air along the cross sectional area for annular patterns is such that a water film is at the wall, while air constitutes the core flow. Figure 2.34 (red lines) shows that at high injection rates the non-dimensional pulsations decrease for the tandem configuration (red circles), while for the *quasi-cross* configuration (red squares) amplitudes initially increase and decrease again for Q_L greater than $0.7e^{-4} \text{ m}^3/\text{s}$. Two hypotheses can be made to explain it.

The first hypothesis concerns the interaction between the source of sound and the liquid film of water on the pipe walls, as discussed at the end of Section 2.4.1 - Low and middle injection rates. For the *Tandem configuration*, although it was not possible to precisely see at the edge of the upstream T-junction, the flow was already annular or annular dispersed two diameters upstream the edge. The (wavy) film of water at the wall was likely interfering with the shear layer, either because there is water in the shear layer or because air flows on a rough surface of water, inducing turbulence. The effects were already observed for the case where the injector is located close to the upstream side branch.

The second hypothesis is, as at low injection rates, an increase of acoustical damping due to the presence of water. Water can add acoustical damping in different manners, e.g. with droplets or also with a stream of water (see Section 2.4.1 – Low and middle injection rates). The flow pattern for the *tandem* and the *quasi cross* is slightly different. For the tandem configuration the flow pattern is annular, whereas it tends to be annular for the quasi cross. In both cases there is liquid entrained in the core flow but for one configuration the pulsations are increasing and for the other they are decreasing. Added damping due to droplets is therefore excluded. On the contrary, it cannot be excluded that the acoustic damping has increased because of water in the middle section between the two side branches (only for the tandem), inducing the decrease of pulsations.

As a consequence, these two hypotheses are neither validated nor excluded by comparing the two trends at high liquid rates.

When the injector is located close to the upstream side branch, for both configurations pulsations monotonically decrease at high injection rates. The mechanism at the basis is thought to be the same as the one of low injection rates for the close injector configuration, i.e. the interference between liquid and the shear layer. The decrease in this case is stronger because the film of water is expected to be thicker.

2.4.2. Frequency

In Figure 2.35, the peak-whistling frequency at the maximum of pulsations is plotted versus the injection rate for the different configurations. Note that the frequency without injection is different for the tandem configuration (circle markers) and quasi-cross (square markers) since the distance between the side branches in the Quasi-Cross configuration is not equal to zero, but 7 cm (see Table 2.2). When water is injected, even at very low rates, a decrease of whistling frequency is observed. This can be explained by the decrease of temperature as soon as the water is sprayed in the pipe. Since the water is injected as small droplets in a relatively dry air flow, these droplets first evaporate until the air is saturated, which reduces the temperature.

After this initial decrease, the frequency is relatively steady, except for the injection close to the first Tee of the tandem configuration.

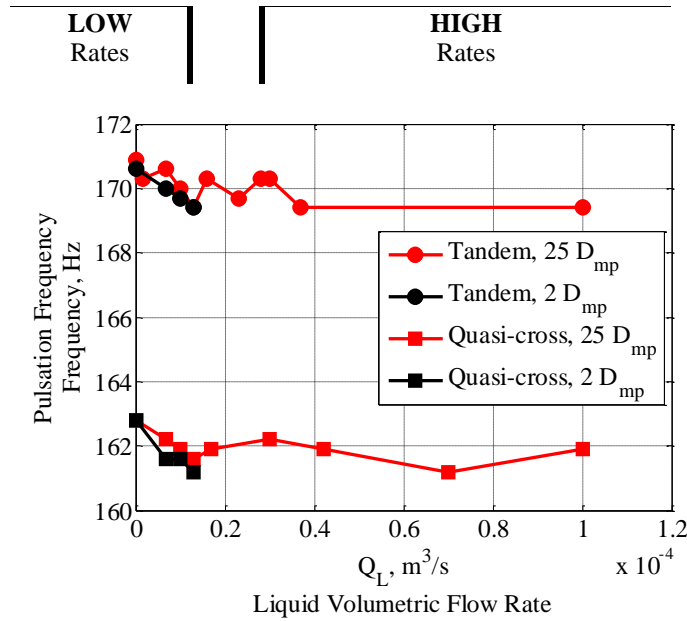


Figure 2.35. Pulsation frequency [Hz] as function of the liquid volumetric flow rate Q_L [m³/s].

2.4.3. Strouhal number

In Figure 2.36, the Strouhal number at the maximum of pulsations is plotted versus the injection rate for the different configurations. It is interesting to see that the Strouhal number increases at low injection rates for the close injector (black curves) and at high injection rates $Q_L > 0.3 \times 10^{-4} \text{ m}^3/\text{s}$ for the far injector (red curves). The Strouhal number is related to the ratio of the frequency to the gas velocity and the diameter of the side branch is used as characteristic length. Normally, changes in the Strouhal number are related either to an increase of the frequency or a decrease of the gas velocity. Figure 2.35 shows that the frequency is decreasing and it stays stable at higher injection rates. The change in the gas velocity could therefore explain this increase. The actual gas velocity is effectively changing because water is partially occupying part of the cross sectional area. However, in Section 2.3.1 (injector at 25 D_{mp}) it was seen that the use of the actual velocity instead of the superficial velocity (see Section 2.1.2 for the different definitions) did not fully explain the increase of the Strouhal number. On the contrary, the analysis showed that the accumulation of water at the edges of the T-junction possibly caused a reduction of the effective diameter of the side branch, which could explain the increase of the Strouhal number at high injection rates when the injector is located far from the upstream side branch. Accumulation of water is only possible when water is present on the upper wall of the pipe, for instance as is the case when the flow pattern is annular (high injection rates for the injector at 25 D_{mp} and low injection rates for the injector at 2 D_{mp}) and not when it is stratified (low injection rates when the injector is at 2 D_{mp}).

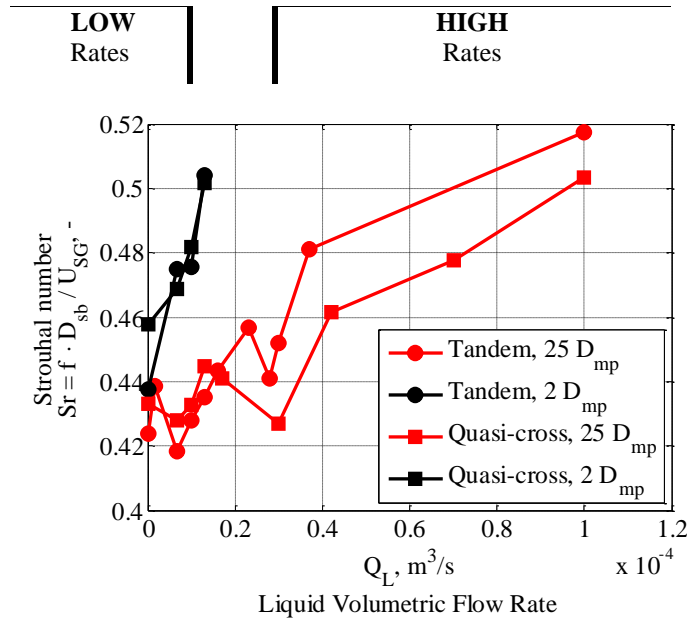


Figure 2.36. Strouhal number [-] based on the superficial gas velocity U_{SG} [m/s] as function of the liquid volumetric flow rate Q_L [m³/s].

2.5. Conclusions

Two common industrial and academic configurations, namely the *Tandem* and the *Quasi-Cross* configurations have been used and compared to estimate the effects of liquid on FIPs. The only difference between the two is the relative distance between the two T-junctions; for the tandem configuration the relative distance is the double of the acoustic length of each side branch, while for the quasi-cross configuration it is very small.

For each configuration, dynamic pressure amplitudes have been measured when a gas flow is grazing in the main pipe with different gas velocities (10-20 m/s) while liquid volumetric flow rates up to 1.0×10^{-4} m³/s are injected by means of nozzles. For each configuration, the experiments have been repeated both with the injector located far (25 diameters) and close (2 diameters) to the upstream T-junction.

The results between the two resonators have been compared by distinguishing three different liquid rates' ranges for the location located far from and close to the upstream side branch.

Three main important features are reported:

- The acoustic attenuation in the middle section is increased by the presence of water, especially for the stratified and stratified wavy flow patterns. For these patterns, liquid is not interfering with the vortex shedding since the film of water does not come in the shear layer.
- In presence of annular flow, liquid can interfere with the shear layer, inducing a decrease of the pulsations amplitude. This is in line with the results of Chapter 3, where another set of experiments on a tandem configuration is presented.
- Together with the decrease of pulsations, an increase of Strouhal number is observed in the configurations where liquid is accumulated on top of the pipe. This is possibly due to the decrease of the side branch diameter as consequence of water accumulation.

By covering a wide range of liquid injection rates, this work provides with a deeper knowledge on the effect of liquid on Flow Induced Pulsations. From the general comparison among different configurations, it has been

demonstrated that the interaction between the shear layer and liquid affects the source. Moreover, water in a stratified flow adds acoustical damping.

References

- Baldwin, R.M., and Simmons H.R., 1986, "Flow-Induced vibration in safety relief valves," *ASME Journal of Pressure Vessel Technology*, 108(3): 267-272.
- Belfroid, S.P.C., Golliard J., and Vijlbrief O., 2013, "Singing mitigation in corrugated tubes with liquid injection," *ASME Pressure Vessels & Piping Conference*, Paris, France.
- Belfroid, S.P.C., Korst H.J.C., Beek P. van, Lunde K., Eidsvik I.G., and Hansen F., 2014, "Singing mitigation in an export riser via liquid injection: a field case study," *ASME Pressure Vessels & Piping Conference*, Anaheim, California, USA.
- Bernstein, M., and Bloomfield W., 1989, "Malfunction of safety valves due to flow-induced vibrations," In *Flow-Induced Vibrations-1989, ASME Publication No. 154* (eds M.K. Au-Yang, S.S. Chen, S. Kaneko and R. Chilukuri), pp. 155-164.
- BETE, nozzles for industry, pollution control and fire protection catalogue.
- Blake, W.K., 1986, "*Mechanics of flow-induced sound and vibration*," Academic Press, Orlando.
- Blake, W.K., and Powell A., 1986, "The development of contemporary views of flow-tone generation" in *Recent advances in aeroacoustics*, Springer-Verlag, New York.
- Bodén, H. and Åbom M., 1986, "Influence of errors on the two-microphone method for measuring acoustic properties in ducts," *Journal of the Acoustical Society of America*, 79(2): 541-549.
- Bruggeman, J.C., 1987, "*Flow-Induced pulsations in pipe systems*," Doctoral Dissertation, Technische Universiteit Eindhoven, Eindhoven, The Netherlands.
- Bruggeman, J.C., Hirschberg A., Dongen M.E.H. van, Wijnands A.P.J., and Gorter J., 1989, "Flow Induced Pulsations in Gas Transport Systems: Analysis of the Influence of Closed Side Branches," *Journal of Fluids Engineering*, 111(4): 484-491.
- Bruggeman, J.C., Hirschberg A., Dongen M.E.H. van, Wijnands A.P.J., and Gorter J., 1991, "Self-sustained aero-acoustic pulsations in gas transport systems: experimental study of the influence of closed side branches," *Journal of Sound and Vibration*, 150(3), 371-393.
- Chen, Y.N., and Florjancic D., 1975, "*Flow Induced resonance in a pipe system due to branching*, *International conference on Vibration and Noise in Pumps, Fan and Compressor Installations*," University of Southampton, England, pp. 79-86.
- Chen, Y.N., and Stürchler R., 1977, "Flow-induced vibrations and noise in a pipe system with blind branches due to coupling of vortex shedding," *Internoise 77*, Zürich, B189-B203.
- Chen, Y.N., and Ziada S., 1982, "*Sromungserregte Schwingungen infolge Wirbelkopplung in der HZUE-Leitung*," Sulzer Brothers Limited, Report No. 1512/2803.
- Coffman, J.T., and Bernstein M.D., 1980, "Failure of safety valves due to flow-induced vibration," *ASME Journal of Pressure Vessel Technology*, 102(1): 112-118.

Continuum Dynamics, Inc., 2002, "Mechanisms resulting in a leakage from Main Steam Safety Valves," CDI Technical Note No 02-16, *Final Report Prepared for Energy Northwest*.

Deboo, G., Ramsden K., Gesior R., and Strub B., 2007, "Identification of quad cities main steam line acoustic sources and vibration reduction," *ASME Pressure Vessels and Piping Division Conference*, San Antonio, Texas.

Demetz, F.C., and Farabee T.M., 1977, "Laminar and turbulent shear flow induced cavity resonances," 4th *AIAA Aeroacoustics Conference*, Atlanta, Georgia.

Dowling, A.P. and Ffowcs Williams J.E., 1983, "*Sound and sources of sound*," Ellis Horwood, Chichester.

East, L.F., 1966, "Aerodynamically induced resonance in rectangular cavities," *Journal of Sound and Vibration*, 3(3): 227-287.

Elder, S.A., 1978, "Self-excited depth-mode resonance for a wall-mounted cavity in turbulence flow," *Journal of the Acoustical Society of America*, 64(3): 877-890.

Elder, S.A., Farabee T.M., and Demetz F.C., 1982, "Mechanisms of flow-excited cavity tones at low Mach number," *Journal of the Acoustical Society of America*, 72(2): 532-549.

Gillessen, R., and Roller R., 1989, "Verminderung und Beseitigung von Schwingungen an Rohrleitungssystemen (Reduction and elimination of vibration of piping systems)," in *Minderung von Rohrleitungsschwingungen*, VDI Berichte Vol. 748, pp. 195-222. Düsseldorf: VDI Verlag.

Golliard, J., Belfroid S.P.C., and Vijlbrief O., 2013, "Acoustic damping in smooth and corrugated pipes with and without liquid injection," *ASME Pressure Vessels & Piping Conference*, Paris, France.

Gorter, J., Hirschberg A., Wijnands A., and Bruggeman J.C., 1989, "Flow Induced pulsations in gas transport systems," *International Gas Research Conference*, Tokyo, Japan.

Graf, H.R., 1989, "*Experimental and computational investigation of the flow excited resonance in a deep cavity*," Doctoral dissertation, Department of Mechanical Eng., Worcester Polytechnic Institute, USA.

Graf, H.R., and Ziada S., 1992, "Flow-Induced acoustic resonance in closed side branches: An experimental determination of the excitation source," *ASME International Symposium on Flow-Induced Vibration and Noise*.

Graf, H.R., and Ziada S., 2010, "Excitation source of a side-branch shear layer," *Journal of Sound and Vibration*, 329(14): 2825-2842.

Hourrigan, K., Stokes A.N., Thompson M.C., and Welsh M.C., 1986, "Flow Induced Acoustic Resonances for a Bluff Body in a Duct: a Numerical Study," 9th *Australian Fluid Mechanics Conference*, Auckland, 504-507.

Hourrigan, K., Welsh M.C., Thompson M.C., and Stokes A.N., 1990, "Aerodynamic sources of acoustic resonance in a duct with baffles," *Journal of Fluids and Structures*, 4(4): 345-370.

Howe, M.S., 1975, "Contributions to the theory of aerodynamics sound, with application to excess jet noise and the theory of the flute," *Journal of Fluid Mechanics*, 71(4): 625-673.

Howe, M.S., 1984, "On the absorption of sound by turbulence," *IMA Journal of Applied Mathematics*, 32(1-3): 187-209.

Howe, M.S., 1997, "Edge, cavity and aperture tones at very low mach numbers," *Journal of Mechanics*, 330: 61-84.

- Howe, M.S., 1998a, "*Acoustics of fluid-structure interactions*," Cambridge University Press, Cambridge.
- Howe, M.S., 1998b, "Rayleigh conductivity and self-sustained oscillations," in *Theoretical and computational fluid dynamics*, Springer-Verlag, New York.
- Ishii, 2003, "*Lecture notes: short course Modeling and computation of multiphase flow*," ETH, Zurich.
- Jungowski, W.M., Botros K.K., and Studzinski W., 1989, "Cylindrical side branch as tone generator," *Journal of Sound and Vibration*, 131(2): 265-285.
- Kriesels, P.C., Peters M.C.A.M., Hirschberg A., Wijnands P.J., Iafrati A., Riccardi G., Piva R., and Bruggeman J.C., 1995, "High Amplitude Vortex-Induced Pulsations in a gas transport system," *Journal of Sound and Vibration*, 184(2): 343-368.
- Lopez de Bertodano, M.A., Jan C.S. and Beus S.G., 1997, "Annular flow entrainment rate experiment in a small vertical pipe," *Nuclear engineering and Design*, 178(1): 61-70.
- Munjal, M.L., 1987, "*Acoustics of ducts and mufflers*," John Wiley and Sons, Chichester.
- Nakiboğlu, G., Belfroid S.P.C., Willems J.F.H. and Hirschberg A., 2010, "Whistling behavior of periodic systems: Corrugated pipes and multiple side branch system," *International Journal of Mechanical Sciences*, 52(11): 1458-1470.
- Nederveen, C.J., Jansen J.K.M. and Hassel R.R. van, 1998, "Corrections for woodwind tone-hole calculations," *Acta Acustica united with Acustica*, 84(5): 957-966.
- NRC, 2004, "Additional flow-induced vibration failures after a recent power uprate, NRC Information Notice 2002-26," *Supplement 2, January 9, US Nuclear Regulatory Commission*, Washington, D.C., United States.
- OLGA, URL: <http://www.software.slb.com/products/foundation/Pages/olga.aspx>
- Oliemans, R.V.A., 2008, *Applied Multiphase flows*, Lecture Notes.
- Parthasarathy, S.P., Cho Y.I., and Back L.H., 1985, "Sound generation by flow over relatively deep cylindrical cavities," *Journal of the Acoustical Society of America*, 78(5): 1785-1795.
- PCB, URL: www.pcb.com
- Peters, M.C.A.M., 1993, "*Aeroacoustic sources in internal flows*," Doctoral Dissertation, Technische Universiteit Eindhoven, Eindhoven, The Netherlands.
- Peters, M.C.A.M., and Bokhorst E., 2000, "Flow-Induced pulsations in pipe systems with closed side-branches, impact of flow direction," *Proceeding of the 7th International Conference on Flow-Induced Vibration*, Lucerne, Switzerland.
- Peters, M.C.A.M., and Riezebos H.J., 2001, "Analysis of the occurrence of flow-induced pulsations in a gas control station," *International Gas Research Conference*, Amsterdam, The Netherlands.
- Pierce, A.D., 1981, "*Acoustics*," McGraw Hill, New York.
- Polifke, W., 2007, "*System modelling and stability analysis*," Von Karman Lecture Notes 2007-02, Brussels, Belgium.

- Powell, A., 1990, "Some aspects of aeroacoustics: from Rayleigh until today," *Journal of Vibration and Acoustics*, 112(2): 145-159.
- Rockwell, D., and Naudascher E., 1978, "Review: self-sustaining oscillations of flow past cavities," *ASME Journal of Fluids Engineering*, 100(2): 152-165.
- Rockwell, D., 1979, "Self-sustained oscillations of impinging free shear layers," *Annual Review of Fluid Mechanics*, 11: 67-94.
- Rockwell, D., 1983, "Oscillations of impinging shear layers," *American Institute of Aeronautics and Astronautics Journal*, 21(5): 645-664.
- Sanna, F., Golliard J., and Belfroid S.P.C., 2015, "On the effect of water film on Flow-Induced Pulsations in closed side branches in tandem configuration," *ASME Pressure Vessels & Piping Conference*, Boston, Massachusetts.
- Shoeibi Omrani, P., Golliard J., Belfroid S.P.C. and González Díez N., 2012, "On the effects of droplets modulating the acoustic source powers generated in T-joints," *10th International Conference on Flow-Induced Vibration*, Dublin, Ireland.
- Shoham, O., 2006, "*Mechanistic modeling of Gas-Liquid Two-Phase Flow in Pipes*," Society of Petroleum Engineers.
- Stoneman, S.A.T., Hourigan K., Stokes A.N., and Welsh M.C., 1988, "Resonant sound caused by flow past two plates in tandem in a duct," *Journal of Fluid Mechanics*, 192: 455-484.
- Tonon, D., Nakiboglu G., Willems J.F.H., Hirschberg A., Leandro R.E., Polifke W., and Riezebos H.J., 2009, "Self-sustained aeroacoustic oscillations in multiple side branch pipe systems," *15th AIAA/CEAS Aeroacoustics conference*, Miami, Florida, United States.
- Tonon, D., Willems J.F.H., and Hirschberg A., 2010, "Flow-Induced pulsations in pipe systems with closed side branches: study of the effectiveness of detuning as remedial measure," *20th International Congress on Acoustics ICA*, Sydney, Australia.
- Tonon, D., Willems J.F.H., and Hirschberg A., 2011a, "Self-sustained oscillations in pipe systems with multiple deep side branches: Prediction and reduction by detuning," *Journal of Sound and Vibration*, 330(24): 5894-5912.
- Tonon, D., Hirschberg A., Golliard J., and Ziada S., 2011b, "Aeroacoustics of pipe systems with closed side branches," *International Journal of Aeroacoustics*, 10(2-3): 201-276.
- Uchiyama, Y. and Morita R., 2013, "Experimental Evaluation of Resonance frequency at Branch section in Each Dry and Wet Steam Flow," *ASME Pressure Vessels & Piping Conference*, Paris, France.
- Uchiyama, Y. and Morita R., 2015, "Experimental investigation for acoustic resonance in tandem branches under each dry and wet steam flow," *ASME Pressure Vessels & Piping Conference*, Boston, Massachusetts, United States.
- Webb, M., and Ellenberger P., 1995, "Piping Retrofit Reduces Valve-Damaging Flow Vibration," *Power Engineering*, 99(1): 27-29.
- Ziada, S., 1993, "Flow-excited resonances of piping systems containing side-branch: Excitation mechanism, counter-measures and design guidelines, *International Seminar on Acoustic Pulsations in Rotating Machinery*, 1-34, AECL CANDU, Mississauga, Ontario, Canada.

Ziada, S., 1994, "A flow visualization study of flow-acoustic coupling at the mouth of a resonant side-branch," *Journal of Fluids and Structures*, 8(4): 391-416.

Ziada, S., 2010, "Flow-excited acoustic resonance in industry," *Journal of Pressure Vessel Technology*, 132(1): 1-9.

Ziada, S., and Bühlmann E.T., 1992, "Self-excited resonances of two side-branches in close proximity," *Journal of Fluids and Structures*, 6(5): 583-601.

Ziada, S., and Shine S., 1999, "Strouhal Numbers of Flow-Excited Acoustic Resonance of Closed Side Branches," *Journal of Fluids and Structures*, 13(1): 127-142.

Ziada, S., and Lafon P., 2013, "Flow-Excited Acoustic Resonance Excitation Mechanism, Design Guidelines and Counter Measures," *ASME Applied Mechanics Review*, 66(1).

Chapter 3

On the effect of water film on flow-induced pulsations in closed side branches in tandem configuration

Résumé

Dans le chapitre précédent on a montré que la réduction des oscillations auto-induites peut être expliquée par deux mécanismes possibles: l'interaction entre le liquide et la couche mélange et l'augmentation de l'amortissement acoustique. L'étude présentée dans ce chapitre² est destinée à vérifier la première hypothèse.

Les expériences ont toutes été faites sur un résonateur avec deux branches en tandem. La différence la plus importante entre ce résonateur et celui utilisé dans le premier chapitre est que le rapport des diamètres pour cette configuration est unitaire.

Dans une première série d'expériences, le point d'injection d'eau est situé loin en amont du premier embranchement, ce qui permet d'obtenir un écoulement stratifié bien établi dans la section de mesure. Une deuxième série de mesure avec le point d'injection près du premier embranchement permet d'isoler le seul effet du film.

La décroissance des pulsations est similaire dans presque tous les cas. Il existe une exception quand il existe une interférence du liquide avec la couche de mélange, qui conduit à une diminution soudaine de 60% de l'amplitude des pulsations. Dans tous les autres cas, la réduction progressive des pulsations est causée par une augmentation de l'amortissement acoustique due à l'écoulement stratifié présent entre les deux embranchements.

² This work has been presented and published as: Sanna, F., Golliard J. and Belfroid S.P.C., 2015, "On the effect of water film on Flow-Induced Pulsations in closed side branches in Tandem Configuration," *ASME Pressure Vessels & Piping Conference*, Boston, Massachusetts.

Nomenclature

A	Upstream length [m]	f_n	Resonant frequency [Hz]
B	Middle length [m]	Q_G	Gas volumetric flow rate [m ³ /s]
C	Downstream length [m]	Q_L	Liquid volumetric flow rate [m ³ /s]
c_0	Speed of sound [m/s]	Sr	Strouhal number [-]
D	Injector location [m]	U_{SG}	Superficial Gas Velocity [m/s]
D1	Length of the upstream side branch [m]	U_{SL}	Superficial Liquid Velocity [m/s]
D2	Length of the downstream side branch [m]	δ	Ratio of the main pipe inner diameter to the side branch inner diameter [-]
D_{mp}	Diameter of the main pipe [m]	λ	No slip Liquid Volume Fraction [-]
D_{sb}	Diameter of each side branch [m]	ρ	Density of the gas [kg/m ³]
FFT	Fast Fourier Transform		
FIP	Flow Induced Pulsation		

3.1 Introduction

Piping layouts typically used in gas transport systems are characterized by branches along the main process flow line. The presence of T-junctions can have a dramatic effect on the safety and on the productivity of the plant. In fact, these configurations are characterized by trapped, or nearly trapped acoustic modes, which favor the occurrence of high-amplitude Flow-Induced Pulsations (FIPs), i.e. whistling. Pressure pulsations are driven by vortex shedding at the upstream edge of each side branch (Figure 3.1a). Under particular circumstances, this fluid dynamic phenomenon turns into an acoustical one, leading to dangerous conditions of fatigue caused by large structural vibrations.

Over the past 70 years, the effects have been experienced in several fields. For a detailed overview of the historical development and experiences see Tonon et al. (2011), Graf and Ziada (2010), and Ziada and Lafon (2013).

However, almost all these studies are for single phase gas and limited research has been done to determine the effect of the presence of liquids. Recently, more attention has been paid by the scientific community, either in corrugated pipes (Belfroid et al., 2013; Golliard et al., 2013; Belfroid et al., 2014) or in pipes with side branches (Sanna and Golliard, 2014a-b; Shoeibi Omrani et al., 2012). For instance, the experimental investigations of Golliard et al. (2013) were conducted to investigate the effect of small quantities of liquid on damping both in a

smooth pipe and in a corrugated pipe (internal diameter 49.0×10^{-3} m), at different gas velocities. In addition, the resonance frequency in a piping system was studied in steam conditions (Uchiyama and Morita, 2013-2015).

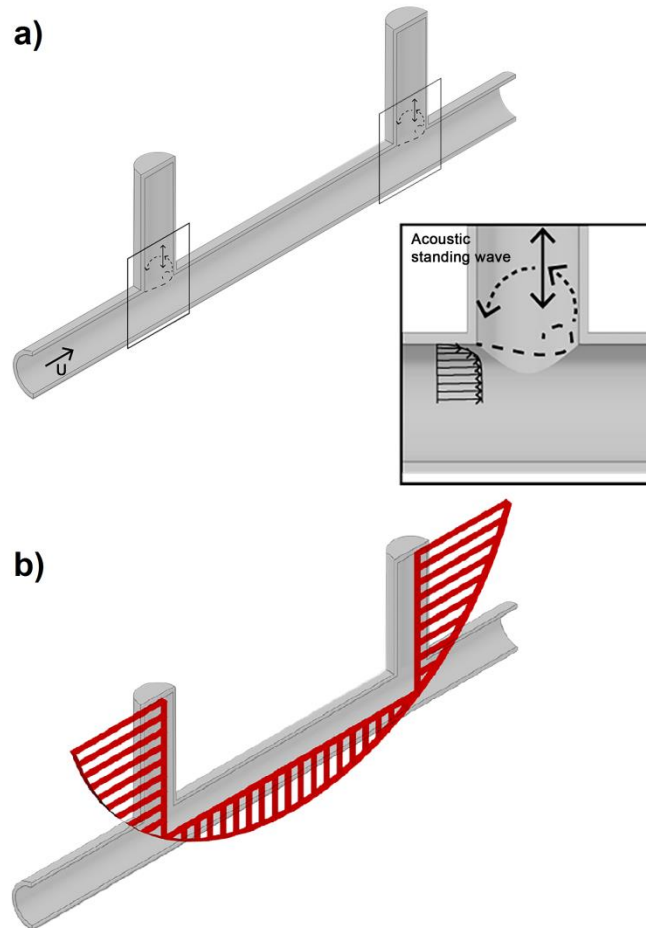


Figure 3.1. Double side branch - Tandem configuration. Generation of the vortex shedding and mechanism loop (a), and pressure distribution (b).

Concerning pipes with T-junctions, tests were recently performed with a mixture of gas and water on two configurations of two closed side branches along a main pipe, both in tandem (Sanna and Golliard, 2014b) and in quasi-cross configuration (Sanna and Golliard, 2014a). In his tests, into a 2-inch inner diameter pipe Sanna injected liquid at different flow rates together with air. Pressure pulsations generated by the grazing air flow were measured at the closed end of the two side branches. It was observed that at the highest liquid injection rates, when the distribution of water and air mixture was clearly annular, the pressure amplitude decreased. The liquid film, typical of annular flow patterns, was considered one of the main causes of the reduction of the pulsations amplitudes. The liquid film affects the shear layer instability via both the presence of liquid droplets in the shear layer and via changes in the boundary layer profile at the cavity edge (see Figure 3.1a). The aim of this work is to investigate the sole effect of the liquid film on the FIPs trend. To investigate it in the tandem configuration, three different sets of experiments are performed.

This configuration has been chosen because of the extensive experimental available data. Indeed, when tuned to maximum pulsation levels the configuration is characterized by a standing pressure wave whose wavelength perfectly fits in the resonator. The standing pressure wave has the nodes at the T-junctions and the maximum amplitudes at the closed end of each side branch (Figure 3.1b).

Different liquid volumetric flow rates Q_L are injected in a horizontal smooth main pipe where air flows at different air volumetric flow rates Q_G .

In this paper, the experimental method and the design of the experimental setup are first presented. Last, the results are shown and discussed.

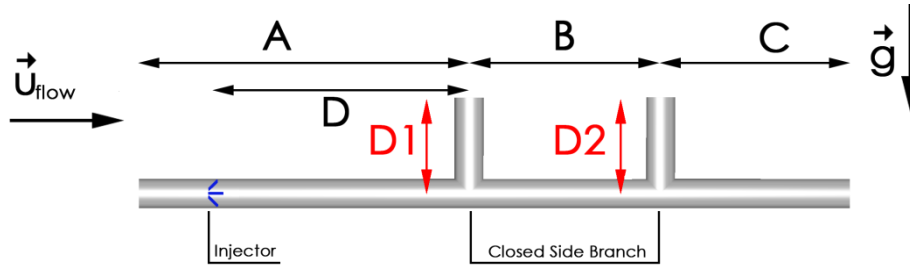


Figure 3.2. Geometrical details of the configuration tested.

3.2 Design of the experimental setup and experimental method

In this section, the technical details of the facility are firstly provided, followed by the description of the methodology used to conduct the experiments.

3.2.1. Setup

The resonator chosen is characterized by the distance B between the side branches equal to the double of the length of the side branches ($D1=D2=B/2$). Figure 3.2 provides a general description of the setup tested while in Table 3.1 the geometrical details are reported. As for the tandem configuration used in Chapter 2, the side branches are mounted upwards to avoid accumulation of water due to gravity. However, there are some differences in the setup.

First, the inner diameters of the main pipe D_{mp} and D_{sb} of the side branches are equal to 1 inch (0.025 m) and the material of the whole facility is transparent Plexiglas with a wall thickness of 3.5×10^{-3} m.

Concerning the lengths D1 and D2, they were chosen such that their acoustic length is 0.268 m. The frequency corresponding to the first acoustic mode f_1 is about 320 Hz. The definition of the acoustical length of

the side branches includes the length corrections. According to the model proposed by Nederveen et al. (1998), the no-mean-flow acoustic correction length for this resonator ($\delta = 1$) is equal to 4.0×10^{-3} m. D1 and D2 (physical lengths) are thus equal to 0.264 m.

Analogously to the configurations used in the previous setup, the upstream and downstream lengths A and C were chosen based on two considerations: minimal influence of other acoustical resonances on the Tandem resonance in the velocity bandwidth of interest and sufficient multiphase flow development length. The same 1D-acoustical-No flow model built for the previous campaigns is used also here. For the 1D simulations, a reflection coefficient equal to 0.86 and an open boundary condition have been imposed, upstream and downstream respectively. The first is the acoustical reflection coefficient at a frequency equal to 320 Hz of the system inlet, i.e. the 2-pipe main injector used to drive air and water into the main pipe.

The entrance length A is $68 D_{mp}$ which is sufficient development length in case of stratified flow. In case of annular/dispersed flow this is on the edge. However, the expected onset of entrainment is at $U_{SG} = 19$ m/s (Ishii, 2003). This is at or above the measurement range for the current experiments. Therefore, no or very low entrained fractions are expected and developed flow is assumed.

The final lengths of the entire system are reported in Table 3.1.

Table 3.1. Physical and equivalent acoustical lengths of the experiments setup (Figure 3.2).

	A	B	C	D	D1	D2
Tandem configuration – Far Injector						
Physical length [m]	1.70	0.536	1.34	1.70	0.264	0.264
Tandem configuration – Close Injector						
Close injector – TOP						
Physical length [m]	1.70	0.536	1.34	0.052	0.264	0.264
Close injector – BOTTOM						
Physical length [m]	1.70	0.536	1.34	0.052	0.264	0.264

3.2.2. Experimental technique and post-processing

Two different lines bring water and air to the setup, respectively from a pressurized vessel (4-7 bar) and a compressor. They are equipped with flow meters in order to regulate the flow mass rate of air and the water flow rate.

Three sets of experiments were conducted:

- Far Injector
- Close Injector:
 - Top Injection
 - Bottom Injection

For the first set, the water injection point is located far from the upstream side branch. The gas velocity was varied between $U_{SG} = 10$ and 20 m/s at constant liquid rate up to $U_{SL} = 0.022$ m/s (1.1×10^{-5} m³/s). Note that $U_{SG} = 4Q_G / (\pi D_{mp}^2)$ and $U_{SL} = 4Q_L / (\pi D_{mp}^2)$. In this operating range, the flow is expected to be stratified or stratified wavy. Indeed, depending on the combination of the superficial liquid and air velocities, the distribution of a fully developed flow along the cross sectional area of the pipe can vary. Figure 3.3 shows what it would be seen in a smooth horizontal pipe with an inner diameter of 1 inch.

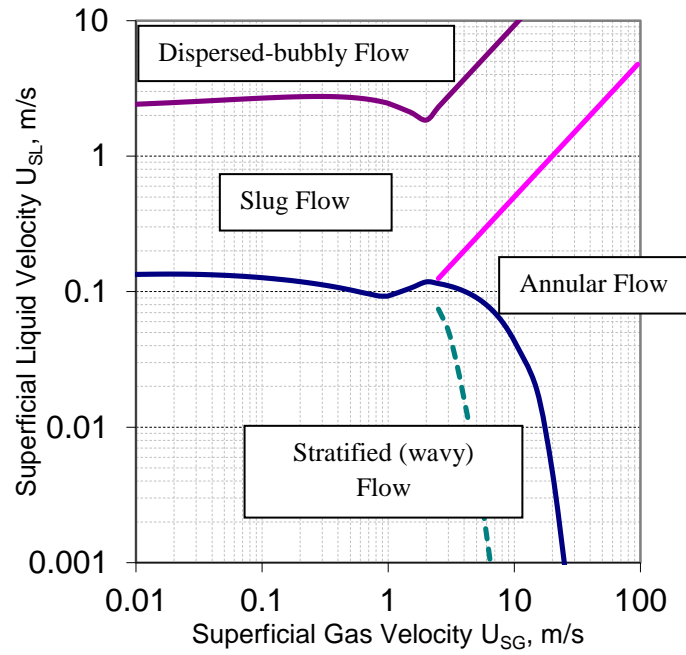


Figure 3.3. Flow pattern map for horizontal smooth pipes with inner diameter $D_{mp} = 0.025$ m (Shoham, 2006).

All experiments are performed at near atmospheric conditions at a temperature of approximately 18°C.

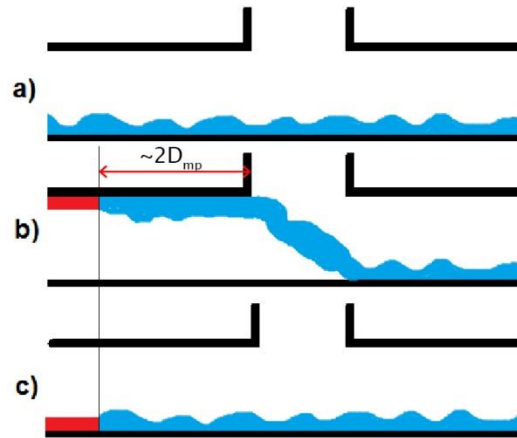


Figure 3.4. Inside view sketch of the upstream T-junction: a) Far liquid injection, b) Close top liquid injection, c) Close bottom liquid injection.

Concerning the two *Close Injector* configuration test sets, the injection point is located $2D_{mp}$ from the upstream side branch. Liquid was injected using 4 small straws (ID = 1 mm) combined in a plane attached to the inner pipe wall. In this way a thin film could be generated (see Figure 3.4b and Figure 3.4c). For both sets, a first test series with dry gas is performed to obtain the gas velocity corresponding to the pressure pulsation maximum. At that fixed superficial gas velocity, the water injection rate was increased up to the full elimination of pressure pulsations. This last procedure was also repeated for slightly higher and lower gas velocities to investigate the influence of liquid injection on the condition for maximum pulsation level.

For all the experiments, dynamic pressure measurements are conducted with two flush-mounted piezometric sensors (PCB Piezotronics Pressure Division) type 116A located at the closed end of the two side branches.

The software DEWESoft 6.6.5 (DEWESoft) is used to store the data and the FFT (Fast Fourier Transform) is used to post-process the pressure measurements (30 seconds time signal) and to obtain the acoustic whistling characteristics. In the following, from the power spectrum obtained with the FFT, the amplitude peak value of the pressure pulsations is considered.

In addition, to monitor the behavior of water, two dewe-cam-fw-70 cameras are used. Particularly, Camera 1 is initially used to have a visualization of the water distribution along the longitudinal direction of the main pipe (Figure 3.5). For the *Close-Top injector* it is located next to Camera 2 to observe the behaviour of the liquid film. Camera 2 is instead used only for the experiment with *Close-Top Injector* to check whether any water accumulation occurs at the edges of the Tee and whether water bypasses or spans the mouth together with the shear layer. Figure 3.5 shows the locations of the two cameras.

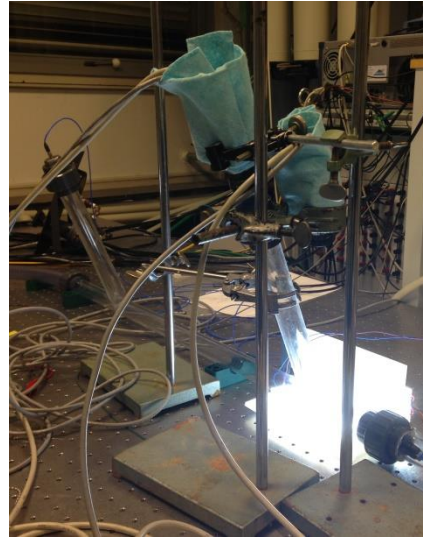
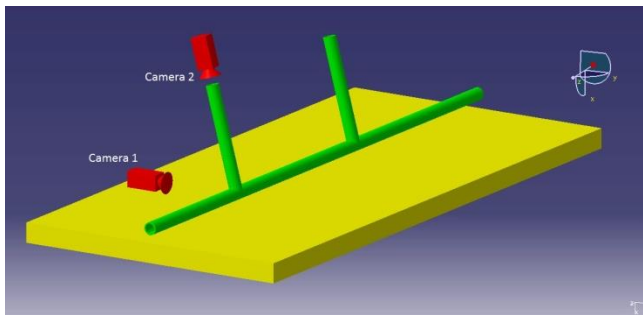


Figure 3.5. Location of cameras.

3.3. Flow visualizations recordings

In this section, for the first two experimental test sets, snapshots taken from the recording videos are provided at different water injection rates and discussed.

Concerning the first series with the injector far upstream, Figure 3.6 depicts the flow at the (upstream) T-junction. Particularly for the superficial gas velocity which corresponds to the pressure pulsation maximum ($U_{SG} \approx 15$ m/s), Figure 3.6 shows the behavior of the liquid film at different increasing injection rates. For the peak velocity of $U_{SG} \approx 15$ m/s the maximum expected hold-up at $Q_L = 1.1 \times 10^{-5}$ m³/s is approximately 2%. Note that the hold-up is the ratio of the pipe cross-section occupied by the liquid phase to the total cross-sectional area.

From the visualizations, it is clear that, at higher liquid rates, the liquid hold-up (film height) increases. The flow regime is completely stratified with no or limited entrainment. At the highest injection rates, water starts being entrained in the gas flow. This behavior was expected, being in line with the flow pattern map (see Figure 3.3).

For the test with *Close-Top injection*, two cameras have been used: respectively Camera 1 is used to monitor the liquid film behavior, while Camera 2 is positioned to observe the film through the side branch.

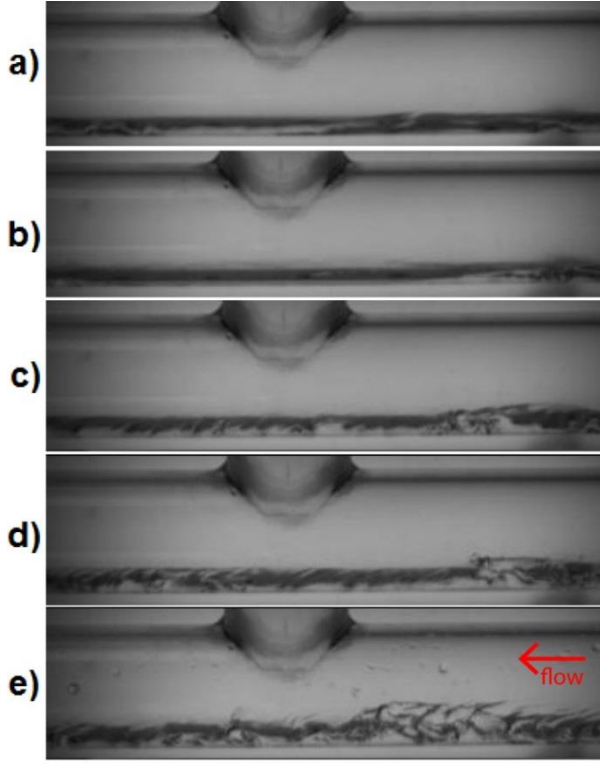


Figure 3.6. Tandem configuration, far injector. Flow visualizations at the upstream T-junction for different liquid volumetric flow rate Q_L and no-slip liquid volume fractions λ : a) $Q_L = 1.1 \times 10^{-6} \text{ m}^3/\text{s}$, $\lambda = 1.46 \times 10^{-4}$; b) $Q_L = 1.9 \times 10^{-6} \text{ m}^3/\text{s}$, $\lambda = 2.53 \times 10^{-4}$; c) $Q_L = 4.2 \times 10^{-6} \text{ m}^3/\text{s}$, $\lambda = 5.59 \times 10^{-4}$; d) $Q_L = 6.9 \times 10^{-6} \text{ m}^3/\text{s}$, $\lambda = 9.19 \times 10^{-4}$; e) $Q_L = 1.1 \times 10^{-5} \text{ m}^3/\text{s}$, $\lambda = 1.46 \times 10^{-3}$. The superficial gas velocity is the one corresponding to the peak. The air/water mixture flows from right to left.

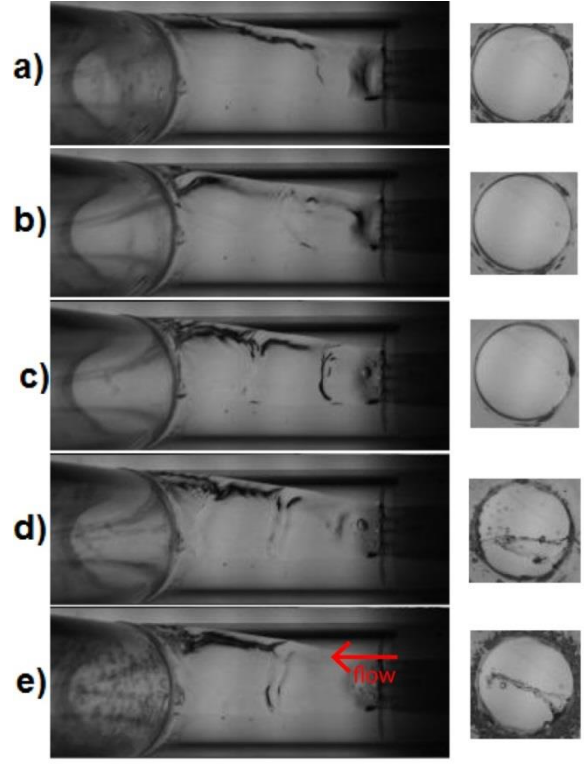


Figure 3.7. Tandem configuration, close-top injector. Flow visualizations at the upstream T-junction for different liquid volumetric flow rate Q_L and no-slip liquid volume fractions λ : a) $Q_L = 1.7 \times 10^{-7} \text{ m}^3/\text{s}$, $\lambda = 2.46 \times 10^{-5}$; b) $Q_L = 1.1 \times 10^{-6} \text{ m}^3/\text{s}$, $\lambda = 1.59 \times 10^{-4}$; c) $Q_L = 2.5 \times 10^{-6} \text{ m}^3/\text{s}$, $\lambda = 3.62 \times 10^{-4}$; d) $Q_L = 2.7 \times 10^{-6} \text{ m}^3/\text{s}$, $\lambda = 3.91 \times 10^{-4}$; e) $Q_L = 3.0 \times 10^{-6} \text{ m}^3/\text{s}$, $\lambda = 4.34 \times 10^{-4}$. The superficial gas velocity is the one corresponding to the maximum amplitude ($U_{SG} \approx 14 \text{ m/s}$). The air/water mixture flows from right to left. Left photos for Camera 1, right photos of Camera 2.

Relevant information can be extracted only by looking at the frames recorded by Camera 1 (left side) and by Camera 2 (right side) (Figure 3.7). Especially at low injection rates, it was rather difficult to align the liquid film to the main pipe axis and be sure that liquid was at the upstream edge of the T-junction. However, Figure 3.7 depicts a different behavior of the film depending on the amount of liquid injected. The first noticeable physical feature is that at higher injection rates the film width increases and the liquid is better aligned to the upstream side branch edge. Moreover, water bypasses the side branch mouth up to a liquid rate of $Q_L = 2.5 \times 10^{-6} \text{ m}^3/\text{s}$. At higher rates, liquid is transported partly via droplets through the shear layer.

3.4 Experimental results

The results of the three test sets are discussed in three different sub-sections. First, the results obtained with the far injector are discussed followed by the close injector results.

The pressure pulsation amplitude is made dimensionless by using the superficial gas velocity, the constant (gas) density ρ of 1.2 kg/m^3 , and the speed of sound c_0 equal to 343.2 m/s . The Strouhal number is calculated by using the diameter of the side branch D_{sb} and the superficial gas velocity U_{SG} .

Only the pressure amplitudes measured at the closed end of the downstream T-junction are hereby reported.

3.4.1. Results – Far Injector

Dry gas

The single phase results show at the peak a Strouhal number of $Sr = 0.52$ and an amplitude of 121 Pa. Figure 3.8 shows the measured pressures at the ends of the side branches. From 30-seconds time signals, the amplitude peak is considered by doing the FFT.

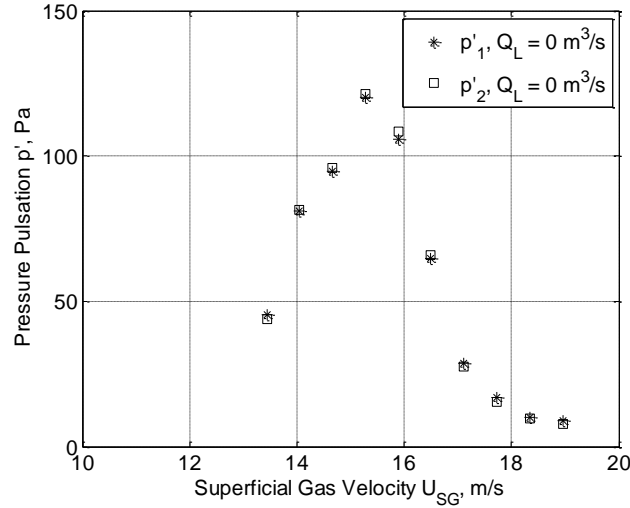


Figure 3.8. Tandem configuration, far injector. Dry gas: pressure pulsation amplitude [Pa] as function of the superficial gas velocity U_{SG} [m/s].

The Strouhal number is higher than measured in the 2-inch experiments (Sanna and Golliard, 2014b) in which a Strouhal number of 0.42 was found. The difference can be attributed to the increase in the diameter ratio δ (Ziada and Shine, 1999). While δ is now unitary, in the 2-inch experiments of 2014 (Sanna and Golliard, 2014b) this ratio was equal to $\delta = 0.83$. In terms of amplitudes, they are in line with the source strengths.

The peak amplitude is 80% lower than measured values in the 2-inch. In the previous experiments a non-dimensional value of $\frac{p'}{\rho U_{SG} c_0} = 0.1$ was measured, while in the current setup only a value of 0.02 is measured.

Wet gas

In Figure 3.9, the pulsations measured at the downstream side branch are plotted as function of gas velocity for different liquid volumetric flow rates.

The peak amplitude decreases with increasing liquid rate. The same behaviour was observed in the 2-inch pipe at low injection rates (Sanna and Golliard, 2014b). In both sets of experiments, the flow regime was stratified or stratified wavy.

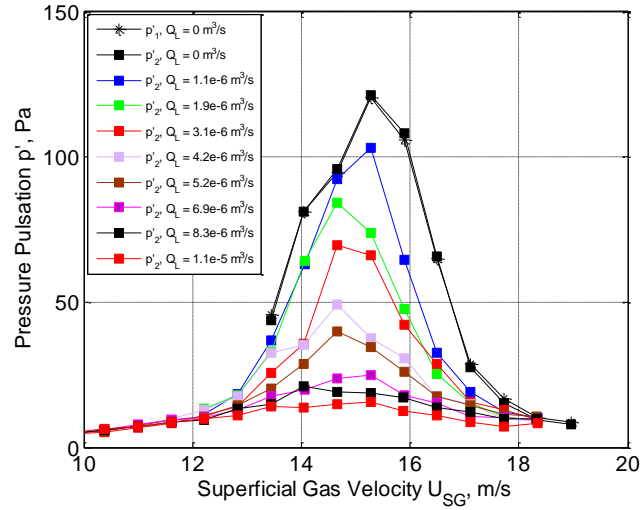


Figure 3.9. Tandem configuration, far injector. Wet gas: pressure pulsations [Pa] as function of the superficial gas velocity U_{SG} [m/s].

In Figure 3.10 the variation in frequency as function of the superficial gas velocity is reported. The frequency corresponding to the peak is not changing with increasing liquid rate. This indicates that the effective speed of sound is hardly changed.

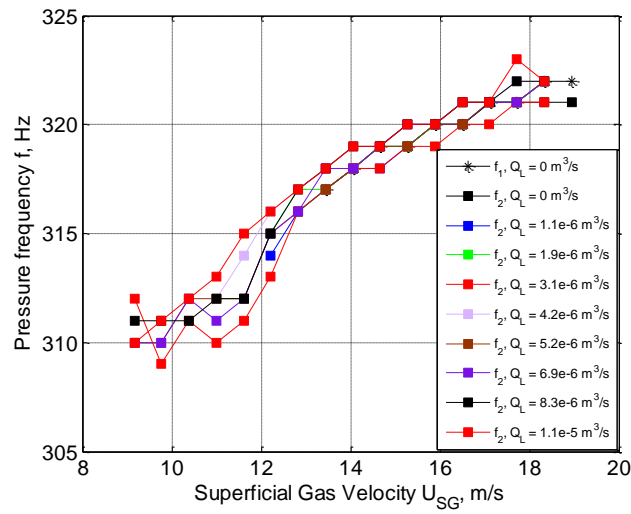


Figure 3.10. Tandem configuration, far injector. Wet gas: pulsation frequency [Hz] as function of the superficial gas velocity U_{SG} [m/s].

Figure 3.11 finally shows the non-dimensional pressure as function of the Strouhal number. The Strouhal number is calculated by using the diameter of the side branch D_{sb} and the superficial gas velocity U_{SG} . For dry gas, the peak Strouhal number is equal to $Sr = 0.522$. At liquid injection, the peak Strouhal number increases slightly to $Sr = 0.54$. At higher injection rates, this Strouhal remains constant.

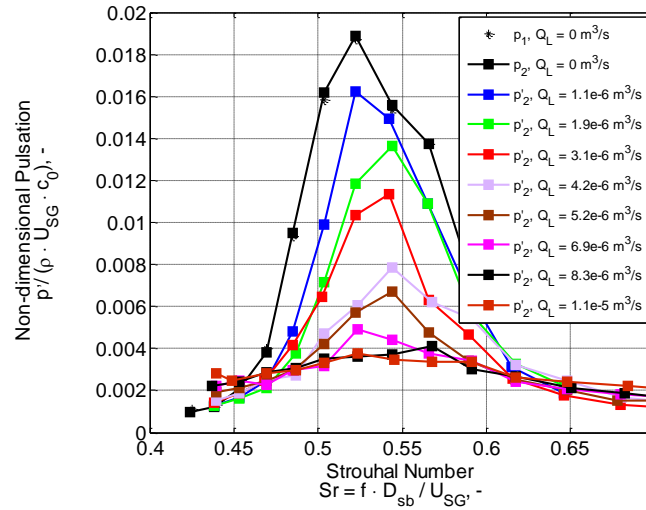


Figure 3.11. Tandem configuration, far injector. Wet gas: non-dimensional pulsations [-] as function of the Strouhal number [-] based on the superficial gas velocity U_{SG} [m/s].

3.4.2. Results– Close Injector – Top Injection

The injection point is now located at the top of the main pipe, 2 diameters D_{mp} upstream from the upstream edge of the upstream side branch. Further details of the experimental technique are provided in Section 3.2.2 (Figure 3.4b). In this set of experiments, the pressure transducer of the upstream T-junction was replaced by a transparent close end, enabling the camera to see through the side branch.

Dry gas

In the first series, only the superficial gas velocity was varied. These tests aimed at finding the superficial gas velocity which corresponds to the pressure pulsation peak.

Figure 3.12 shows that the peak of 121 Pa is at the superficial gas velocity equal to 14.1 m/s. The pulsation amplitude measured is similar to the pulsation peak of the *Far Injector* configuration, whose results are reported in Figure 3.8. Therefore, although the velocity at which the peak occurs is 8% lower than the previous experiment, the amplitudes measurements do not seem to be affected by the supposedly intrusive effects of the injector, installed just 2 D_{mp} upstream the upstream edge of the T-junction.

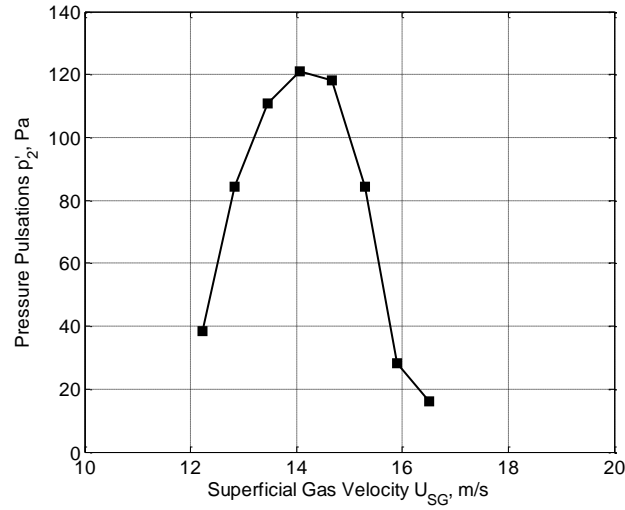


Figure 3.12. Tandem configuration, close-top injection. Dry gas: pressure pulsations [Pa] as function of the superficial gas velocity U_{SG} [m/s].

Wet gas

At the specific superficial gas velocity equal to $U_{SG} = 14.3$ m/s ($Q_G = 7.0 \times 10^{-3}$ m³/s), the liquid injection rate was varied. The same procedure has been adopted also for superficial gas velocities around the one of the pulsations peak, aiming at investigating the behavior of pulsations in the surroundings of the peak.

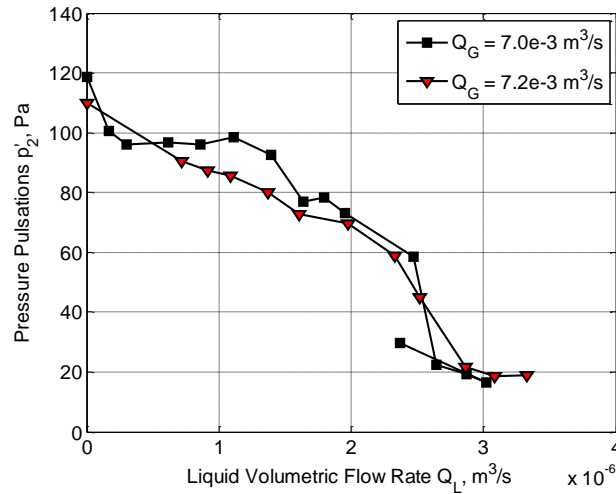


Figure 3.13. Tandem configuration, close-top injector. Wet gas: pressure pulsations [Pa] as function of the liquid volumetric flow rate Q_L [m³/s], for $U_{SG} = 14.3$ and 14.7 m/s.

A decrease of the pulsation amplitude with increasing injection rates is observed in Figure 3.13. Particularly for liquid volumetric flow rates larger than $Q_L = 2.5 \times 10^{-5}$ m³/s, the amplitude collapses from 60 to 20 Pa. This 60% drop is due to the presence of liquid in the shear layer. As explained and shown in Figure 3.7, liquid stopped bypassing the mouth and starts to interfere with the shear layer, i.e. the hydrodynamic instability which generates sound.

In addition, after eliminating pulsations, the liquid rate was reduced to 2.3×10^{-5} m³/s and a clear hysteresis can be observed.

3.4.3. Results – Close Injector – Bottom Injection

The results presented in the following are obtained with the injection point located at the bottom of the main pipe and $2 D_{mp}$ upstream the upstream side branch (see Figure 3.2 and Figure 3.4c).

Dry gas

A first test with dry gas aimed at disclosing the pressure pulsations peak and the corresponding superficial gas velocity. This was found equal to 15.3 m/s, similarly to the one of the *Far injector* configuration. On the other hand, Figure 3.14 shows the pressure amplitude is about the 30% lower. This difference in amplitude could be due to the obstruction generated by the injector. Nevertheless, the Strouhal corresponding to the pulsation peak is equal to 0.52, the same reported in Figure 3.11.

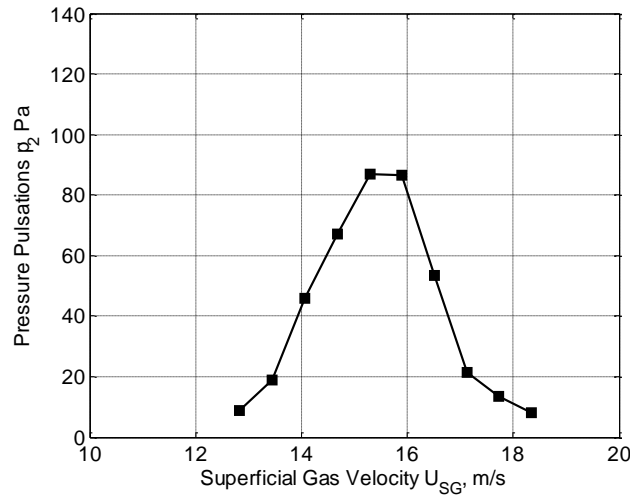


Figure 3.14. Tandem configuration, close-bottom injection. Dry gas: pressure pulsations [Pa] as function of the superficial gas velocity U_{SG} [m/s].

Wet gas

At the superficial gas velocity of 15.3 m/s ($Q_G = 7.5 \times 10^{-3} \text{ m}^3/\text{s}$), tests with liquid have been conducted and the results are provided in Figure 3.15. The experiments were also repeated at two other superficial gas velocities. Figure 3.15 shows that pulsations start to decrease as soon as water is injected in the system. Moreover, at the three different gas velocities the behavior is not changing.

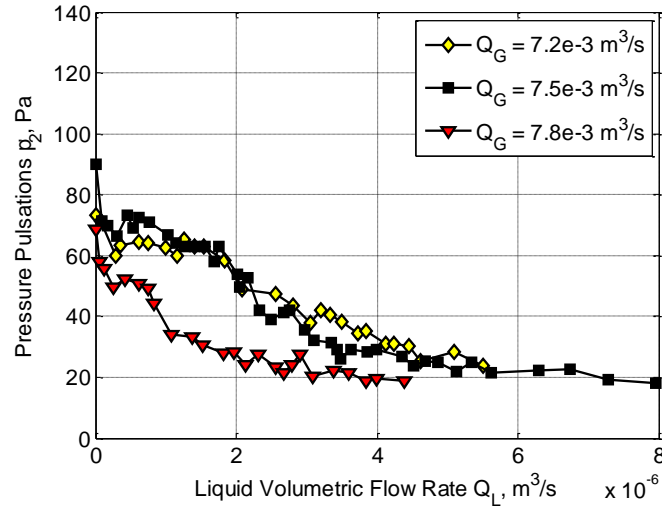


Figure 3.15. Tandem configuration, close-bottom injection, wet gas: Pressure pulsations [Pa] as function of liquid volumetric flow rate Q_L [m^3/s], for $U_{SG} = 14.7, 15.3$ and 15.9 m/s.

3.5. Discussion

For the three experimental sets, only the pulsations' behavior at the superficial gas velocity corresponding to the pressure peak is considered and compared in Figure 3.16.

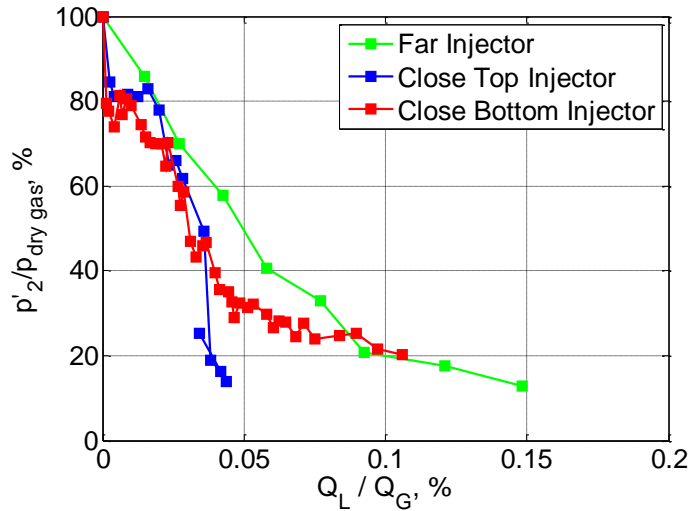


Figure 3.16. Comparison of the pressure measurements results.

Although it was expected that the injection of liquid at the top of the main pipe would have been much more effective than the other two cases, by making a comparison, not a remarkable difference can be highlighted. This would suggest that the effect of liquid films at the top of the main pipe, which is typical for instance of annular flow patterns, would not significantly affect the pressure trend. Nevertheless, as discussed in the results Section 3.4.2 (*Close-Top injection*), the drop of pulsations occurring in the range of Q_L/Q_G between 0.03% and 0.05% could be due to the passage of liquid in the shear layer, as indicated by flow visualizations (see Figure 3.7).

Furthermore, it is still an open discussion how water affects the acoustical damping in pipes and how the latter does influence the FIPs behavior. It is important to remind that a common element in the three

experimental sets is the presence of water with a stratified pattern in the distance B between the two side branches (see Figure 3.2). Even for the configuration with top injection, water immediately overpasses the mouth of the upstream side branch, draining at the bottom of the main pipe. The water stream accumulated in the main pipe would change the acoustical damping. To the author's knowledge, there is especially one experimental work which tries to give an estimate of damping in presence of liquid (Golliard et al., 2013). It aims at evaluating the damping in a 2-inch inner diameter steel pipe at different superficial gas velocities for different flow injection rates (0, 150 ml/min, 250 ml/min and 350 ml/min). The results obtained with a superficial gas velocity of 15 m/s at different injection rates as function of the varying frequency are particularly interesting, being the superficial gas velocity of the experiments hereby discussed in the range between 13 and 16 m/s. Only experimental results up to the ratio of Q_L/Q_G equal to 0.02% are provided. With a crude approximation, the expected damping behavior could be extrapolated to have a potential estimate even at higher Q_L/Q_G ratios (see Figure 3.17).

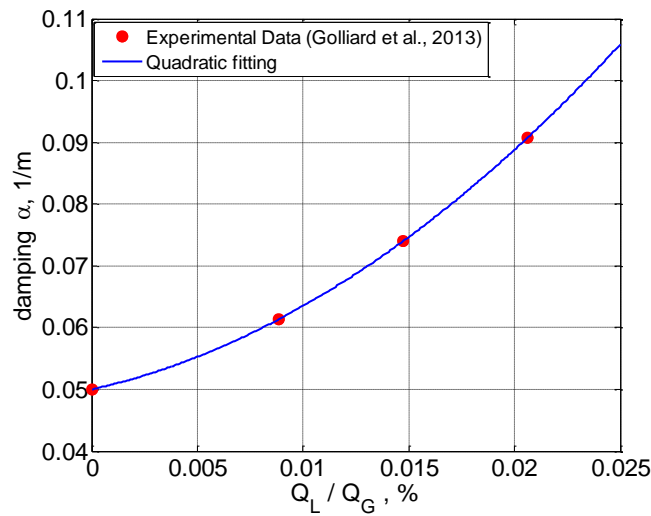


Figure 3.17. Extrapolated experimental data and quadratic fitting of damping measurements [1/m] at 320 Hz as function of the percentage ratio (Golliard et al., 2013).

1D acoustical simulations have been run with the same source at the Tees and different damping values varied only in the middle distance B. The values are the ones extrapolated by using the experimental results of Golliard et al. (2013), calculated for the 1-inch pipe. Note also that the damping estimated with the Kirchhoff law for the 1-inch pipe is around 0.046 1/m. From the comparison shown in Figure 3.18 it is possible to see that the experimental results obtained in the three sets and the ones of the 1D simulations are in agreement. As the acoustical field in the upstream and downstream segments (A and C, see Figure 3.2) of the setup is very weak, the damping in these segments does not affect the pulsation level. This was confirmed by our 1D acoustical model.

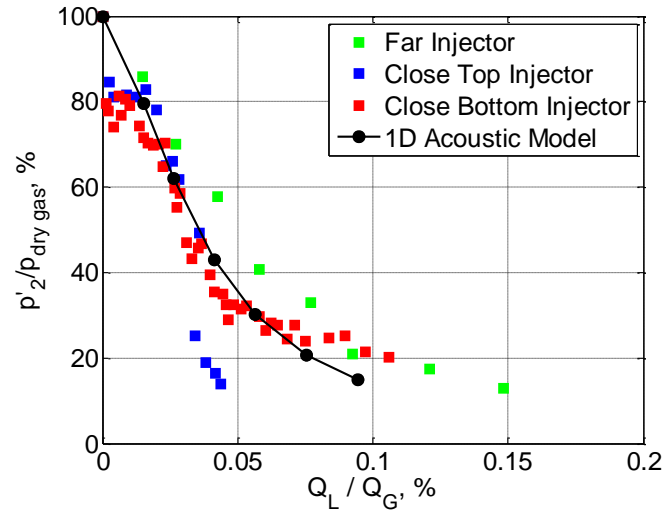


Figure 3.18. Comparison between the experimental results and the 1D acoustical model as function of the percentage volume fraction [%].

Based on this estimation, the main decrease in pulsation amplitude is attributed to the additional damping in the B section pipe. However, predictions of the additional acoustic damping due to the liquid are quite uncertain and therefore, further investigations on damping are needed. The acoustic damping in presence of water is the subject of a follow-up experimental study (Chapter 4) to determine whether the assumptions made (and particularly the extrapolation of Figure 3.17) are reasonable.

3.6. Conclusions

Depending on the combination of superficial gas and liquid velocities, the annular flow pattern can occur, typically characterized by a liquid film at the pipe wall.

For the *tandem* configuration, the interaction between the liquid film and the shear layer generated at the upstream edge of each T-junction was thought to be the reason of the pressure amplitude decrease reported in previous experimental investigations.

To evaluate the FIPs trend as function of that liquid film at the top of the main pipe, three sets of experiments have been conducted. Firstly, the water injection point has been located around 68 diameters upstream the upstream T-junction. Secondly, the injection point was moved to 2 diameters upstream the side branch, first generating a film of water only at the top of the main pipe, later only at the bottom.

The results obtained show that the pressure pulsations trend is not significantly changing while varying either the distance of the injection point from the upstream side branch or the different location in the cross sectional area. From flow visualizations it seems that for the closer top injection a large drop in pulsations amplitudes occurred only if water is convected together with the shear layer. Nevertheless, the pressure amplitude decrease (typically observed in annular flow patterns) cannot be only due to the presence of the liquid film at the top of the main pipe.

Extra damping due to the presence of water is a good candidate for explaining the reduction in pulsation amplitude. This extra damping can occur in different ways. It could be linked to the acoustical wave attenuation during the propagation from one branch to the other in the tandem configuration. This idea will be tested in the

next chapter. But it could also be linked to tube vibrations excited by the high level pulsations that can be highly attenuated by water film (Génevaux et al., 2009).

References

Belfroid, S.P.C., Golliard J., and Vijlbrief O., 2013, "Singing mitigation in corrugated tubes with liquid injection," *ASME Pressure Vessels & Piping Conference*, Paris, France.

Belfroid, S.P.C., Korst H.J.C., Beek P. v., Lunde K., Eidsvik I.G., and Hansen F., 2014, "Singing mitigation in an export riser via liquid injection: a field case study," *ASME Pressure Vessels & Piping Conference*, Anaheim, California, USA.

DEWESoft, URL: <http://www.dewesoft.com/>.

Génevaux, J.M., Dauchez N., Doutres O., 2009, "Nonlinear damping of a plate using Faraday instability of a fluid film," *Journal of Sound and Vibration*, 326(1-2): 150-160.

Golliard, J., Belfroid S.P.C, and Vijlbrief O., 2013, "Acoustic damping in smooth and corrugated pipes with and without liquid injection," *ASME Pressure Vessels & Piping Conference*, Paris, France.

Graf, H.R., and Ziada S., 2010, "Excitation source of a side-branch shear layer," *Journal of Sound and Vibration* 329(14): 2825-2842.

Ishii, M., 2003, "*Lecture notes: short course Modeling and computation of multiphase flow*," ETH, Zurich.

Nederveen, C.J., Jansen J.K.M. and Hassel R.R. van, 1998, "Corrections for woodwind tone-hole calculations," *Acta Acustica united with Acustica*, 84(5): 957-966.

PCB, URL: www.pcb.com

Shoham, O., 2006, "*Mechanistic Modeling of Gas-Liquid Two-Phase Flow in Pipes*," Society of Petroleum Engineers.

Sanna, F., and Golliard J., 2014, "Effect of water-droplets on flow-induced pulsations in pipe with two closed side branches: an experimental study," *20th AIAA/CEAS Aeroacoustics Conference*, Atlanta, Georgia, USA.

Sanna, F., and Golliard J., 2014, "Flow-Induced Pulsations in closed side branches with wet gas," *ASME Pressure Vessels & Piping Conference*, Anaheim, California, USA.

Shoeibi Omrani, P., Golliard J., Belfroid S.P.C., and González Díez N., 2012, "On the effects of droplets modulating the acoustic source powers generated in T-joints," *10th International Conference on Flow-Induced Vibration*, Dublin, Ireland.

Tonon, D., Willems J.F.H., and Hirschberg A., 2011, "Self-sustained oscillations in pipe systems with multiple deep side branches: Prediction and reduction by detuning," *Journal of Sound and Vibration*, 330(24): 5894-5912.

Uchiyama, Y., and Morita R., 2013, "Experimental Evaluation of Resonance frequency at Branch section in Each Dry and Wet Steam Flow," *ASME Pressure Vessels & Piping Conference*, Paris, France.

Uchiyama, Y. and Morita R., 2015, "Experimental investigation for acoustic resonance in tandem branches under each dry and wet steam flow," *ASME Pressure Vessels & Piping Conference*, Boston, Massachusetts, United States.

Ziada, S., and Shine S., 1999, "Strouhal Numbers of Flow-Excited Acoustic Resonance of Closed Side Branches," *Journal of Fluids and Structures*, 13(1): 127-142.

Ziada, S., and Lafon P., 2013, "Flow-Excited Acoustic Resonance Excitation Mechanism, Design Guidelines and Counter Measures," *ASME Applied Mechanics Review*, 66(1).

Chapter 4

Acoustical damping in a smooth horizontal pipe with stratified/stratified wavy air-water mixture flows

Résumé

Dans ce chapitre³, on évalue l'augmentation de l'amortissement lorsque la propagation acoustique se fait dans un mélange d'air et d'eau. Les résultats sont comparés avec l'atténuation mesurée sans ou avec écoulement de gaz, et lorsque le tube est en partie rempli d'eau, mais sans écoulement moyen. On observe que la présence d'eau dans le conduit provoque toujours une augmentation de l'amortissement acoustique. La cause la plus importante en est le changement du diamètre hydraulique du conduit induit par la présence d'eau. Les effets de convection sont similaires au cas de l'écoulement en gaz sec.

Par ailleurs, pour les hautes vitesses, les effets induits par la turbulence sont sensiblement différents du cas de la propagation en gaz sec. En effet, la turbulence à l'interface est modifiée par la présence de vaguelettes. Avec une combinaison de deux modèles ad hoc, il est possible de prédire les effets générés par la turbulence.

³ Part of this work will be presented as: (1) Sanna, F., Golliard J., Aurégan Y., and Belfroid S.P.C., 2016, "Atténuation des ondes acoustique propagées dans un conduit en partie rempli d'eau," *Congrès Français d'Acoustique*, Le Mans, France; (2) Sanna, F., Golliard J., and Belfroid S.P.C., 2016, "Acoustical damping in a circular pipe with an air-water mixture flow : a new setup design," *11th Conference on Flow-Induced Vibrations*, Delft, The Netherlands (submitted) .

Nomenclature

A_{mp}	Cross-sectional area of the main pipe [m^2]	U_G	Actual Gas velocity [m/s]
$A_{mp,G}$	Cross-sectional area of the main pipe occupied by air [m^2]	U_L	Actual Liquid velocity [m/s]
$A_{mp,L}$	Cross-sectional area of the main pipe occupied by water [m^2]	U_{SG}	Superficial Gas Velocity [m/s]
c_p	Specific heat coefficient [$m^2 / (K s^2)$]	U_{SL}	Superficial Liquid Velocity [m/s]
c_0	Speed of sound [m/s]	V	Voltage measured by the capacitance probes with liquid (V)
D_G	Hydraulic diameter for gas [m]	V_0	Voltage measured by the capacitance probes without liquid (V)
D_L	Hydraulic diameter for liquid [m]	v^*	Friction velocity [m/s]
D_{mp}	Inner diameter of the main pipe [m]	x	Axial direction of the duct [-]
FFT	Fast Fourier Transform		
f_G	Fanning friction factor at the wall for the gas phase [-]	α	Acoustical damping [1/m]
f_i	Fanning friction factor at the interface [-]	α_0	Acoustical Kirchhoff damping [1/m]
f_L	Fanning friction factor at the wall for the liquid phase [-]	β_L	Liquid hold-up [-]
h	height of the liquid phase [m]	γ	Ratio of the specific heats or Poisson's ratio
ID_{fh}	Inner diameter of the flexible hose [m]	δ_{ac}	Acoustic boundary layer thickness [m]
K_0	Correction factor for wave number [-]	δ_l	Viscous sublayer thickness [m]
k	Wave number [rad/m]	κ	Von Karman constant [-]
L_{mp}	Length of the test object [m]	κ_{th}	Thermal conductivity [$kg m / (K s^3)$]
L_{2p}	Perimeter of the pipe [m]	μ_G	Dynamic viscosity for gas [kg/ms]
M	Mach number [-]	μ_L	Dynamic viscosity for liquid [kg/ms]
OD_{fh}	Outer diameter of the flexible hose [m]	ν	Kinematic viscosity for the gas phase [m^2/s]
Q_L	Volumetric liquid flow rate [m^3/s]	ν_L	Kinematic viscosity for the liquid phase [m^2/s]
Q_G	Volumetric gas flow rate [m^3/s]	ρ_G	Density of the gas phase [kg/m^3]
p	Unsteady pressure amplitude [Pa]	ρ_L	Density of the liquid phase [kg/m^3]
Pr	Prandtl number [-]	σ_L	Surface tension [N/m]
R^\pm	Reflection coefficient [-]	τ_i	Shear wall stress at the liquid/gas interface [Pa]
Re_G	Reynolds number for gas [-]	τ_{WG}	Shear wall stress for the gas phase [Pa]
Re_L	Reynolds number for liquid [-]	τ_{WL}	Shear wall stress for the liquid phase [Pa]
R_{mp}	Radius of the main pipe [m]	ω	Angular frequency [rad·Hz], $e^{-i\omega t}$ - convention
S_G	Gas interface perimeter [m]		
S_i	Liquid/gas interface perimeter [m]		
S_L	Liquid interface perimeter [m]		
Sh	Shear wavenumber [-]		
SWR	Standard Wave Ratio		
t	Time [s]		
T^\pm	Transmission coefficient [-]		
T	Temperature [K]		
TMM	Two Microphone Method		

Subscripts and superscripts

+/-	Quantity considered in direction of (+) or against (-) the flow
U/D	Quantity considered upstream (U) or downstream (D) the test object

4.1. Introduction

In this first section, initially an overview and the motivations for quantifying the acoustical damping in presence of water are provided. Second, since this work couples acoustics and multiphase flows, it was considered necessary to provide the reader with some theoretical insights about the two fields. First, the acoustical damping is discussed, as well as the available models which describe the factors which contribute to its change. Second, the attention is more focused on multiphase flows, both on general aspects and in particular on the models available to describe important parameters characterizing the stratified (wavy) flow pattern.

When designing pipe systems, for example for gas compression, gas transport or gas metering, it is necessary to avoid the occurrence of Flow-Induced Pulsations. One of the aspects playing a role is the quality factor of the resonators. Indeed, high quality factor resonators can be accidentally assembled and high resonances can occur. However, to quantify the quality factor it is necessary to estimate the acoustical damping in the piping. This

damping comes from visco-thermal losses and the turbulence generated by the mean flow (Peters et al., 1993; Tonon et al., 2011). These parameters have been extensively studied and nowadays models are available to study the phenomenon. For instance, the acoustic properties in ducts, such as the reflection of the open end of a smooth pipe and the acoustical damping, have been studied by Ronneberger and Ahrens (1977) and Peters et al. (1993), focusing the attention especially on the turbulence effects. Also Allam and Åbom in 2006 measured the acoustical damping, while accurately measuring the reflection of an open ended pipe with flow, trying to validate the model of Munt (1990). With their work, Allam and Åbom verified the turbulence effects proposed in Howe's model (1995). The latter relies on the eddy viscosity to control the momentum and the thermal boundary layers, averaging the momentum and continuity equations over the cross sectional area. An overview of the available models is provided by Peters et al. (1993), Hirschberg (1997), and Allam and Åbom (2006), as well as in the next section.

Among the works already available on damping, there are only a few on acoustical damping measurements with gas-liquid mixture flows. Some investigations were done in the past on the mitigating effect of liquid on the singing in corrugated pipes (Belfroid et al., 2013; Golliard et al., 2013). In particular, Golliard (2013) aimed at experimentally quantifying the additional damping due to the presence of droplets in a mist flow in a smooth pipe and in a corrugated pipe. On a frequency range 150-2200 Hz, Golliard et al. (2013) measured the acoustical damping injecting in a 49 mm inner diameter smooth pipe different liquid injection rates (up to 350 ml/min) in a droplet form while a gas flow was grazing at different velocities (0, 15, and 30 m/s). Golliard et al. (2013) reported a linear increase of damping.

In previous experiments, Sanna et al. (2014a-b) investigated the effects of liquid in two configurations of pipes with two side branches. The difference between the two configurations was only on the relative distance between the two T-junctions: in one case the distance was the double of the acoustical length of the two side branches, and in the other the branches were very close. Especially at low injection rates, the pulsations measured at the closed end of each side branch behave differently. In particular, pulsations' amplitudes decreased for the case where the two side branches are far from each other, while when the T-junctions were close they did not. Sanna referred this different behavior to the increased damping due to the presence of water in the middle horizontal distance between the two branches. Sanna et al. (2015) investigated the effect of the liquid film on the FIPs source. The acoustical pulsations in a *Tandem* configuration were first measured with an injector located far from the upstream side branch. Second, the injector was located close to the upstream side branch, placing it initially at the top and later at the bottom of the main pipe. By comparing the pulsations peaks for the three configurations, although a decrease of 60% was observed when water was interfering with the shear layer, overall the same behavior in amplitude has been reported. This indicated that the acoustical damping was increased by the presence of water in the duct between the two side branches.

The purpose of the present paper is therefore to quantify the acoustical damping in a smooth horizontal pipe in presence of an air/water mixture at different flow conditions.

As a reference case, damping is measured in a dry pipe, first without and second with gas mean flow. Third, the damping is measured when a layer of stagnant water is present in the pipe. For this third campaign, both air and water velocities are equal to zero. The last experimental campaign consists of measuring acoustical damping at different liquid velocities for three different and constant gas velocities. All the measurements have been repeated both with the source located upstream and downstream, i.e. in direction and against flow.

The two-microphone method is used to measure the acoustical damping. This allows independent measurements of the propagation in positive (in direction of the flow) and negative (against the flow) direction.

In the following sections, basic information on acoustics and multiphase flows is provided. In particular, the acoustic and multiphase flow models available in literature are discussed and combined together into a new model. In Section 4.3 the facility and each component of the setup are described. In the last Section 4.4, the flow patterns are depicted and the results are discussed.

4.1.1. Different contributions to the acoustical damping

For investigations in the range of frequencies below the cut-off frequency, it is assumed that only plane waves are propagating in a duct. For plane harmonic waves, the acoustic pressure can be described as follows:

$$\begin{aligned} p(x, t) &= \hat{p}(x)e^{j\omega t} \\ \hat{p}(x) &= \hat{p}_+e^{-jk_+x} + \hat{p}_-e^{jk_-x} \end{aligned} \quad (4.1)$$

Where x is the axial direction of the pipe, \hat{p}_+ and \hat{p}_- the acoustic pressure amplitudes of the travelling waves propagating in a pipe respectively in the positive and in the negative direction, and $k = \omega/c_0$ is the wave number.

The damping in ducts is caused by visco-thermal losses at the wall. To take into consideration those losses, Kirchhoff (1868) introduced a correction ($k = K_0 \omega/c_0$) inversely proportional to the shear wavenumber Sh :

$$K_0 = 1 + \frac{(1-i)}{\sqrt{2}Sh} \left(1 + \frac{(\gamma-1)}{\sqrt{Pr}} \right) \quad (4.2)$$

Where γ is the specific heat ratio, $Pr = \mu_G c_p / \kappa_{th}$ is the Prandtl number, $Sh = a\sqrt{\omega/\nu}$ is the shear wavenumber, ν the kinematic viscosity, $\omega = 2\pi f$ is the angular frequency, and a for circular ducts corresponds to the radius of the pipe R_{mp} and for any other shape it can be replaced by the half of the hydraulic diameter $D_G = 4A_{mp}/L_{2p}$, where L_{2p} and A_{mp} are respectively the perimeter and the area of the pipe. With this correction the wave number k becomes complex. It can be noted that Eq. (4.2) is an approximation of the complete expression of Kirchhoff, which is valid to the first order in Sh and when the volume viscosity is neglected (Davies 1988; Morse and Ingard, 1968; Pierce 1989, Allam and Åbom, 2006). In some very precise analyses, the second order contribution in Sh has been considered (Peters et al., 1993). The wave number, neglecting the second order term of the constant K_0 with no mean flow, can be written:

$$k = \frac{\omega}{c_0} K_0 = \frac{\omega}{c_0} + (1-i)\alpha_0 \quad (4.3)$$

The acoustical damping in a quiescent fluid can be therefore considered by taking the imaginary part of the complex wave number and it can be written as:

$$\alpha_0 = \frac{L_{2p}}{2A_{mp}c_0} \sqrt{\frac{\omega\nu}{2}} \left(1 + \frac{\gamma-1}{\sqrt{Pr}} \right) \quad (4.4)$$

The wavenumbers, as well as the acoustic damping in both directions, are influenced also by the mean flow velocity. The latter is defined as the volume flux divided by the cross sectional area. To take into account the convection effects due to the presence of the mean flow, a correction to K_0 is needed. In literature, two corrections are proposed by Davies (1988):

$$K_{0,conv}^{\pm} = \frac{K_0}{(1 \pm M)} \quad (4.5)$$

and by Dokumaci (1995):

$$K_{0,conv}^{\pm} = \frac{K_0}{(1 \pm K_0 M)} \quad (4.6)$$

However, if the approach of Davies is empirical and not based on any particular physical argumentation, Dokumaci (1995, 1998) analyzes the dissipation for a uniform flow grazing in a pipe and he also shows that the results do not significantly differ from the ones obtained with a parabolic flow.

In addition to the correction of the visco-thermal losses and the convection term, also turbulence should be taken into account. Turbulence is a chaotic motion dominated by non-linear convective forces. The interaction between turbulence and sound can lead to the sound attenuation due to the production of secondary waves (scattering mechanism) and the transfer of energy to turbulence (absorption mechanism) (Howe, 1995). To estimate those losses, several models are available in literature (Ingard and Singal, 1974; Ronneberger and Ahrens, 1977; Peters et al., 1993; Howe, 1995). They show that the correction related to turbulence can be neglected if the acoustic boundary layer thickness $\delta_{ac} = \sqrt{2\nu/\omega}$ is small compared to the thickness of the viscous sublayer $\delta_l \approx 12.5\nu/v^*$ of a turbulent flow ($v^* = \sqrt{\tau_{WG}/\rho_G}$ is the friction velocity). Note that ν is the kinematic viscosity and τ_{WG} and ρ_G are respectively the shear stress and density at the wall.

In particular, since in this paper three tests are conducted with a mean flow gas velocities U_{SG} equal to ~ 2.5 , ~ 5.5 , and ~ 10 m/s, the ratio of the acoustical boundary layer to the viscous sublayer is smaller than 1. Turbulence can be therefore neglected when (only) a gas mean flow is grazing in the pipe. The effects of turbulence can become relevant when part of the cross-sectional area is occupied by water. In this case, the gas velocity would increase, as well as the Reynolds number, which in turn would change the friction coefficient and finally the shear stress at the wall. The effects of turbulence can therefore become relevant enough to be considered in the analysis for the estimate of the acoustical damping.

Among different models on the effect of turbulence, Howe's model is here considered to be the most accurate.

The model of Howe (1995) is a frequency-dependent model of the effect of the effective turbulent boundary layer eddy viscosity and it works strictly at small Mach numbers. It is based on the assumption that the two mechanisms are responsible for the effects of turbulence on acoustical damping, respectively the scattering and absorption. The general idea is that sound of low frequency propagating through turbulence is dissipated due to the transfer of energy to turbulent kinetic and thermal energy.

Equation (4.7) reports the attenuation in the direction of (+) and against (-) flow:

$$\alpha^{\pm} = \frac{\sqrt{2}\omega}{c_0 D_G (1 \pm M)} Re \left\{ \sqrt{2} e^{-i\pi/4} \left[\frac{\sqrt{\nu}}{(1 \pm M)^2} \times F_A \left(\sqrt{\frac{i\omega\nu}{\kappa^2 v_*^2}}, \delta_l \sqrt{\frac{i\omega}{\nu}} \right) + \frac{\beta c_0^2}{c_p} \sqrt{\chi} \right. \right. \\ \left. \left. \times F_A \left(\sqrt{\frac{i\omega\chi Pr^2}{\kappa^2 v_*^2}}, \delta_l \sqrt{\frac{i\omega}{\chi}} \right) \right] \right\} \quad (4.7)$$

Where ω is the radian frequency, D_G the hydraulic diameter, M the Mach number, ν the kinematic viscosity, κ is the von Karman constant (≈ 0.41), v_* the friction velocity, δ_l the thickness of the viscous sublayer, $\beta = 1/T$

is a function of the mean temperature T , c_p is the specific heat at constant pressure, $\chi = \kappa_{th}/\rho_G c_p$ ($2 \times 10^{-5} \text{ m}^2/\text{s}$, air at 20°C), Pr the Prandtl number.

$F_A(a, b)$ in Eq. (4.7) is expressed as in Eq. (4.8), where H_j is the Hankel function.

$$F_A(a, b) = \frac{i(H_1^{(1)}(a) \cos(b) - H_0^{(1)}(a) \sin(b))}{(H_0^{(1)}(a) \cos(b) - H_1^{(1)}(a) \sin(b))} \quad (4.8)$$

In the model proposed by Howe (1995) the friction velocity v_* is calculated with:

$$\frac{U_G}{v_*} = 2.44 \ln(v_* D_G / 2\nu) + 2.0 \quad (4.9)$$

The frequency dependent viscous sublayer δ_l can be calculated with the empirical relation:

$$\frac{\delta_l v_*}{\nu} = 6.5 \left(1 + \frac{1.7(\omega/\omega_*)^3}{1 + (\omega/\omega_*)^3} \right) \quad ; \quad \frac{\omega_* \nu}{v_*^2} \approx 0.01 \quad (4.10)$$

Note that the ratio ω/ω_* becomes progressively smaller as the Mach number M increases (Howe, 1995).

4.1.2. Multiphase flow in a duct

A multiphase flow is characterized by two or more immiscible phases of matter (gas, liquid or solid). The air/water mixture considered in this experimental work corresponds to this definition. Figure 4.1 shows the different flow patterns a water/air mixture would have at different superficial liquid and gas velocity in a smooth horizontal 25.0 mm inner diameter pipe.

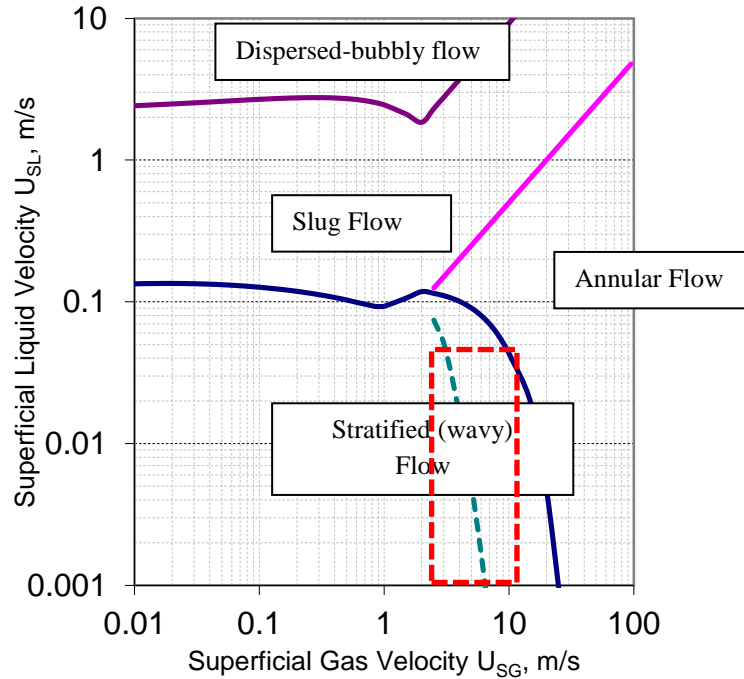


Figure 4.1. Flow pattern map for 25.0 mm horizontal smooth pipe (Shoham, 2006). Experiments were conducted in the range of U_{SG} and U_{SL} highlighted by the red dashed rectangle.

As it can be seen, in the range of gas velocities between 1 and 10 m/s and liquid velocities between 0.001 and 0.1 m/s the flow is mainly stratified or stratified wavy. At high liquid injection rates, there is the tendency to become slug flow. Depending on the different flow pattern, the distribution of the two phases along the cross sectional area A_{mp} is different. It means that, depending on the flow pattern, the area occupied by liquid $A_{mp,L}$, and consequently the area occupied by gas $A_{mp,G}$, changes. This difference is evaluated by means of a quantity called liquid volume fraction or liquid hold-up β_L , defined as the ratio of the area occupied by liquid $A_{mp,L}$ to the full cross sectional area of the main pipe A_{mp} :

$$\beta_L = \frac{A_{mp,L}}{A_{mp}} \quad ; \quad A_{mp} = A_{mp,L} + A_{mp,G} \quad (4.11)$$

There are different ways to estimate the hold-up, either experimentally or by means of numerical simulations. Figure 4.2 shows the hold-up estimated numerically as function of the superficial gas velocities, for different superficial liquid velocities. The values reported in Figure 4.2 are obtained by means of 1D multiphase flow simulations run with the software OLGA 7.3.4, for a 25.0 mm inner diameter smooth pipe for a mixture of air and water.

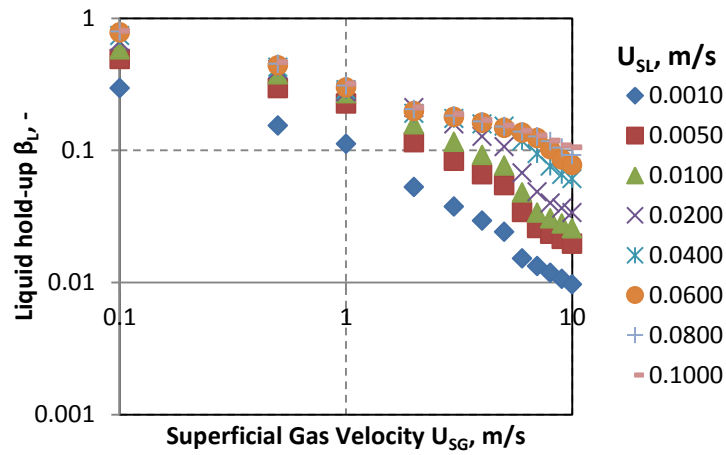


Figure 4.2. 1D multiphase flow simulations with the software OLGA: estimation of the liquid hold up β_L in a 25.0 mm inner diameter pipe at different superficial liquid and gas velocities.

Figure 4.2 shows that if the gas velocity U_{SG} increases, the hold-up decreases. Moreover, this decrease becomes less significant as the superficial liquid velocity increases. In addition, according to 1D multiphase simulations, the minimum hold-up value should be around 0.01 at $U_{SG} = 10$ m/s.

Another way to estimate the liquid hold-up is by means of capacitance probes. Here, the liquid void fraction is estimated by using capacitance probes and their mechanism is discussed in Section 4.3.2.

As discussed above, the properties of a multiphase flow are different from the ones of a single phase. In particular, each phase has an effect on the behavior of the other one. Multiphase flow models have been developed and are used to describe the behavior of the flow at the interface.

In the past 50 years, acoustics and multiphase flows rarely have been linked. Gas-liquid flow in horizontal or near horizontal pipes became really important because of its application in several industries, such as the oil, gas, and geothermal ones (Tzotzi and Andritsos, 2013).

As said in Section 4.1, this work is about the effects of multiphase flows on acoustical damping in gas liquid systems. In particular, a smooth horizontal pipe is considered for this experimental campaign. However,

depending on flow conditions and characteristics, and the properties of the pipe, the flow pattern might be different. According to Figure 4.1, in the range of gas velocities up to 20 m/s and liquid velocity up to 0.045 m/s, the flow pattern should be stratified or stratified wavy. On the basis of previous tests campaigns, the increase of acoustical damping due to the presence of an air/water mixture in a stratified (wavy) flow is considered the reason of the decrease of Flow Induced Pulsations amplitudes. This is the reason why it this work is conducted with a stratified or stratified wavy flow pattern.

Although this is considered the simplest case to analyze and to describe, not always a satisfactory degree of accuracy can be reached, in particular at high pressures or when the properties of the two phases are very different from each other. In literature, analyses on stratified (wavy) flow are often the starting point of other studies, such as the ones on slug or annular flows (Taitel and Dukler, 1976a; Lin and Hanratty, 1968).

Four different subregimes are distinguished for a stratified gas-liquid flow in horizontal pipes (Andritsos and Hanratty, 1987b; Tzotzi et al., 2011):

1) Smooth region.

This regime occurs at very low gas and liquid velocities. The interface in this case is smooth.

2) Two-dimensional (2-D) wave region.

In this region, small amplitude, short wavelengths and regular disturbances are covering the surface. The 2-D waves are periodic and uniform, maintaining their identity for several wave periods (Andritsos, 1992). This type of waves is affected by the liquid viscosity.

3) Very wavy region.

This region is characterized by large amplitude, irregular waves. Sometimes they are also called roll waves. These irregular waves interact with each other, and it is impossible to study their correlation. Moreover, these waves are influenced neither by the viscosity nor by the diameter of the pipe. The onset of these waves is normally associated to the pressure variations which are varying as the wave height (Andritsos and Hanratty, 1987b). Tzotzi in her model refers to Kelvin-Helmholtz waves (Tzotzi and Andritsos, 2013).

4) Atomization region.

In this region, droplets or liquid filament separate from the crests of the large-amplitude waves and deposit at the wall. For this specific case, the behavior depends on the pipe diameter. Moreover, the approximation that the surface is flat is not valid anymore, especially for pipe diameters smaller than 0.05m (Tzotzi and Andritsos, 2013).

Several models are available to describe the interaction between liquid and gas for a stratified flow (see for instance Taitel and Dukler, 1976b; Andritsos and Hanratty, 1987a; Tzotzi and Andritsos, 2013). All the models particularly try to describe the interfacial friction between water and air. However, all these models assume that the surface between air and water is flat. This is not formally correct because it is known that at certain conditions liquid climbs up from the bottom and the interface becomes curved. Several people tried to investigate this behavior in the last decades (Hart and al., 1989; Grolman and Fortuin, 1997; Vlachos et al., 1999; Chen et al., 1997).

In the following, the model proposed by Tzotzi and Andritsos (2013) is used to describe the interfacial friction.

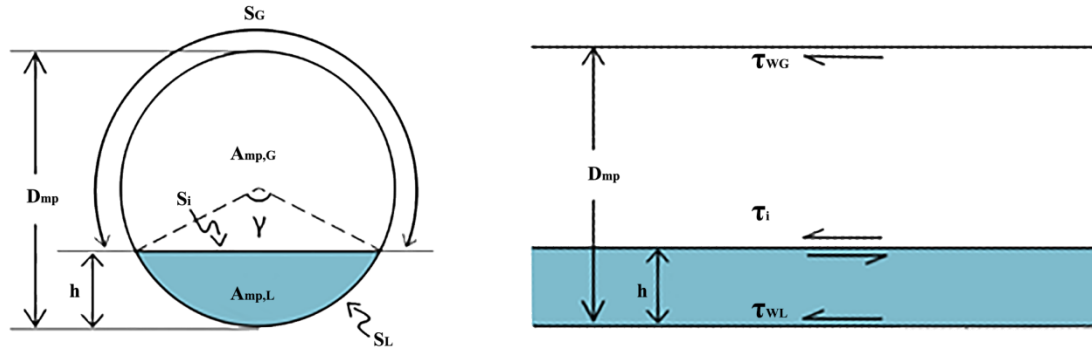


Figure 4.3. Scheme of a stratified gas-liquid flow in a fully horizontal pipe.

Figure 4.3 provides a scheme of the distribution of air and water, including also the quantities important for the analysis. For a fully developed horizontal flow, two distinguished equations can be written for each phase:

$$\begin{aligned} -A_{mp,G} \left(\frac{dp}{dL} \right)_G - \tau_{WG} S_G - \tau_i S_i &= 0 \\ -A_{mp,L} \left(\frac{dp}{dL} \right)_L - \tau_{WL} S_L + \tau_i S_i &= 0 \end{aligned} \quad (4.12)$$

To estimate the shear stress at the wall for the gas phase τ_{WG} , as well as the interfacial shear stress τ_i , the model of Tzotzi and Andritsos (2013) relies on the model of Taitel and Dukler (1976b):

$$\begin{aligned} \tau_{WG} &= f_G \frac{\rho_G U_G^2}{2} \\ \tau_i &= f_i \frac{\rho_G (U_G - U_L)^2}{2} \\ \tau_{WL} &= f_L \frac{\rho_L U_L^2}{2} \end{aligned} \quad (4.13)$$

Where U_G and U_L are respectively the actual gas and liquid velocities, i.e. the velocities calculated by considering the presence of the second phase in the cross sectional area and f_L , f_G are the friction factors for each phase, which are Reynolds dependent:

$$f_L = \frac{C_L}{Re_L^n} \quad ; \quad f_G = \frac{C_G}{Re_G^m} \quad (4.14)$$

The two phases are considered independently. For turbulent flow (Re_L or Re_G greater than 2000), the coefficients C_L or C_G are equal to 0.046 and n or m are equal to 0.2. If the Reynolds is smaller than 2000 (laminar flow), C_L or C_G are equal to 16 and n or m are equal to 1. The Reynolds numbers are written as:

$$Re_L = \frac{D_L U_L}{\nu_L} \quad ; \quad Re_G = \frac{D_G U_G}{\nu} \quad (4.15)$$

Where the hydraulic diameter for liquid D_L and for gas D_G are defined as:

$$D_L = \frac{4 A_{mp,L}}{S_L} \quad ; \quad D_G = \frac{4 A_{mp,G}}{S_G + S_i} \quad (4.16)$$

On the basis of the friction coefficients reported in Eq. (4.14), the friction at the interface can be expressed in different ways (Taitel and Dukler, 1976b; Andritsos and Hanratty, 1987a; Tzotzi and Andritsos, 2013). The estimate of f_i proposed by Tzotzi and Andritsos (2013) is discussed and used.

On the distinction of the three regimes discussed before, Tzotzi and Andritsos (2013) proposed two velocities which work as transition threshold velocities. In particular, $U_{GS,2-D}$ is the transition velocity between the smooth region and the 2-D wave region, whereas $U_{GS,K-H}$ is the one between the 2-D wave region and the very wavy region. They are empirically defined as follows:

$$\begin{aligned} U_{SG,2-D} &= \frac{1}{1.95} \left(\frac{\rho_W}{\rho_L} \right)^{-0.1} \left(\frac{\rho_G}{\rho_A} \right)^{-0.5} \left(\frac{\mu_L}{\mu_W} \right)^{0.35} \times \ln \left[\frac{0.8}{U_{SL}} \left(\frac{\mu_L}{\mu_W} \right)^{0.2} \right] \\ U_{SG,K-H} &= \frac{1}{0.65} \left(\frac{\rho_G}{\rho_A} \right)^{-0.5} \left(\frac{\rho_W}{\rho_L} \right)^{-0.5} \left(\frac{\sigma_W}{\sigma_L} \right)^{-0.33} \times \ln \left[\frac{1.39}{U_{SL}} \left(\frac{\mu_L}{\mu_W} \right)^{-0.15} \right] \end{aligned} \quad (4.17)$$

Where the subscripts W and A refer to water and air at 1 atm and 20 °C. Note that ρ , μ , and σ are respectively density, dynamic viscosity and surface tension.

On the basis of experiments conducted on a 24 mm inner diameter smooth Plexiglas pipe, Tzotzi and Andritsos (2013) modified the approach developed by Andritsos and Hanratty (1987), by proposing the following design procedure to estimate the friction at the interface:

$$\begin{aligned} \frac{f_i}{f_G} &= 1 & U_{SG} < U_{SG,2-D} \\ \frac{f_i}{f_G} &= 1 + 0.35 \left(\frac{h}{D_{mp}} \right)^{0.5} (U_{SG} - U_{SG,2-D}) & U_{SG,2-D} < U_{SG} < U_{SG,K-H} \\ \frac{f_i}{f_G} &= 2 \left(\frac{h}{D_{mp}} \right)^{0.1} \left(\frac{\mu_L}{\mu_W} \right)^{0.1} + 4 \left(\frac{h}{D_{mp}} \right)^{0.5} (U_{SG} - U_{SG,K-H}) & U_{SG} > U_{SG,K-H} \end{aligned} \quad (4.18)$$

With the friction coefficient at the interface f_i , also the shear stress can be calculated (see Eqs. (4.13)).

4.2. A new model to describe the interaction between turbulent multiphase flows and acoustics at low frequencies and low Mach numbers

As explained in Section 4.1.1., Howe's model can be used to estimate the effects of turbulence at low frequency. For the case discussed in this paper, a wavy stream of water is present at the bottom of the main pipe. It is expected that waves generate turbulence at the interface between the two phases. How to include the turbulence effects of water in Howe's model to predict the acoustical damping?

For a sound wave which travels in a circular pipe with an air flow at a certain non-zero velocity, Howe's model provides with a good approximation of the effects of turbulence on the acoustical damping. In particular for a dry pipe, the hydraulic diameter corresponds exactly to the diameter of the pipe, and the stress at the wall is τ_{WG} .

For a stratified (wavy) flow in a horizontal pipe, water and air behave independently. Assuming that sound is propagating only in air, the travelling sound wave sees a gas mean flow grazing in a smaller pipe, since part of the cross sectional area is occupied by water. Effectively, the hydraulic diameter D_G has changed and it can be calculated as in Eq. (4.16), once the liquid void fraction (or hold-up) β_L is known. However, it is important to remind that the physics at the wall is completely different. In a horizontal pipe, the air flow sees the solid wall on the perimeter S_G and a liquid (moving) wall at the interface S_i (see Figure 4.3). The change of the boundary conditions has to be included in the analysis, because the shear at the two different "walls" is different.

Damping is therefore calculated twice. The first time, it is assumed that the sound wave sees just a smaller diameter pipe, considering the wall as it was only solid, i.e. a dry pipe with a small hydraulic diameter than the actual diameter. For this case, Eq. (4.7) (Section 4.1.1) and this estimate is called α_{dry}^{\pm} .

The acoustical damping is estimated again assuming that the air flow was passing in a pipe with a liquid moving wall. Damping, namely α_{wet}^{\pm} , is therefore based on the friction velocity v_* calculated as function of the shear at the interface τ_i :

$$v_* = \sqrt{\frac{\tau_i}{\rho_G}} \quad (4.19)$$

Where the shear at the interface τ_i is calculated from Eq. (4.13), following the procedure discussed for the multiphase flow model proposed by Tzotzi and Andritsos (2013).

Note that for the estimate of α_{dry}^{\pm} and α_{wet}^{\pm} , the hydraulic diameter is used, as well as the Mach calculated by using the actual velocity U .

The final damping is a weighted balance between the two estimated values. The weight coefficient is the ratio between “wet” and “dry” parts of the perimeter $S_i/(S_i + S_G)$. In this way it is possible to consider the change of the area, as well as the influence of water on damping. Equation (4.20) shows how to calculate the acoustical damping.

$$\alpha^{\pm} = \alpha_{wet}^{\pm} \frac{S_i}{S_i + S_G} + \alpha_{dry}^{\pm} \left(1 - \frac{S_i}{S_i + S_G}\right) \quad (4.20)$$

4.3. Setup and experimental procedure

In this section, the information concerning the facility as well as the information on the technique used is provided. Figure 4.4 provides a scheme of the facility, as well as of the setup used to conduct the experiments on damping.

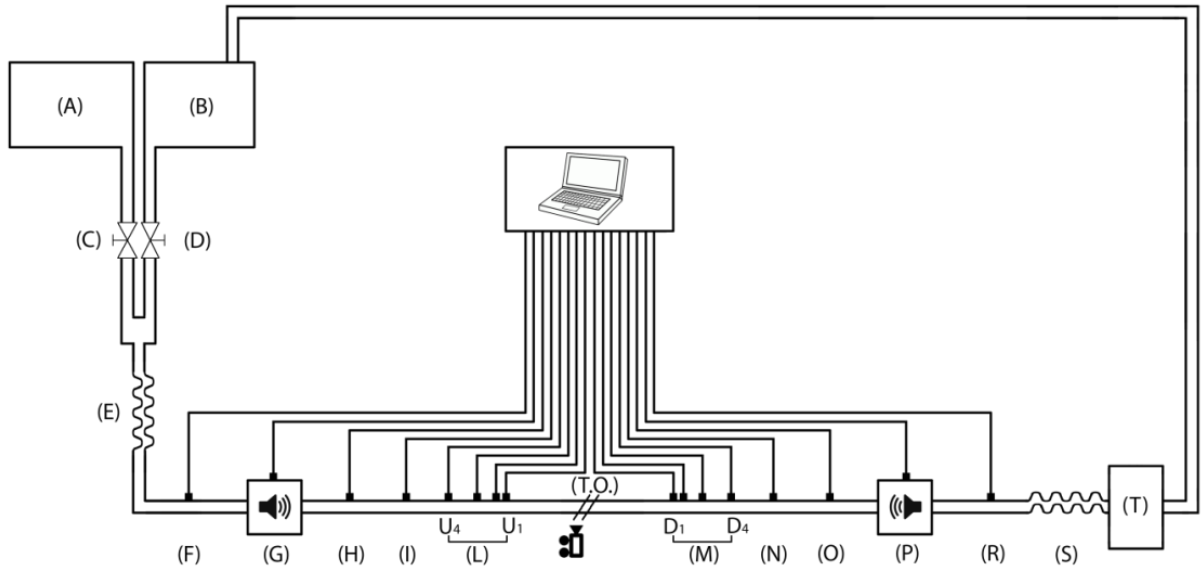


Figure 4.4. Experimental facility and setup.

4.3.1. Test facility

Two different lines bring water and air to the setup, respectively from a pressurized vessel at 4-7 bar [B]⁴ and a compressor [A]. They are equipped with two flow meters EL-FLOW-MCF-F-203AV-1M0 and EL-FLOW-MCF-F-202AV-M10 (Bronkhorst) in order to control the flow mass rate of air [C] and two flow meters M55-AAD-33-0C and M54C5I-AAD-55-K-B [D] are used to regulate the water flow rate.

From the volumetric gas flow rate, the mean (superficial) gas velocity is computed by using the static pressure and temperature values measured immediately upstream the test object.

Two 45 m flexible hoses [E] and [S] are respectively located upstream and downstream the horizontal smooth pipe. They serve as anechoic terminations. For damping measurements, it is indeed preferable that the setup terminations are anechoic to avoid the existence of standing waves. The hoses are characterized by an inner diameter ID_{th} equal to 25.0 mm and the outer diameter OD_{th} to 32.0 mm. Each of them has a length of 45 m and they are wrapped up around a cylinder of diameter of 0.965 m. The flexible nature of the tube induces damping through wall vibrations and visco-thermal losses.

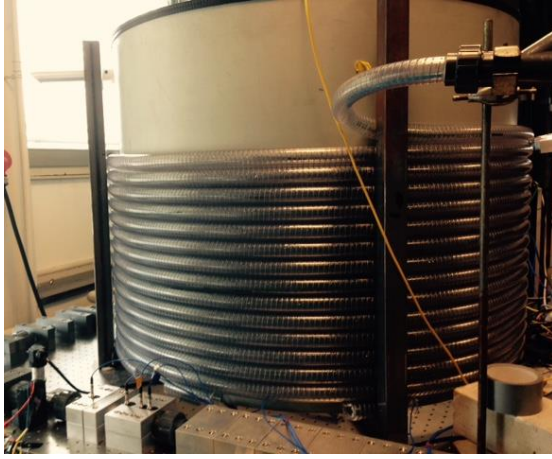


Figure 4.5. Upstream 45 m hose used as anechoic boundary condition. A similar one is used downstream.

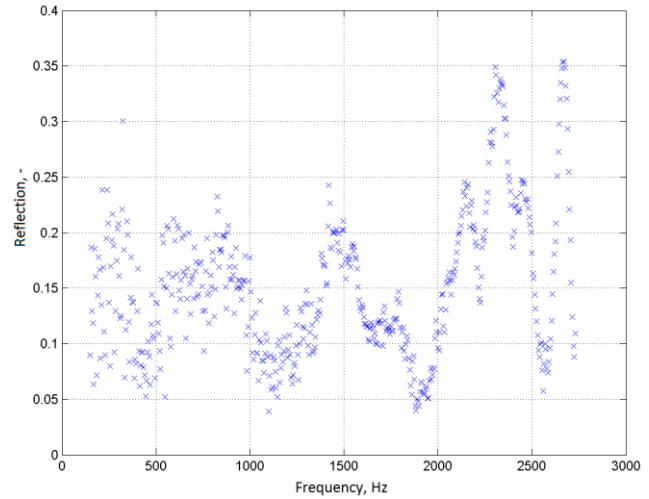


Figure 4.6. Acoustical preliminary test results: reflection coefficient [-] of a 45 m hose as function of frequency [Hz].

Acoustical tests were preliminarily conducted to verify the efficiency of these hoses.

Figure 4.6 shows that the reflection coefficient measured for a 45 m long hose is always below 0.25 in the frequency range 150-2300 Hz, and below 0.35 in the range 2300-2730 Hz. This is considered acceptable since most experiments would be performed with air/water mixture, which would increase the acoustical damping and reduce the reflection coefficient at the ends of the measurement sections.

4.3.2. Test Setup

The test object [T.O.] is a 2 meters smooth plastic transparent (Perspex) pipe. The inner diameter D_{mp} is 25.0 mm, while the outer diameter is 32.0 mm. The pipe is horizontal and clamped to the table.

By means of ATM.ECO 0...2 bar pressure transmitters, the static pressure is monitored both upstream [H] and downstream [O] the test object. Their measurement uncertainty is of 5 mbar.

⁴ The square brackets refer to Figure 4.4.

Two thermocouples Velleman TP01 – K type are respectively installed on the two hoses upstream [F] and downstream [R] the test object, immediately close to the horizontal setup.

A loudspeaker JBL-2490H (JBL) is used to generate the sound wave. Only one loudspeaker is used, firstly located upstream [G] the test object and later downstream [P]. The loudspeaker is installed on a loudspeaker case.

For the final analysis it is indispensable to quantify the liquid void fraction (or hold-up). As discussed more in detail in Appendix A, among different possible methods (see Bo an Lee, 2012) which can be used to estimate the liquid hold-up β_L , capacitance probes are used for this experimental work. This choice was preliminarily made because a non-intrusive and not expensive technique was required. Moreover, on the basis of multiphase flow numerical simulations with the software OLGA 7.3.4 (OLGA, 2015), the minimum hold-up was around 2% (see Section 4.1.2) and this makes capacitance probes suitable to these

investigations. If the hold-up were lower than 2%, it would have been difficult to measure the hold-up. This type of probes has been extensively used in literature (see for instance Geraets and Borst, 1988; Bigonha Tibiriçá et al., 2010; De Kerpel and De Paepe, 2012; Canière et al., 2007; An et al., 2014).

Two capacitance probes have been used for this experimental campaign, one located upstream [I] and one downstream [N] of the test object. Each probe consists of two parallel identical copper plates (30x20 mm), glued outside the pipe. Note that the pipe has an inner diameter of 25.0 mm and an outer diameter of 30.0 mm.

The probes have been calibrated; on the basis of the difference of the voltage V measured during the experiment with liquid and the voltage V_0 measured when the pipe is dry, the hold-up β_L is estimated with a fitting polynomial of the 6th order.

The hold-up estimate is used for two sets of experiments, respectively when water and air are mixed up with different velocities and for the test with a stagnant layer of water in the horizontal pipe (in this last case both U_{SG} and U_{SL} equal to 0).

Figure 4.8 shows the hold-up in percentage as function of the superficial liquid velocity for the three constant gas velocities $U_{SG} \sim 2.5$ m/s, ~ 5.5 m/s, and ~ 10.5 m/s. The same hold-up values are used both for the upstream and downstream sources.

For the three plots, the solid black line with diamonds provides the average values of the hold-up measured (only) with the capacitance probes. The same values are also reported in Table 4.5 and they are the ones used for the analysis of the results.

The dashed black lines give the hold-up measurements including the standard deviation σ . The information from these dashed lines is the presence of waves (if any) in the axial direction. Regarding this aspect, if the three plots are compared it is possible to see how the presence of waves occurs at lower liquid velocities if the superficial gas velocity is larger. This is in line with our expectations. Indeed, the flow pattern map for a 25 mm

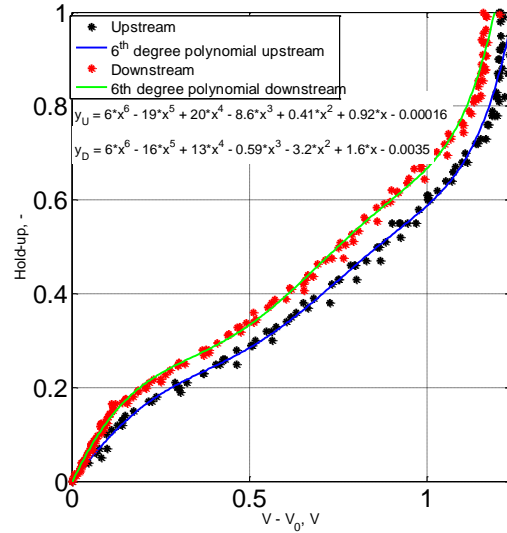


Figure 4.7. Hold-up interpolation curves as function of the voltage difference $V-V_0$ [V].

inner diameter horizontal pipe (Figure 4.1) shows that at $U_{SG} \sim 10$ m/s, the flow is supposed to be wavy even at low liquid rates. These values will be used to study the sensitivity analysis of the hold-up parameter on the damping estimates. This would repair eventual mistakes based on error in the hold-up measurements and the use of the same values for both sources.

A particular attention is needed for the case of $U_{SG} \sim 2.5$ m/s (Figure 4.8a), where at high injection rates the standard deviation values are very far from the average value. This is related to the presence of slugs passing in the system. It was impossible to eliminate their presence. The slope of the coils surely favored the generation of slugs. However, the use of coils as (anechoic) boundary conditions was the sole solution and compromise to reduce the reflection coefficient, as well as to drive water to the horizontal setup.

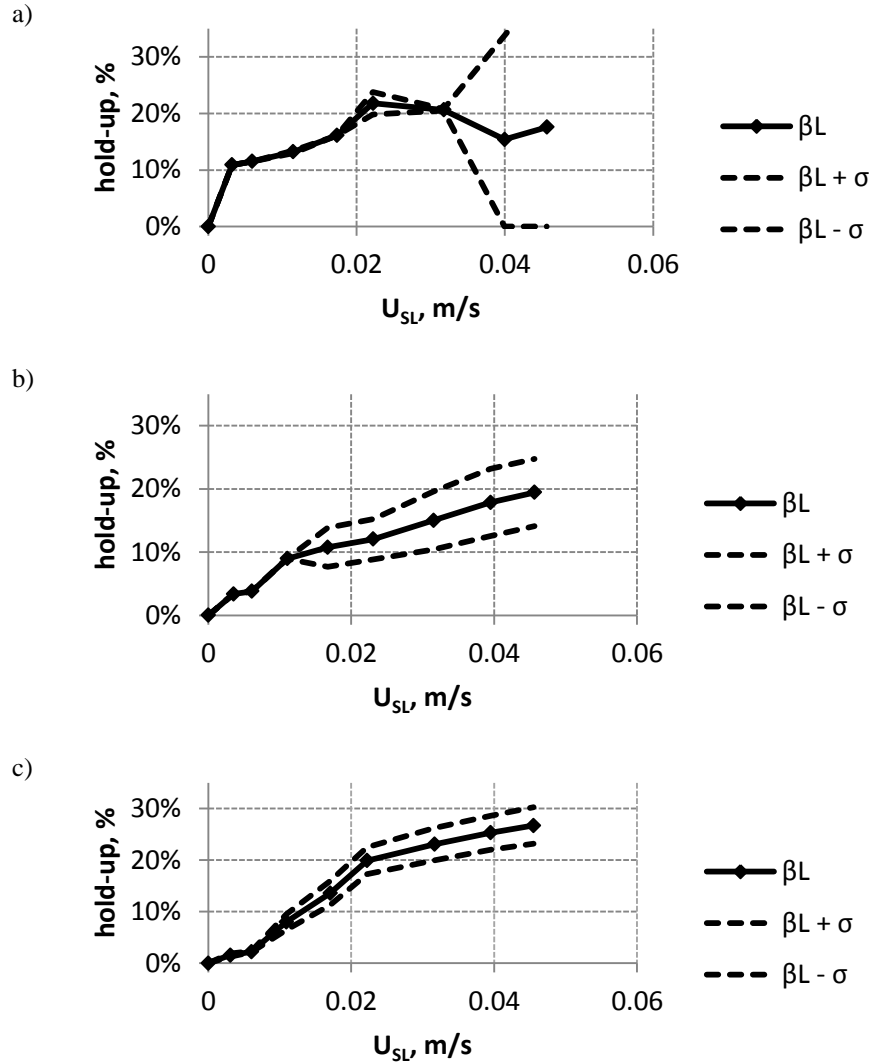


Figure 4.8. Hold-up [-] as function of the superficial liquid velocity (U_{SL}) for constant superficial gas velocity (U_{SG}): (a) $U_{SG} \sim 2.5$ m/s, (b) $U_{SG} \sim 5.5$ m/s, (c) $U_{SG} \sim 10.5$ m/s.

By means of microphones' pairs, the amplitude and phase in the positive and negative direction can be reconstructed. To ensure an accurate experimental two-port analysis and to reduce the error, on the basis of the over-determination more microphones are used (Holmberg et al., 2011).

8 PCB-102B06 piezometric transducers (PCB) are used, respectively four installed upstream [L] and four downstream [M] the test object [T.O.]. All the transducers are flush-mounted to avoid acoustical leakages

(Åbom and Bodén, 1988) and some gluey material is used to ensure no flow leakages. Two groups of four microphones are installed in two identical pipes. As shown in Figure 4.4, U1 and D1 are the closest microphones to the test object, respectively located upstream and downstream the horizontal pipe.

For each set of 4 microphones, the relative distance has been chosen to ensure highly precise measurements between 150 and 4100 Hz, minimizing the influence of errors (Bodén and Åbom, 1986; Åbom and Bodén, 1988). In particular Bodén and Åbom (1986) proved that the two microphones method (discussed in Section 4.3.4) has the lowest sensitivity to errors in the region around $ks = \pi(1 - M^2)/2$ and two years later Åbom and Bodén (1988) suggested to use Eq. (4.21):

$$0.1\pi(1 - M^2) < ks < 0.8\pi(1 - M^2) \quad (4.21)$$

For the case discussed here, the frequency range has been restricted considering the variation of the product of the wave number and the relative distance between microphones ks between 0.12π and 0.48π . This analysis is considered in absence of mean flow (Mach number $M = 0$). For the wave number k , the speed of sound equal to 340 m/s has been used. Table 4.2 shows the distance between different combinations of microphones, as well as the range of frequency each combination can cover (Table 4.2 and Figure 4.9). However, the max inner tolerance achieved while manufacturing the pieces is $\pm 2.0 \times 10^{-5}$ m. This is valid for the group of transducers located upstream and the one located downstream the test object. Moreover, both the distances of U1 and D1 from the extremities of the test object are 0.05 m.

Table 4.2. Minimum and maximum frequency obtained by combining 2 microphones.

Combination	1-2	1-3	1-4	4-2	3-4	3-2
f_{\min} [Hz]	1020.0	630.4	389.6	240.8	174.2	148.8
f_{\max} [Hz]	4080.0	2521.6	1558.4	963.2	697.0	595.3
Manufacturing Distance s [m]	0.0200	0.0524	0.1377	0.1171	0.0847	0.0324

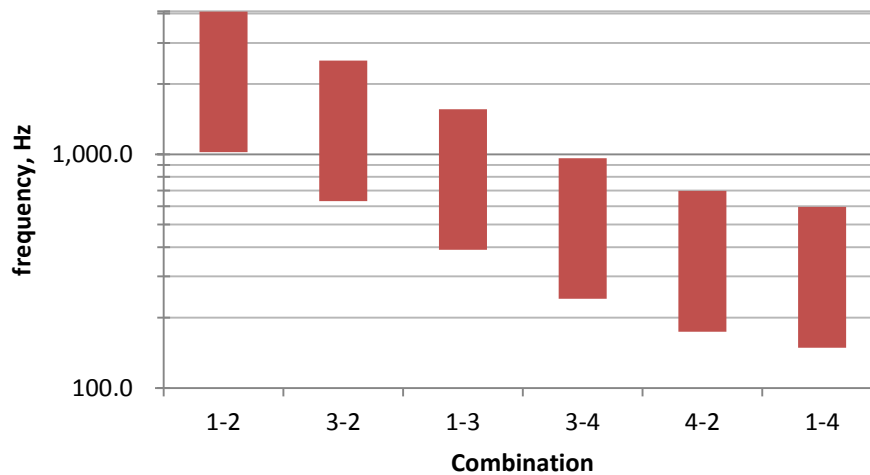


Figure 4.9. Frequency range [Hz] for each 2 microphones' combination.

4.3.3. Test Matrix

Four main campaigns are conducted, first locating the source upstream the test object and second downstream. The scheme is provided in Figure 4.10.

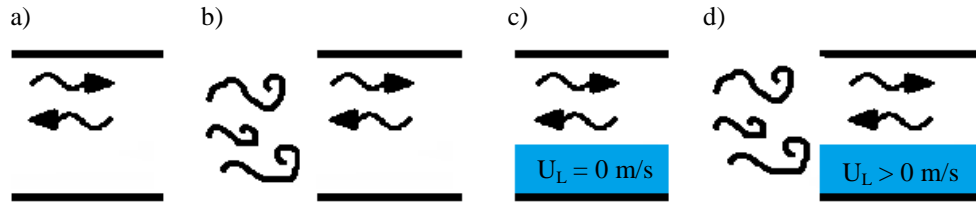


Figure 4.10. Scheme of the four experimental campaigns: no mean flow (a), only gas mean flow (b), different liquid void fractions (c), and gas and liquid mixture flow (d).

The four experimental campaigns are the following:

- #1 (Figure 4.10a): the pipes are all dry and there is no mean flow;

- #2 (Figure 4.10b): the pipes are all dry and there is a gas mean flow grazing at different gas velocities.

The mean value of the gas velocity is reported in Table 4.3;

Table 4.3. Campaign #2: test matrix for the tests with only gas mean flow ($U_{SL} = 0$ m/s; $\beta_L = 0$ %).

	UPSTREAM			DOWNSTREAM		
U_{SG}	2.51	5.54	9.98	2.63	5.76	10.68

- #3 (Figure 4.10c): the test object is not dry, while the anechoic terminations are both dry. Water is poured in the smooth horizontal pipe at different hold-ups. Nevertheless, both the superficial gas velocity and the superficial liquid velocity are equal to zero. Table 4.4 provides the hold-up values. Note that during these experiments the surface of water is perfectly smooth.

Table 4.4. Campaign #3: test matrix for the tests with water poured in the pipe ($U_{SG} = 0$ m/s; $U_{SL} = 0$ m/s; hold-up $\beta_L > 0$ %).

	UPSTREAM							DOWNSTREAM						
β_L	16.3	17.2	27.3	40.0	42.4	51.7	68.9	18.9	21.7	29.9	45.0	51.2	60.3	63.5

- #4 (Figure 4.10d): the pipes are not dry. From the inlet of the upstream hose, water and air with different velocities are injected into the system. Table 4.5 depicts all the different combinations of air and water velocities.

Table 4.5. Campaign #4: test matrix at different water velocity U_{SL} [mm/s], gas velocity U_{SG} [m/s] and hold-up β_L [%].

	UPSTREAM								DOWNSTREAM							
	U _{SG} ~ 2.5 m/s															
U _{SG}	2.62	2.62	2.62	2.60	2.60	2.58			2.59	2.60	2.61	2.60	2.59	2.57		
U _{SL}	1.7	5.6	11.5	17.4	23.1	31.5			3.1	5.5	11.5	17.0	22.7	31.0		
β _L	10.8	11.5	13.2	16.1	21.8	20.6			10.8	11.5	13.2	16.1	21.8	20.6		
	U _{SG} ~ 5.5 m/s															
U _{SG}	5.82	5.80	5.80	5.71	5.69	5.67	5.65	5.62	5.82	5.80	5.69	5.68	5.66	5.63	5.58	5.57
U _{SL}	3.3	5.8	11.2	14.9	22.7	30.8	39.4	44.5	3.0	5.8	11.8	17.0	23.2	31.1	39.2	45.6
β _L	3.3	3.8	9.0	10.8	12.0	15.0	17.9	19.5	3.3	3.8	9.0	10.8	12.0	15.0	17.9	19.5
	U _{SG} ~ 10.5 m/s															
U _{SG}	10.3	10.3	10.2	10.1	10.0	9.9	9.8	9.6	10.3	10.3	10.3	10.1	10.0	9.8	9.7	9.7
U _{SL}	3.5	5.9	11.3	17.1	23.0	30.9	39.9	45.6	3.4	6.0	11.3	15.0	22.7	31.3	39.7	44.6
β _L	1.6	2.2	8.0	13.6	19.9	23.1	25.3	26.7	1.5	2.2	8.0	13.5	19.8	23.1	25.3	26.7

Due to gravity and entrainment by the air flow at a fixed velocity greater than 0 m/s, water is transported downstream, passing first in the test object and second in the downstream hose. At the outlet of the downstream hose, water from the floor is driven to the separator [T] by using another air injection. To ensure the same initial conditions, at the beginning of each experiment, the pipe has been always dried.

4.3.4. Experimental technique and post-processing

For each test set discussed in Section 4.3.3, unsteady pressure signals are recorded by a DEWETRON 801 (48 channels) acquisition system at acquisition frequency of 10,000 Hz for a total time of 5 seconds at each frequency, in the frequency range between 150 and 4100 Hz, with a frequency step of 5 Hz.

The software DEWESoft 6.6.7 is used to store the signals and the FFT (Fast Fourier Transform) is used to compute the spectrum of pressure measurements. Data were processed in the MATLAB environment.

With a dewe-cam-fw-70 camera, videos were recorded to characterize the flow pattern within the horizontal pipe. See the location of the camera in Figure 4.4. More information on flow visualizations is provided in Section 4.4.4.

The two microphone method

A sound wave $p(x, t)$ can be decomposed as function of space and time as follows:

$$\begin{aligned} p(x, t) &= \hat{p}(x)e^{j\omega t} \\ \hat{p}(x) &= \hat{p}_+e^{-jk_+x} + \hat{p}_-e^{jk_-x} \end{aligned} \quad (4.22)$$

\hat{p} is the amplitude of the acoustic pressure, ω is the angular frequency. Moreover, the acoustical pressure in space can be considered as the sum of two travelling waves, respectively in the positive (+) and negative (-) directions.

To measure the acoustic properties in the pipe, two standard methods can be used: the standard wave ratio (SWR, ISO 10534-1) and the two-microphone method (TMM, ISO 10534-2). The SWR can provide accurate results but it is very time consuming (Allam and Åbom, 2006). Moreover, the two-microphone method is more convenient than the traversing probe method (Chu, 1986; Munjal and Doige, 1990). In addition, SWR is very difficult to use with turbulent flows (Panicker and Munjal, 1981). Since the 80s, many researchers invested on improving the two microphone method originally proposed by Seybert and Ross (1977). However, for the transfer function approach the decomposition of the standing wave pressure into the progressive wave components is not needed (see Chung and Blaser, 1980a-b; To and Doige, 1980; Bodén and Åbom, 1986; Åbom and Bodén, 1988; Seybert and Soenarko, 1981; Munjal and Doige, 1990).

The method based on the transfer function approach aims at determining the reflection coefficients, starting from pressure measurements in two different points of the setup (Ajello, 1997).

Given two microphones located at the abscissa x_i and x_j , the transfer function is defined as:

$$H_{ij}(f) = \frac{\hat{p}(x_i)}{\hat{p}(x_j)} \quad (4.23)$$

If the reflection coefficient at the entrance $R_1^{(u)}$ is equal to $R_1^{(u)} = p_1^-/p_1^+$, the transfer function can be written as function of the reflection $R_1^{(u)}$ as:

$$R_1^{(u)} = \frac{H_1^{ij}e^{-jk_1^+x_{1j}} - e^{-jk_1^+x_{1i}}}{e^{-jk_1^-x_{1i}} - H_1^{ij}e^{jk_1^-x_{1j}}} \quad (4.24)$$

In an analogous way, the reflection coefficient downstream the test object (at the exit of the two port) for a source downstream $R_2^{(D)} = \frac{p_2^+}{p_2^-}$ can be related to the transfer function H_2^{ij} as follows:

$$R_2^{(D)} = \frac{H_2^{ij} e^{-jk_2^+ x_{2j}} - e^{-jk_2^+ x_{2i}}}{e^{-jk_2^- x_{2i}} - H_2^{ij} e^{jk_2^- x_{2j}}} \quad (4.25)$$

To complete the scattering matrix, the transmission coefficients T_{12} and T_{21} are needed. They are defined as the transmission coefficients respectively if the source of sound is located upstream or downstream the test-object. They can be calculated by using the transfer function $H_{21}^{ii} = p_2(x_{2i})/p_1(x_{1i})$ and $H_{12}^{ii} = p_1(x_{1i})/p_2(x_{2i})$ as:

$$\begin{aligned} T_{12}^{(U)} &= H_{21}^{ii} \left(\frac{e^{-jk_1^- x_{1i}} + R_1 e^{jk_1^- x_{1i}}}{e^{-jk_2^+ x_{2i}} + 1/R_2 e^{jk_2^- x_{2i}}} \right) \\ T_{12}^{(D)} &= H_{21}^{ii} \left(\frac{R_2 e^{-jk_2^+ x_{2i}} + e^{jk_2^- x_{2i}}}{1/R_1 e^{-jk_1^- x_{1i}} + e^{jk_1^- x_{1i}}} \right) \end{aligned} \quad (4.26)$$

These are the coefficients to be used for each source location in the system (4.29).

For the method used to post-process the data, the distances between microphones have to be as accurate as possible. Small errors due to the manufacturing process have to be corrected. For this reason the microphones have been calibrated.

For each group of four microphones [L] and [M], the smooth pipe [T.O.] has been replaced by a blind flange. The measured transfer matrices have been compared with the one estimated analytically. Note that the analytical model includes the acoustical damping (Kirchhoff law), assuming that the reflection coefficient of the blind flange is 0.96. Since the measured and the analytical curves are expected to be equal, from the initial values used (see Table 4.2) as input for the analytical estimate, the distances and the amplitudes have been corrected. As reference, the microphones U1 and D1 have been respectively used to create the transfer functions. Moreover, it is known that for the case without mean flow, the transmission coefficient, as well as the acoustical damping, has to be the same. For this reason, the amplitude ratio between U1 and D1 has been regulated. All the corrections are reported in Table 4.6.

More details about the calibration are provided in Appendix B.

Table 4.6. Calibration of the piezometric transducers: final correction of the relative distances and amplitude.

	Upstream		Downstream	
Combination	Distance Correction [x10 ⁻³ m]	Amplitude	Distance Correction [x10 ⁻³ m]	Amplitude
1-1	0.00	1.000	0.00	1.000
1-2	0.60	0.988	0.50	1.005
1-3	0.50	1.010	0.65	1.005
1-4	0.30	0.980	0.65	0.975
U1/D1		1.009		

Equations (4.27) explain how density, the dynamic viscosity and the speed of sound are estimated from temperature and static pressure in the two microphone method code used.

$$\mu_G = (18.27e^{-6}) \cdot \frac{\rho = p/RT}{\frac{291.15 + 120}{T + 120}} \cdot (T/291.15)^{3/2} \quad (4.27)$$

$$c_0 = \sqrt{\frac{T}{293.15}} \cdot 343.5611$$

The scattering matrix

A generic system, in this case a smooth pipe, can be considered. This constitutes the test object of the two-port system shown in Figure 4.11.

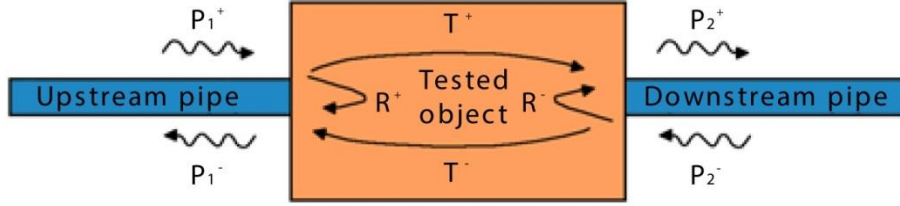


Figure 4.11. Definitions and notation for diffraction matrix of the tested object.

Two equations can be written, one upstream and one downstream the test object. By determining the reflection coefficients at the entrance of the two ports $R^+ = p_1^-/p_1^+$ and at the exit of the two ports $R^- = p_2^+/p_2^-$, and the (anechoic) transmission coefficients $T^+ = p_2^+/p_1^-$ and $T^- = p_1^-/p_2^+$, the full scattering matrix S of the system (4.28) can be reconstructed. The matrix $[S]$ can depend on the geometry of the system, on the acoustical frequency, and on the characteristics of the mean flow (Mach number, temperature, viscosity, etc...).

$$\begin{bmatrix} p_2^+ \\ p_1^- \end{bmatrix} = \underbrace{\begin{bmatrix} T^+ & R^- \\ R^+ & T^- \end{bmatrix}}_{[S]} \cdot \begin{bmatrix} p_1^+ \\ p_2^- \end{bmatrix} \quad (4.28)$$

The scattering matrix S describes the properties of the test object and for this specific case of the smooth pipe. Two different systems can be written for each source location: the first dividing the system (4.28) by p_1^+ and the second by p_2^- . If the two systems are assembled together, the system reported in (4.29) is obtained:

$$\begin{bmatrix} T_{12}^{(U)} & R_2^{(D)} \\ R_1^{(U)} & T_{21}^{(D)} \end{bmatrix} = \begin{bmatrix} T^+ & R^- \\ R^+ & T^- \end{bmatrix} \begin{bmatrix} 1 & T_{21}^{(D)}/R_1^{(D)} \\ T_{12}^{(U)}/R_2^{(U)} & 1 \end{bmatrix} \quad (4.29)$$

The coefficients T^+ , R^- , R^+ , and T^- can be therefore written as function of the transmission and reflection coefficients measured for each source location (for more details see Ajello, 1997) with the two microphones method.

Estimate of damping from scattering matrix

For a pipe of constant diameter, the transmission coefficients can be written as:

$$\begin{cases} T^+ = e^{-ik^+L_{mp}} \\ T^- = e^{-ik^-L_{mp}} \end{cases} \quad (4.30)$$

with k^+ and k^- the wavenumbers in each direction. These wavenumbers are what we want to extract from the measurements:

$$\begin{cases} k^+ = i \frac{\log T^+}{L_{mp}} \\ k^- = i \frac{\log T^-}{L_{mp}} \end{cases} \quad (4.31)$$

For the no-flow condition, the scattering matrix is symmetrical: $T^+ = T^-$, and $k^+ = k^-$.

The damping coefficients are the imaginary part of the wavenumbers and can be written as function of the transmission coefficients absolute value $|T^\pm|$:

$$\begin{cases} \alpha^+ = -\frac{\log |T^+|}{L_{mp}} \\ \alpha^- = -\frac{\log |T^-|}{L_{mp}} \end{cases} \quad (4.32)$$

4.3.5. Presentation of the results

In this section it will be explained how the results are going to be presented in Section 4.4. This aims at facilitating the reader with reading and interpreting the results.

As said in Section 4.3.3, the test matrix consists of 4 main campaigns. For each campaign, the damping in the positive direction (direction of the flow) α^+ is compared with the damping in the negative direction (against flow) α^- . With each test, the goal is to build up a reasoning and to quantify the influence on damping of the different factors, such as convection, turbulence, and the hydraulic diameter effects. For this reason, the results will be presented as the ratio between the measured damping and the Kirchhoff damping α_0 , with and without the corrections of the aforementioned factors. Moreover, in Section 4.3.2 the hold-up values estimated by using the capacitance probes have been reported; in particular, of the original capacitance probes' signal, the average value and its standard deviation are reported (see Figure 4.8). The standard deviation was considered as a good parameter for describing how wavy the flow was. However, if waves are generated, the hold-up changes, as well as the hydraulic diameter. For this reason, in each corrected plot, it is possible to evaluate the effect of waves on damping by means of bands. These are also a way to evaluate the sensitivity of the measured damping to the error made on the hold-up measurements.

First, in Section 4.4.1, the results without gas mean flow and without liquid are presented. These provide with a reference and they have been used to calibrate the downstream microphones.

In Section 4.4.2, only the tests with gas mean flow are considered. The convection effects will be analyzed both with the correction provided by Davies and by Dokumaci.

In section 4.4.3, the tests with only quiescent water without gas mean flow are conducted. These tests aim at understanding how the hydraulic diameter is relevant for the analysis of the results and whether it can be assumed that sound is only propagating in air.

In Section 4.4.4, the tests for the cases with a mixture flow of air and water at different velocities are treated. The results will be analyzed singularly for each constant gas velocity. Moreover, it will be discussed the importance of the turbulence effects, especially for the highest gas velocity. The hybrid model proposed in Section 4.2 will be used to evaluate those effects.

4.4. Experimental Results

The multi-microphone method has been used to estimate the damping coefficient in a smooth horizontal pipe assuming that plane waves are travelling in a multiphase medium. In particular, by using Eq. (4.32), the acoustical damping is estimated from the transmission coefficient T of the scattering matrix. Different cases have been considered and compared. The source has been located first upstream (+) and second downstream (-) the test object. Section 4.3.3 describes all the tests conducted.

4.4.1. Dry pipe – No mean flow (Campaign #1)

A first test with only dry gas without mean flow has been conducted. The transmission coefficient T of the diffraction matrix as function of the frequency is shown in Figure 4.12. Note that these two tests have been used for the calibration of the downstream pressure transducers relative to the upstream pressure transducers (see Section 4.3.4). Indeed, in absence of mean flow, the transmission coefficients, and in turn the damping coefficients (Eq. (4.32)), measured with the sound source located upstream (+) and with the sound source located downstream (-) are equal. The irregularity in the frequency range 1000-1800 Hz is due to the vibration of the pipe induced by the coupling with the mechanical response of the pipe. It is important to remind that the material of the pipe is plastic (Perspex).

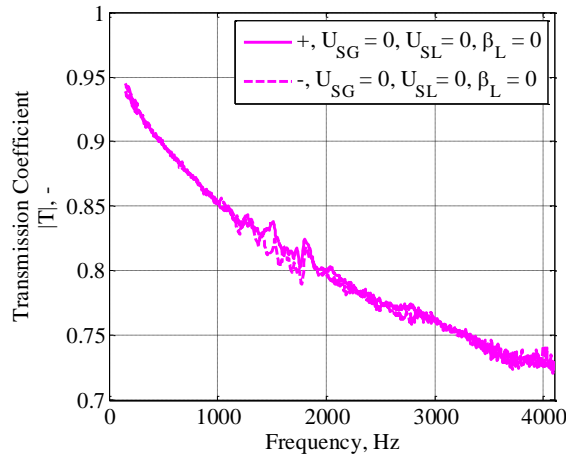


Figure 4.12. No gas mean flow, no liquid: transmission coefficient T [-] as function of frequency [Hz].

By using Eq. (4.32), the acoustical damping coefficient in both directions can be estimated from the measured transmission coefficient. In Figure 4.13 the acoustical damping is shown together with the visco-thermal damping estimated with the first order of the Kirchhoff law (Eq. (4.4)). For this analysis, for each frequency, temperature is averaged on a 5 seconds time signal and it is used to estimate speed of sound and dynamic viscosity (see Eqs. (4.27)). Figure 4.14 provides the comparison with the Kirchhoff damping α_0 calculated as in Section 4.1.1 and shows that the max percentage error is 10% (except in the range 1000-1800 Hz). Regarding this particular range, mechanical resonances perturb the results. For completeness, they have been not filtered out.

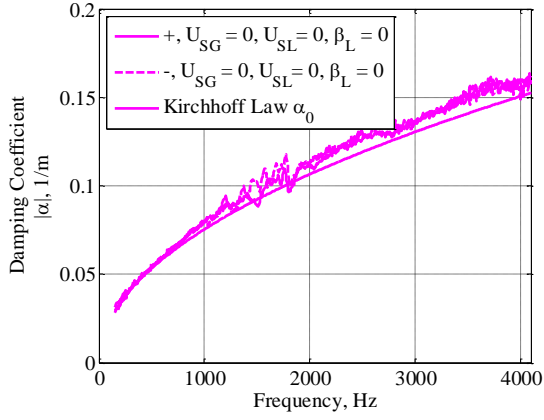


Figure 4.13. No gas mean flow, no liquid: damping coefficient α [1/m] as function of frequency [Hz].

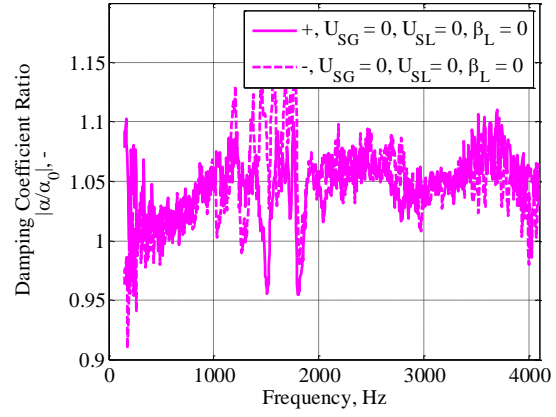


Figure 4.14. No gas mean flow, no liquid: damping coefficient ratio α/α_0 [-] as function of frequency [Hz].

4.4.2. Only gas mean flow (Campaign #2)

In this section the results with only dry air are discussed. Only a gas mean flow is grazing in the system. In particular, in addition to the test without mean flow, three different gas velocities (see Table 4.3 – Campaign #2) are considered. The damping measured in both directions is shown in Figure 4.15a. With respect to the test without mean flow (magenta curves of Figure 4.15a), the curves at only two different velocities are compared: ~ 2.5 m/s (green), and ~ 10.5 m/s (red). As expected from the convection effects, they get farther from each other, the higher the gas velocity. Indeed, when the source is located downstream (--) the damping is higher because the sound wave travels against flow. On the contrary, in the flow direction (-) the acoustical damping decreases.

As it has been done several times in the past, the second term of the acoustical damping is neglected for this analysis (Davies 1988; Morse and Ingard, 1968; Pierce 1989, Allam and Åbom, 2006). Its contribution is not considered fundamental for the general purpose of this work.

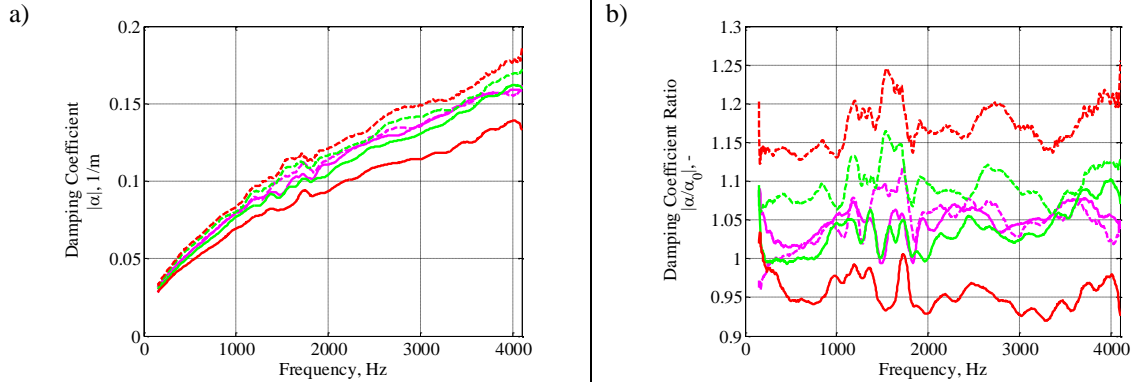


Figure 4.15. Only gas mean flow: damping coefficient α [1/m] (a), the ratio of the measured damping to the Kirchhoff damping α_0 (b), as function of frequency [Hz] in the direction of the flow (-) and against flow (--) at different gas velocities U_{SG} : 0 m/s (magenta), ~ 2.5 m/s (green), ~ 10.5 m/s (red).

As explained in Section 4.1.1, two different approaches are available to correct the convection term. Equations (4.5) and (4.6) in Section 4.1.1 provides the reader with the correction factors proposed by Davies and Dokumaci. Regarding the second approach of Dokumaci (1995), Golliard et al. (2015), manipulating Eq. (4.6), proposed an approximation of the acoustical damping as:

$$\alpha_{0,conv}^{\pm} = \frac{\alpha_0}{(1 \pm 2M)} \quad (4.33)$$

Where α_0 is the first order of approximation of Eq. (4.4). It has been verified that this approach is particularly suitable at low Mach number and it will be used because the max Mach number is around 0.03. Figure 4.16 shows indeed that for a frequency equal to 320 Hz, the differences between the approximation of Golliard (green lines) and the full model proposed by Dokumaci (black lines) are negligible for very low Mach numbers. Indeed, the higher the Mach number is, less accurate the approximation of Golliard et al. (2015) is. Figure 4.17 shows the expected effects of convection on acoustical damping for a frequency range between 150 and 4100 Hz.

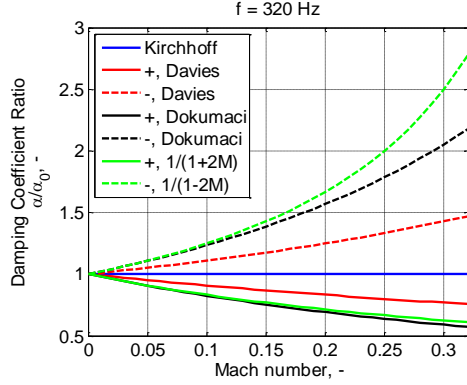


Figure 4.16. Comparison between the different models used to take into account the convection effects (Davies, and Dokumaci) and their approximation for different Mach numbers at 320 Hz.

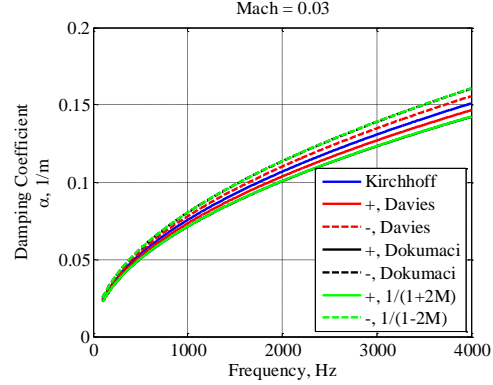


Figure 4.17. Comparison between the different models used to take into account the convection effects (Davies, and Dokumaci) and their approximation for different frequencies at Mach $M = 0.03$.

On the basis of Figure 4.16 and Figure 4.17, the model of Davies and the approximation of Golliard et al. (2015) will be compared to evaluate the effects of convection in Figure 4.18. In particular, Figure 4.18a shows the ratio of the acoustical damping measured to the estimated Kirchhoff damping corrected by the term proposed by Davies $1 \pm M$. On the right side, Figure 4.18b shows the approximation proposed by Golliard et al. (2015) for the term proposed by Dokumaci (1995). Compared to Figure 4.15b, the two terms $1 \pm M$ (Figure 4.18a) and $1 \pm 2M$ (Figure 4.18b) are expected to correct the convection and all the curves to collapse on the dry gas scenario (magenta curves). After a comparison of the two plots of Figure 4.18, the approximation of Golliard et al. (2015) of the correction of Dokumaci (1995) gives a better alignment of the curves with gas mean flow to the magenta lines (without mean flow). Also Golliard et al. in his work (2015) reported that the model of Dokumaci was better at describing the convection effects. Therefore, this correction will be always used also to evaluate the effects of convection, if there is any gas mean flow grazing in the main pipe.

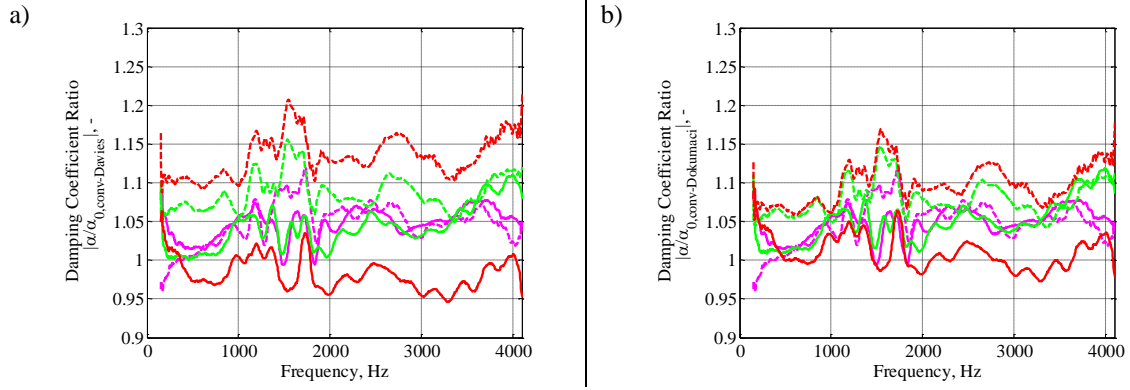


Figure 4.18. Only gas mean flow: damping coefficient ratio corrected by the convection term of Davies (1988) - $1\pm M$ - (a), and by the convection term of Golliard (2015) as approximation of Dokumaci (1995) - $1\pm 2M$ - (b) as function of frequency [Hz] in the direction of the flow (-) and against flow (--) at different gas velocities U_{SG} : 0 m/s (magenta), ~ 2.5 m/s (green), ~ 10.0 m/s (red).

As discussed in Section 4.1.1, the effects of turbulence should also be considered if the ratio of the acoustic boundary layer to the viscous sublayer is greater than 1.

Figure 4.19 shows the ratio of the acoustic boundary layer δ_{ac} to the viscous sublayer δ_l at different frequencies. Note that in this case there is no water in the system (hold-up $\beta_L = 0$). For the three tested gas velocities (~ 2.5 m/s, ~ 5.5 m/s, and ~ 10.5 m/s) the effects of turbulence are always negligible, the ratio δ_{ac}/δ_l being greatly smaller than 1 in the frequency range investigated. For this reason, the turbulence effects are not here treated. This plot shows also that the lower the frequency is, the more relevant the effects of turbulence are. Moreover, these effects are more relevant if, as expected, the gas velocity is higher, the mean flow being more turbulent.

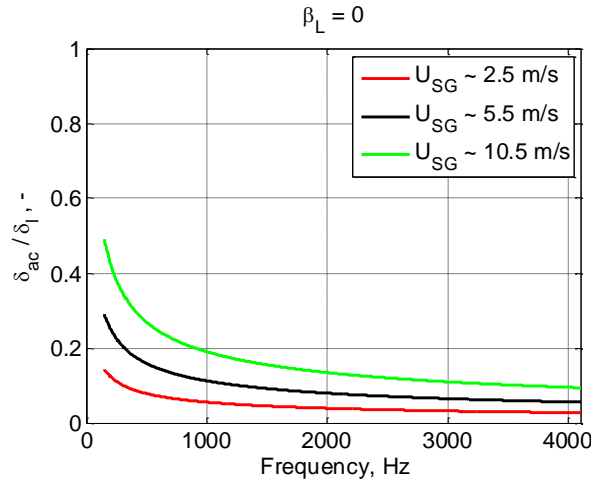


Figure 4.19. Only gas mean flow: estimate of the ratio of the acoustic boundary layer δ_{ac} to the sub-viscous boundary layer δ_l as function of frequency [Hz].

4.4.3. Quiescent water without gas mean flow (Campaign #3)

For this set of experiments, as explained in Section 4.3.3, different amounts of water have been poured in the horizontal pipe. There is no mean flow ($U_{SG} = 0$ m/s and $U_{SL} = 0$ m/s) and for this reason the interfacial surface is smooth. The upstream and the downstream hoses are dry while the main pipe contains different amounts of water for each test. The hold-up β_L has been estimated by means of the capacitance probes (see Table 4.4). These tests aim at understanding how damping is modified by the presence of the layer of water in the pipe, in absence of mean flow.

Figure 4.20 shows the acoustical damping measured upstream (-) and downstream (--) the test object. Compared to the case with dry gas (magenta lines), the higher the hold up, the higher the damping. However, for some of the experiments there is a particular range of frequencies where the measured acoustic damping is not a smooth curve. This is likely related to the coupling between the acoustical field and the mechanical response of the pipe. It has been verified that the mechanical response of the pipe occurs in the range of frequency between 1300 and 2000 Hz, generating resonant peaks. As a consequence, in this frequency range data is affected. For this reason, a grey surface is used to indicate that the results are considered not reliable.

On the basis of the Kirchhoff law (see Eq. (4.4)), on the assumption that the sound is travelling only in air, it is expected that the acoustical damping would increase in presence of water. Indeed, the area of the pipe filled with air is reduced by the presence of steady water. The hydraulic diameter is therefore decreased, which increases the damping.

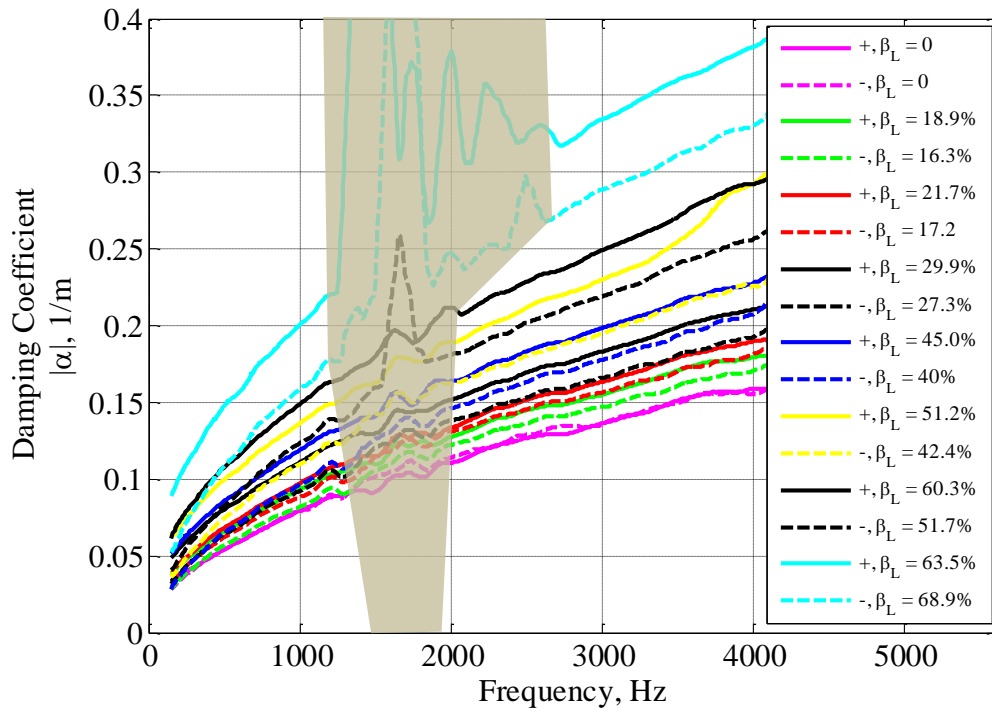


Figure 4.20. No gas mean flow, only liquid ($U_{SL} = 0$ m/s): Acoustical damping coefficient [1/m] as function of frequency [Hz] measured at different liquid hold-up β_L [%]. The grey surface indicates a range of frequency where data it not considered reliable.

To evaluate the effects of the change of the area, the measured acoustical damping is divided by the damping estimated with the Kirchhoff law (Eq.(4.4)). The latter is inversely proportional to the hydraulic diameter of the pipe, as already commented in Section 4.1.1. The analysis has been repeated twice, first as the pipe had been dry

(Figure 4.21a1-b1) and second by using the effective hydraulic diameter (Figure 4.21a2-b2). In the first case, the perimeter $L_{2p} = S_G + S_i = \pi D_{mp}$ and the area A_{mp} of the main pipe are used for the Kirchhoff's equation (see Eq.(4.4)). The second time, by using the hold-up values measured with the capacitance probes, the perimeter is the sum $S_G + S_i$ (see Figure 4.3) and the area is the one effectively occupied by air $A_{mp,G}$. S_G and S_i are the parts of the perimeter that air sees, i.e. the wall and the interface between water and air (see Figure 4.3).

From the comparison proposed in Figure 4.21, it is possible to quantify whether and how much the change in damping due to different liquid hold-ups is relevant to estimate the damping. Looking at the corrected ratios (Figure 4.21a2-b2), the error is in general within the 10%, compared to the dry no mean flow case (magenta line), both in direction of (a2) and against flow (b2). As shown in Figure 4.21a2, only for the highest amount of liquid in the positive direction ($\beta_L = 63.5\%$, cyan line), the error is higher than 20%. It is therefore possible to conclude that the change in the measured damping is due to the reduction of the area due to the increased liquid hold-up and this error can be due to the hold-up measurements error.

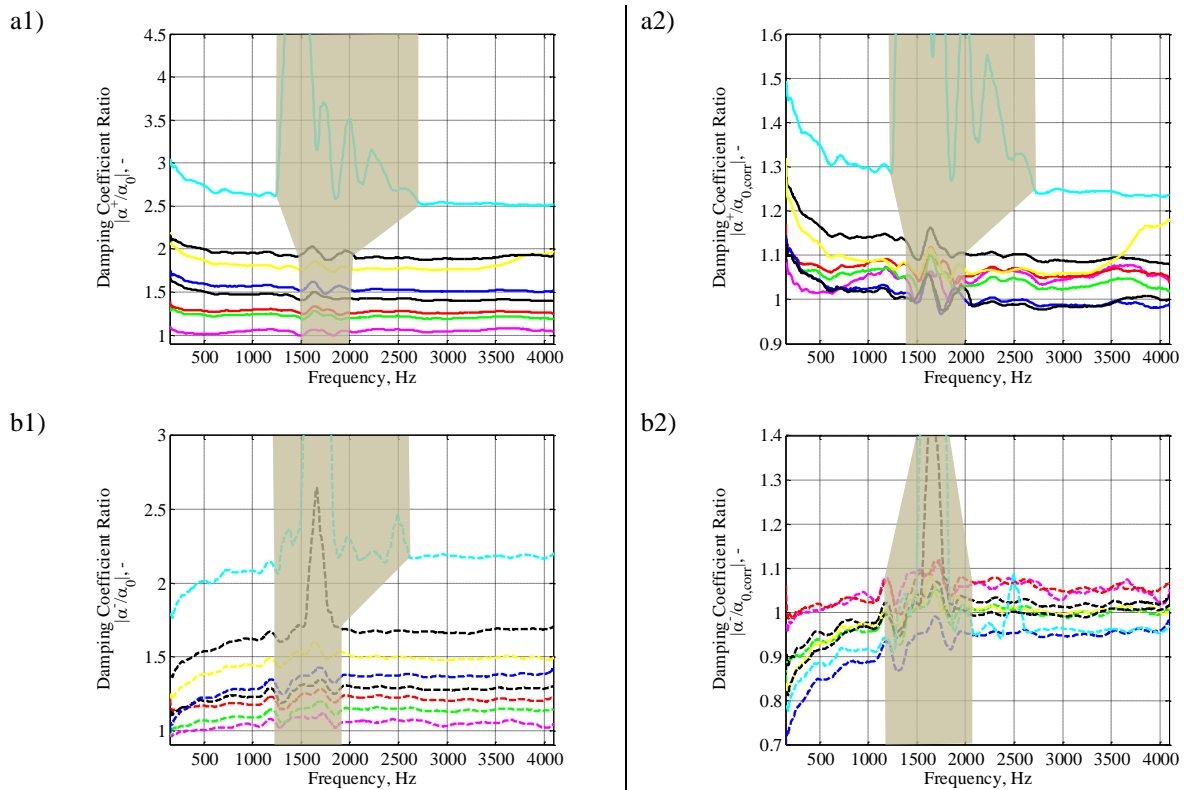


Figure 4.21. No gas mean flow, only liquid ($U_{SL} = 0$ m/s): ratio of the acoustical damping coefficient α to the Kirchhoff damping α_0 and as function of frequency [Hz] by using the full and the corrected hydraulic diameter in the direction of (a1 and a2) and against (b1 and b2) flow. The legend is the same as in Figure 4.20. The grey surface indicates a range of frequency where data is not considered reliable.

4.4.4. Mean gas flow and liquid (Campaign #4)

As shown in Table 4.5, the acoustical damping has been measured with air and water flowing with different superficial velocities. In particular, at three and constant superficial gas velocities ($U_{SG} \sim 2.5$ m/s, 5.5 m/s, and 10 m/s), the liquid volumetric flow rate has been increased. The maximum liquid velocity U_{SL} reached was around 0.045 m/s. The analysis of the results has been split into three different sections, one for each superficial gas velocity.

As said in Section 4.3.4, a dewe-cam-fw-70 camera recorded several videos to characterize the flow pattern within the horizontal pipe. Figure 4.22 shows snapshots of the different combinations of liquid and gas velocities. At $U_{SG} \sim 2.5$ m/s, the surface is smooth, up to U_{SL} 0.023 m/s. At high injection rates, slugs are generated in the upstream hose because of the small downwards slope. These slugs are driven downstream first in the horizontal line and then in the downstream hose. For this reason the acoustic analysis could not be performed at high injection rates $U_{SL} > 0.023$ m/s. At $U_{SG} \sim 5.5$ m/s, the flow at low rates (U_{SL} 0 – 0.012 m/s) is stratified smooth, while at high rates it becomes stratified wavy. At $U_{SG} \sim 10.5$ m/s, visualizations show that already at low rates the flow is wavy and waves become higher when more water is injected in the pipe.

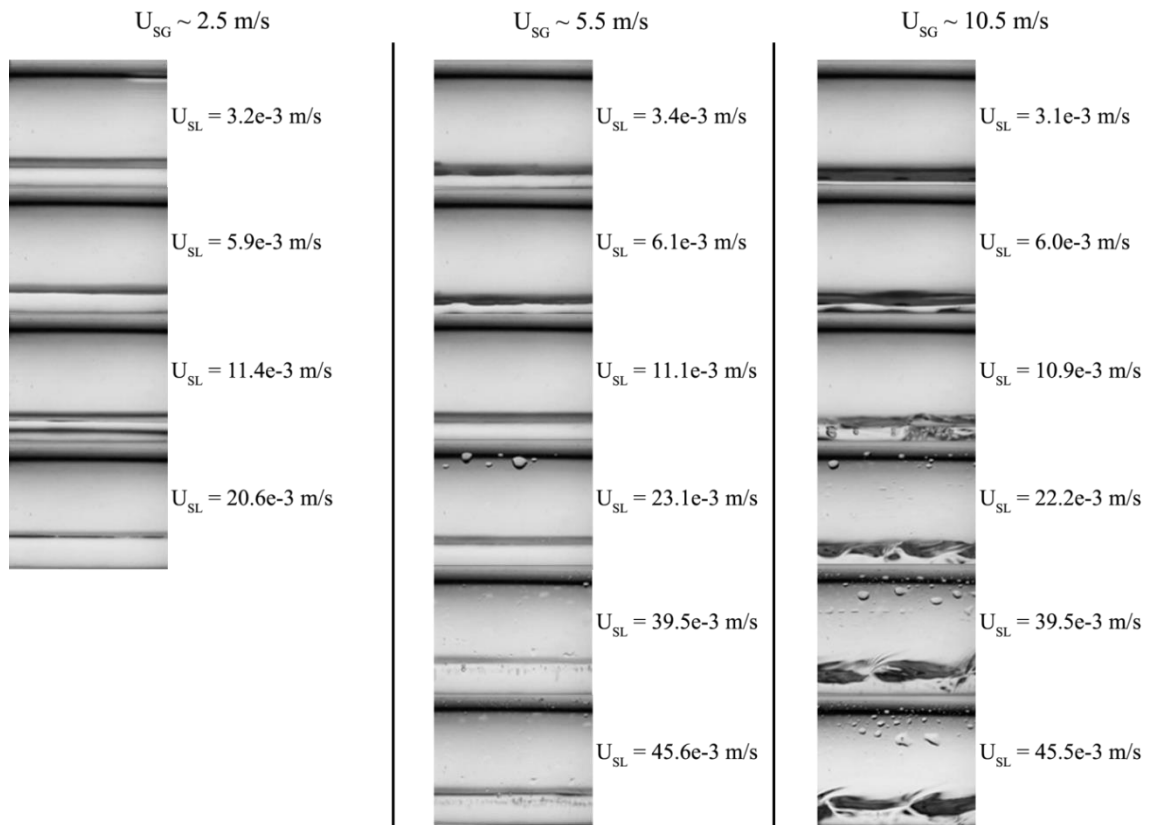


Figure 4.22. Flow visualizations at different gas and liquid velocities.

On the basis of previous results discussed in Section 4.4.2 and 4.4.3, different contributions are expected to play a role when an air-water mixture flows in a smooth pipe:

- 1) Convection effects (superficial gas velocity $U_{SG} > 0$ m/s)
- 2) Hydraulic diameter effects (hold-up $\beta_L > 0$)
- 3) Turbulence effects (ratio of the acoustic boundary layer to the viscous sublayer $\delta_{ac}/\delta_l > 1$)

Concerning the third point, the effects of turbulence can become more relevant at low frequencies, being the acoustic boundary layer inversely proportional to the root square of frequency. At low frequency, it is therefore more likely that the ratio is greater than the unit.

As already discussed in Section 4.4.2, with only mean flow the turbulence effects can be neglected because the ratio δ_{ac}/δ_l is much lower than the unit. For this set of experiments, water is present in the pipe. For this reason, it is here important to remind the concepts of the superficial and actual gas velocity. The superficial velocity is defined as the velocity a phase (gas or liquid) would obtain when flowing alone in a pipe. The actual velocity of one phase takes into account the ratio of cross section area occupied by this phase to the total cross-section area of the pipe (the phase hold-up) (Oliemans, 2008). In presence of water the superficial and the actual velocities are different from each other.

Compared to Figure 4.19, Figure 4.23a shows the highest ratio δ_{ac}/δ_l at the three constant gas velocities, if also the effects of the hold-up were included in the calculations. The friction coefficient, i.e. the friction velocity, necessary to calculate the viscous sublayer is estimated on the basis of the Reynolds number estimated by using the hydraulic diameter and the actual velocity. Assuming the gas flow mass rate is constant, if the area occupied by gas decreases because of the presence of water, the gas velocity increases. Figure 4.23a shows that considering only the change of the hydraulic diameter, the ratio is still lower than 1, although it gets close to the unit when the superficial gas velocity is around 10.5 m/s. On the basis of this plot, turbulence could be neglected.

However, visualizations show that waves occur and the friction at the liquid surface is not the same as the one at the pipe wall. This indicates that a correct description of the boundary layer at the water interface should include the effect of the waves. This is the approach taken in Section 4.2, where an interfacial friction is defined for a stratified or stratified wavy flow. This leads to a different evaluation of the boundary layer thickness. As described in Section 4.1.2, the empirical model uses two threshold velocities defining the transition from the *smooth region* to the *two-dimensional wave region*, and from the *two-dimensional wave region* to the *very wavy region*.

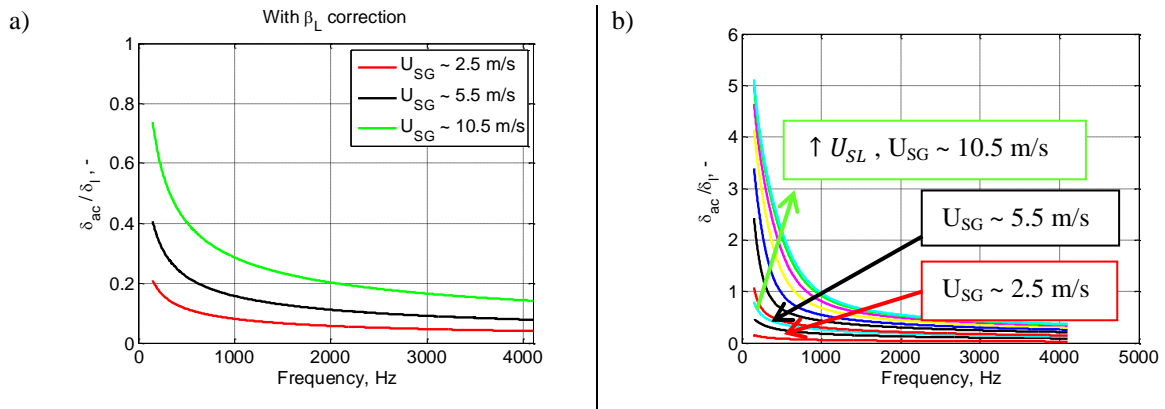


Figure 4.23. Gas and liquid mean flow: ratio of the acoustic boundary layer to the viscous sublayer. The latter has been calculated with the friction coefficient estimated (a) with the shear stress at the wall by using the actual gas velocity and the hydraulic diameter and (b) with the interfacial shear stress calculated with Tzotzi and Andritsos model (2013).

With the comparison between Figure 4.23a and Figure 4.23b, it can be highlighted that at $U_{SG} \sim 10.5$ m/s this ratio can become much greater than 1. For this specific case ($U_{SG} \sim 10.5$ m/s), to evaluate the turbulence generated by the liquid “moving wall”, the model proposed in Section 4.2 is used. This is a weighted model based on the combination of the multiphase flow model proposed by Tzotzi and Andritsos (2013) and the

acoustical model of Howe (1995). In particular, the friction coefficient estimated by the multiphase flow model of Tzotzi and Andritsos is used to estimate the friction velocity needed for the acoustical model.

For the analysis of the results for each constant gas velocities, the corrections related to the convection terms, the hydraulic diameter and turbulence are discussed. The analysis will be conducted with the mean hold-up values (see Section 4.3.2).

In the following sections the results will be analyzed by using the mean hold-up values shown in Figure 4.8a. The results with liquid will be compared with the case without and with gas mean flow. Moreover, the convection and the area corrections will be applied onto the Kirchhoff damping. Since the approximation of Golliard et al. (2015) of Dokumaci's model (1995) described the convection effects for only gas mean flow better than Davies' model (see Section 4.4.2), the approximation of Golliard et al. (2015) is used for this analysis. From the average hold-up β_L (see Section 4.3.2), the (corrected) hydraulic diameter together with the convection are taken as input for the Kirchhoff law (Eq.(4.4)).

Mean gas flow and liquid: $U_{SG} \sim 2.5$ m/s

Different liquid volumetric flow rates have been injected in the pipe system where an air flow is grazing at around 2.5 m/s.

Figure 4.24a-b show the uncorrected measured damping (a) in the direction of, and (b) against flow. As reference, the magenta curves indicate the damping measured without gas mean flow upstream (solid lines) and downstream (dashed lines) the test object. The green curves refer to the case with only a gas mean flow ($U_{SG} \sim 2.5$ m/s). The other colors are related to the different liquid rates injected and mixed with a gas mean flow at a superficial gas velocity $U_{SG} \sim 2.5$ m/s. By comparing Figure 4.24a and Figure 4.24b, it is noticeable that in presence of water the acoustical damping increases both in the direction of and against flow. With only gas mean flow (see Section 4.4.2, Figure 4.15b), the damping increased if the wave was against flow and decreased in the direction of the flow.

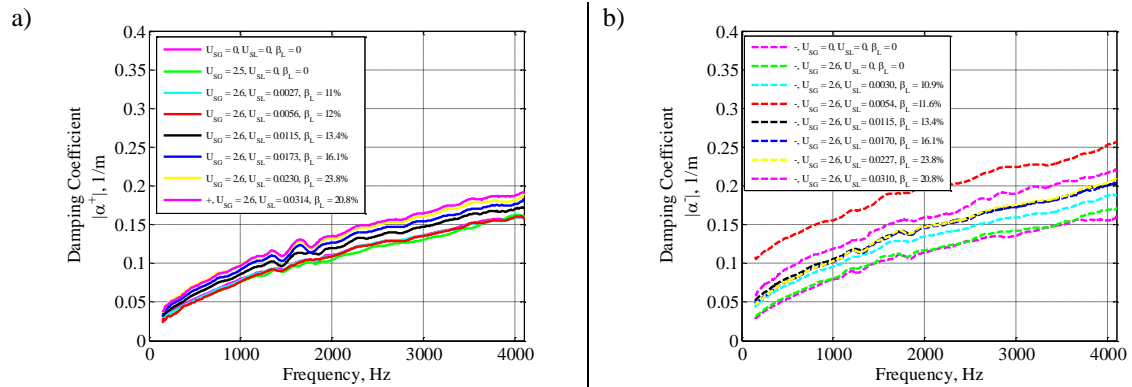


Figure 4.24. Gas and liquid mean flow: acoustical damping coefficient [1/m] measured as function of frequency [Hz] in the direction of (a) and against flow (b) at a superficial gas velocity $U_{SG} \sim 2.5$ m/s. As a reference, the damping measured without any flow (magenta) and with a flow of dry air (green) is provided.

However, this increase is different in the two cases. For the source located upstream (Figure 4.24a), this growth is monotonic. When the source is located downstream, the acoustical damping has a local peak at $U_{SL} = 5.5 \times 10^{-3}$ m/s.

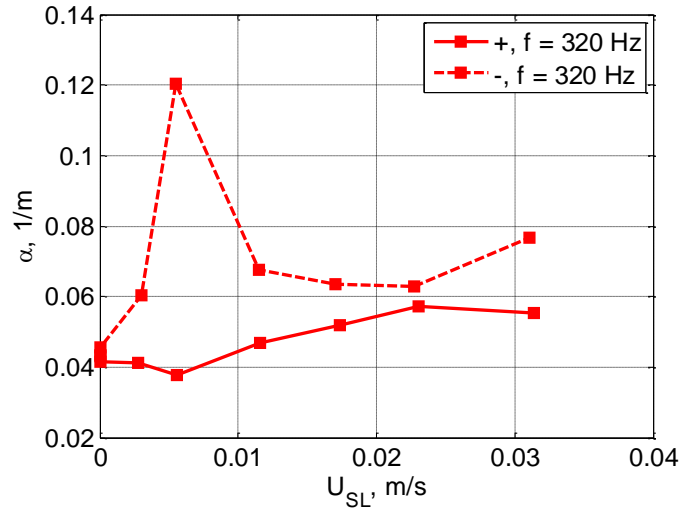


Figure 4.25. Acoustical damping coefficient measured at 320 Hz for an (almost) constant superficial gas velocity ($U_{SG} \sim 2.5$ m/s) as function of the superficial liquid velocity U_{SL} [m/s].

Figure 4.25 helps the reader to understand the different behavior of the acoustical damping as function of the different superficial liquid velocities, at a fixed arbitrary frequency equal to 320 Hz. Although it is sure that it has been conducted in the same way as the other experiments, it is not clear whether the local peak is a mistaken tests set or not.

To evaluate the different expected contributions to the increase of the acoustical damping, the measured damping is divided by the damping expected with the Kirchhoff law and the different contributions are evaluated by correcting Eq. (4.4) with the Mach number and the corrected hydraulic diameter. Note that the convection term is the one proposed by Golliard et al. (2015), i.e. $1 \pm 2M$.

Figure 4.26 compares the ratio of the measured acoustical damping to the Kirchhoff estimate without (Figure 4.26a1-b1) and with correction of convection and of the hydraulic diameter (Figure 4.26a2-b2). With the convection and the hydraulic diameter correction, it is expected that the curves collapse to the magenta line ($U_{SG} = 0$ m/s, $U_{SL} = 0$ m/s, $\beta_L = 0$). Except for the case against flow (red dashed line) at hold-up $\beta_L = 13.2$ %, for all the other cases the max error is about $\pm 5\%$ in direction of the gas mean flow. It can be therefore concluded that the convection together with the reduction of the hydraulic diameter are responsible for the acoustical damping increase.

Although it is not very visible, around the lines in Figure 4.26a2 and Figure 4.26b2 there is a small band which indicates the error due to the presence of waves. For this particular case, the standard deviation of these tests was really small (see Section 4.3.2) and, as a consequence, its effects are not visible.

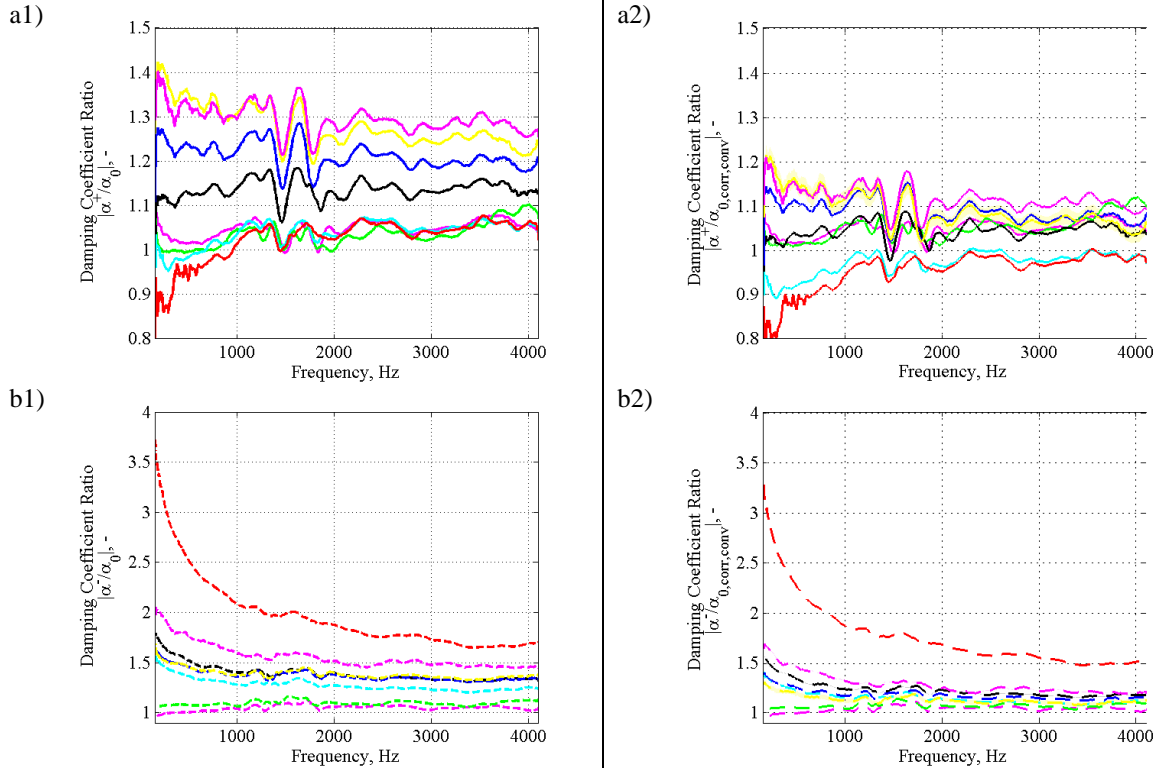


Figure 4.26. Mean gas flow and liquid: $U_{SG} \sim 2.5$ m/s. Damping coefficient ratio [-] as function of frequency [Hz] without corrections in direction (a1, solid lines) and against flow (b1, dashed lines). Damping coefficient ratio [-] as function of frequency [Hz] including the effects of convection and the hydraulic diameter (a2-b2). Additionally, the uncertainty margin is provided (a2-b2) by using the hold-up values $\beta_L \pm$ the standard deviation σ (see Section 4.3.2). The legend is the same as in Figure 4.24.

Mean gas flow and liquid: $U_{SG} \sim 5.5$ m/s

In this section, the analysis of the results is repeated for the superficial gas velocity U_{SG} equal to 5.5 m/s. Figure 4.27 shows the acoustical damping measured (a) in the direction of, and (b) against flow as function of the frequency. Analogously to the case at $U_{SG} \sim 2.5$ m/s, the acoustical damping increases as soon as water is present in the pipe.

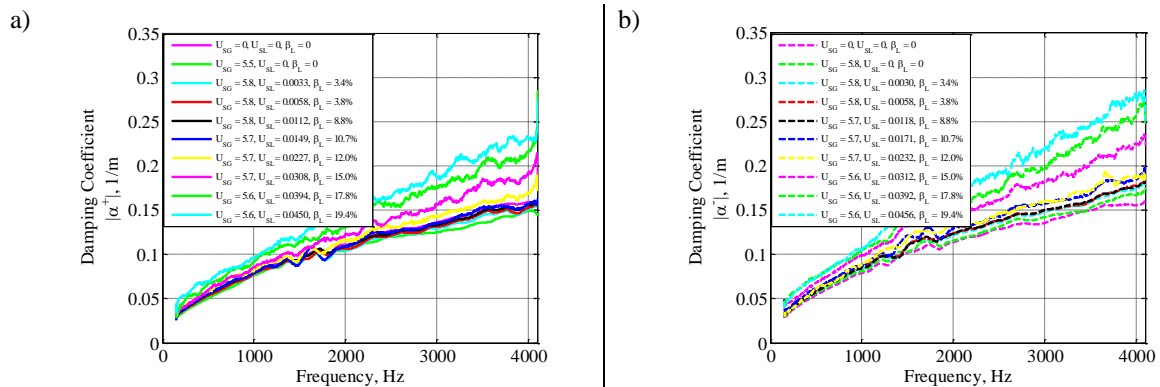


Figure 4.27. Gas and liquid mean flow: $U_{SG} \sim 5.5$ m/s: acoustical damping coefficient [1/m] measured as function of frequency [Hz] in the direction of (a) and against flow (b) at a superficial gas velocity $U_{SG} \sim 5.5$ m/s. As a reference, the damping measured without (magenta) and with (green) flow is provided.

Compared to the previous case, the “translational” effect is less visible. Indeed, for U_{SL} greater than ~ 0.02 m/s (yellow lines), the measured damping does not follow the root mean square of the frequency over the full

range of frequencies. This behavior is consistent in both directions, although it is more remarkable for the case against flow (Figure 4.27b).

Figure 4.28 shows the ratio of the measured acoustical damping to the Kirchhoff damping α_0 , as well as the comparison with the Kirchhoff damping $\alpha_{0,corr,conv}$, corrected with the convection term and the hydraulic diameter. In this case, at a superficial gas velocity U_{SG} equal to 5.5 m/s, there are two different behaviors to highlight. First, in the frequency range between 500 Hz and 2000 Hz, the ratio is almost constant but the corrections do not fully explain the increase of damping at a liquid superficial velocity greater than 0.039 m/s in the direction of the flow (Figure 4.28a2) and greater than 0.031 m/s against flow (Figure 4.28b2). Second, at frequency greater than 2000 Hz, at high superficial liquid velocities, the constant behavior is lost. No reasons for that can be found. In addition, the error generated by the capacitance probes measurements has been evaluated in Figure 4.28a2-b2. Even if considering this error, it is not possible to fully explain why the acoustical damping increases so much at high frequency.

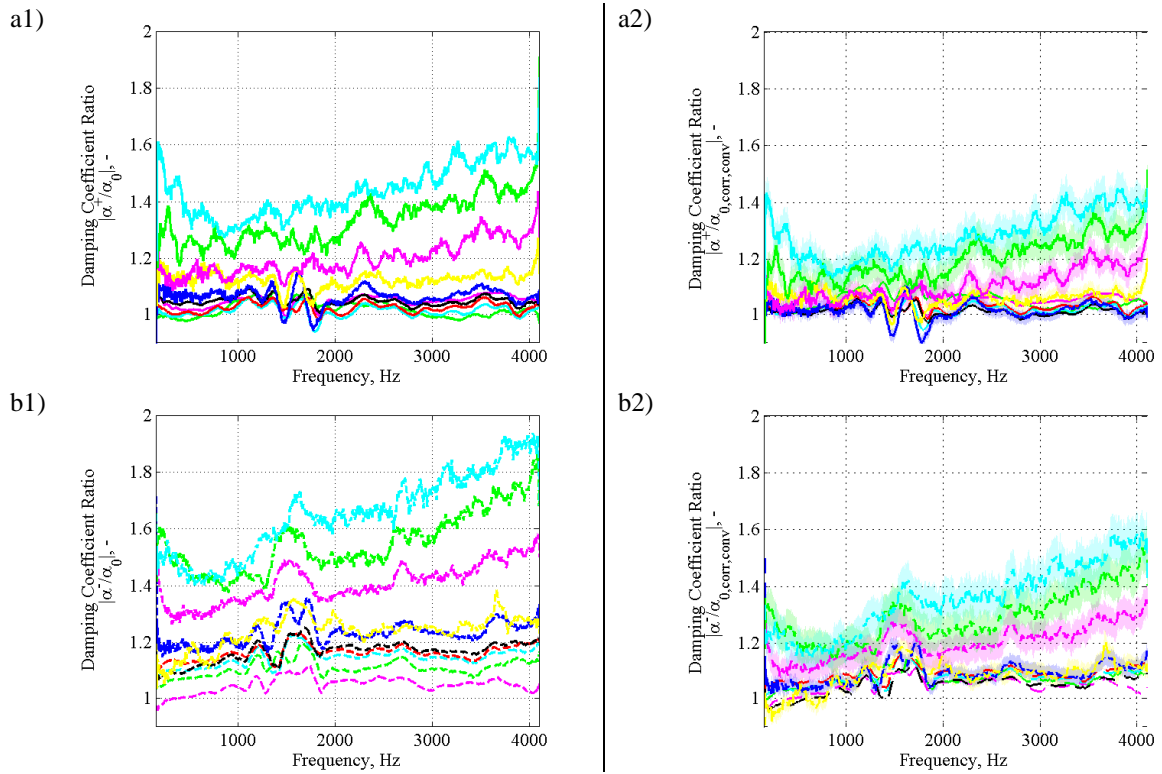


Figure 4.28. Mean gas flow and liquid: $U_{SG} \sim 5.5$ m/s. Damping coefficient ratio [-] as function of frequency [Hz] without corrections in direction (a1, solid lines) and against flow (b1, dashed lines). Damping coefficient ratio [-] as function of frequency [Hz] including the effects of convection and the hydraulic diameter (a2-b2). Additionally, the uncertainty margin is provided (a2-b2) by using the hold-up values $\beta_L \pm$ the standard deviation σ (see Section 4.3.2). The legend is the same as in Figure 4.27.

Mean gas flow and liquid: $U_{SG} \sim 10.5$ m/s

The results at the constant superficial gas velocity equal to 10.5 m/s are discussed in this section. The damping measured at different superficial liquid velocity is provided in Figure 4.29, in direction of the flow (a) and against flow (b). As already discussed for the other fixed superficial gas velocities, the acoustical damping is increasing as soon as water is present in the system.

It is interesting to observe how in the direction of the flow the acoustical damping at high frequencies and at the highest liquid velocity (cyan line) is about the 70-75% higher than the damping with only mean flow.

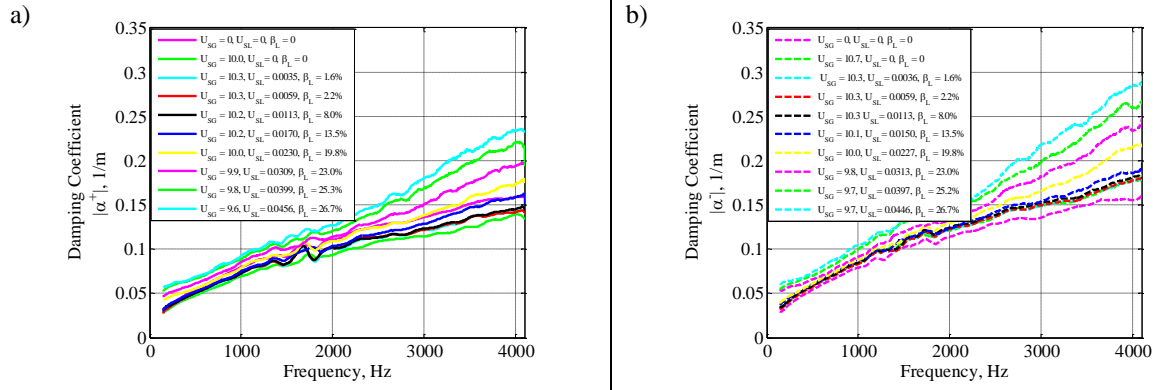


Figure 4.29. Gas and liquid mean flow: $U_{SG} \sim 10.5$ m/s: acoustical damping measured in the direction of (a) and against flow (b) at a superficial gas velocity $U_{SG} \sim 10.5$ m/s. As a reference, the damping measured without (magenta) and with (green) flow is provided.

Figure 4.30 shows the ratio of the measured acoustical damping to the Kirchhoff, corrected with the hydraulic diameter and the convection effects (a2 and b2) and not corrected (a1 and b1).

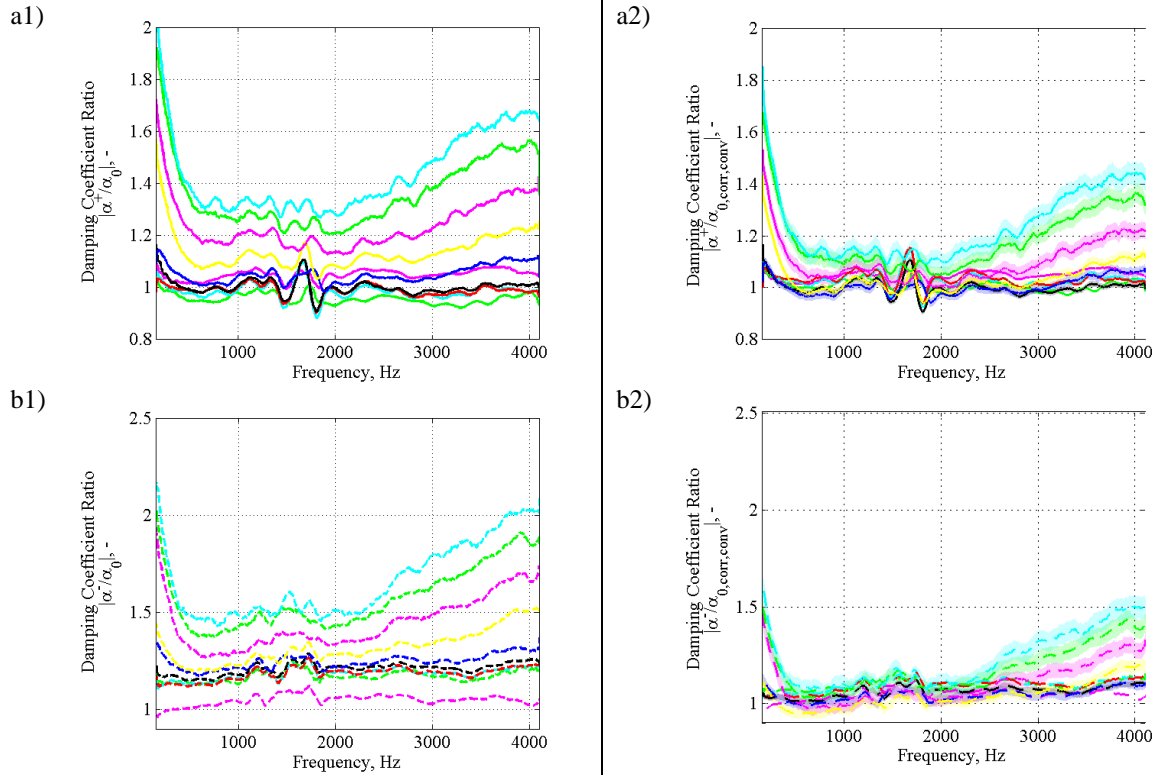


Figure 4.30. Mean gas flow and liquid: $U_{SG} \sim 10.5$ m/s. Damping coefficient ratio [-] as function of frequency [Hz] without corrections in direction (a1, solid lines) and against flow (b1, dashed lines). Damping coefficient ratio [-] as function of frequency [Hz] including the effects of convection and the hydraulic diameter (a2-b2). Additionally, the uncertainty margin is provided (a2-b2) by using the hold-up values $\beta_L \pm$ the standard deviation σ (see Section 4.3.2). The legend is the same as in Figure 4.29.

Considering only the case of acoustical damping not corrected (Figure 4.30a1-b1), three frequency ranges can be distinguished: a low frequency range between 150 Hz and about 600 Hz, middle frequency range between 600 Hz and 2000 Hz, and a high frequency range between 2000 Hz and 4100 Hz. In particular, as the amount of water increases, the trend of the ratio as function of the frequency is different. The ratio decreases at low frequency, it is constant in the middle range, and it increases at high frequency.

In the middle range frequency the ratio is constant and Figure 4.30a2-b2 prove that the correction of the convection and the hydraulic diameter can increase the damping. Indeed, in this range, by correcting the

Kirchhoff damping α_0 (see Eq. (4.4)), all the curves collapse in a 5% error band around the no flow condition curve (magenta lines).

As already said, the higher the gas velocity, the stronger the effects of turbulence. This is when there is only gas. In presence of water, it was added that if the different friction velocity at the interface had considered, it would have implied a much higher ratio of the acoustical boundary layer to the viscous sublayer.

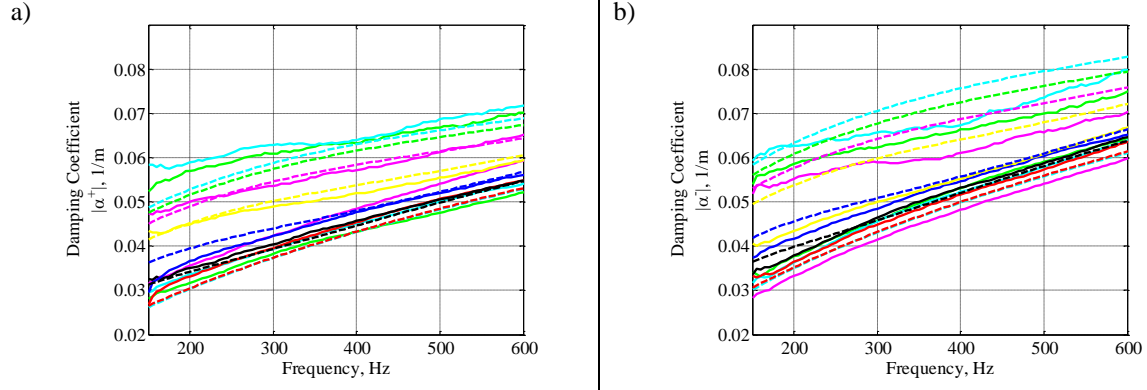


Figure 4.31. Mean gas flow and liquid: $U_{SG} \sim 10.5$ m/s. Comparison between the measured acoustical damping (solid lines) and the estimated with Sanna's hybrid model (dashed lines), in the direction of (a) and against (b) flow. The legend is the same as in Figure 4.29.

To take into consideration this reasoning, at low frequencies, Figure 4.31 shows the comparison of the damping measured (solid lines) in the direction of the flow (a) and against flow (b) with the damping estimated with the hybrid model (dashed lines) proposed in Section 4.2.

Figure 4.31 shows that the model proposed as the combination of a multiphase flow model for stratified (wavy) flow and the acoustical model of Howe is able to well capture the turbulence effects at low frequencies in presence of an air/water mixture.

Concerning the high frequencies, as well as for the superficial gas velocity ~ 5.5 m/s, the reasons why damping increases remain unexplained. Nevertheless, this growth seems to be related to the gas velocity, i.e. to the flow pattern.

4.5. Conclusions

The acoustical damping has been measured for a water/air flow passing with a stratified flow pattern in a smooth horizontal pipe.

By means of the two-microphone method, the acoustical damping is reconstructed for a 2 m smooth horizontal pipe where a gas mean flow is grazing at a constant velocity in the pipe together with water at different liquid velocities. The results have been compared with the dry case scenario, with and without mean flow, and with a test set with different amounts of quiescent water in absence of gas mean flow.

The presence of water leads to an increase of the acoustical damping both in direction of and against flow. It has been verified that the change of the hydraulic diameter due to the presence of water and the convection effects are the responsible of the increase. Moreover, at higher gas velocities, the effects of turbulence must be considered and can be well predicted by using a hybrid model which combines a multiphase flow model and the acoustical model of Howe. Nevertheless, more investigations are needed to explain why at high frequencies the acoustical damping increases.

References

- Åbom, M., and Bodén H., 1988, "Error analysis of two-microphone measurements in ducts with flow," *Journal of the Acoustical Society of America*, 83(6): 2429-2438.
- Ajello, G., 1997, "*Mesures acoustique dans les guides d'ondes en présence d'écoulement : Mise au point d'un banc de mesure applications à discontinuités*," Ph.D. Thesis, Université du Maine, Le Mans, France.
- Allam, S., and Åbom M., 2006, "Investigation of damping and radiation using full plane wave decomposition in ducts," *Journal of Sound and Vibration*, 292(3-5): 519-534.
- An, Z., Ningde J., Lusheng Z., and Zongke G., 2014, "Liquid holdup measurement in horizontal oil-water two-phase flow by using concave capacitance sensor," *Measurement*, 49: 153-163.
- Andritsos, N., and Hanratty T.J., 1987a, "Influence of interfacial waves in stratified gas-liquid flow," *AIChE Journal*, 33(3): 444-454.
- Andritsos, N., and Hanratty T.J., 1987b, "Interfacial instabilities for horizontal gas-liquid flows in pipelines," *International Journal of Multiphase Flow*, 13(5): 583-603.
- Andritsos, N., 1992, "Statistical analysis of waves in horizontal stratified gas-liquid flow," *International Journal of Multiphase Flow*, 18(3): 465-473.
- Belfroid, S.P.C., Golliard J., and Vijlbrief O., 2013, "Singing mitigation in corrugated tubes with liquid injection," *ASME Pressure Vessels & Piping Conference*, Paris, France.
- Bigonha Tibiriçá, C., Nascimento J.F. do, and Ribatski G., 2010, "Film thickness measurement techniques applied to micro-scale two phase flow systems," *Experimental Thermal and Fluid Science*, 34(4): 463-473.
- Bo An Lee, Byong Jo Yun, and Kyung Youn Kim, 2011, "Estimation of local liquid Film Thickness in Two Phase Annular Flow," *Nuclear Engineering and Technology*, 44(1): 71-78.
- Bodén, H. and Åbom M., 1986, "Influence of errors on the two-microphone method for measuring acoustic properties in ducts," *Journal of the Acoustical Society of America*, 79(2): 541-549.
- Bronkhorst, URL: <http://www.bronkhorst.com/> .
- Canière, H., T'Joel C., Willockx A., De Paepe M, Christians M., Rooyen E. van, Liebenberg L., and Meyer J.P., 2007, "Horizontal two-phase flow characterization for small diameter tubes with a capacitance sensor," *Measurement Science and Technology*, 18(9): 2898-2906.
- Chen, T., Cai X.D., and Brill J.P., 1997, "Gas-liquid stratified-wavy flow in horizontal pipelines," *Journal of Energy Resources Technology*, 119(4): 209-216.
- Chu, W.T., 1986, "Extension of the two-microphone transfer function method for impedance tube measurements," *Journal of the Acoustical Society of America*, 80(1): 347-348.
- Chung, J.Y., and Blaser D.A., 1980a, "Transfer function method of measuring in-duct acoustic properties. I: theory," *Journal of Acoustical Society of America*, 68(3): 907-913.
- Chung, J.Y., and Blaser D.A., 1980b, "Transfer function method of measuring in-duct acoustic properties. II: experiment," *Journal of Acoustical Society of America*, 68(3): 914-921.

De Kerpel, K., and De Paepe M., 2012, "Void Fraction Measurements of refrigerant flow in small diameter tubes using a capacitive sensor," *9th International Conference on Heat Transfer, Fluid Mechanics and Thermodynamics*, Malta.

Davies, P.O.A.L., 1988, "Practical flow duct acoustics," *Journal of Sound and Vibration*, 124(1): 91-115.

Dokumaci, E., 1995, "Sound Transmission in narrow pipes with superimposed uniform mean flow and acoustic modelling of automobile catalytic converters," *Journal of Sound and Vibration*, 182(5): 799-808.

Dokumaci, E., 1998, "On transmission of sound in circular and rectangular narrow pipes with superimposed mean flow," *Journal of Sound and Vibration*, 210(3): 375-389.

Geraets, J.J.M., and Borst J.C., 1988, "A capacitance sensor for two-phase void fraction measurement and flow pattern identification," *International Journal of Multiphase Flow*, 14(3): 305-320.

Golliard, J., Belfroid S.P.C., and Vijlbrief O., 2013, "Acoustic damping in smooth and corrugated pipes with and without liquid injection," *ASME Pressure Vessels & Piping Conference*, Paris, France.

Golliard, J., Belfroid S.P.C., Vijlbrief O., and Lunde K., 2015, "Direct Measurements of acoustic damping and sound amplification in corrugated pipes with flow," *ASME Pressure Vessels & Piping Conference*, Boston, Massachusetts, USA.

Grolman, E., and Fortuin J.M.H., 1997, "Gas-liquid flow in slightly inclined pipes," *Chemical Engineering Science*, 52(24): 4461-4471.

Hart, J., Hamersma P.J., and Fortuin J.M.H., 1989, "Correlations predicting frictional pressure drop and liquid holdup during horizontal gas-liquid pipe flow with a small liquid holdup," *International Journal Multiphase Flow*, 15(6): 947-964.

Hirschberg, A., 1997, "Self-sustained aeroacoustical oscillations in gas transport systems: a prediction method for pulsations induced by closed pipe segments," *Technical Report R-1428-D*, Technische Universiteit Eindhoven.

Holmberg, A., Åbom M., and Bodén H., 2011, "Accurate experimental two-port analysis of flow generated sound," *Journal of Sound and Vibration*, 330(26): 6336-6354.

Howe, M.S., 1995, "The damping of sound by wall turbulent shear layers," *Journal of Acoustical Society of America*, 98(3): 1723-1730.

JBL, URL: <http://www.jbl.com/> .

Kirchhoff, G., 1868, "Über den Einfluss der Wärmeleitung in einem Gase auf die Schallbewegung," *Pogg. Ann.*, 134(6): 177-193.

Ingard, U., and Singhal V.K., 1974, "Sound attenuation in turbulent pipe flow," *Journal of Acoustical Society of America*, 55(3): 535-538.

Lin, P.Y., and Hanratty T.J., 1986, "Prediction of the initiation of slugs with linear stability theory," *International Journal of Multiphase Flow*, 12(1): 79-98.

Morse, P.M., and Ingard K.U., 1968, "*Theoretical acoustics*," McGraw-Hill book company.

Munjal, M.L., and Doige A.G., 1990, "The two-microphone method incorporating the effects of mean flow and acoustic damping," *Journal of Sound and Vibration*, 137(1): 135-138.

Munt, R.M., 1990, "Acoustic transmission properties of a jet pipe with subsonic jet flow, I: the cold jet reflection coefficient," *Journal of Sound and Vibration*, 142(3): 413-436.

OLGA, 2015, URL: <http://www.software.slb.com/products/foundation/Pages/olga.aspx> .

Oliemans, R.V.A., 2008, "*Applied Multiphase flows*," Lecture Notes.

PCB, URL: www.pcb.com .

Panicker, V.B., and Munjal M.L., 1981, "Impedance tube technology for flow acoustics," *Journal of Sound and Vibration*, 77(4): 573-577.

Peters, M.C.A.M., Hirschberg A., Reijnen A.J., and Wijnands A.P.J., 1993, "Damping and reflection coefficient measurements for an open pipe at low Mach and low Helmholtz numbers," *Journal of Fluid Mechanics*, 256: 499-534.

Pierce, A., 1989, "*Acoustics – An introduction to its Physical Principles and Applications*," Mc Graw-Hill, New York.

Ronneberger, D., and Ahrens C.D., 1977, "Wall shear stress caused by small amplitude perturbations of turbulent boundary-layer flow: an experimental investigation," *Journal of Fluid Mechanics*, 83(3): 433-464.

Sanna, F., and Golliard J., 2014a, "Effect of water-droplets on flow-induced pulsations in pipe with two closed side branches: an experimental study," *20th AIAA/CEAS Aeroacoustics Conference*, Atlanta, Georgia, USA.

Sanna, F., and Golliard J., 2014b, "Flow-Induced Pulsations in Closed side branches with wet gas," *ASME Pressure Vessels & Piping Conference*, Anaheim, California, USA.

Sanna, F., Golliard J., and Belfroid S.P.C., 2015, "On the effect of water film on Flow-Induced Pulsations in closed side branches in tandem configuration," *ASME Pressure Vessels & Piping Conference*, Boston, Massachusetts, USA.

Seybert, A.F., and Ross D.F., 1977, "Experimental investigation of acoustic properties using a two-microphone random-excitation technique," *Journal of Acoustic Society of America*, 61(5): 1362-1370.

Seybert, A.F., and Soenarko B., 1981, "Error analysis of spectral estimates with application to the measurement of acoustic parameters using random sound fields in ducts," *Journal of Acoustical Society of America*, 69(4): 1190-1199.

Shoham, O., 2006, "*Mechanistic modeling of Gas-Liquid Two-Phase Flow in Pipes*," Society of Petroleum Engineers.

SWR ISO 10534-1, Acoustics-Determination of Sound Absorbing Coefficient and Impedance in Impedance Tubes, Part I: Method Using Standing Wave Ratio, 1996.

Taitel, Y., and Ducker A.E., 1976a, "A model for predicting flow regime transitions in horizontal and nearly horizontal gas-liquid flow," *AIChE Journal*, 22: 47-55.

Taitel, Y., and Ducker A.E., 1976b, "A theoretical approach to the Lockhart-Martinelli correlation for stratified flow," *International Journal of Multiphase Flow*, 2(5-6): 591-595.

TMM ISO 10534-2, Acoustics-Determination of Sound Absorbing Coefficient and Impedance in Impedance Tubes, Part II: Transfer-Function method, 1998.

To, C.W.S., and Doige A.G., 1980, "The application of a transient testing method to the determination of acoustic properties of unknown systems," *Journal of Sound and Vibration*, 71(4): 545-554.

Tonon, D., Hirschberg A., Golliard J., and Ziada S., 2011, "Aeroacoustics of pipe systems with closed branches," *International Journal of Aeroacoustics*, 10(2-3): 201-276.

Tzotzi, C., and Andritsos N., 2013, "Interfacial shear stress in wavy stratified gas-liquid flow in horizontal pipes," *International Journal of Multiphase Flow*, 54: 43-54.

Tzotzi, C., Bontozoglu V., Vlachogiannis M., and Andritsos N., 2011, "Effect of fluid properties on flow patterns in two-phase gas-liquid flow in horizontal and downward pipes," *Industrial and Engineering Chemistry Research*, 50(2): 645-655.

Vlachos, N.A., Paras S.V., and Karabela A.J., 1999, "Prediction of holdup, axial pressure gradient and wall shear stress in wavy stratified and stratified/atomization gas-liquid flow," *International Journal of Multiphase Flow*, 25(2): 365-376.

Chapter 5

Conclusions and Perspectives

Résumé

Les oscillations auto-induites ont des conséquences importantes dans beaucoup de domaines (usines de chimie ou de production d'électricité, transport de gaz, etc.). Dans les systèmes complexes de tuyauterie, pouvant avoir des résonances de forte amplitude, ces auto-oscillations peuvent entraîner des arrêts de production pour des raisons de sécurité. Même si de nombreux chercheurs ont travaillé pour expliquer les mécanismes à la base de ces pulsations, peu d'études se sont intéressées au cas où un mélange de gaz et de liquide est présent. L'objectif de cette thèse est donc d'étudier l'effet d'un mélange diphasique sur la production et la propagation d'auto-oscillations en conduits.

Après une première série d'expériences montrant une diminution de l'amplitude des oscillations quand le pourcentage de liquide augmente (Chapitre 2), deux hypothèses explicatives ont été proposées: l'interaction entre le liquide et la couche mélange instable et l'augmentation de l'amortissement acoustique dû à la présence d'eau. En ce qui concerne la première hypothèse, on a pu confirmer que si un film d'eau interagissait avec la couche mélange, on observerait une décroissance du 60 % des amplitudes des pulsations auto-induites (Chapitre 3). Ce phénomène ne suffisant pas à expliquer toutes les réductions observées, la seconde hypothèse a été étudiée au Chapitre 4 où l'amortissement a été mesuré dans une conduite horizontale en présence d'eau. L'analyse des résultats expérimentaux montre que les principaux paramètres influant sur l'amortissement acoustique sont les effets de convection, le changement du diamètre hydraulique (une partie de la surface du conduit est occupée par l'eau) et la turbulence. Un nouveau modèle combinant les effets diphasiques et les effets de la turbulence, prenant en compte le frottement à la surface entre l'eau et l'air, a été proposé pour expliquer l'augmentation de l'amortissement due à la turbulence en présence de liquide.

L'amortissement acoustique en conduit rigide étudié au Chapitre 4 n'est toutefois pas capable d'expliquer à lui seul les diminutions d'amplitude observées. D'autres hypothèses devront donc être explorées par la suite comme un possible couplage avec des vibrations du conduit.

Flow Induced Pulsations (FIPs), if experienced, may lead to severe consequences in several engineering fields (steam lines, gas turbines, gas transport systems, etc.). Concerning gas transport systems, safety first can be affected, followed by the interruption of plants' production.

The causes which generate this phenomenon have been extensively investigated with only gas and, up to now, only a few studies about the effects of multiphase flows on acoustics are available. Thus, this work took shape as an exploratory research.

First, as a follow-up of the experiments of Omrani et al. (2012), the effects of liquid on the acoustics of two well-known configurations have been compared (Chapter 2). The only difference between these two configurations lays on the distance between the two side branches: equal the double of the side branch length for the tandem, and almost equal to zero for the quasi cross configuration. By looking at the response of the pulsations in the two configurations while changing the liquid volumetric flow rate, four main features have been observed:

- In presence of annular flow, the interference between liquid and the shear layer induces a decrease of the pulsations amplitude. This also confirmed the observations of Omrani et al. (2012).
- For stratified wavy flow patterns, water increases the acoustical damping in the middle “wet” section between the side branches. The reduction of pulsations has not been observed only for the quasi-cross configuration, where the distance between the two branches is very small;
- The flow profile in the pipe is modified by the presence of water at the walls, which enhances the turbulence in the pipe. This modifies the stability of the shear layers, and therefore their coupling with the acoustic field;
- When water accumulates at the T-junction, the effective geometry of the connections can be modified, which modifies the singing behavior;

Regarding the interference between liquid and the shear layer, other measurements always in a tandem configuration were dedicated to observe the sole effect of the liquid film on the source strength (Chapter 3). With the help of visual observations, it was confirmed that a large drop in pulsations amplitudes occurs if water is convected with the shear layer. In addition, in spite of changing the method and the position of the water injection, overall the same decrease in amplitude has been observed. This gave indication that the extra damping due to the presence of water in the middle section was still actively playing an important role. In a 1D acoustical model built for this research, the extra damping was imposed only in the middle section to force the acoustical system to respond as in the experimental measurements. This led to further experimentally investigate the increase of the acoustical damping due to the presence of water.

In Chapter 4, the goal was to evaluate experimentally the attenuation of acoustic waves in the ducts when they contain a mixture flow of air and water. The tests were mainly performed with stratified flow, as this was also the flow regime present as a common factor during the flow-induced tests of Chapter 3. From these tests, to evaluate the effects of a mixture of water/air, damping in dry gas, provided the following corrections are done:

- The visco-thermal losses should be computed using an effective diameter of the pipe, which is the hydrodynamic diameter of the section where air is present (since part of the pipe is filled with water);
- The convection term of the attenuation with flow should be computed using the actual air velocity, which is higher than the superficial velocity since part of the pipe section is blocked by the water;

- The losses due to turbulence can be evaluated replacing the wall friction by the interfacial friction for the wetted area. The interfacial friction can be significantly larger, particularly when small wavelets are present on the water surface.

In Chapter 4 the acoustical damping has been measured up to a gas velocity around 10.5 m/s. From those results, the acoustical damping at ~15 m/s does not match the damping values estimated in Chapter 3 with the 1D model. The hybrid model used in Chapter 4 to evaluate the turbulence effects does not provide such high values damping. There is a difference of almost of one order of magnitude between the damping measured in Chapter 4 and the damping needed to explain the amplitude decrease in Chapter 3.

Some remarks can be made to try to explain this difference. First, in Chapter 3 the acoustical damping is shown as function of the ratio of the volumetric flow rates but important information like the effective area of the pipe or the type of flow patten are not known. A more advised way would be to plot everything as function of the hold up. However, hold-up measurements were not available for the experiments discussed in Chapter 3 and for the experiments of Golliard et al (2013). In addition, at low frequency (in the experiments of Chapter 3 the resonant frequency was about 320 Hz), turbulence is the factor leading the increase of the acoustical damping. Nevertheless, this is still not enough to lead to such a high increase, as the hybrid model confirms. Moreover, in the 1D model used to estimate the acoustical damping, the source at the T-junction was imposed to be always the same. This was assumed because the decrease for the three cases discussed in Chapter 3 was overall the same, even if the location and the distance of the injector were changed. Although it is not fully certain that the source would not be modified, this should not be the reason. It is known that the source strength is related to the square of the velocity. If the actual velocity (instead of the superficial) were used, the increase on the source and in the pressure amplitude would be much greater than the increase of the acoustical damping, and the measured decrease in pressure would not be explained. Finally, the most probable factor which could lead to an increase of the damping is the coupling between the acoustical and the mechanical damping. Unfortunately, no investigations have been conducted on that. Nevertheless, it can be seen in Figure 4.20 that the bump in attenuation around 1500 Hz attributed to vibrations of the tube increases significantly with the amount of liquid. Even if it is not a rigorous proof (the vibrations of the tube has not been measured), it is an indication that the vibrations can lead to a very high damping of acoustic waves.

As already said, the work for this Ph.D. thesis is an exploratory research. Further investigations are therefore needed.

Regarding the open questions at the end of this Ph.D., it is suggested to repeat the experiment with two side branches in tandem. The resonator should be designed in such a way that the resonant frequency is out of the range of frequency where turbulence effects are expected to be dominant. Moreover, the setup should be properly fully clamped. The tested gas velocities should be the ones used in Chapter 4 (~ 2.5 m/s, 5.5 m/s, and 10.5 m/s). Moreover, it is indispensable to monitor the hold-up for each experiment.

Concerning the interaction between the liquid film and the shear layer, it would be interesting to:

- Analyze how the droplets interact with the vortex. From visualizations, droplets could be seen at the T-junctions but no information on the size, velocity or the direction was available.
- Repeat the experiments with the double side branch and accurately clamp the whole setup
- Repeat the experiments for the quasi cross configuration
- Relate the turbulence generated by the liquid film and the vortex at the T-junction

Regarding the acoustical damping, repeating the experiments for the same diameter but with fully annular flow and comparing the effect of the effective diameter is essential to extend the analysis to other cases. Moreover, it would be important to evaluate the effect of different sizes of the droplets at the wall both to investigate their effect and quantify the effect of the size. In addition, it is still unclear how several multiphase flow parameters relate to the damping. Accurately monitoring the height of waves or their frequency would definitely add some information on the evaluation of the current study. It would be also interesting to have more understanding on why the acoustical damping increases at high frequency for stratified (wavy) flow patterns and in particular evaluate the relation between the properties of bubbles in water and the acoustical damping. Moreover, from the analysis of the experimental results, it has been assumed that sound is only propagating in air. Theory and analytical methods should confirm this hypothesis.

In view of practical applications, it seems also interesting to investigate the coupling between the acoustical damping and the vibrational behavior of the tube with a mixture of air and water. But this vibro-aero-acoustical study in two phases flow is another story...

References

- Golliard, J., Belfroid S.P.C., and Vijlbrief O., 2013, "Acoustic damping in smooth and corrugated pipes with and without liquid injection," *ASME Pressure Vessels & Piping Conference*, Paris, France.
- Shoeibi Omrani, P., Golliard J., Belfroid S.P.C., and González Díez N., 2012, "On the effects of droplets modulating the acoustic source powers generated in T-joints," *10th International Conference on Flow-Induced Vibration*, Dublin, Ireland.

Appendix A

Evaluation and calibration of capacitance probes for hold-up estimation: a comparison between different methods for a stratified (wavy) air-water mixture

Abstract

Among the available techniques to detect the liquid void fraction (or hold-up) of a multiphase flow mixture, capacitance probes are considered here since they are not intrusive. This makes them suitable to be used during the measurements on the acoustical damping in presence of a mixture air/water in a stratified pattern. In this appendix, the working principle, calibration and the use of the probes are discussed. The hold-up measured with the probes will be also compared with flow visualizations and numerical simulations.

A.1. Capacitance probes

A.1.1. Literature review

For a mixture of water and air, the distribution of each phase along the cross sectional area depends on the combination of the superficial liquid and gas velocities, the surface tension, on the properties (geometry and roughness) of the pipe, and on the angle. The ratio of the pipe cross-sectional area occupied by the liquid phase to the whole cross sectional area is called the liquid volume fraction or the liquid hold-up. For stratified and stratified wavy flow, gravity dominates and water remains at the bottom of the pipe, creating a layer of liquid.

There are different techniques to estimate the height of liquid (Bo an Lee et al., 2012):

- Acoustical techniques (Pedersen et al., 2000; Lu et al., 1993)
- Radiological techniques (Stahl et al., 2004; Saito et al., 2005)
- Electrical techniques (Coney, 1973; Fukano, 1998; Conte, 2003; Geraci et al., 2007)
- Optical techniques (Coney et al., 1989; Ursenbacher et al., 2004; Yu et al., 1996; Schubring et al., 2010).

Acoustic, radiological and optical techniques are normally very expensive and very complicated to implement. Only electrical techniques are therefore considered for our case. The most used types of electrical sensors are the conductance probes (double wire or wire mesh) which require a direct contact with the fluid inside the pipe and are thus intrusive by design. Because of this, they are not suitable during acoustical measurements. Overall, the only remaining alternative technique relies on capacitance probes in which two plate electrodes are mounted on the exterior of the pipe to form a capacitor. The capacitance of the plates depends on the dielectric constant of the medium. Since the dielectric constant of water is roughly eighty times higher than that of air, a change in hold-up can be detected as a change of capacitance between the electrodes. This type of probes has been extensively used in several studies (see for instance Geraets and Borst, 1988; Bigonha Tibiriçá et al., 2010; De Kerpel and De Paepe, 2012; Canière et al., 2007; An et al., 2014). A simple capacitance probe built at TNO has been used in this study.

A.1.2. Description of a capacitance probe

Each probe consists of two parallel copper plates (30x20 mm), glued outside the pipe (see Figure A.1). The pipe has an inner diameter of 25.0 mm and an outer diameter of 30.0 mm.

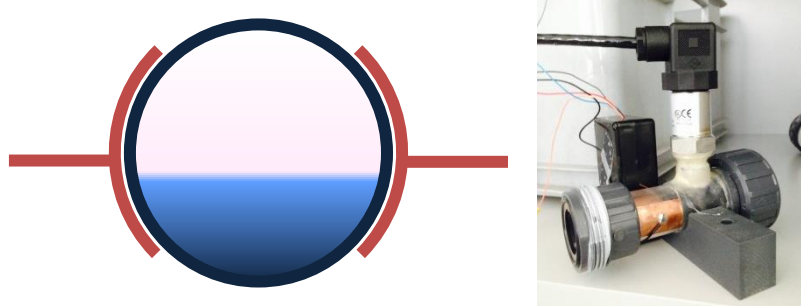


Figure A.1. Capacitance probes scheme (left) and real probe (right).

The capacitance probes rely on the difference in electric permeability of air and water. The dielectric permeability of air is nearly eighty times lower than for water. Capacitance is a property revealed only under a voltage transient (AC) provided by an external excitation. The capacitance probe amplifier used for these investigations are based on a “Twin-T” measurement circuit (see Figure A.2), which is similar to a Wheatstone bridge, but for capacitors. The advantage of this circuit in regard to other designs is the use of a grounded electrode. In addition, AC voltage source, low pass filter and buffer amplifier are used for signal conditioning.

In the next session both the geometrical properties and the calibration will be explained.

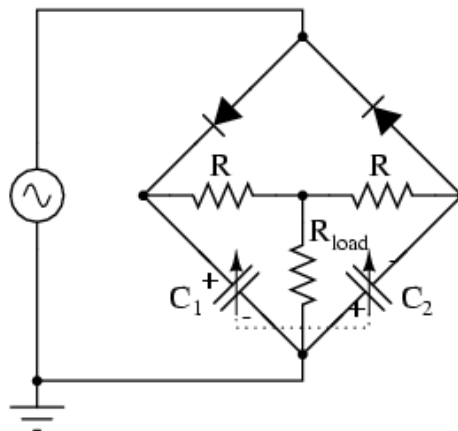


Figure A.2. “Twin-T” measurement circuit. The input is a high frequent AC signal, the connection to the sensor is replacing one of the two capacitors. The output is in the center of the diamond formed by the diodes and the capacitor in the schematic. The output signal is an AC signal which is biased depending on the capacitance of C_1 and C_2 , which needs to be low-pass filter to obtain a DC output signal.

A.1.3. Calibration of the probe without flow

As said in Section A.1.2, for each capacitance probe, two copper plates are glued on a piece of pipe. The calibration of each probe formally consists of associating a certain voltage recorded by the probe to a hold up value. To be able to precisely control the level of water, the piece where the probe is installed has been closed (see Figure A.3). For the final experiment, two capacitance probes have been used. The geometrical details of each capacitance probe used are provided in Table A.1. The hole shown in Figure A.3 is the one of the static pressure sensor (see Figure A.1).

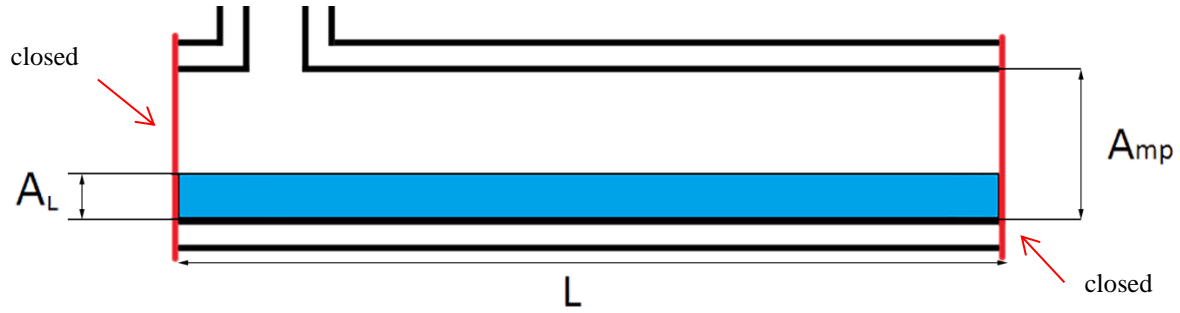


Figure A.3. Geometrical details of the capacitance probe.

Table A.1. Geometrical details of the capacitance probes.

	Upstream Capacitance Probes	Downstream capacitance probes
L [m]	119.96×10^{-3}	119.95×10^{-3}
D_{mp} [m]	24.98×10^{-3}	24.98×10^{-3}
A_{mp} [m ²]	4.90×10^{-4}	4.90×10^{-4}

Calibration procedure

For the calibration, a syringe and an accurate scale (for this case the Mettler AE200) are needed. The calibration procedure is as follows:

- 1) Weigh the empty syringe;
- 2) Fill the syringe with water and weigh again. The real amount of water is therefore the weight difference;
- 3) Pour a small amount of liquid into the capacitance probe via the hole shown in Figure A.3;
- 4) Record the voltage with the software DEWESoft 6.6.7 and report the average voltage during the time sample. The weight of water and the corresponding average voltage are reported in the calibration table;
- 5) Go back to point 3) and repeat until the capacitance probe tool is full, i.e. the volume of the circular duct is full of water.

To associate the voltage V measured to the corresponding amount of water in the pipe, the volume of liquid V_L in m³ is given by knowing the weight of the amount of water poured into the capacitance tool. The weight (mass) and the volume are indeed related by the water density, which is taken equal to 1000 kg/m³. The area occupied by water A_L can be therefore calculated dividing the volume V_L by the length of the probe L (Eq. (A.1)).

$$A_L = \frac{V_L}{L} \quad (\text{A.1})$$

According to the definition, the hold-up β_L is the ratio of the area occupied by liquid A_L to the full cross sectional area A_{mp} :

$$\beta_L = \frac{A_L}{A_{mp}} \quad (\text{A.2})$$

Reference hold-up estimate

The calibration procedure described in the preceding section has been repeated five times for each of the two probes. Figure A.4 shows the results of these 10 measurements sets, respectively 5 for the upstream and 5 for the downstream probe. In this figure, the voltage is plotted versus the weight of water. Figure A.5 shows the hold-up as function of the recorded voltage, using equations (A.1) and (A.2) and the geometrical details provided in Table A.1.

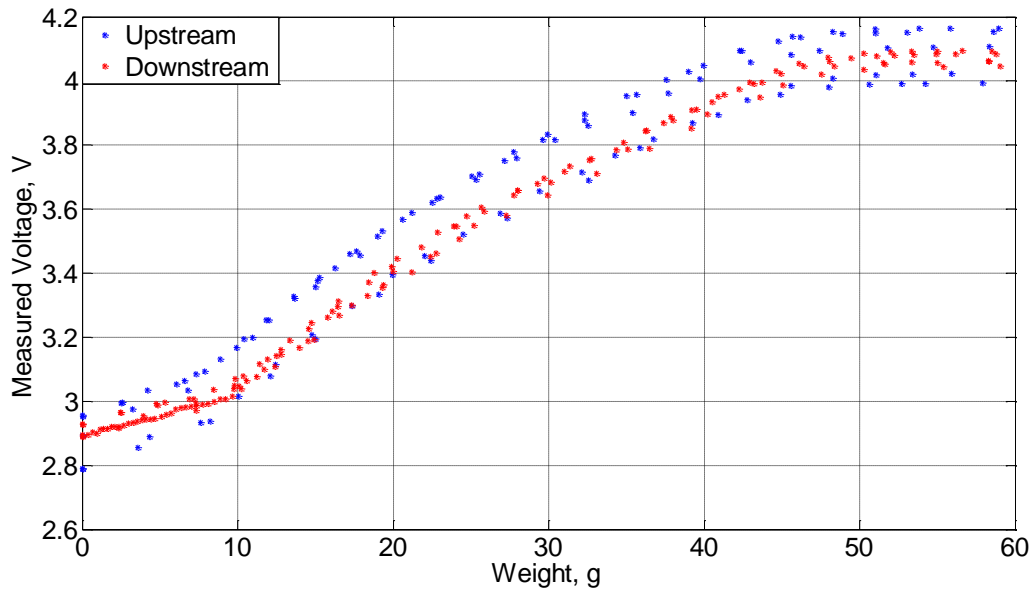


Figure A.4. Measured voltage [V] as function of the weight [g], for the upstream and downstream capacitance probes.

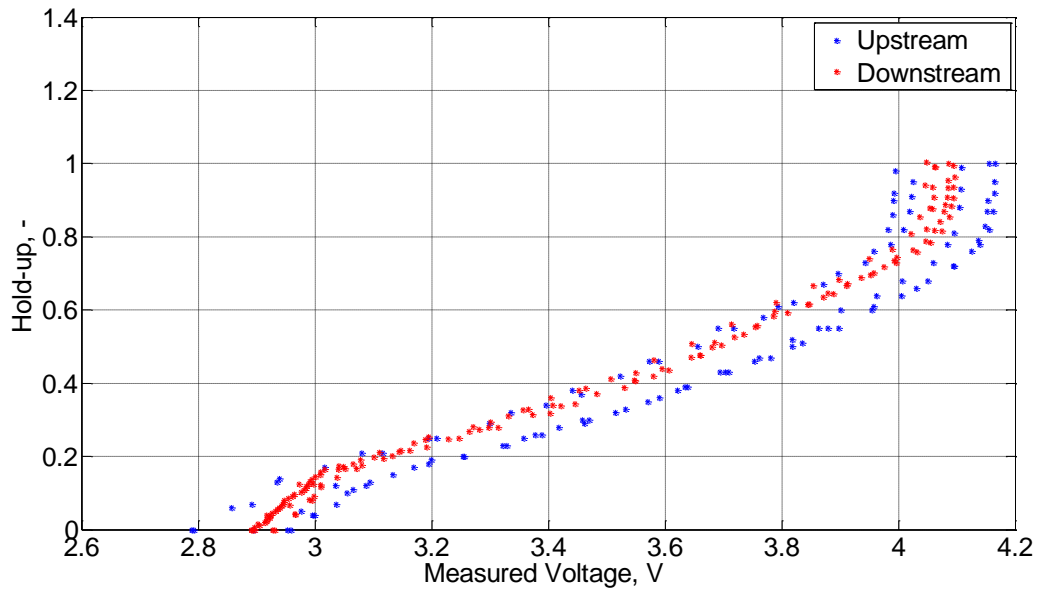


Figure A.5. Hold-up measurements [-] as function of the absolute measured voltage [V].

As seen in Figure A.5, some scattering of the points is observed. Further investigations showed that the voltage with an empty pipe is not constant. It seems that the curves are simply shifted by the voltage V_0 which corresponds to the hold-up $\beta_L = 0$. The cause of this shift is not known. This offset was accounted for using the calibration method described in the following.

Offset correction and calibration

In this approach, we assume that the calibration error done when V_0 changes results in an offset applied on the output voltage. Thus, the second approach is based on the analysis of the hold-up β_L as function of the difference of the voltage V measured with different liquid volumes to the voltage V_0 measured when the pipe is dry, (see Figure A.6 and Table A.2). Equation (A.3) shows the 6th order fitting polynomial used to approximate the hold-up function.

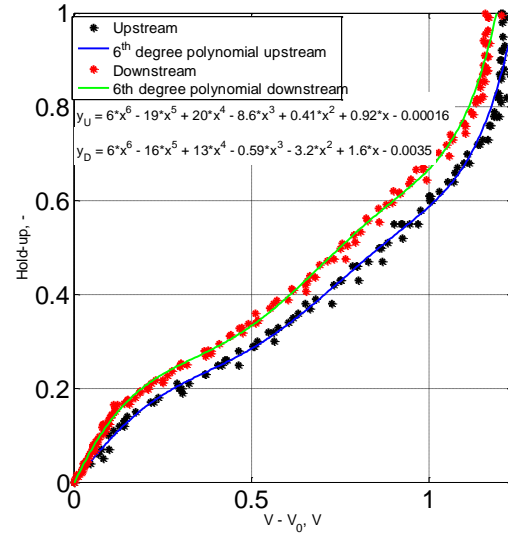


Figure A.6. Hold-up interpolation curves as function of the voltage difference $V-V_0$ [V].

$$\beta_L = a_6(V - V_0)^6 + a_5(V - V_0)^5 + a_4(V - V_0)^4 + a_3(V - V_0)^3 + a_2(V - V_0)^2 + a_1(V - V_0) + a_0 \quad (\text{A.3})$$

Table A.2. Coefficients values of the fitting polynomial for the hold-up as function of the difference $V-V_0$.

	a_6	a_5	a_4	a_3	a_2	a_1	a_0
Up, $V-V_0$	6.0416	-18.7052	20.4686	-8.5517	0.4113	0.9233	-0.0002
Down, $V-V_0$	5.9916	-15.9530	12.7764	-0.5913	-3.1740	1.6213	-0.0035

A.1.4. Use of the calibrated capacitance probe with flow

Here the procedure to estimate the hold-up when an air and water mixture is flowing in a pipe:

- 1) Measure before starting the measurement the voltage V_0 and verify that it is stable. Note that the pipe is dry. For the analysis reported in this document the mean value of the voltage as function of time is considered;
- 2) Start the flow. Once the flow is stabilized in the desired conditions, start the measurement of the voltage as function of the time $V=V(t)$. Estimate both the mean value V and the standard deviation of the output voltage. The latter relates to the fluctuations of the signal around its average, i.e. the height of the waves and possible slugs;
- 3) With the difference $V-V_0$, estimate the hold-up by means of the interpolation fitting curve (Eq. (A.3) and Table A.2).

A.2. Validation of the use of the capacitance probes for an experimental campaign

In this Section, the hold-up values obtained with the capacitance probes during an experimental campaign will be compared with the ones estimated by using flow visualizations and numerical simulations.

The inner diameter of the pipe is equal to 25.0 mm.

At three different and constant superficial gas velocities U_{SG} equal to around 2.5 m/s, 5.5 m/s, and 10.5 m/s, the superficial liquid velocity U_{SL} , was increased up to 0.045 m/s. According to visualizations recorded by means of high speed cameras the flow was in general either stratified or stratified wavy. Only at high injection rates and at $U_{SG} \sim 2.5$ m/s, slugs are passing in the system. Figure A.7 confirms that the flow for the region of our investigations can be either stratified or stratified wavy, tending to become sluggy at higher liquid velocities.

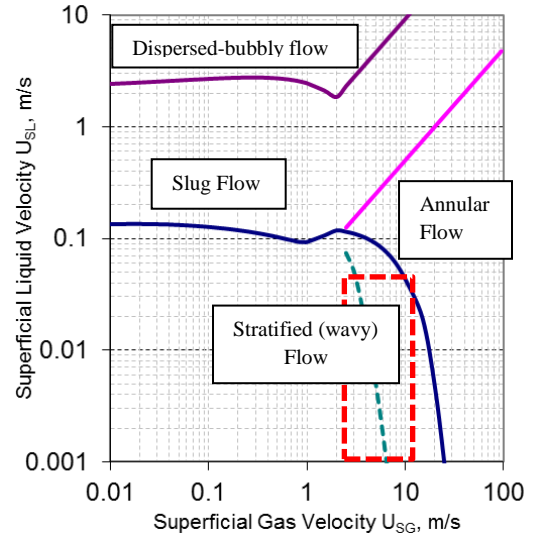


Figure A.7. Flow pattern map for a horizontal smooth horizontal pipe with an inner diameter equal to 0.025 m (Shoham, 2006). Experiments were conducted in the range of U_{SG} and U_{SL} highlighted by the red dashed rectangle.

A.2.1. Hold-up estimated by means of two capacitance probes

Two capacitance probes have been used to measure the liquid hold up, respectively one located upstream and one downstream the smooth pipe. The technical details of the capacitance probes are the same as the ones provided in Table A.1.

The procedure used to estimate the hold-up is based on the difference between the voltage measured with liquid flow and the voltage V_0 measured when the pipe is dry (see Figure A.6). Indeed, for the three constant gas velocities, the voltage V_0 has been recorded. Second, the voltage signal V when liquid is flowing with air within the system. From their difference, the hold-up β_L has been estimated (solid black lines in Figure A.8).

In addition, depending on the combination of gas and liquid velocities, the recorded voltage V was more perturbed because of waves. To take into account these oscillations and the consequent change in cross sectional area, the standard deviation σ is also provided (dashed black lines).

The red rectangle in Figure A.7 provides the full range of investigation, while the dashed green line represents the transition from stratified to stratified wavy flow. At higher gas velocities, the generation of waves occurs at a smaller liquid velocity. The same information is confirmed by Figure A.8. Indeed, positive standard deviation values are measured at lower liquid velocities for higher gas velocities.

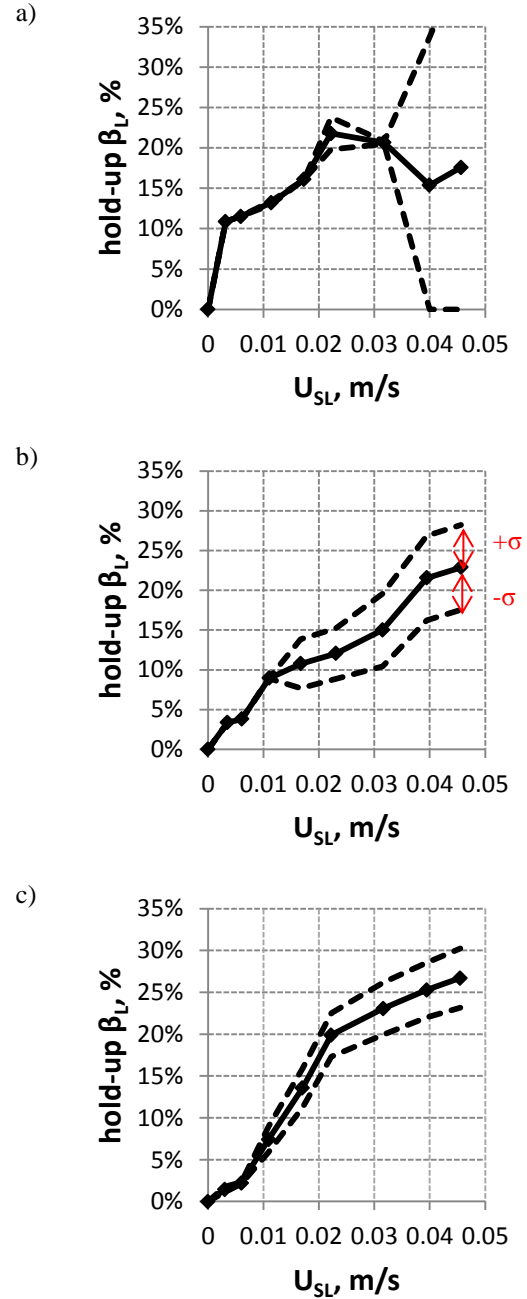


Figure A.8. Hold-up [%] estimated at $U_{SG} \sim 2.5$ m/s (a), $U_{SG} \sim 5.5$ m/s (b), $U_{SG} \sim 10.5$ m/s (c) by means of the capacitance probes: average value (-) and standard deviation $\pm\sigma$ (--).

A.2.2. Hold Up estimated by means of flow visualizations

Flow visualizations represent an alternative way to estimate the hold-up within a pipe. A camera (type dewe-cam-fw-70) has been used to record the flow behavior on the side of the setup. The distance of the camera from the pipe and the refraction from the wall of the pipe cause some distortion of the image. It is thus necessary to account for this distortion to measure the water height from the images captured by the camera. This can be done on theoretical basis, using the refraction properties of water, air and Perspex, the curvature of the pipe, the parallax of the camera lens, etc. A simpler alternative was chosen for the analysis presented below, based on application of graph paper on the pipe wall (see Figure A.9).

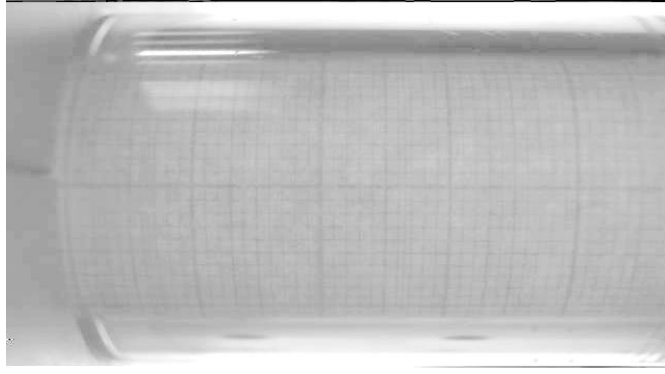


Figure A.9. Graph paper used to calibrate the optical distortion.

The graph paper has been applied in the pipe wall. The camera is located at exactly the same position relative to the tube as during the measurements. The steps to estimate the hold-up from camera visualizations are the following:

1) First, the lines which correspond to the outer diameter (red crosses on Figure A.10) and the points corresponding to the horizontal lines of the millimeter paper (blue crosses on Figure A.10) are pointed on the image. The vertical coordinates of these points are recorded and normalized between -1 and 1: $\widetilde{Y}_n = \frac{Y_n - Y_0}{|Y_{top} - Y_{bottom}|}$ with Y_{top} and Y_{bottom} the outer wall of the pipe, $Y_0 = \frac{Y_{top} + Y_{bottom}}{2}$ the position of the pipe axis and Y_n the positions of the 23 visible horizontal line on the millimeter paper ($n = -11, -10, \dots, 10, 11$, with corresponding positions on the circumference of the pipe: $x_n = -11 \text{ mm}, -10 \text{ mm}, \dots, 10 \text{ mm}, 11 \text{ mm}$). A least-square optimization is applied to fit a sine curve to these points: $\widetilde{Y}_n = \beta_1 \sin(\beta_2 x_n)$, with β_1 and β_2 the fit parameters. The fit parameters are $\beta_1 = 0.3921$ and $\beta_2 = 0.1009 \text{ mm}^{-1}$. The result of this fit is given in Figure A.11 and the positions of the fitted lines are also plotted as red lines in Figure A.10.

2) When analyzing a picture captured by the camera during the actual measurements, the inverse procedure is followed:

- Determine vertical coordinate of outer diameter of the pipe Y_{top} and Y_{bottom} ;
- Determine vertical coordinate of air-water interface Y_{int} ;
- Compute $\widetilde{Y}_{int} = \frac{Y_{int} - Y_0}{|Y_{top} - Y_{bottom}|}$;
- Compute projection of air-water interface on pipe circumference: $x_{int} = \frac{1}{\beta_2} \arcsin\left(\frac{\widetilde{Y}_{int}}{\beta_1}\right)$;
- Compute hold up β_L from position of interface: $\beta_L = \frac{1}{2\pi} [\theta - \sin(\theta)]$, where $\theta = \pi - \frac{2}{R} x_{int}$.

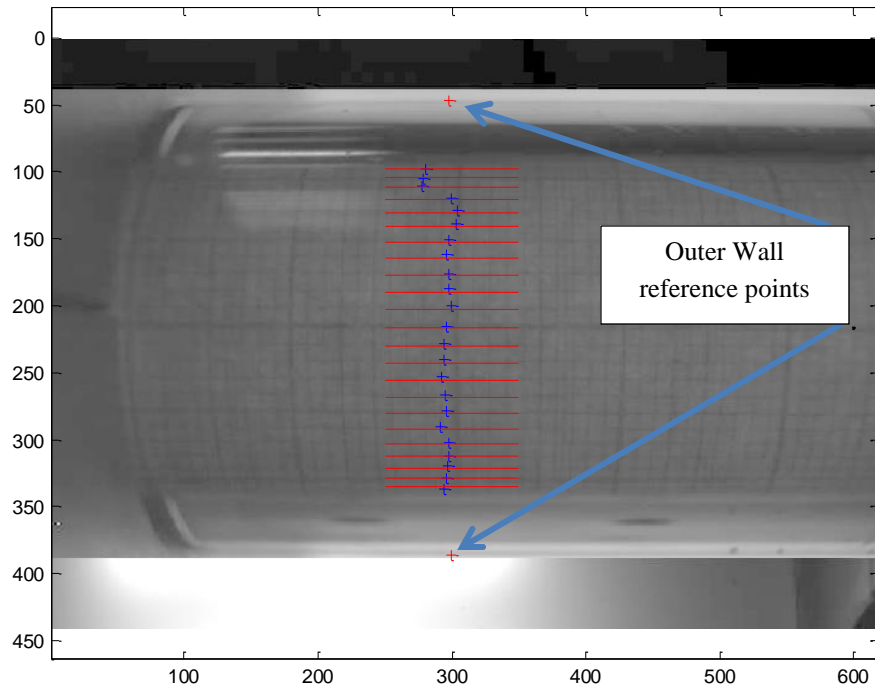


Figure A.10. Order the horizontal line with respect to the axis of the pipe.

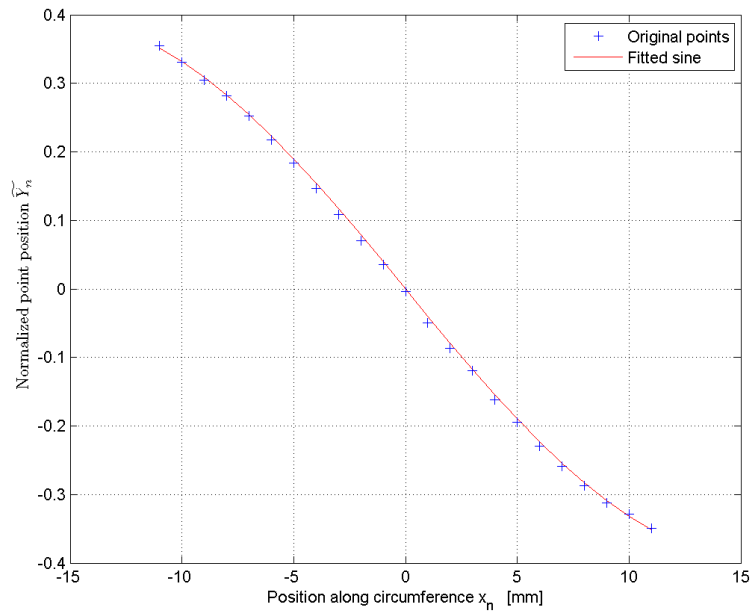


Figure A.11. Fitting curve expressing the location of the points.

Figure A.12 shows the images used to estimate the hold-up with the technique explained before. As expected from Figure A.7, when the superficial gas velocity U_{SG} is 2.5 m/s or 5.5 m/s, the flow is stratified, while it is stratified wave at $U_{SG} \sim 10.5$ m/s. In particular for the superficial gas velocity of 2.5 m/s, some figures are intentionally missing. It is impossible to make a decision on the hold-up values because the flow in these two cases is particularly sluggish.

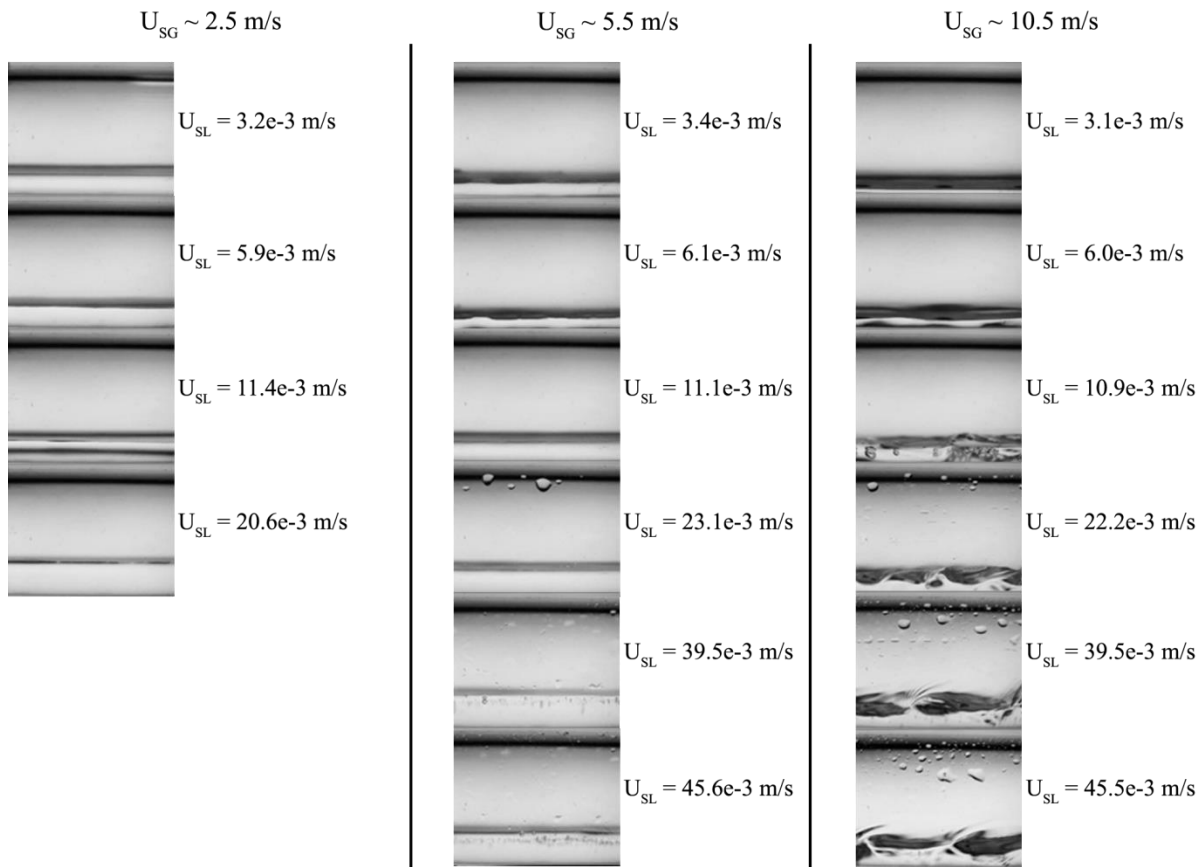


Figure A.12. Frames of the videos recorded during the measurements.

Figure A.13 shows the percentage hold-up values as function of the superficial liquid velocity. As already said, a few points are missing at high injection rates for the superficial gas velocity ~ 2.5 m/s. Also at low injection rates some points are missing for the other two gas velocities. The liquid height is indeed below the minimum detectable with the technique explained in this section.

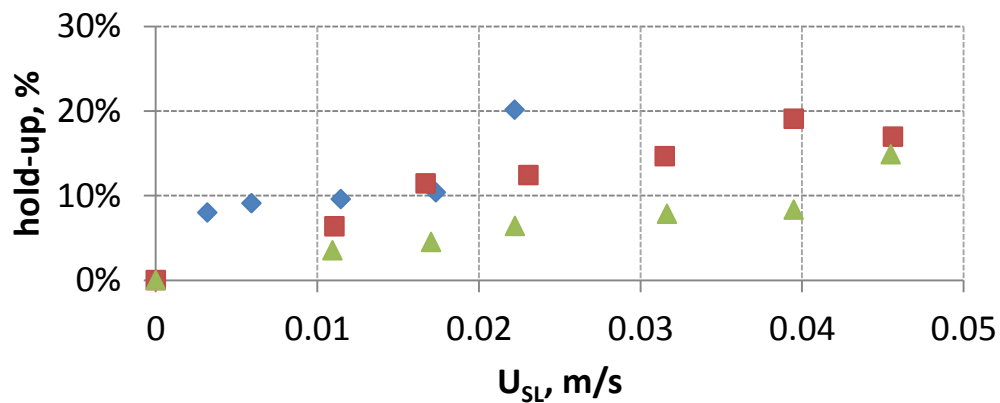


Figure A.13. Hold-up estimated by means of the visualizations. at three and constant gas velocities U_{SG} : ~ 2.5 m/s (blue diamonds), ~ 5.5 m/s (red squares), ~ 10.5 m/s (green triangles).

A.2.3. Hold Up estimated by means of OLGA simulations

OLGA 7.3.4 is a modelling tool for multiphase flows (OLGA). For our specific case, simulations were run for a 1 m smooth pipe whose inner diameter is equal to 0.025 m, at 1 bar. The two phases chosen are water and air. Table A.3 provides all the information of the input parameters used to run the simulations in 1 m long pipe.

Table A.3. Input parameters for OLGA simulations.

Pipe angle	Wall Roughness	Air density	Water density	Gas Viscosity	Liquid Viscosity	Surface Tension
0 rad	5.00e-6	1.2641	1000	1.80e-5	1.0e-4	0.073

Figure A.14 provides the hold-up values obtained by running OLGA simulations for three different constant gas velocities, while increasing the liquid velocity.

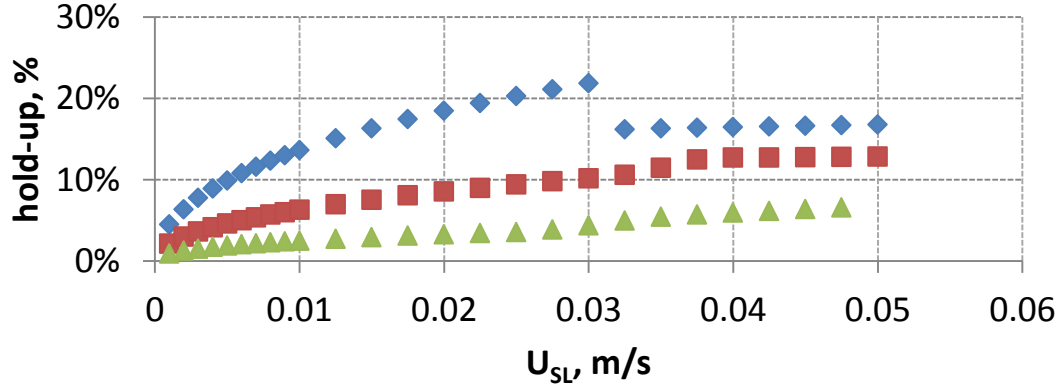


Figure A.14. Hold-up estimated by means of OLGA simulations at three and constant gas velocities U_{SG} : ~ 2.5 m/s (blue diamonds), ~ 5.5 m/s (red squares), ~ 10.5 m/s (green triangles).

A.2.4. Comparison and discussion

In this last section, a comparison between the different hold-up values is made. In Table A.4 the hold-up values estimated with different techniques are reported.

The same values are graphically shown in Figure A.15: (a) for $U_{SG} \sim 2.5$ m/s, (b) $U_{SG} \sim 5.5$ m/s, and (c) $U_{SG} \sim 10.5$ m/s. From the comparison of all the results obtained between the different techniques, a good agreement between the capacitance probes and the other methods have been observed at $U_{SG} \sim 2.5$ m/s and at $U_{SG} \sim 5.5$ m/s, while the results differ for $U_{SG} \sim 10.5$ m/s. The discrepancy for this last case is due to the presence of the big waves in the horizontal pipe. Especially for the visualization method, it was impossible to accurately determine precise hold-up values due to the high inconstant waves.

Table A.4. Hold-up estimates with different techniques.

Superficial Gas Velocity	Superficial Liquid Velocity	Capacitance probes Hold-up	Standard Deviation	OLGA hold-up	Visualizations hold-up
U_{SG}	U_{SL}	β_L	σ		
m/s	m/s	%	%	%	%
4.32	0	0	0	0	0
4.32	0.0032	10.8	-	7.8	6.7
4.32	0.0059	11.5	-	10.8	7.9
4.32	0.0115	13.2	0.23	14.4	8.7
4.32	0.0173	16.1	0.0005	16.9	10.0
4.32	0.0222	21.7	1.98	19.0	18.8
4.32	0.032	20.6	0.16	19.0	n.a.
4.32	0.040	15.4	18.3	16.4	n.a.
4.32	0.046	17.6	25.4	16.6	n.a.
5.50	0	0	0	0	0
5.50	0.0035	3.37	0.05	4.0	n.a.
5.50	0.0061	3.8	0.03	5.0	n.a.
5.50	0.011	8.9	0.05	6.3	6.4
5.50	0.017	10.7	3.09	7.8	11.4
5.50	0.023	12.0	3.18	9.0	12.4
5.50	0.032	15.0	4.57	10.4	14.7
5.50	0.040	21.5	5.32	12.6	19.1
5.50	0.046	22.9	5.33	12.8	16.9
10.39	0	0	0	0	0
10.40	0.0031	1.45	0.33	1.7	n.a.
10.39	0.0060	2.21	0.10	2.06	n.a.
10.39	0.011	7.4	1.53	2.6	3.5
10.39	0.017	13.6	2.33	3.1	4.5
10.39	0.022	19.9	2.61	3.5	6.4
10.39	0.032	23.1	3.13	4.4	7.8
10.39	0.039	25.3	3.27	6.0	8.3
10.39	0.046	26.7	3.53	6.4	14.9

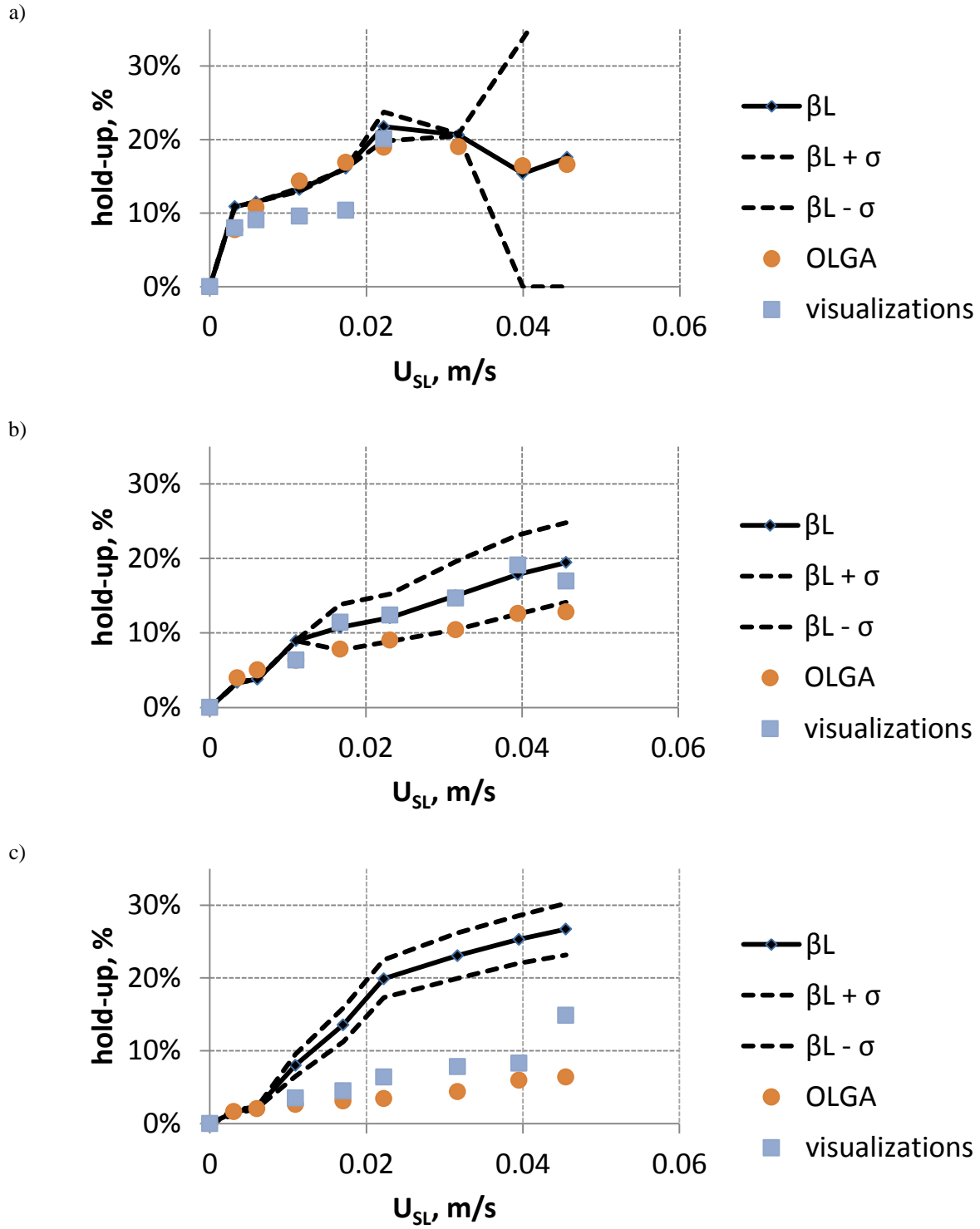


Figure A.15. Final comparison for the hold-up estimate with different techniques for the three different superficial gas velocities U_{SG} : ~ 2.5 m/s (a), ~ 5.5 m/s (b), and ~ 10.5 m/s (c).

References

- An, Z., Ningde J., Lusheng Z., and Zongke G., 2014, "Liquid holdup measurement in horizontal oil-water two-phase flow by using concave capacitance sensor," *Measurement*, 49: 153-163.
- Bigonha Tibiriçá, C., Nascimento J.F. do, and Ribatski G., 2010, "Film thickness measurement techniques applied to micro-scale two phase flow systems," *Experimental Thermal and Fluid Science*, 34(4): 463-473.

Bo An Lee, Byong Jo Yun, and Kyung Youn Kim, 2011, "Estimation of local liquid Film Thickness in Two Phase Annular Flow," *Nuclear Engineering and Technology*, 44(1): 71-78.

Canière, H., T'Joel C., Willockx A., De Paepe M., Christians M., Rooyen E. van, Liebenberg L., and Meyer J.P., 2007, "Horizontal two-phase flow characterization for small diameter tubes with a capacitance sensor," *Measurement Science Technology*, 18(9): 2898-2906.

Coney, M.W.E., 1973, "The Theory and Application of conductance Probes for the Measurement of Liquid Film Thickness in Two-Phase Flow," *Journal of Physics E: Scientific Instruments*, 6: 903-910.

Coney, J.E.R., El-Shafei E.A.M., and Sheppard C.G.W., 1989, "A Dual Laser Beam Method for Wavy Film Thickness Measurement," *Optics and Lasers in Engineering*, 11(1): 1-14.

Conte, G., 2003, "Film Thickness Variation about a T-junction," *International Journal of Multiphase Flow*, 29(2): 305-328.

De Kerpel, K., and De Paepe M., 2012, "Void Fraction Measurements of refrigerant flow in small diameter tubes using a capacitive sensor," *9th International Conference on Heat Transfer, Fluid Mechanics and Thermodynamics*, Malta.

Fukano, T., 1998, "Measurement of Time Varying Thickness of Liquid Film Flowing with High Speed Gas Flow by a Constant Electric Current Method," *Nuclear Engineering and Design*, 184(2-3): 363-377.

Geraci, G., Azzopardi B.J., and Maanen H.R.E. van, 2007, "Effect of Inclination on Circumferential Film Thickness Variation in Annular Gas/Liquid Flow," *Chemical Engineering Science*, 62(11): 3032-3042.

Geraets, J.J.M., and Borst J.C., 1988, "A capacitance sensor for two-phase void fraction measurement and flow pattern identification," *International Journal of Multiphase Flow*, 14(3): 305-320.

Lu, Q., Suryanarayana N.V., and Christodoulou C., 1993, "Film thickness measurement with an ultrasonic transducer," *Experimental Thermal and Fluid Science*, 7(4): 354-361.

OLGA, URL: <http://www.software.slb.com/products/foundation/Pages/olga.aspx> .

Pedersen, P.C., Cakareski Z., and Hermanson J.C., 2000, "Ultrasonic Monitoring of film Condensation for Applications in Reduced Gravity," *Ultrasonics*, 38(1-8): 486-490.

Saito, Y., Mishima K., Tobita Y., Suzuki T., and Matsubayashi M., 2005, "Measurements of Liquid-Metal Two-Phase Flow by Using Neutron Radiography and Electrical Conductivity Probe," *Experimental Thermal and Fluid Science*, 29(3): 323-330.

Shoham, O., 2006, "*Mechanistic Modeling of Gas-Liquid Two-Phase Flow in Pipes*," Society of Petroleum Engineers.

Schubring, D., Ashwood A.C., Shedd T.A., and Hurlburt E.T., "Planar Laser-Induced Fluorescence (PLIF) Measurements of Liquid Film Thickness in Annular Flow Part I: Methods and Data," *International Journal of Multiphase Flow*, 36(10): 815-824.

Stahl, P., and Rohr P.R. von, 2004, "On the accuracy of void fraction measurements by single-beam gamma-densitometry for gas-liquid two-phase flows in pipes," *Experimental Thermal and Fluid Science*, 28(6): 533-544.

Ursenbacher, T., Wojtan L., and Thome J.R., 2004, "Interfacial measurements in Stratified Types of Flow. Part I: New Optical Measurement Technique and Dry Angle Measurements," *International Journal of Multiphase Flow*, 30(2): 107-124.

Yu, S.C.M., Tso C.P., and Liew R., 1996, "Analysis of Thin Film Thickness Determination in Two-phase flow using a multifiber Optical Sensor," *Applied Mathematical Modelling*, 20(7): 540-548.

Appendix B

Calibration of the microphones

The calibration of the microphones is essentially based on the comparison between the transfer functions measured during the calibration tests and the ones calculated analytically assuming that standing waves are propagating along the axis direction of a circular duct.

Two independent tests have been conducted by means of a blind flange, respectively to calibrate the 4 microphones mounted upstream and the 4 mounted downstream the test object.

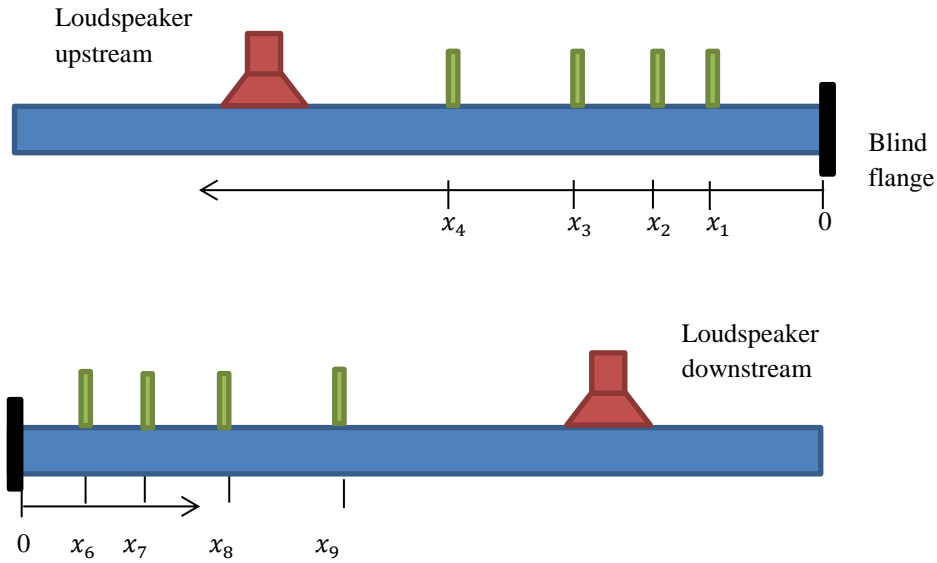


Figure B.1. Scheme of the experimental test for the calibration of the 8 microphones.

To estimate the analytical transfer function H , it is assumed that the loudspeaker generates a sound wave, whose amplitude is p_L :

$$p_L(x_i) = p_L^+ e^{-ik_\alpha x_i} + p_L^- e^{ik_\alpha x_i}$$

$$H_{1i} = \frac{p_L(x_i)}{p_L(x_1)} \quad (\text{B.1})$$

Where k_α is the wavenumber and x_i is the location of each microphone from the blind flange (see Figure B.1). Note the wave number $k_\alpha = \frac{\omega}{c} + (1 - i)\alpha$ is a complex number, of which negative imaginary part corresponds to the acoustical damping. Moreover, on the assumption that there is a wave propagating in the positive direction (p_L^+) and a wave in the negative direction (p_L^-), it is important to consider the reflection coefficient $R = \frac{p_L^-}{p_L^+}$. For the two tests the distance between the flange and the closest transducer is equal to 5.0×10^{-2} m. Note that this distance does not change in the whole analysis. On the contrary, in the optimization code the relative distance d_{1i} and d_{6j} between each microphone and the closest microphone to the blind flange (microphone 1 when the source is located upstream, microphone 6 when the source is located downstream) is varied. The piece where the transducers are installed was manufactured with specification indicating the relative distances reported in Table B.1. The calibration reported in this document is to correct for possible manufacturing tolerances, and for possible phase error of the microphones.

Table B.1. Distance between the transducers and the reference transducer.

	Upstream				Downstream			
	d ₁₁	d ₁₂	d ₁₃	d ₁₄	d ₆₆	d ₆₇	d ₆₈	d ₆₉
Initial Distance [m]	0.00	20.00	52.24	137.10	0.00	20.00	52.24	137.10

The combined effect of the errors on the calibration due to the transducers' distance, the reflection coefficient and the damping is complex. Therefore, corrections for each of these errors are brought one by one.

As a starting configuration, it is assumed that there are no visco-thermal losses (acoustical damping equal to zero), i.e. the wave number k can be expressed as:

$$k \cong \frac{\omega}{c} = 2\pi \frac{f}{c} \quad (\text{B.2})$$

Where f is the frequency and c is the speed of sound of the medium where the wave is propagating, i.e. air. It is also assumed that the reflection coefficient at the blind flange is unitary and that the relative distances between microphones are accurately known.

From Eq. (B.1) and assuming $R=1$ at the blind flange ($p_L^+ = p_L^-$), $p_L(x_i)$ reduces to $p_L(x_i) = 2p_L^+ \cos(kx_i)$. The transfer function for the transducers located upstream and downstream can be defined as follows in Eq. (B.3):

$$\begin{aligned} H_{1i} &= \frac{p_L(x_i)}{p_L(x_1)} = \frac{\cos(kx_i)}{\cos(kx_1)}; \quad i = 1, \dots, 4 \\ H_{6j} &= \frac{p_L(x_j)}{p_L(x_6)} = \frac{\cos(kx_j)}{\cos(kx_6)}; \quad j = 6, \dots, 9 \end{aligned} \quad (\text{B.3})$$

Note that the transfer function as proposed in Eq. (B.3) is here independent of the reflection coefficient at the other end of the pipe.

Figure B.2 shows the measured and computed transfer functions, assuming $R=1$ at the blind flange, that the visco-thermal losses are negligible and the distance between microphones as given in Table B.1.

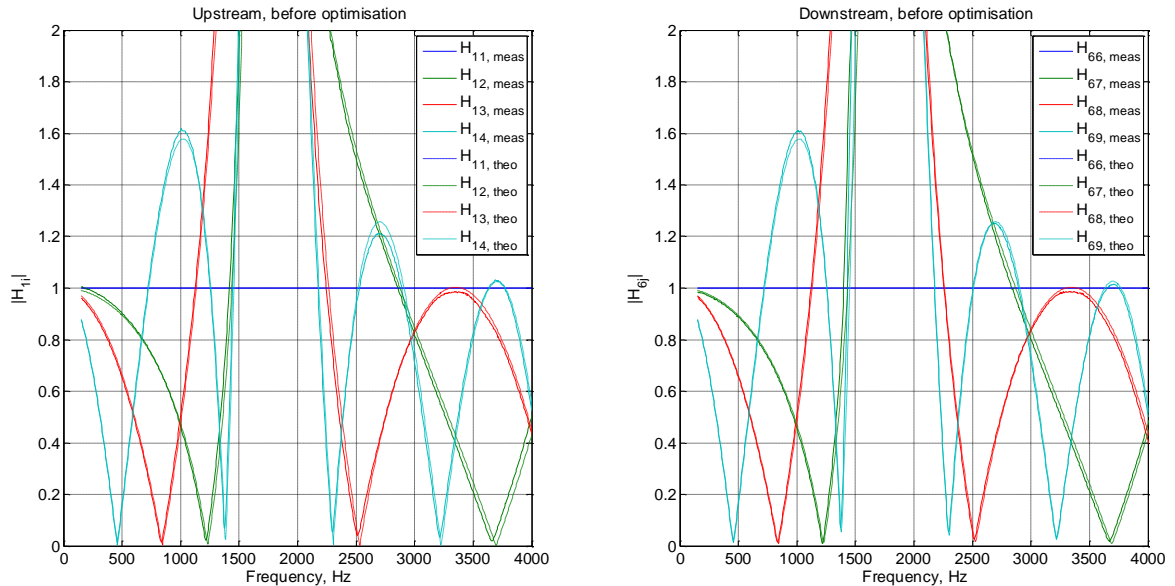


Figure B.2. Measured and computed transfer functions between upstream microphone 1 and the other upstream microphones, and between downstream microphone 6 and the other microphones.

As it is possible to see in Figure B.2, the measured transfer functions and the analytical ones, are not aligned. A calibration is therefore needed and for the case discussed in this manuscript, it consists of 4 main steps:

B.1. Empirical calibration of the relative distance between microphones

If a blind flange closes a pipe, it can be assumed that the reflection coefficient at the flange is unitary, the sound wave being in theory perfectly reflected ($p_{up}^+ = p_{up}^-$). Moreover, depending on the distance of each microphone from the blind flange, the transfer functions are zero (pressure amplitude equal to zero) at different frequencies. Indeed, if λ is the wavelength of the pressure wave generated by the loudspeaker, each microphone is located at $\lambda/4$ from the blind – closed flange. Note that kx_i is optimized, but it is assumed that the speed of sound is known. Indeed, it is easier to correct an error on k (or c) than on x_i during the post processing with the two-microphone method. Moreover, it is also assumed that the relative phase shift between microphones is zero.

The distances were adjusted to minimize the error in the positions of the zeros of the transfer functions. As seen in Figure B.2, where the measured and theoretical transfer functions are compared, the zeros are shifted. The “correct” distances d_{1i} and d_{6j} are determined by zooming around one of the zeros for each microphone combination and adjusting the microphone position x_i until the match between the 2 curve is satisfactory.

The final distances for our configuration are corrected with the correction factors C_i (see Table B.2) as proposed in Eq. (B.4):

$$\begin{aligned} d_{1i} &= d_{1i} + C_{1i} ; \quad i = 1, \dots, 4 \\ d_{6j} &= d_{6j} + C_{6j} ; \quad j = 6, \dots, 9 \end{aligned} \quad (\text{B.4})$$

Table B.2. Corrected relative distances between the transducers.

	Upstream				Downstream			
	C_{11}	C_{12}	C_{13}	C_{14}	C_{66}	C_{67}	C_{68}	C_{69}
Correction [mm]	0.00	6.00	0.50	0.30	0.00	0.50	0.65	0.65

The transfer functions for the upstream and downstream transducers corrected for the distance are shown in Figure B.3:

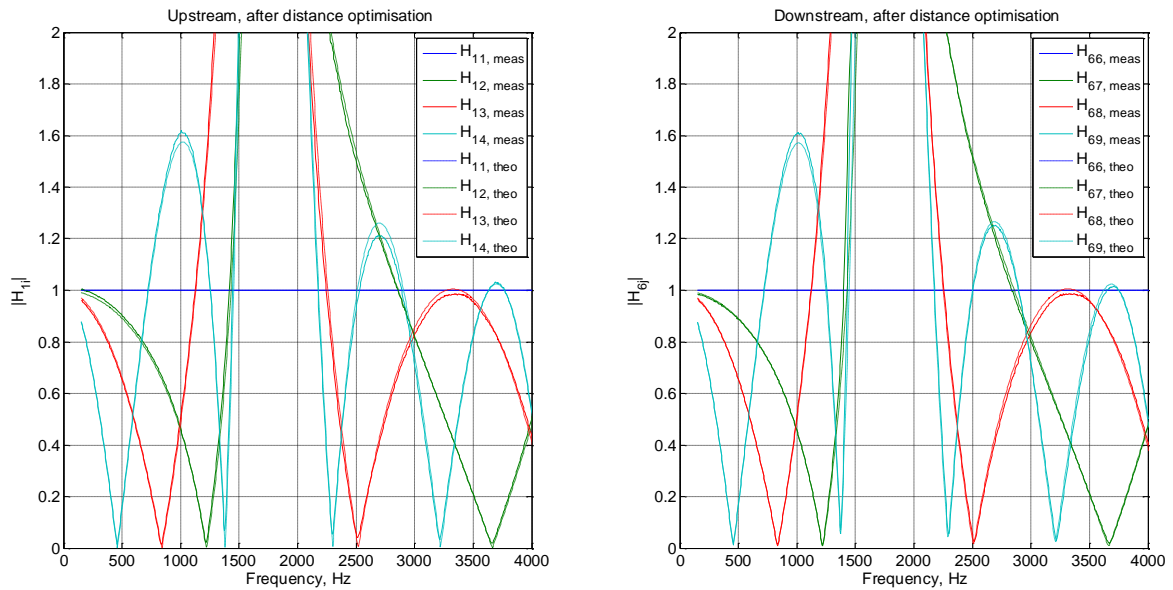


Figure B.3. Measured and computed transfer functions after the optimization on microphone positions.

B.2. Empirical calibration of the sensitivity of the microphones, including the effect of non-perfect reflection coefficients and acoustical damping

B.2.1. Correction on the reflection coefficient

The assumption that the reflection coefficient R of a closed end (the blind flange) is unitary is not completely correct due to possible vibrations of the flange. This has an effect on the amplitude of the transfer function, which will be used in next section to calibrate the relative amplitude of the microphones. In this section, a realistic reflection coefficient is derived.

If a reflection coefficient R lower than 1 is considered, the amplitude of a sound wave p_L generated by the loudspeaker, as well as the transfer functions H_{i1} and H_{j6} can be modified as follows in Eqs. (B.5) and (B.6).

$$p_L(x_i) = p_L^+ e^{-ikx_i} + p_L^- e^{ikx_i} = p_L^+ (e^{-ikx_i} + R e^{ikx_i}) \quad (\text{B.5})$$

$$\begin{aligned} H_{i1,R} &= \frac{p_L(x_i)}{p_L(x_1)} = \frac{(e^{-ikx_i} + R e^{ikx_i})}{(e^{-ikx_1} + R e^{ikx_1})} ; \quad i = 1, \dots, 4 \\ H_{j6,R} &= \frac{p_L(x_j)}{p_L(x_6)} = \frac{(e^{-ikx_j} + R e^{ikx_j})}{(e^{-ikx_6} + R e^{ikx_6})} ; \quad j = 6, \dots, 9 \end{aligned} \quad (\text{B.6})$$

For the case considered here, it was found that the best reflection coefficient to align the analytical transfer functions to the experimental ones is $R = 0.96$. This value is the same for the calibration of the transducers located upstream and downstream the test object. These reflections coefficients were adjusted to minimize the error on the “depth” of the zeros of the transfer functions.

The transfer functions for the upstream and downstream transducers corrected for the distance and the reflection coefficient are shown in Figure B.4.

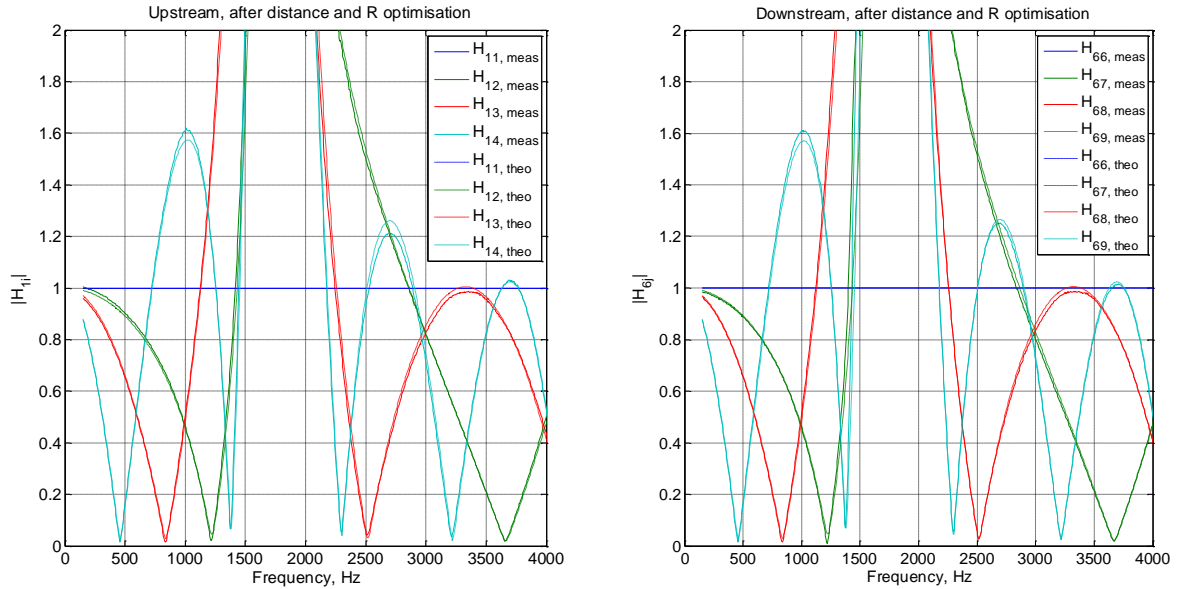


Figure B.4. Measured and computed transfer functions after the optimization on microphone positions and considering the reflection of the blind flange.

B.2.2. Implementation of acoustical damping

Last, in order to use the amplitude of the transfer function to calibrate the microphone sensitivity, the visco-thermal losses should be considered. Equation (B.7) shows the expression of the complex wave number, whose negative imaginary part corresponds to the acoustical damping α .

$$k_\alpha = \frac{\omega}{c} + (1 - i)\alpha = 2\pi \frac{f}{c} + (1 - i)\alpha \quad (\text{B.7})$$

For this case, the model of Kirchhoff is used, specifically for a smooth pipe, whose inner diameter is 25.0 mm. The model of Kirchhoff for the acoustical damping is reported in Eq. (B.8).

$$\alpha \cong \frac{L_{2p}}{2 A_{mp} c_0} \sqrt{\frac{\pi f \mu}{\rho}} \left(1 + \frac{\gamma - 1}{\sqrt{Pr}}\right) \quad (\text{B.8})$$

Where L_{2p} and A_{mp} are respectively the perimeter and the area of the pipe, c_0 the speed of sound, μ and ρ the dynamic viscosity and the density of the medium (air), γ (=1.4) the heats specific ratio and Pr (=0.71) is the Prandtl number.

From temperature T and static pressure p measured for each calibration test, the speed of sound c_0 , the density ρ , and the dynamic viscosity μ are calculated from Eqs. (B.9).

$$\begin{aligned} \rho &= p/RT \\ \mu &= (18.27e^{-6}) \frac{291.15 + 120}{T + 120} (T/291.15)^{3/2} \\ c_0 &= 20.0457 \sqrt{T} \end{aligned} \quad (\text{B.9})$$

Note that R is the gas constant.

$$\begin{aligned} H_{i1,R,\alpha} &= \frac{p_L(x_i)}{p_L(x_1)} = \frac{(e^{-ik_\alpha x_i} + R e^{ik_\alpha x_i})}{(e^{-ik_\alpha x_1} + R e^{ik_\alpha x_1})}; \quad i = 1, \dots, 4 \\ H_{j6,R,\alpha} &= \frac{p_L(x_j)}{p_L(x_6)} = \frac{(e^{-ik_\alpha x_j} + R e^{ik_\alpha x_j})}{(e^{-ik_\alpha x_6} + R e^{ik_\alpha x_6})}; \quad j = 6, \dots, 9 \end{aligned} \quad (\text{B.10})$$

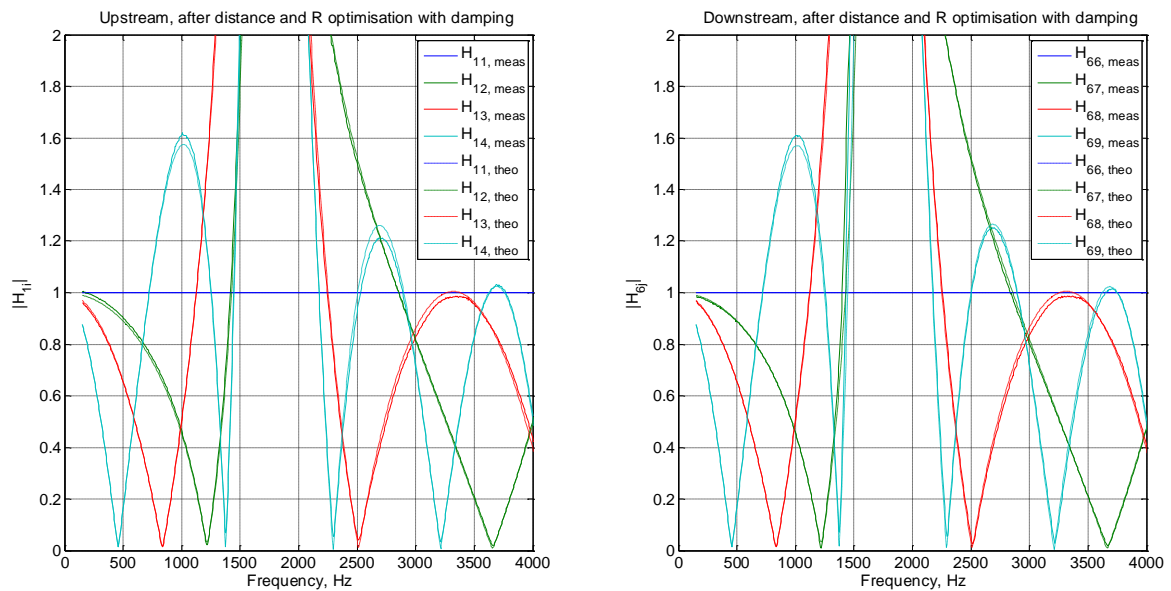


Figure B.5. Measured and computed transfer functions after the optimization on microphone positions, considering the reflection of the blind flange and the acoustic damping in the complex wave number.

B.2.3. Empirical calibration of the sensitivity of the microphones

In this section, the sensitivity of the microphones, relative to the sensitivity of microphone 1 and microphone 6, is adjusted empirically.

This is done by introducing a correction factors CA_{i1} , resp. CA_{j6} , for the microphones mounted upstream, resp. downstream, the test object. The objective is to minimize the difference between the amplitude of the lobes of the analytical and experimental transfer functions. This correction is frequency independent and it is related only to the transducers.

Table B.3. Correction factors on amplitude for the transfer functions, considering the corrected relative distance, the reflection coefficient of the blind flange, and the damping in the complex wave number.

CA11	CA21	CA31	CA41	CA66	CA76	CA86	CA96
1.000	0.988	1.010	0.980	1.000	1.005	1.005	0.975

$$\begin{aligned} H_{i1,R,\alpha,CA} &= \frac{H_{i1,R,\alpha}}{CA_{i1}} ; \quad i = 1, \dots, 4 \\ H_{j6,R,\alpha,CA} &= \frac{H_{j6,R,\alpha}}{CA_{j6}} ; \quad j = 6, \dots, 9 \end{aligned} \quad (\text{B.11})$$

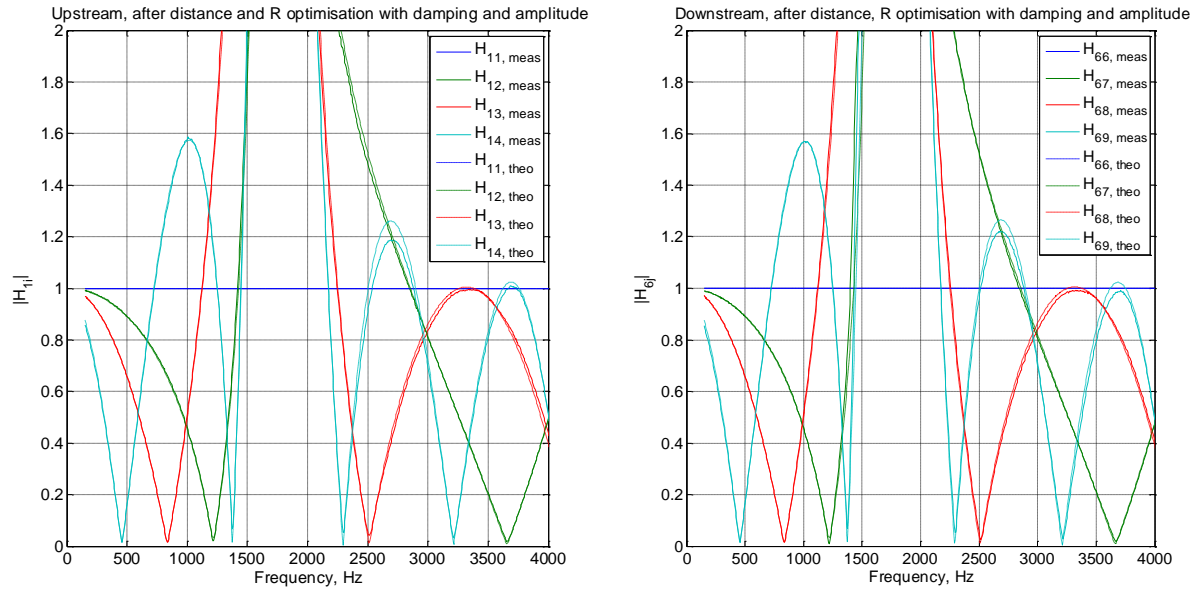


Figure B.6. Measured and computed transfer functions after the optimisation on microphone positions, considering the reflection of the blind flange, the acoustic damping in the complex wave number, and the correction in amplitude.

B.3. Relative calibration between the transducers located upstream and downstream the test object

The calibration of the sensitivity of the microphones, as described above, was made relative to the sensitivity of microphone 1 upstream and of microphone 6 downstream. If these two microphones have a different sensitivity, an error is made when these two sets of microphones are used to measure the acoustic attenuation across a pipe. To find the calibration factor between the two transducers' group, the acoustical measurements when the pipe is dry and without mean flow is used as reference. If the pipe is empty, the acoustical damping in both directions (with and against flow) has to be the same. The equality is therefore sought. Figure B.7 shows the acoustical damping measured in both directions as function of frequency for a smooth horizontal pipe, whose inner diameter is equal to 25.0 mm, without mean flow. Figure B.8 shows the percentage ratio of the acoustical damping measured when the wave is travelling in the same direction as the flow to the one measured when the wave is against flow. When $C = 1$, the calibration factors are the ones obtained in Section B.2.3, whose results are shown in Figure B.7. For this case, the percentage ratio is between 85 and 95%. The calibration between the two transducers' groups is indeed needed.

The best calibration is chosen on the basis of a factor $C = CA_{11}/CA_{66}$ (see Table B.3). This procedure is effectively modifying the measured transfer functions by a factor C . Therefore, the transfer functions become:

$$\begin{aligned} H_{i1,R,\alpha,CA} &= \frac{H_{i1,R,\alpha}}{CA_{i1}} ; \quad i = 1, \dots, 4 \\ H_{j6,R,\alpha,CA} &= C \frac{H_{j6,R,\alpha}}{CA_{j6}} ; \quad j = 6, \dots, 9 \end{aligned} \quad (\text{B.12})$$

Different factors C around the unitary value are considered and compared together. Figure B.8 shows that $C = 1.009$ is considered to be the best and it will be used for the full analysis.

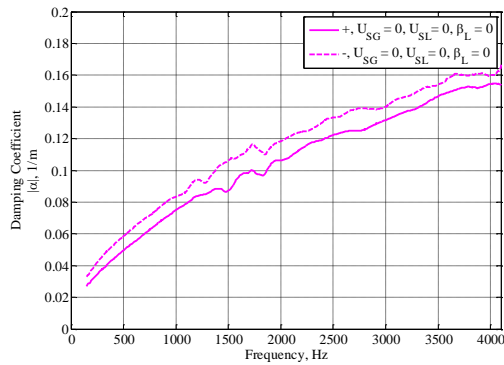


Figure B.7. Damping coefficient for a horizontal smooth pipe in both directions, with (-) and against (--) flow. No relative calibration between the two groups of transducers is considered.

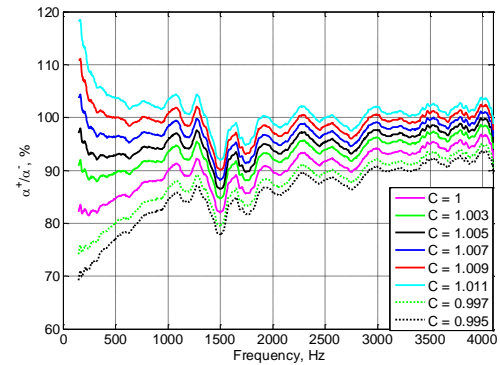


Figure B.8. Percentage ratio between the acoustical damping measured in the direction of the flow (α^+) to the damping measured against flow (α^-).

B.4. Script (Only for the upstream source)

```
load Close_piston_upstream.mat

%%% --- Upstream --- %%%%
for ii=1:4
    FRF_A(:,ii)=FRF(:,ii)/FRF(:,1);
end
eval(['F_A(1,:)=[f(,1)];']);
corr_T_up = 2.0375 ; Temp_A = T_U- corr_T_up;
eval(['Temp_A'='[Temp_A(,1)];']);

c_A = 20.0457*sqrt(273.15+mean(Temp_A));

Lu=0.05;
u1_u2 = 0.02;
u1_u3 = 0.05224;
u1_u4 = 0.1371;
Xmics_up    = Lu+[ 0 u1_u2 u1_u3 u1_u4 ];
Xmics_up_corr = Xmics_up+[0 .6 .5 .3]/1000;

R=0.96;

corr21 = .988+0*F_A.'; %CA21
corr31 = 1.01+0*F_A.'; %CA31
corr41 = 0.98+0*F_A.'; %CA41

k_A_0=2*pi*F_A/c_A;

nu    = 1.5e-5;
Dp    = 0.025; %

alpha_0 = damp_kirchh(c_A,pi*Dp,pi/4.*Dp.^2,1.4,0.71,
    F_A',Temp_A,Stat_press(:,1)*10^5);
k_A    = k_A_0 + alpha_0*(1-1j);

figure(1);clf
set(gca,'FontName','Times New Roman','FontSize',16);
plot(F_A,abs(FRF_A));
axis([0 4000 0 2]);

hold on
plot(F_A,1+0*F_A,'-', ...
    F_A,abs(cos(k_A_0*Xmics_up(2))./cos(k_A_0*Xmics_up(1))),'-', ...
    F_A,abs(cos(k_A_0*Xmics_up(3))./cos(k_A_0*Xmics_up(1))),'-', ...
    F_A,abs(cos(k_A_0*Xmics_up(4))./cos(k_A_0*Xmics_up(1))),'-', ... );
xlabel('Frequency [Hz]')
ylabel('H_{1i}')
title('Upstream, before optimisation')
legend('H_{11, meas}','H_{12, meas}','H_{13, meas}','H_{14, meas}', ...
    'H_{11, theo}','H_{12, theo}','H_{13, theo}','H_{14, theo}' )
print -dpng 'Dist_up_before_opt'

if 1
figure(2);clf
set(gca,'FontName','Times New Roman','FontSize',16);
plot(F_A,abs(FRF_A));
axis([0 4000 0 2]);

hold on
plot(F_A,1+0*F_A,'-', ...
    F_A,abs(cos(k_A_0*Xmics_up_corr(2))./cos(k_A_0*Xmics_up_corr(1))),'-', ...
    F_A,abs(cos(k_A_0*Xmics_up_corr(3))./cos(k_A_0*Xmics_up_corr(1))),'-', ...
    F_A,abs(cos(k_A_0*Xmics_up_corr(4))./cos(k_A_0*Xmics_up_corr(1))),'-', ... );
xlabel('Frequency [Hz]')
ylabel('H_{1i}')
title('Upstream, after distance optimisation')
legend('H_{11, meas}','H_{12, meas}','H_{13, meas}','H_{14, meas}', ...
    'H_{11, theo}','H_{12, theo}','H_{13, theo}','H_{14, theo}' )
print -dpng 'Dist_up_after_dist_opt'

figure(3);clf
set(gca,'FontName','Times New Roman','FontSize',16);
plot(F_A,abs(FRF_A));
axis([0 4000 0 2]);

hold on
plot(F_A,1+0*F_A,'-', ...
    F_A,abs(exp(-1i*k_A_0*Xmics_up_corr(2))+R*exp(1i*k_A_0*Xmics_up_corr(2))), ...
    ./exp(-1i*k_A_0*Xmics_up_corr(1))+R*exp(1i*k_A_0*Xmics_up_corr(1))),'-', ...
    F_A,abs(exp(-1i*k_A_0*Xmics_up_corr(3))+R*exp(1i*k_A_0*Xmics_up_corr(3))), ...
    ./exp(-1i*k_A_0*Xmics_up_corr(1))+R*exp(1i*k_A_0*Xmics_up_corr(1))),'-', ...
    F_A,abs(exp(-1i*k_A_0*Xmics_up_corr(4))+R*exp(1i*k_A_0*Xmics_up_corr(4))), ...
    ./exp(-1i*k_A_0*Xmics_up_corr(1))+R*exp(1i*k_A_0*Xmics_up_corr(1))),'-', ... );
xlabel('Frequency [Hz]')
ylabel('H_{1i}')
title('Upstream, after distance and R optimisation')
legend('H_{11, meas}','H_{12, meas}','H_{13, meas}','H_{14, meas}', ...
    'H_{11, theo}','H_{12, theo}','H_{13, theo}','H_{14, theo}' )
print -dpng 'Dist_up_after_dist_R_opt'

figure(4);clf
set(gca,'FontName','Times New Roman','FontSize',16);
plot(F_A,abs(FRF_A));
axis([0 4000 0 2]);
hold on
plot(F_A,1+0*F_A,'-', ...
    F_A,abs(exp(-1i*k_A*Xmics_up_corr(2))+R*exp(1i*k_A*Xmics_up_corr(2))), ...
    ./exp(-1i*k_A*Xmics_up_corr(1))+R*exp(1i*k_A*Xmics_up_corr(1))),'-', ...
    F_A,abs(exp(-1i*k_A*Xmics_up_corr(3))+R*exp(1i*k_A*Xmics_up_corr(3))), ...
    ./exp(-1i*k_A*Xmics_up_corr(1))+R*exp(1i*k_A*Xmics_up_corr(1))),'-', ...
    F_A,abs(exp(-1i*k_A*Xmics_up_corr(4))+R*exp(1i*k_A*Xmics_up_corr(4))), ...
    ./exp(-1i*k_A*Xmics_up_corr(1))+R*exp(1i*k_A*Xmics_up_corr(1))),'-', ... );
xlabel('Frequency [Hz]')
ylabel('H_{1i}')
title('Upstream, after distance and R optimisation with damping')
legend('H_{11, meas}','H_{12, meas}','H_{13, meas}','H_{14, meas}', ...
    'H_{11, theo}','H_{12, theo}','H_{13, theo}','H_{14, theo}' )
print -dpng 'Dist_up_after_dist_R_alpha_opt'
end

figure(5);clf
set(gca,'FontName','Times New Roman','FontSize',16);
plot(F_A,abs(FRF_A(:,1)), ...
    F_A,abs(FRF_A(:,2)).*corr21, ...
    F_A,abs(FRF_A(:,3)).*corr31, ...
    F_A,abs(FRF_A(:,4)).*corr41 );
axis([0 4000 0 2]);
hold on
plot(F_A,1+0*F_A,'-', ...
    F_A,abs(exp(1i*k_A*Xmics_up_corr(2))+R*exp(1i*k_A*Xmics_up_corr(2))), ...
    ./exp(-1i*k_A*Xmics_up_corr(1))+R*exp(1i*k_A*Xmics_up_corr(1))),'-', ...
    F_A,abs(exp(-1i*k_A*Xmics_up_corr(3))+R*exp(1i*k_A*Xmics_up_corr(3))), ...
    ./exp(-1i*k_A*Xmics_up_corr(1))+R*exp(1i*k_A*Xmics_up_corr(1))),'-', ...
    F_A,abs(exp(-1i*k_A*Xmics_up_corr(4))+R*exp(1i*k_A*Xmics_up_corr(4))), ...
    ./exp(-1i*k_A*Xmics_up_corr(1))+R*exp(1i*k_A*Xmics_up_corr(1))),'-', ... );
xlabel('Frequency [Hz]')
ylabel('H_{1i}')
title('Upstream, after distance and R optimisation with damping')
legend('H_{11, meas}','H_{12, meas}','H_{13, meas}','H_{14, meas}', ...
    'H_{11, theo}','H_{12, theo}','H_{13, theo}','H_{14, theo}' )
print -dpng 'Dist_up_after_dist_ampl_opt'
```

Appendix C

Acoustic damping in corrugated pipes: An experimental study

Nomenclature

A_{mp}	Area of the pipe [m ²]	r_{up}	Upstream edge radius [m]
c_0	Speed of sound [m/s]	r_{down}	Downstream edge radius [m]
c_{eff}	Effective speed of sound [m/s]	U	Velocity of the gas [m/s]
D_{mp}	Inner diameter of the main pipe [m]	W	Width of the cavity [m]
$D_{mp,out}$	Outer Diameter [m]		
FIP	Flow Induced Pulsation	α	Damping coefficient [1/m]
H	Depth of the cavity [m]	α_0	Kirchhoff damping coefficient [1/m]
L	Length of the pipe [m]	δ_{ac}	Acoustic boundary layer thickness [m]
L_p	Plateau [m]	δ_l	Viscous sublayer thickness [m]
M	Mach number [-]	ρ	Density of the gas [kg/m ³]
Pt	Pitch [m]	\pm	Quantity considered in direction of (+) or against (-) the flow

C.1. Introduction

A corrugated pipe is a pipe characterized by the presence of periodic shallow cavities in the longitudinal direction. Because of their global flexibility without losing their local structural strength, these particular pipes are largely used in various industrial applications. They are for instance used in ventilation systems and heat exchangers (Petri and Huntley, 1980; Elliott, 2004), as well as in gas transportation systems (Belfroid et al., 2007; Goyder, 2009).

However, depending on the flow characteristics and on the geometrical properties of the pipe cavities, critical conditions can occur. Indeed, Flow Induced Pulsations (FIPs) can be caused and high amplitude sound, i.e. whistling, can be generated.

The first studies on corrugated pipes are from the 20s. In particular, Burstyn (1922) suggested that corrugations work as numerous lips and Cermak (1922) independently made investigations on the singing, noticing that it was difficult to excite the fundamental tone (Kristiansen and Wiik, 2007). It was pointed out that the generation of sound was due to an oscillation driven by a flow-acoustic interaction. The same flow unsteadiness generated by the separation of the flow at the upstream edge of the cavity is therefore the reason of an unsteady hydrodynamic force on the bounding walls, which in turn generates sound (Gutin, 1948; Curle, 1955). Although mechanical vibrations can significantly affect the singing behavior as observed by Ziada and Bühlmann (1991), in the same year Nakamura and Fukamachi (1991) showed that flexibility is indispensable for the sound generation.

However, the coupling between the shear layers and the longitudinal acoustic standing waves has been more often observed and studied (Silverman and Cushman, 1989; Crawford, 1974; Cadwell, 1994; Serafin and Kojs, 2003; Petri and Huntley, 1980; Nakamura and Fukamachi, 1991; Elliott, 2004; Kristiansen and Wiik, 2007; Kop'ev et al., 2008; Nakiboğlu et al., 2010).

First, this work aims at familiarizing with the techniques needed to measure the acoustical damping. It was decided to conduct the experiments on corrugated pipes because the results would have been assembled together

with an ongoing parallel work (Golliard et al., 2016). Although the final goal is to isolate the effect of the inner diameter in corrugated pipes, here only one experimental campaign will be presented.

In this Appendix, the experimental setup and the facility are first presented together with the procedure and the post-processing. Last, the results are shown and discussed.

C.2. Experimental setup and experimental method

The final aim of this experimental campaign is the damping estimate in a corrugated pipe and to compare the obtained results with the ones of a smooth pipe. The experimental investigations have been conducted at the Laboratoire d'acoustique de l'Université du Maine (LAUM).

The system under investigation is mounted between two measurement sections, upstream and downstream. Each measurement section consists in a hard walled steel duct (diameter 30 mm) where four microphones (B&K 4136 and 2670 with Nexus 2690 amplifier) are mounted. The distances between microphones are reported in Table C.1, approximated to the fourth digit. This enables the determination of the incoming and outgoing waves on both sides of the measured system. Two acoustic sources on both sides of the system give two different acoustic states and the four elements of the scattering matrix (transmission and reflection coefficient on both directions) for plane waves can be evaluated. A more detail description of the measurement technique and the facility can be found in Aurégan and Leroux (2003).

Table C.1. Relative distance [m] between microphones.

Microphones' combination	1-2	1-3	1-4
Upstream	0.030	0.1301	0.2820
Downstream	0.030	0.1300	0.2750

After mounting the setup and the calibration of the microphones, damping is measured in the following three configurations (see Figure C.1) at around 1 bar:

1. Smooth pipe, $L = 2.997$ m
2. Corrugated pipe, configuration A (see Figure C.1b), $L = 2.016$ m
3. Corrugated pipe, configuration B (see Figure C.1c), $L = 2.016$ m

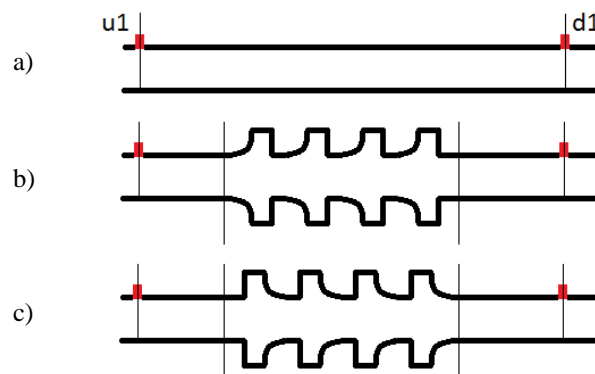


Figure C.1. Configurations tested: a) smooth pipe; b) Corrugated pipe - Conf. A (see Table C.2); c) Corrugated pipe - Conf. B (see Table C.2). The flow is going from the left to the right.

The technical details of the geometry tested are provided in Table C.2.

Table C.2. Geometrical details of the three test objects (see Figure C.2).			
	Smooth Pipe	Corrugated Pipe	
		Config. A	Config. B
D_{mp} [mm]	30.0	30.0	
$D_{mp,out}$ [mm]	38.0	70.0	
W [mm]	-	4.0	
H [mm]	-	4.0	
r_{up} [mm]	-	3.0	1.0
r_{down} [mm]	-	1.0	3.0
L_p [mm]	-	4.0	
Pt [mm]	-	12.0	

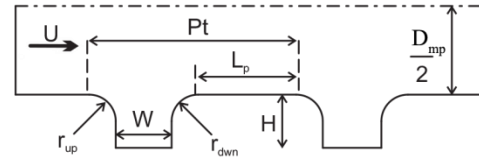


Figure C.2. Geometrical parameters of a corrugated pipe [Nakiboğlu et al., 2010].

For each configuration, the acoustical damping is measured with and without mean flow, firstly using the upstream loudspeaker and secondly the downstream one. Table C.3 provides the test matrix.

Table C.3. Test Matrix: Mach number M [-] for each configuration.

Configuration	Smooth Pipe	Corrugated Pipe, Configuration A	Corrugated Pipe, Configuration B
Mach number [-]	0	0	0
	0.0746	0.0367	0.0359
	0.01551	0.0712	0.0710
	0.3141	0.1076	0.1068
		0.1417	0.1417
		0.1793	0.1779

For each experiment, the loudspeaker, either located upstream or downstream, generates a ‘step sine’, investigating a range of frequency between 100 Hz and 4000 Hz. This is split into three different ranges: 100-800 Hz, 800-2000 Hz, and 2000-4000 Hz. For each frequency range, the sampling frequency of 12800 Hz, the frequency step is of 2 Hz, and the number of settle cycles is 10. Only the number of integration cycles is different: 100 for the first range, 500 for the second one, and 1000 for the third one.

From the microphones’ measurements, the scattering matrix and the acoustical damping have been calculated. The method is the same used to estimate the work on damping in presence of water (see Section 4.3.4).

C.3. Results

In this section, the results for each configuration tested will be presented and discussed. In particular, in the first section, the results for a smooth pipe are used as a comparison. For the tests on the smooth pipe (Section C.3.1), both the transmission coefficients and the damping calculated are reported as function of frequency. For the results on the two corrugated pipe configurations will be presented in Section C.3.2.

C.3.1. Results – Smooth pipe

In this section, the results on the smooth pipe will be presented. Figure C.3 shows the transmission coefficient of the scattering matrix and, from it, the estimated damping both in direction (solid line) and against (dashed line) flow. In cyan color, the results without mean flow are presented. They are compared with the Kirchoff law (see Eq. (4.4)), which estimates the damping generated by the visco-thermal losses. The

experimental results (cyan curves) and the Kirchhoff law (magenta line) are in good agreement (always below the 10%).

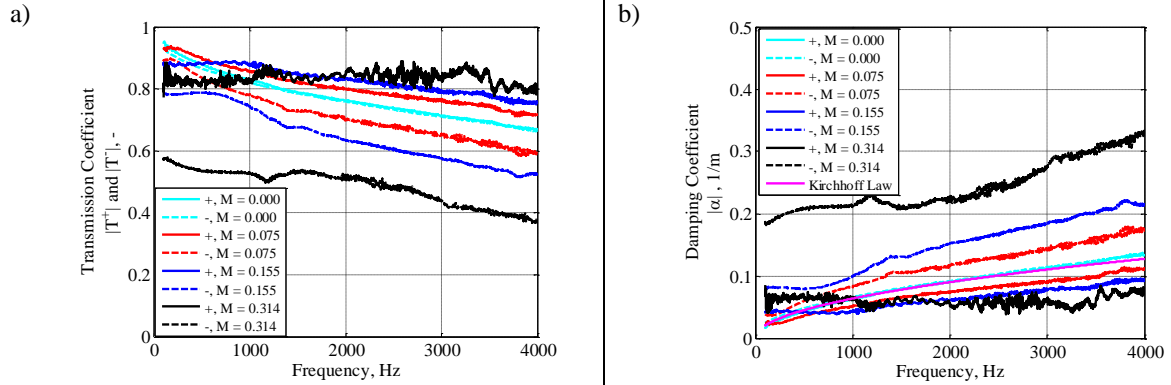


Figure C.3 Smooth pipe: transmission coefficient T [-] of the scattering matrix (a) and measured damping [1/m] as function of frequency [Hz] in direction (-) and against (-) flow.

Two elements have to be evaluated: the convection and the turbulent effects on the damping. For more information about these effects, the reader can find more details in Section 4.1.1. The ratio α/α_0 where α_0 is the damping without flow is the analyzed quantity (see Figure C.5).

Concerning the convection effects on damping, Figure C.4 shows that the approximation of Golliard et al. (2015) – $\alpha = \alpha_0/(1 \pm 2M)$ – does not give a good approximation of Dokumaci' model (1995) for the Mach number greater than 0.2.

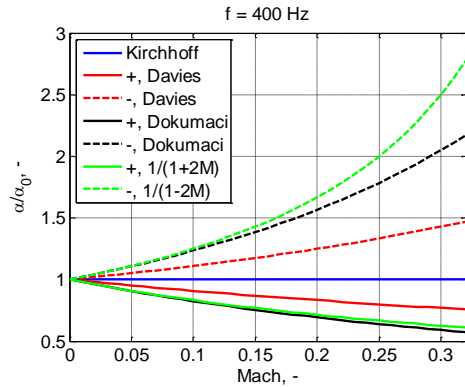


Figure C.4. Smooth pipe (30 mm), 400 Hz: approximation of Davies (1988) and Dokumaci (1995) for the convection effects.

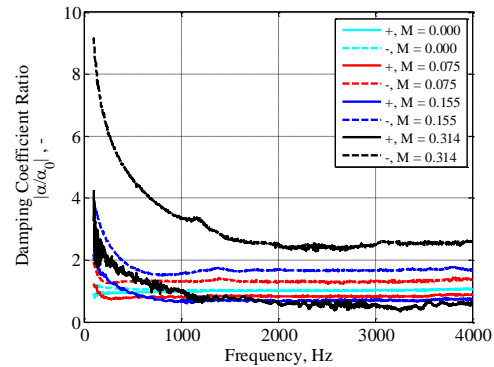


Figure C.5. Smooth pipe: damping coefficient ratio [-] as function of frequency [Hz] without any correction.

Figure C.6 shows how the ratio α/α_0 can be corrected from the convection effects (the corrected damping is about the same in both directions) by using the approximation provided by Dokumaci.

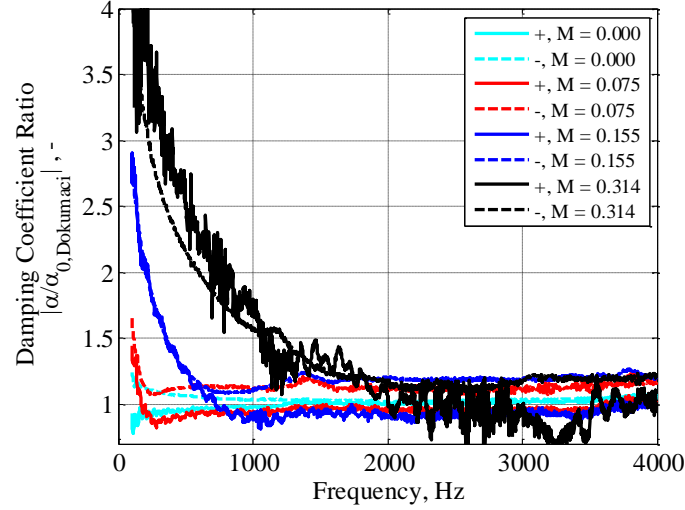


Figure C.6. Smooth pipe: damping coefficient ratio α/α_0 [-] as function of the frequency [Hz] corrected by the convection term proposed by Dokumaci (1995).

The high values of the ratios α/α_0 at low frequencies are due to turbulence. As explained also in Section 4.1.1, the parameter to disclose whether it is worth evaluating the turbulent effects is the ratio of the acoustic boundary layer δ_{ac} to the viscous sublayer δ_1 . If the ratio is above the unity, it implies that the acoustic boundary layer is thicker than the viscous sublayer and these effects have to be considered. Figure C.7a shows that for the three Mach numbers of these tests, turbulence has always a relevant effect at low frequency.

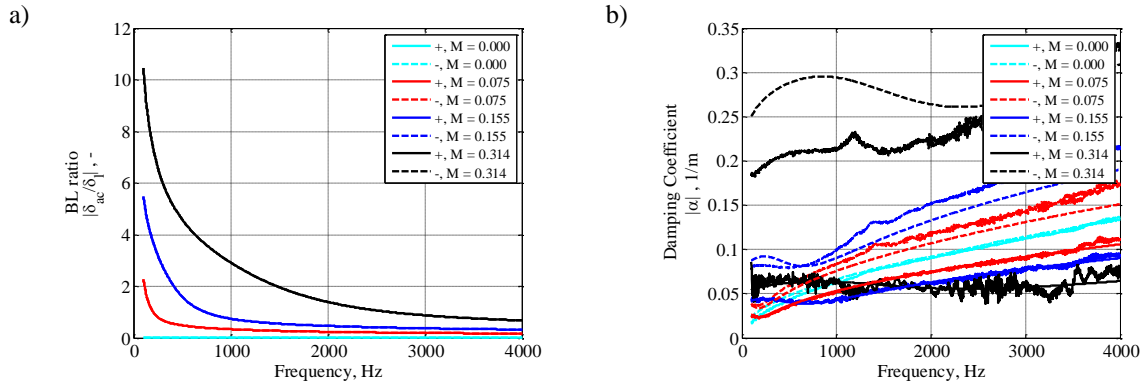


Figure C.7. Smooth pipe: (a) the boundary layers ratio δ_{ac}/δ_1 and (b) comparison between the experimental results and the turbulence model of Howe (1995) as function of frequency [Hz].

By means of the turbulence model of Howe (1995), these effects have been evaluated. In Figure C.7b, the value of the attenuation in both directions computed by using this Howe model (smooth dashed and continuous lines) are in good agreement with the experimental curves, especially when the flow is in the same direction as the sound wave. The agreement is less convincing at the highest Mach number for wave propagating against the flow. It was expected since Howe's model works properly at low Mach numbers.

C.3.2. Results – Corrugated pipe: configuration A and Configuration B

In this section, the results for both corrugated pipe configurations are presented.

First, Figure C.8, without mean flow, shows the comparison between the damping in the corrugated pipes and the ones in the smooth pipe (cyan). Those damping coefficients are equal in the two directions, at the measurement errors precision, because of reciprocity.

The damping values for the corrugated pipes are higher than the ones in a smooth pipe. This effect was expected since the surface of contact between air and the pipe is larger (here in a factor ≈ 1.85) for a corrugated tube than for a smooth pipe. The acoustical damping in corrugated pipes follows, as the Kirchhoff law, a square root variation as a function of frequency and it seems to be just multiplied by a constant factor (here ≈ 1.4), which is not far from the square root of the ratio of contact surfaces.

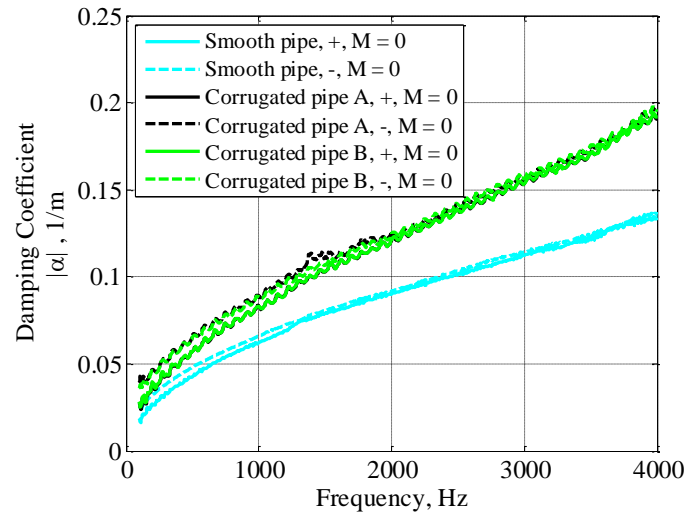


Figure C.8. Acoustical damping [1/m] without gas mean flow as function of frequency [Hz] in the positive (-) and in the negative (-) direction for the three different configurations: smooth pipe (cyan), corrugated pipe - Conf. A (black), corrugated pipe - Conf. B (green).

Figure C.9 shows the damping measured for the configuration A (a1 and a2) and for the configuration B (b1 and b2). It can be seen that the damping α is negative in some frequency range, meaning that the sound is amplified. This can happen if the transmission coefficient is greater than 1. The large differences between the two configurations are a clear example of how the damping and amplification in a corrugated tube depends on the details of the corrugation geometry (the only difference between the two configuration is the radius of entrance and exit bevel of the cavity, see Table C.2). It can be noted that, during the experiment, the corrugated pipe in Configuration A was always clearly whistling (at a frequency close to the maximum in negative value) even at a low gas velocity, while it was not always clear whether the tube in Configuration B was whistling or not.

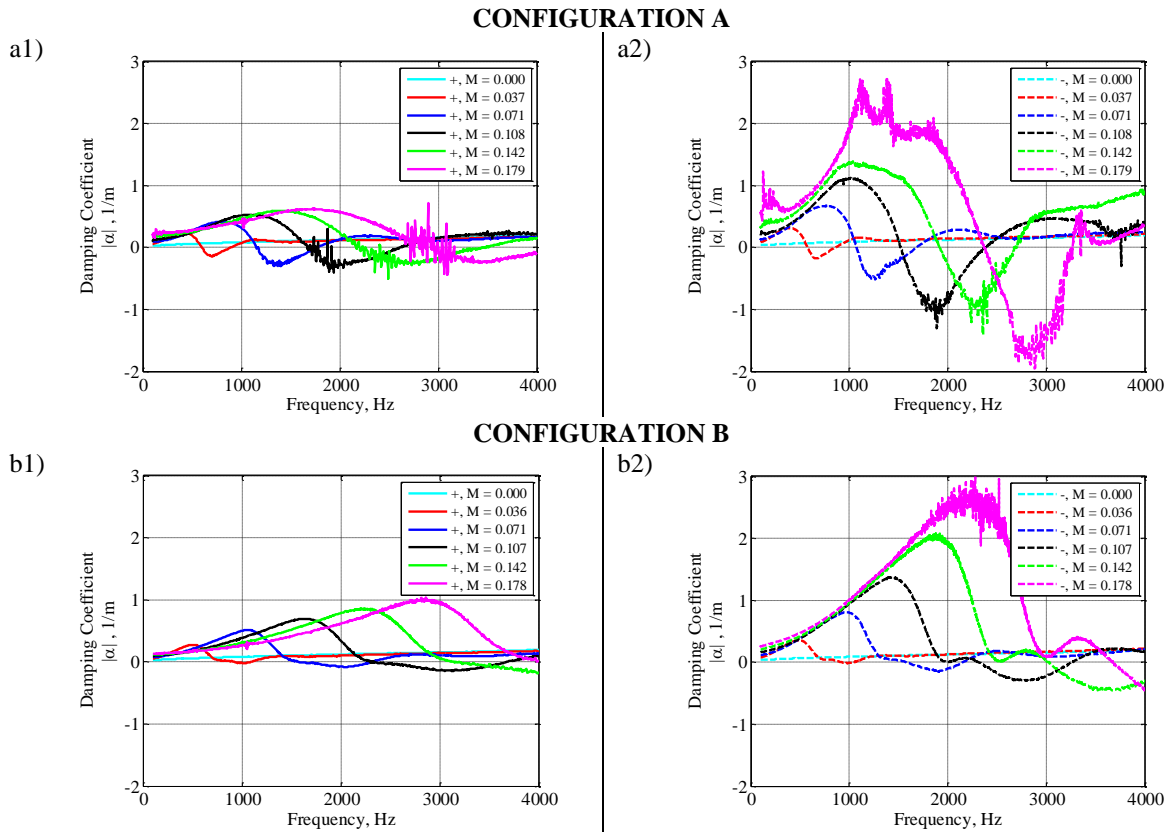


Figure C.9. Corrugated pipe - configuration A (a1-a2) and configuration B (b1-b2): damping measured without and with gas mean flow in the direction of (solid lines) and against (dashed lines) flow.

The results of Configuration A in the positive direction are compared with the results obtained by Golliard et al. (2013a) with the same corrugation geometry but with an inner diameter $D_{mp} = 49$ mm instead of 30 mm in our case in Figure C.10. In this figure, the first (positive) peak value and the second (negative) peak damping coefficients are plotted for our geometry and for Golliard's geometry. Since the only difference is the inner diameter, Figure C.10 shows that smaller inner diameters corrugated pipes are able to absorb more, as well as to amplify more.

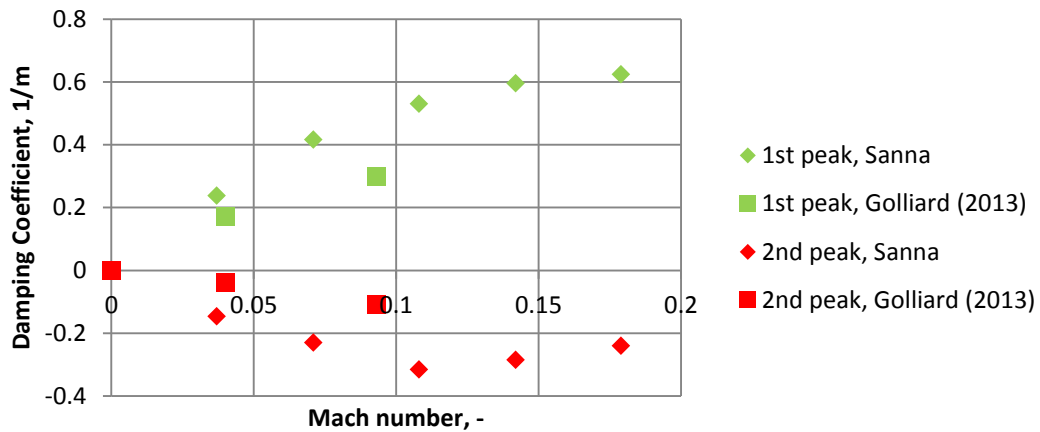


Figure C.10. Corrugated pipe, configuration A: comparison between the first (positive) and the second (negative) peak of the damping coefficients between the experiments of Sanna (diamonds) and Golliard et al. (2013a) (squares).

Golliard et al. (2013b, 2016) relates the damping measured in a corrugated duct with flow to the power $\langle P_{\text{flow}} \rangle$ transferred from the flow to the acoustic waves travelling in the pipe:

$$\frac{\langle P_{\text{flow}} \rangle}{\rho U A_{mp} |u'|^2} = - \frac{c_0}{c_{\text{eff}}} \frac{Pt}{4M} \left(\frac{\alpha_{\text{corr.flow}}^+}{1+2M} + \frac{\alpha_{\text{corr.flow}}^-}{1-2M} \right) \quad (\text{C.1})$$

with c_{eff} the effective speed of sound in the corrugated duct, Pt the pitch and $\alpha_{\text{corr.flow}}^\pm$ the flow-dependent part of the damping coefficient measured with flow. In particular, the final damping including the correction for convection is $\alpha_{\text{corr.U}}^\pm = \frac{1}{1 \pm 2M} (\alpha_{\text{corr.flow}}^\pm + \alpha_{\text{corr.0}})$, where $\alpha_{\text{corr.0}}$ is the steady damping, i.e. independent from the flow velocity. $\langle P_{\text{flow}} \rangle$ is defined as the power produced by the flow. It is therefore positive when there is amplification, that is, when $\alpha_{\text{corr.flow}}^\pm$ is negative. The power $\langle P_{\text{flow}} \rangle$ corresponds to the time-averaged source power for a single corrugation cavity, as computed in Golliard (Nakiboğlu et al., 2012; Golliard et al., 2013b).

Figure C.7 shows the non-dimensional power as function of the Strouhal number calculated by using as characteristic length the sum of the width and the upstream radius, multiplied by a factor $1 \pm M$.

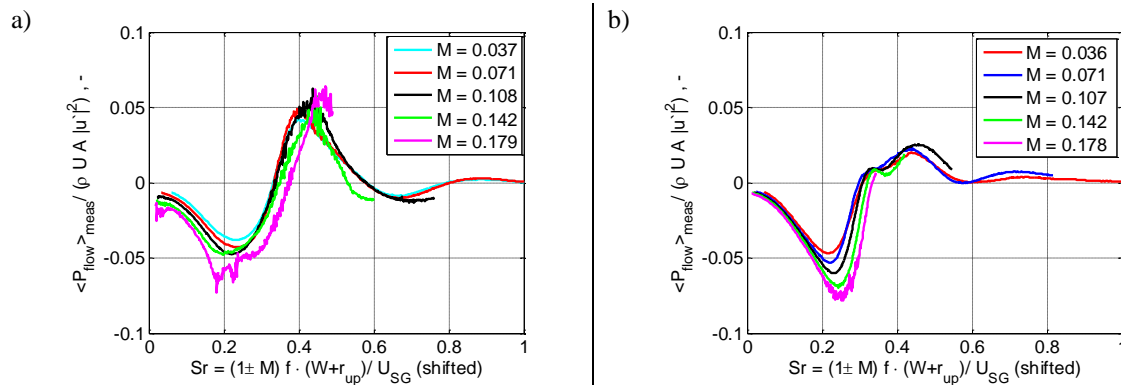


Figure C.11. Corrugated pipe, configuration A (a) and configuration B (b). Measured non-dimensional time-averaged source power for a single pitch of the 30 mm pipe as function of the (shifted) Strouhal number.

References

- Aurégan, Y., and Leroux M., 2003, “Failures in the discrete models for flow duct with perforations: an experimental investigation,” *Journal of Sound and Vibration*, 265(1): 109-121.
- Belfroid, S.P.C., Shatto D.P., and Peters M.C.A.M., 2007, “Flow-Induced Pulsations caused by corrugated tubes,” *ASME Pressure Vessels & Piping Conference*, San Antonio, Texas, USA.
- Burstyn, W., 1922, “Eine neue pfeife (a new pipe),” *Z. Tech. Phys.*, 3: 179-180.
- Cadwell, L.H., 1994, “Singing Corrugated pipes revisited,” *American Journal of Physics*, 62(3): 224-227.
- Cermak, A.F., 1922, “Über die tonbildung bei metallschläuchen mit eingedrücktem spiralgang (on the sound generation in flexible metal hoses with spiraling grooves),” *Phys. Z.*, 23: 394-397.
- Crawford, F.S., 1974, “Singing corrugated pipes,” *American Journal of Physics*, 42(4): 278-288.
- Curle, N., 1955, “The influence of solid boundaries upon aerodynamic sound,” *Proceedings of the Royal Society of London A*, 231: 505-514.

- Davies, P.O.A.L., 1988, "Practical flow duct acoustics," *Journal of Sound and Vibration*, 124(1): 91-115.
- Dokumaci, E., 1995, "On transmission of sound in circular and rectangular narrow pipes with superimposed mean flow," *Journal of Sound and Vibration*, 210(3), 375-389.
- Elliott, J.W., 2004, "Corrugated pipe flow," in *Lecture Notes on the Mathematics of Acoustics*, M.C.M. Wright, Ed., Imperial College Press, 207-222.
- Golliard, J., Belfroid S.P.C., and Vijlbrief O., 2013a, "Acoustic damping in smooth and corrugated pipes with and without liquid injection," *ASME Pressure Vessels & Piping Conference*, Paris, France.
- Golliard, J., González Díez N., Belfroid S.P.C., Nakiboğlu G., and Hirschberg A., 2013b, "U-Rans model for the prediction of the acoustic sound power generated in a whistling corrugated pipe," *ASME Pressure Vessels & Piping Conference*, Paris, France.
- Golliard, J., Belfroid S.P.C., Vijlbrief O., and Lunde K., 2015, "Direct measurements of acoustic damping and sound amplification in corrugated pipes with flow," *ASME Pressure Vessels & Piping Conference*, Boston, Massachusetts, USA.
- Golliard, J., Sanna F., Violato D., and Aurégan Y., 2016, "Measured Source Term in Corrugated Pipes with Flow. Effect of Diameter on Pulsation Source," 22nd *AIAA/CEAS Aeroacoustics Conference*, Lyon, France (submitted).
- Goyder, H., 2009, "On the modelling of noise generation in corrugated pipes," *ASME Pressure Vessels & Piping Conference*, Prague, Czech Republic.
- Gutin, L., 1948, "On the sound field of a rotating propeller," NACA TM No1195, Original in Russian: *Zhurnal Tekhnicheskoi Fiziki* 1936, 12: 76-83.
- Howe, M.S., 1995, "The damping of sound by wall turbulent shear layers," *Journal of Acoustical Society of America*, 98(3): 1723-1730.
- Kop'ev, V.F., Mironov M.A., and Solntseva V.S., 2008, "Aeroacoustic interaction in a corrugated duct," *Acoustical Physics*, 54(2): 197-203.
- Kristiansen, U.R., and Wiik G.A., 2007, "Experiments on sound generation in corrugated pipes with flow," *Journal of Acoustical Society of America*, 121(3): 1337-1344.
- Nakamura, Y., and Fukamachi N., 1991, "Sound generation in corrugated tubes," *Fluid Dynamics Research*, 7(5-6): 255-261.
- Nakiboğlu, G., Belfroid S.P.C., Willems J.F.H., and Hirschberg A., 2010, "Whistling behavior of periodic systems: corrugated pipes and multiple side branch system," *International Journal of Mechanical Science*, 52(11): 1458-1470.
- Nakiboğlu, G., Manders, H. B. M., and Hirschberg, A., 2012, "Aeroacoustic power generated by a compact axisymmetric cavity: Prediction of self-sustained oscillation and influence of the depth," *Journal of Fluid Mechanics*, 703: 163-191.
- Petrie, M.A., and Huntley I.D., 1980, "The acoustic output produced by a steady airflow through a corrugated duct," *Journal of Sound and Vibrations*, 70(1): 1-9.

Popescu, M., Johansen S.T., and Shyy W., 2009, "A model for flow-induced acoustics in corrugated pipes," 47th *AIAA Aerospace Sciences Meeting*, Orlando, Florida, USA.

Serafin, S., and Kojs J., 2003, "The voice of the dragon: A physical model of a rotating corrugated tube," 6th *International Conference on Digital Audio Effects (DAFex-03)*, London, U.K.

Silverman, M.P., and Cushman G.M., 1989, "Voice of the dragon: The rotating corrugated resonator," *European Journal of Physics*, 10(4): 298-304.

Ziada, S., and Bühlmann E.T., 1991, "Flow-Induced Vibrations in long corrugated pipes," *IMechE, England International conference on Flow-Induced Vibrations*.

Curriculum Vitae

- 15 October 1987 Born in Sassari (Italy)
- 2006-2009 **Bachelor of Science in Aerospace Engineering**
University of Pisa
Thesis: *Fluidodynamic characteristics of airfoils at low Reynolds numbers for wind turbines applications*
- 2009-2012 **Master of Science in Aerospace Engineering**
Specialization: Aerodynamics
University of Pisa
Thesis: *Parametric Uncertainty Quantification and calibration of the K-epsilon turbulence model by generalized Polynomial Chaos*
- 2012-2015 **Scientist Innovator**
TNO, Dept. of Heat Transfer and Fluid Dynamics
Delft, The Netherlands
- 2012-2016 **Ph.D. in Mechanical Engineering**
Laboratoire d'Acoustique de l'Université du Maine (LAUM)
Thesis: *Interaction between Flow Induced Pulsations and Multiphase Flows in Gas-Liquid Systems*
Université du Maine
Le Mans, France

Thèse de Doctorat

Francesco SANNA

Oscillations auto-induites en systèmes de conduites en présence d'écoulement diphasique air/eau

Interaction between Flow-Induced Pulsations and Multiphase flows in gas-liquid systems

Résumé

Le couplage entre un écoulement instable et des résonances acoustiques dans des systèmes de conduites peut conduire à des phénomènes d'oscillations auto-induites. Ce type de phénomènes trouve principalement place dans des conduites latérales fermées, par exemple dans des systèmes de transport ou de compression de gaz. L'objectif de ce travail est d'étudier les oscillations auto-induites dans le cas où le fluide transporté ne se limite pas à un gaz, mais est un mélange de gaz et de liquide. Les pulsations sont mesurées dans des conduites latérales fermées, pour deux types de configurations (en tandem et en croix), avec écoulement d'un mélange variable d'air et d'eau. La position de l'injection d'eau est variable afin d'obtenir plusieurs régimes d'écoulement diphasique. Les résultats indiquent que la présence d'eau a un effet important sur les niveaux de pulsations dans les conduites. Cet effet a pu être attribué à deux mécanismes dus à la présence d'eau : les instabilités de couches de mélange sont modifiées et l'amortissement des ondes acoustiques est amplifié.

Le deuxième mécanisme a été quantifié à l'aide de mesures sur un montage expérimental dédié conçu pour avoir un écoulement stratifié. On a observé que, dans tous les cas, la présence d'eau augmente l'amortissement. Cette augmentation a pu être attribuée à la réduction de la section effective de la conduite (due au remplissage partiel par l'eau) et à l'augmentation de la friction turbulente à l'interface entre les phases liquide et gazeuse.

Mots clés

Oscillations auto-induites, Conduites latérales fermées, Ecoulement diphasique stratifié, Acoustique, Turbulence, Cavité résonnantes profondes, Amortissement acoustique.

Abstract

Coupling between flow instabilities and acoustic resonances in ducts with closed side branches leads to Flow Induced Pulsations (FIPs). This is a typical phenomenon in engineering applications (gas transport systems, compressor installations, and chemical plants). The objective of this work is to extend the knowledge about FIPs when the transported medium is not uniquely gas but a combination of gas and (a small quantity of) liquid. For two configurations of double side branches (in tandem and in quasi-cross), the amplitude of pressure pulsations in the side branches was measured for different liquid injection rates. This was repeated with the liquid injection point located at different places to allow different flow regimes at the pipe connections. The results show a strong effect of the water content on the pulsations. On basis of these results and additional measurements, the following hypotheses for the effect of liquid were made: (1) interaction of the liquid with the flow instability and (2) increase of the acoustical damping in the ducts in presence of liquid.

The effect of liquid on damping was measured with a dedicated test setup designed to have a stratified flow. It was found that the liquid always increases the acoustical damping, mainly due to the reduction of the effective cross section by the liquid, and because of the increased turbulent friction at the interface between gas and liquid.

Key Words

Flow Induced Pulsations, Side branch, Multiphase stratified flow, Acoustics, Turbulence, Deep cavities, Acoustical damping.